

2020

## Design and Optimization of Dynamic System for a One-kW Free Piston Linear Engine Alternator-GENSETS Program

Nima Zamani Meymian

West Virginia University, [nizamanimeymian@mix.wvu.edu](mailto:nizamanimeymian@mix.wvu.edu)

Follow this and additional works at: <https://researchrepository.wvu.edu/etd>



Part of the [Acoustics, Dynamics, and Controls Commons](#), [Computer-Aided Engineering and Design Commons](#), and the [Electro-Mechanical Systems Commons](#)

---

### Recommended Citation

Zamani Meymian, Nima, "Design and Optimization of Dynamic System for a One-kW Free Piston Linear Engine Alternator-GENSETS Program" (2020). *Graduate Theses, Dissertations, and Problem Reports*. 7927.

<https://researchrepository.wvu.edu/etd/7927>

This Dissertation is protected by copyright and/or related rights. It has been brought to you by the The Research Repository @ WVU with permission from the rights-holder(s). You are free to use this Dissertation in any way that is permitted by the copyright and related rights legislation that applies to your use. For other uses you must obtain permission from the rights-holder(s) directly, unless additional rights are indicated by a Creative Commons license in the record and/ or on the work itself. This Dissertation has been accepted for inclusion in WVU Graduate Theses, Dissertations, and Problem Reports collection by an authorized administrator of The Research Repository @ WVU. For more information, please contact [researchrepository@mail.wvu.edu](mailto:researchrepository@mail.wvu.edu).

2020

## Design and Optimization of Dynamic System for a One-kW Free Piston Linear Engine Alternator-GENSETS Program

Nima Zamani Meymian

Follow this and additional works at: <https://researchrepository.wvu.edu/etd>



Part of the [Acoustics, Dynamics, and Controls Commons](#), [Computer-Aided Engineering and Design Commons](#), and the [Electro-Mechanical Systems Commons](#)

---

# **Design and Optimization of Dynamic System for a One-kW Free Piston Linear Engine Alternator-GENSETS Program**

Nima Zamani Meymian

Dissertation Submitted  
to the Benjamin M. Statler College of Engineering and Mineral Resources  
at West Virginia University  
In partial fulfillment of the requirements for the degree of

Doctor of Philosophy in Mechanical Engineering

Gregory Thompson, Ph. D., Chair  
Nigel Clark, Ph. D.  
Derek Johnson, Ph. D.  
Terence Musho, Ph. D.  
Parviz Famouri, Ph. D.

Mechanical and Aerospace Engineering Department  
Morgantown, West Virginia  
August 2020

**Key Words:** *Flexure Spring, Linear Bearing, Design, Optimization, Structural Dynamics,  
GENSETS*

**Copyright 2020 Nima Zamani Meymian**

# **Abstract**

## **Design and Optimization of Dynamic System for a One-kW Free Piston Linear Engine Alternator-GENSETS Program**

Nima Zamani Meymian

In power/energy systems, free-piston linear machines are referred to as a mechanism where the constrained crank motion is eliminated and replaced with free reciprocating piston motion. Depending on the application, the piston motion can be converted into other types of energy and includes compressed air/fluid, electricity, and high temperature/pressure gas. A research group at West Virginia University developed a free-piston linear engine alternator (LEA) in 1998 and have achieved significant accomplishment in the performance enhancement of the LEAs to date. The present LEA design incorporates flexure springs as energy restoration components and as bearing supports. The advantages of using flexure springs are threefold and include: (1) it increases the LEA's stiffness and resonant frequency, and hence the power density; (2) it eliminates the need for rotary or linear bearings and lubrication system; and (3) it reduces the overall frictional contact area in the translator assembly which improves the durability.

The current research focuses on the design and optimization of the flexure springs as the system's resonant dominating component for a 1 kW free-piston LEA. First, the flexure springs were characterized according to the LEA's target outputs and dimensional limitations. The finite element method (FEM) was used to analyze the stress/strain, different modes of deformation, and fatigue life of a range of flexure spring designs under dynamic loadings. Primary geometric design variables included the number of arms, inside and outside diameter, thickness, and arm's length. To find the near-optimum designs, a machine learning algorithm incorporating the FEM results was used in order to find the sensitivity of the target outputs to the geometrical parameters. From the results, design charts were extracted as a guideline to flexure spring selection for a range of operations. Then, methods were introduced, investigated, and analyzed to improve the overall energy conversion performance and service life of the flexure springs and the overall LEA system.



These included: a transient FE tool used for fatigue analysis to quantify the life and factors of safety of the flexure springs as well as the spring's hysteresis; a fluid/structure interaction model used to quantify the energy loss due to drag force applied on the flexures' side surfaces; packaging of multiple flexures to increase the overall stiffness and to reduce the vibration-induced stresses on flexure arms due to higher harmonics; a model to investigate the two-way interactions of the flexures' dynamics with the alternator and engine components to find an optimum selection of the LEA's assembly; a non-linear friction analysis to identify/quantify the energy losses due to the friction of the sliding surfaces of the flexures and spacers; and a series of static and transient experiment to determine the non-linearity of flexures' stiffness and comparison to FEM results and for validation of the energy audit results from numerical and analytical calculations.

With over 6000 flexure designs evaluated using artificial intelligent methods, the maximum achievable resonant frequency of a single flexure spring for a 1 kW LEA was found to be around 150 Hz. From the FEM results, it was found that under dynamic conditions the stress levels to be as high as twice the maximum stress under static (or very low speed) conditions. Modifications of the arm's end shape and implementation of a shape factor were found as effective methods to reduce the maximum stress by 20%. The modal analysis showed that the most damaging modes of deformations of a flexure spring were the second to fourth modes, depending on the number of arms and symmetry of the design. Experiment and FEM results showed that using bolted packaging of the springs can damp a portion of the vibration and improve the performance. The drag force loss was found to account for 10-15% of the mechanical losses in a 100  $W_{\text{net}}$  LEA prototype. From the manufacturing perspective, use of water jet was found the most economical method for manufacturing the flexures which could make the commercial production of the LEAs feasible; however, for high-efficiency, high-durability machines, additional material treatments, and alternative manufacturing methods are essential.

## **Dedication**

**This dissertation is dedicated to my family for their endless  
love and support**

# Acknowledgment

First and foremost, I would like to thank my adviser, Dr. Gregory Thompson, for the valuable support and guidance he has provided me throughout my Ph.D. research. I express my appreciation to my committee members from West Virginia University, Dr. Nigel Clark, Dr. Parviz Famouri, Dr. Derek Johnson, and Dr. Terence Musho for their assistance and technical help that has helped me complete this research.

My warmest gratitude goes to my wife and my family for their support, and patience through the last few years of my Ph.D. program at West Virginia University.

I thank Dr. Jayaram Subramanian, Dr. Mehar Bade, and Mr. Gregory Heiskell, my colleagues in the Electromechanical Systems Lab for their assistance in my projects.

Lastly, I would like to especially thank Mr. Andrew Devillier, a material engineer at Volvo Group Trucks, for his contribution to my research.

# Table of Content

<b>1</b>	<b>Introduction.....</b>	<b>1</b>
1.1	Combined Heat and Power Generation .....	2
1.2	GENSETS Program in WVU .....	3
1.3	Research Goals and Objectives .....	4
1.3.1	<i>Design and Optimization of Flexure Springs via Finite Element Analysis (FEA)</i> .....	6
1.3.2	<i>Energy Analysis of Flexure Springs</i> .....	6
1.3.3	<i>Investigation of the LEA Assembly Dynamic Behavior via FEA</i> .....	6
1.3.4	<i>Experimental Validation</i> .....	7
1.3.5	<i>Design Improvement and Efficiency Enhancement</i> .....	7
<b>2</b>	<b>Literature Review .....</b>	<b>8</b>
2.1	Linear Devices.....	8
2.1.1	<i>Cylinder-Piston Arrangement</i> .....	9
2.1.2	<i>Applications</i> .....	12
2.2	Linear Engine Alternator.....	20
2.3	Current GENSETS Free-piston LEA project in WVU .....	27
2.3.1	<i>Linear Alternator</i> .....	29
2.3.2	<i>Two-stroke Engines</i> .....	31
2.3.3	<i>Flexure Springs (Bearings)</i> .....	33
<b>3</b>	<b>Design and Optimization of Flexure Springs .....</b>	<b>35</b>
3.1	Flexure Springs vs. Coil Springs .....	35
3.2	Flexure Springs vs. Gas Springs (bounce chamber).....	38
3.3	Flexure Design Approach.....	39
3.4	Flexure Design.....	40
3.4.1	<i>Material Selection</i> .....	40
3.4.2	<i>Flexure Arm Shape</i> .....	44
3.4.3	<i>Arm Shape Factor</i> .....	45
3.4.4	<i>Modification of Arm Curves</i> .....	46
3.4.5	<i>Modal Analysis</i> .....	46
3.4.6	<i>Moving Mass</i> .....	48
3.5	Analytical Solution.....	50
3.6	Design Optimization and Sensitivity Analysis .....	58

3.6.1	<i>Optimization of Steel Flexures</i> .....	59
3.6.2	<i>Optimization of Titanium Flexures</i> .....	66
3.6.3	<i>Design Points Data Analysis</i> .....	69
3.7	Experimental Verifications.....	76
<b>4</b>	<b>Manufacturing Methods and Statistical Analysis.....</b>	<b>80</b>
4.1	Material Properties .....	81
4.2	Machining Accuracy.....	84
4.3	Packaging Conditions Analysis .....	90
4.4	Packaging Force Experiments .....	93
4.5	Fatigue Fracture.....	96
4.6	Surface and Edge Quality .....	101
<b>5</b>	<b>Energy Performance Analysis .....</b>	<b>106</b>
5.1	Air Drag Viscous Damping .....	107
5.2	Experimental Validation.....	116
5.3	Vibration.....	118
5.4	Experimental Measurement.....	128
<b>6</b>	<b>The LEA Assembly Dynamic Analysis .....</b>	<b>133</b>
6.1	Test Setup .....	133
6.2	System Damping and Stiffness.....	136
6.3	Modal Analysis.....	140
6.4	FEA Parametric Study.....	144
6.4.1	<i>Translator and Frame Damping</i> .....	146
6.4.2	<i>Frame Stiffness</i> .....	147
6.4.3	<i>Frame Mass</i> .....	150
<b>7</b>	<b>Summary and Recommendations.....</b>	<b>152</b>
7.1	Summary.....	152
7.2	Major Findings .....	153
7.3	Recommendations for Future Work .....	160
<b>8</b>	<b>References .....</b>	<b>162</b>

<b>9</b>	<b>Appendix.....</b>	<b>174</b>
9.1	FEA: Preprocessing, Solution, and Postprocessing.....	174
9.1.1	CAD.....	174
9.1.2	FEA.....	175
9.1.3	Optimization.....	175
9.1.4	CFD.....	176
9.2	Stress-strain Test Rig.....	177
9.3	Analytical Solution Curve Fitting Performance.....	178
9.4	Parametric Study Charts for Titanium Material.....	180
9.5	Neural Network Performance Charts.....	183
9.6	Matlab Function.....	185

# Table of Figures

Figure 1. Sources of electricity generation in the US [9].	2
Figure 2. Comparison of (a) centralized, and (b) distributed electricity generation [10, 11].	2
Figure 3. LEA machine, 1- engine, 2- piston, 3- shaft, 4- flexure springs, 5- windings, 6- translator (moving magnets), 7- fixed frame.	4
Figure 4. Scope of research.	5
Figure 5. Free piston piston-cylinder arrangements [35].	10
Figure 6. Single piston linear alternator with turbocharger [35].	10
Figure 7. Single piston linear alternator with mechanical springs [37].	10
Figure 8. Linear alternator with permanent magnets [24].	11
Figure 9. Dual-piston linear alternator [44].	12
Figure 10. Opposed-piston linear alternator [45].	12
Figure 11. HCCI free-piston air compressor [27].	13
Figure 12. Single-stage air compressor [27].	14
Figure 13. Three-stage air compressor [27].	14
Figure 14. Four-stages air compressor [27].	15
Figure 15. Braun linear air compressor [27].	15
Figure 16. Free-piston single-stage hydraulic pump [27].	16
Figure 17. Schematic of free-piston gas generators [27].	17
Figure 18. Inward gas generator basic operation [27].	18
Figure 19. Pescara's gasifier design [27].	18
Figure 20. Sandia linear alternator early design [27].	19
Figure 21. Schematic of tubular brushless permanent magnet linear engine alternator [57].	20
Figure 22. Sandia National Lab opposed-piston linear alternator [62].	21
Figure 23. West Virginia University free-piston LEA [66].	23
Figure 24. German Aerospace Prototype [25].	25
Figure 25. The layout of the Free Piston Power Pack [79].	26
Figure 26. WVU free-piston LEA-Alpha prototype.	27
Figure 27. Flexural spring geometry. $a$ : outer diameter, $b$ : inner diameter, $c$ : arm width, $d$ : thickness.	35
Figure 28. Dimensional comparison of a flexure spring vs. coil springs.	36
Figure 29. Stiffness and moving mass comparison of flexure spring vs. coil springs.	37
Figure 30. S-N curves of 7C27Mo2 provided by the manufacturer [146]. At 700 MPa the probability of failure was extrapolated to be 1%.	44
Figure 31. Contours of the equivalent stress in MPa for two flexure designs with different spiral shape factor, a) $f = 0.05$ , b) $f = 0$ . The shape factor was one of the parameters used to control stress distribution within the arms. The objective was to distribute the maximum stress throughout the arms as shown for the left spring design compared to the right design.	45
Figure 32. Comparison of stress concentration in MPa at near center endpoints of a spiral cut with three different curve profiles. A tear-drop shape as illustrated in subfigure c significantly decreased stress concentration.	46
Figure 33. The first four mode shapes of a flexure. The contour colors correspond to a scaled displacement with red corresponding to the largest scaled displacement. The outermost radial edge was clamped ( $U_x=U_y=U_z=0$ ).	47
Figure 34. Moving mass percentage.	49
Figure 35. Involute of a circle [137].	51
Figure 36. Force and moments on flexure arms.	53
Figure 37. Comparison of the stiffness results of FEA and initial analytical solution.	56
Figure 38. Coefficients of spiral radius, thickness, and width for the analytical equation.	57
Figure 39. Improvement of the analytical equation in the prediction of one arm's stiffness.	58
Figure 40. Illustration of two fully parameterized models, left: design using the lower bounds, right: design using the upper bounds.	60
Figure 41. Response surface of interactions of outer diameter and sweep angle on frequency (a) and maximum equivalent stress (b), interactions of outer diameter and thickness on frequency (c) and	

maximum equivalent stress (d) and interactions of sweep angle and thickness on frequency (e) and maximum equivalent stress (f). .....	62
Figure 42. Response profile of interactions of number of arms and outer diameter on frequency (a) and maximum equivalent stress (b), interactions of number of arms and thickness on frequency (c) and maximum equivalent stress (d) and interactions of number of arms and sweep angle on frequency (e) and maximum equivalent stress (f). .....	63
Figure 43. Sensitivity charts for design parameters of a flexure with, a) 4 arms, b) 5 arms, c) 6 arms, d) 7 arms. The inner circles are associated with stress and the outer circles are associated with frequency. Sweep angle is demonstrated to have the most influence on both stress and frequency. ....	64
Figure 44. Scattered distribution of design points in frequency/stress chart for a single steel spring. ....	65
Figure 45. Scattered distribution of design points in frequency/stress chart for a single titanium spring. ....	66
Figure 46. Comparison of the maximum resonant frequency of titanium and steel flexures. ....	67
Figure 47. Selected points on the flexure arm. ....	68
Figure 48. Log-log diagram of stress linearity at points along the flexure's arm length. ....	68
Figure 49. Schematic of the neural network model. ....	70
Figure 50. All steel flexure design points pool sorted by the design parameters. ....	71
Figure 51. Steel flexure design points vs. number of arms. left: colored by outer diameter, right: colored by frequency. ....	75
Figure 52. Static test rig with a custom fixture. Label a) is the signal processor, b) is the Shimadzu load frame, and c) is the flexure and fixture. Figure c depicts the placement of strain gauges on the arms of the flexure spring. ....	76
Figure 53. Comparison of FEA and Experimental results of the flexure stiffness as a function of displacement. ....	77
Figure 54. Stiffness linearity of a spring assembly (more than one spring in series). ....	78
Figure 55. Strain gauge measurement at selected locations (see Figure 12c) compared to FEA results of strain at fixed velocity deflection test. Solid lines denote experimental values and dashed lines correspond to FEA values. ....	79
Figure 56. Flexure springs made using EDM (left) and waterjet (right) methods. ....	81
Figure 57. MTS machine (left), Waterjet machine (right). ....	82
Figure 58. Manufactures specimens, finished and unfinished surface (right). ....	83
Figure 59. Sandvik material tensile test results. ....	84
Figure 60. Waterjet kerf angle effect [159]. ....	85
Figure 61. Waterjet nozzle height effects [159]. ....	85
Figure 62. Comparison of directional stiffness of twelve Sandvik flexures, blue: side 1, red: side 2. X axis is deflection in mm and Y axis is the stiffness in kN/m. ....	87
Figure 63. Comparison of directional stiffness of twelve titanium flexures, blue: side 1, red: side 2. X axis is deflection in mm and Y axis is the stiffness in kN/m. ....	88
Figure 64. Sandvik steel stiffness variations with displacement. ....	89
Figure 65. Titanium stiffness variations with displacement. ....	90
Figure 66. Spacer geometry effect on Von-misses stress. ....	91
Figure 67. Flexure-shaft connections variations experiment. ....	92
Figure 68. Stiffness results vs. shaft connections conditions. ....	93
Figure 69. Bolt torque comparison – titanium springs, thin spacers. ....	94
Figure 70. Bolt torque comparison – steel springs, thin spacers. ....	95
Figure 71. Bolt torque comparison – steel springs, thick spacers. ....	96
Figure 72. Fractured flexures, left: Sullivan steel, middle: titanium 6246, right: Sandvik steel. ....	97
Figure 73. Cross section view of Von-misses stress on flexure's arms. ....	98
Figure 74. Schematic representation of fatigue fracture surface marks produced in square and rectangular. ....	99
Figure 75. Fractured surface of left: Sandvik steel, middle: Sullivan steel, right: titanium flexure springs. ....	100
Figure 76. Water jet cut quality of side surfaces: a) Sandvik steel, b) Sullivan steel, c) Sandvik steel-tumbled, d) titanium. ....	102
Figure 77. Two sides of a titanium flexure at the same location. ....	103
Figure 78. Two sides of a steel flexures made by top: waterjet, middle: EDM, bottom: CNC. ....	104
Figure 79. Solid and fluid domains in fluid/structure modeling. ....	109
Figure 80. Flow velocity streamlines and vectors around one oscillating flexure spring (t is normalized time during one cycle of oscillation). ....	110



Figure 81. Cyclic variation of drag coefficient vs. outer diameter of flexure. ....	111
Figure 82. Cyclic variation of drag coefficient vs. gap width of flexure.....	112
Figure 83. Cyclic variation of drag coefficient vs. stroke length.....	112
Figure 84. Cyclic variation of drag coefficient vs. oscillating frequency.....	113
Figure 85. Effective velocity.....	114
Figure 86. Variation of drag force versus distance between two adjacent flexure springs over one cycle. ....	115
Figure 87. Integrated drag force on one flexure spring over one cycle.....	115
Figure 88. Vacuum test cell.....	117
Figure 89. Windage power loss.....	118
Figure 90. Flexure's first four modes of deformation.....	119
Figure 91. Selected points on steel (left) and titanium (right) flexures. ....	120
Figure 92. Amplitude of displacement at different locations of a titanium flexure's arm.....	123
Figure 93. Amplitude of displacement at different locations of a steel 'flexure's arm. ....	124
Figure 94. Two-cycle conversion of potential energy (solid lines) and kinetic energy (dashed lines) - titanium flexure.....	126
Figure 95. Two-cycle conversion of potential energy (solid lines) and kinetic energy (dashed lines) - steel flexure.....	126
Figure 96. Averaged potential and kinetic energy-per-cycle for steel (blue) and titanium (orange).....	128
Figure 97. Decay of displacement amplitude of oscillation. ....	129
Figure 98. Vibrational power loss of alternator vs. time. ....	130
Figure 99. Vibrational power loss of alternator vs. stroke length. ....	131
Figure 100. Resonant frequency vs. number of flexure springs. ....	131
Figure 101. Damping ratio vs. number of flexure springs. ....	132
Figure 102. Damping test setup: 1-LEA machine, 2-signal changing knobs, 3-scopes/power analyzer, 4-shock absorbers, 5-fixed table, 6-high-voltage power supply, 7-low-voltage power supplies, 8-microcontroller, 9-translator linear position sensor, 10-frame lateral position sensor, 11-frame linear position sensor..	134
Figure 103. Two types of shear mounts. ....	135
Figure 104. Translator vs frame vibration, top: 8 springs, blue mount, bottom: 8 springs, black mount. ....	136
Figure 105. LEA damping characteristics, left: damping ratio, middle: mass damping ratio ( $\alpha$ ), right: stiffness damping ratio ( $\beta$ ).....	137
Figure 106. FFT Graphs of LEA with blue shear mounts vs. number of springs, left: translator oscillations, right: frame vibration. ....	138
Figure 107. FFT Graphs of LEA with black shear mounts vs. number of springs, left: translator oscillations, right: frame vibration. ....	139
Figure 108. LEA machine resonating mode shapes. ....	141
Figure 109. Damping ratio vs. number of flexure springs. ....	142
Figure 110. Frequency vs. number of flexure springs, left: translator, right: frame.....	144
Figure 111. Reduced geometry of LEA for the transient FEA analysis. ....	145
Figure 112. Effects of translator and frame damping on the dynamic behavior of LEA. ....	147
Figure 113. Effects of frame stiffness on the dynamic behavior of LEA.....	149
Figure 114. Effects of frame mass on the dynamic behavior of LEA.....	151
Figure 115. Curve fitting details for non-dimensionalized coefficients, top: $C_r$ , middle: $C_{th}$ , and bottom: $C_w$ .....	179
Figure 116. Titanium material - response surface of interactions of outer diameter and sweep angle on frequency (a) and maximum equivalent stress (b), interactions of outer diameter and thickness on frequency (c) and maximum equivalent stress (d) and interactions of sweep angle and thickness on frequency (e) and maximum equivalent stress (f). ....	180
Figure 117. Titanium material - response profiles of interactions of number of arms and outer diameter on frequency (a) and maximum equivalent stress (b), interactions of number of arms and thickness on frequency (c) and maximum equivalent stress (d) and interactions of number of arms and sweep angle on frequency (e) and maximum equivalent stress (f). ....	181
Figure 118. Titanium material - sensitivity charts for design parameters of a flexure with, a) 4 arms, b) 5 arms, c) 6 arms, d) 7 arms. The inner circles are associated with stress and the outer circles are associated with frequency. Sweep angle is demonstrated to have the most influence on both stress and frequency. ....	182
Figure 119. Performance and error results of Bayesian Regularization NN method. ....	183
Figure 120. Performance and error results of Bayesian Regularization NN method. ....	184

## Table of Tables

Table 1. Summary of free-piston applications [27].	19
Table 2. Summary of advantages and disadvantages of two-stroke engines [87].	31
Table 3. Physical properties of flexure and coil springs.	37
Table 4. Operational properties comparison of the selected springs.	38
Table 5. Properties of high fatigue life materials currently available from suppliers*.	42
Table 6. Statistical data of 7C27Mo2 fatigue test.	43
Table 7. Design explorer parameters' ranges.	55
Table 8. Independent variable ranges used for the presented design study.	59
Table 9. Material properties of the steel used in the simulation to evaluate geometric influence.	60
Table 10. Comparison of manufacturing methods.	81
Table 11. Flexure's deformation modes frequencies.	119
Table 12. LEA's deformation modes resonant frequencies (Hz).	143

## Nomenclature

BC	Boundary conditions
BTE	Brake thermal efficiency
CAD	Computer aided design
CFD	Computational fluid dynamics
CHP	Combined heat and power
CI	Compression ignited
CNC	Computer numerical control
COV	Coefficient of variation
CR	Compression ratio
DOE	Department of Energy
DSP	Digital signal processor
EDM	Electrical discharge machining
EGR	Exhaust gas recirculation
EMF	Electric and magnetic fields
FE	Finite element
FEA	Finite element analysis
FEM	Finite element method
FFT	Fast Fourier Transform
FPE	Free piston engine
FSI	Fluid structure interactions
HCCI	Homogeneous charge compression ignition
KE	Kinetic energy
LEA	Linear alternator engines
NG	Natural gas
NN	Neural network
OD	Outer diameter
PE	Potential energy
SI	Spark ignited
SNL	Sandia National Lab
TDC	Top dead center
US	United States
USD	US Dollar
WVU	West Virginia University

# 1 Introduction

Energy utilization and emissions from fossil-fueled combustion have been at the forefront of engine design since the 1960s due to the Clean Air Act, subsequent amendments, and regulations [1]. Electrical power generation from fossil-based fuels in the United States (US), and elsewhere, are characterized as boiler-based Rankine cycle, gas turbine-based Brayton cycle, or reciprocating internal combustion engine-based Otto or Diesel cycles. Other cycles exist but have not seen wide-scale commercialization. Fuels have historically been coal for the Rankine cycle, natural gas (NG) for the Brayton cycle, fuel oil for the Diesel cycle, and natural gas or gasoline for the Otto cycle. Natural gas is considered as a significant energy source due to its domestic availability, lower price, and less harmful environmental impacts [2]. Currently, many of the power generation plants rely on natural gas in large scales [3].

According to [4], the current large scale power generation plants have an averaged thermal efficiency of between 30-40%. The numbers will change by the technology and fuel used. For example, coal and NG power plants have thermal efficiencies at 33% and 43%, respectively. With the economic recovery of natural gas from shale and the significant long-term availability, the US has considered shifting the concept of centralized power generation to a local power generation at the end user [5]. The Advanced Research Projects Agency-Energy (ARPA-E) of the US Department of the Energy (DOE), has been exploring the potential in high-efficiency decentralized power generation. The program Generators for Small Electrical and Thermal Systems (GENSETS) objective is to develop small unit combined heat and power generation (CHP) using natural gas for household applications [6]. Over 60% of US households have access to natural gas. Currently, the main usage of natural gas in the household-scale is for heating and cooking purposes [7, 8]. Figure 1 indicates sources of electricity generation in the US over about 70 years. As shown, the NG has become the main source of electricity generation.

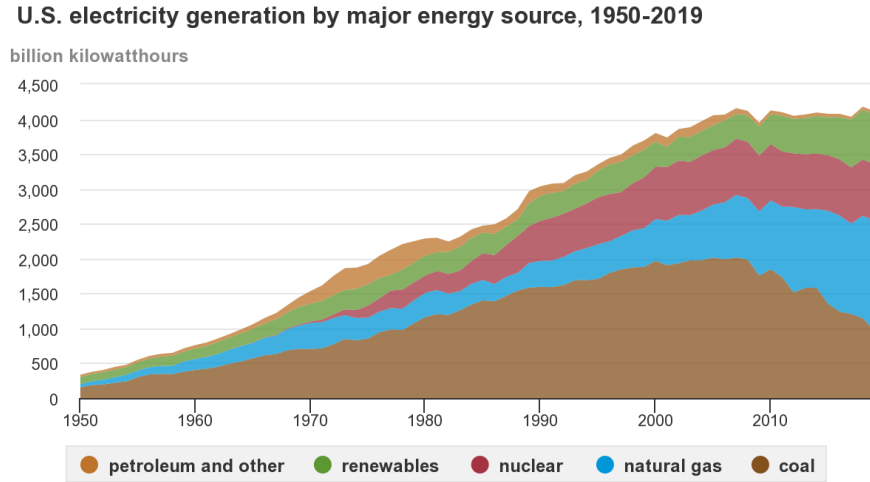


**Figure 1. Sources of electricity generation in the US [9].**

### 1.1 Combined Heat and Power Generation

The final goal of the GENSETS projects is to develop a 1 kW CHP unit with NG fuel [6]. As mentioned above, the fuel to electricity efficiency of the unit must be at a level that can compete with the current power generation methods and transmission. Combining power and heat cycles is a well-proven approach to achieve this goal. The heat generated by the engine that is normally rejected to the ambient can be utilized mainly for space heating and warm water supply in homes. The way that CHP units help reduce the emission is another key point that the Environmental Protection Agency (EPA) has focused on CHP units. Figure 2 shows a schematic of the centralized and distributed electricity generation.

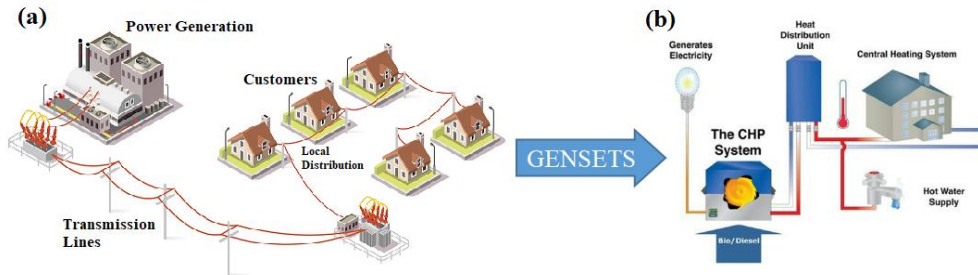


**Figure 2. Comparison of (a) centralized, and (b) distributed electricity generation [10, 11].**

The CHP units using waste heat recovery can increase the combined utilization factor and thermal efficiency to around 85% [12]. However, designing and operating CHP units are more complex and cost more compared to single-cycle power generation methods. Ondek et al. provided a CHP unit for residential applications [13]. Bianchi studied micro-CHP units for homes and analyzed the viability of such systems [14]. They reported the sizing as a key factor for CHP units in small scales.

Research provided in [15] studied high-efficiency economic CHP systems and showed the advantages of decentralized power generation. The results stated that a proper CHP design with NG fuel can reduce GHG and NO<sub>x</sub> emissions. The case study was a 10 kW CHP with NG fuel and advanced internal combustion technologies. They mentioned the Atkinson combustion cycle as a promising approach to achieve higher efficiencies between 24-31.5% [16]. Mikalsen implemented a Miller and Otto cycle to be used in CHP units and reported higher efficiency but lower power density in the Miller cycle [17]. Honda has also worked extensively on efficient CHP systems. They introduced a small unit with a 1.5 kW power capacity using the Atkinson cycle [18]. In [19], details of a commercial 5 kW CHP unit were provided.

## **1.2 GENSETS Program in WVU**

The development of a 1 kW free-piston linear engine alternator was funded by ARPA-E and was a part of the GENSETS program at West Virginia University (Award Number: DE-AR0000608). The final goal is to design and develop a 1 kW electricity generator with the fuel-to-electricity efficiency of more than 30% and low cost – ~3000 USD - that can be used for household applications using residential natural gas which can continuously operate for an extended time (10 years) without major maintenance. The 1 kW output capacity of the generator has been defined to provide the average household electricity consumption in the US [20, 21]. In addition to all of the above challenging conditions, the overall cost including the machine, operation, and maintenance must be reasonable and comparable with the current electricity produced and distributed from existing power plants.

The selection of a linear mechanism for the GENSETS targets was because of the inherited simplicity and higher power density of linear systems compared to rotary generators combined

with reciprocating or slider-crank engines. The conventional cranked powertrain causes additional mechanical losses due to the friction in bearings and the side thrust on piston rings and skirt. Also, a portion of the generated power is consumed by the valve train which reduces the overall efficiency of the slider-crank engines. Solutions to overcome these deficiencies lead to more cost and complexity.

On the other hand, linear powertrain systems have the main advantage of a reduced number of moving parts. This will result in higher power density and hence improved thermal efficiency. The lower friction and moving parts also cause enhanced robustness of the system and longer service life. A scemaic of the proposed LEA machine and its main components are shown in Figure 3. The focus of this research is on the structural dynamics and design/development of the spring system.

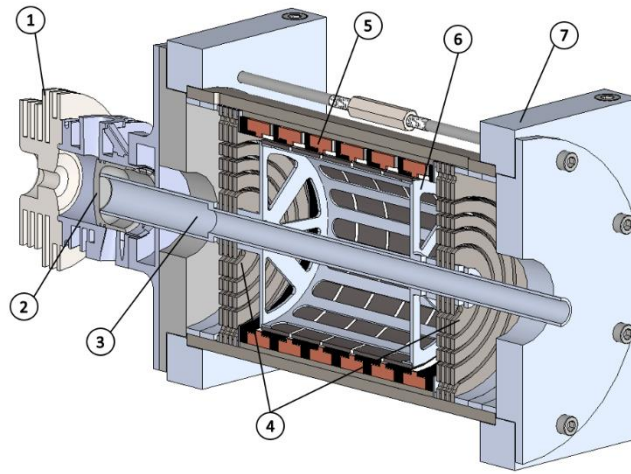


**Figure 3. LEA machine, 1- engine, 2- piston, 3- shaft, 4- flexure springs, 5- windings, 6- translator (moving magnets), 7- fixed frame.**

### **1.3 Research Goals and Objectives**

The core of the proposed research is the study of the dynamic behavior of the LEA incorporating flexure springs as the main suspension components of the LEA and the development of methods and strategies to enhance the overall efficiency of the LEA. The current LEA design has considerable mechanical energy losses; these losses include damped vibration, aerodynamic drag, and friction. The LEA machine has an objective life of 10 continuous years with only yearly maintenance. In the current machine, flexure springs play an important role in the overall

performance for achieving the final targets. Finite Element Analysis (FEA) results have shown that modifications in the design and application of the flexure springs within the LEA can improve their efficiency and life. This research will investigate the design and dynamic behavior of a flexure-spring-assisted LEA in detail to enhance the efficiency of the LEA.

The research will focus on the flexure springs-first as an individual mechanical spring and then as a subassembly of the LEA. The outline of the research is divided into four main parts. The main objective of each part is highlighted in Figure 4 and will be discussed in more detail in the following sections.

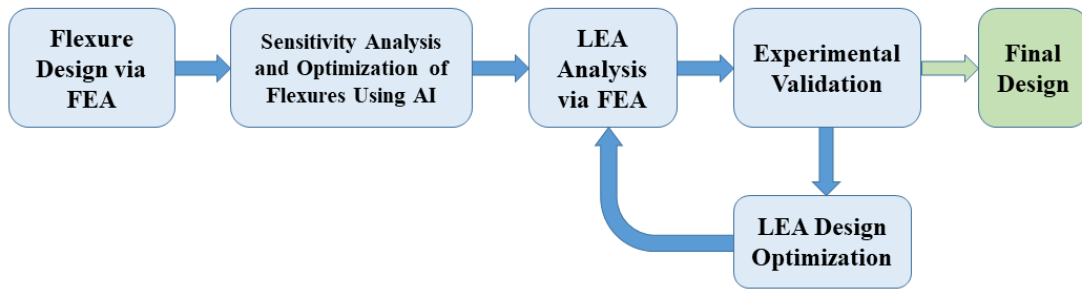


**Figure 4. Scope of research.**

The main tool used to complete this research was FEA. FEA was specifically used for the stress/strain analysis of flexure springs. Also, in the performance analysis of the individual springs and also linear machine assembly, developing test rigs and instrumentation could be very expensive. Hence, FEA was also used for the performance analysis of the LEA system. In addition, for validation of the numerical results, experiments were performed.

Ultimately, the dissertation provides a comprehensive database and methodology for the flexure design for the LEAs in the range of less than 5 kW power output. Practical design charts with tested geometrical design improvement methods are amongst the primary results of this research. In the following sections, several energy-related and packaging criteria are introduced to be considered in flexure-assisted machines. These criteria are investigated and characterized for a range of operations. Also, methods related to the application of the flexure springs that can be implemented to enhance the overall performance are introduced and analyzed for the other applications and future systems. The outlines of the research can be categorized into five main sections as follows.



### **1.3.1 Design and Optimization of Flexure Springs via Finite Element Analysis (FEA)**

The main purpose of this section is to identify all parameters involved in the flexure spring design and use an optimization algorithm to design a system with high natural frequency in the range of 60-80 Hz and an extended life span of 10 years. Prior literature has shown that flexure springs have not been designed for such operating regimes in the past. This section provides the baseline of the flexure design and methods that improve the performance to be implemented in an LEA machine. The main design parameters are discussed in this section. The relatively large number of parameters in flexure design results in the variables interacting non-linearly with each other. A machine learning scheme with a robust design method was utilized to obtain design charts for flexure spring design.

### **1.3.2 Energy Analysis of Flexure Springs**

In the LEA assembly, flexure springs are intermediate media between the energy source – the engine – and the energy sink – the alternator. To transfer the mechanical energy generated by the engine, it is critical to minimize the energy losses in springs during its operations. This section focused on the identification and characterizing of the energy loss mechanisms due to the application of flexure springs. Frictional, drag force, and hysteresis losses were considered in this section as the main energy losses. FEA was used to investigate the harmonics of the flexure arms and the non-linear friction behavior in the spring's pack. A fluid/structure interaction (FSI) analysis was used to study the effects of the air drag force on the spring's surfaces. The results of this section are essential for decision making on the main dimensions and capacities of the LEA system and its operating conditions.

### **1.3.3 Investigation of the LEA Assembly Dynamic Behavior via FEA**

The goal of this section is to develop a mass-spring dynamic model and determine the interactions of the other LEA components with flexure springs and analyzing their effects on the overall stroke/frequency outputs. This section explores the LEA as a whole system. The harmonics of the assembly and the frame vibration were studied in this section. To take the effects of the engine and alternator into account, empirical and analytical formulas representing the engine and alternator

force/displacement behaviors were used as inputs. In these sections, the effects of the springs' neutral positions and the mounting methods of the LEA frame were considered.

#### **1.3.4 Experimental Validation**

The results of this category are spread in other sections for the convenience of the readers. The main goal of experiments was to verify the FEA results with the results of individual flexure's static tests as well as the whole assembly. This is primarily to validate the FEA methodology and approach for this research so that further modeling toward increasing the efficiency of the LEA are realized. Some tests were also performed for the statistical analysis of the spring's stiffness and its coefficient of variation (COV) due to manufacturing influences. A set of experiments was performed to isolate the different loss mechanisms of the individual flexures and the LEA assembly. In addition, a portion of tests were completed to obtain the necessary damping coefficients to be used in the FEA.

#### **1.3.5 Design Improvement and Efficiency Enhancement**

Having the FEA simulations verified by the experimental tests, methods that potentially enhance the overall efficiency of the LEA was implemented, first thorough the FEA and simulations, and then experimentally to observe the efficiency increase rate compared to the primarily quantified efficiency numbers. This section is specifically suitable for future research and achievable methods that can improve the overall efficiency. The main contribution and novelty of this research are presented. The methods include the application of extra components, packaging strategies, and efficiently using the system dynamics to convert the wasted energy into useful output energy.

## 2 Literature Review

In recent years, demands for small unit on-site power generation for household applications has attracted more attention. The main aim of decentralized power generation is to reduce the power outage times due to extreme climate conditions and also to increase overall fuel-to-electricity efficiency by application of CHP systems [8]. Based on the DOE statistics, the average daily electricity consumption of a household in the US is around 30 kW-hr [20]. To provide most of the average power demand, a 1 kW generator is required. At this range of power generation, a free-piston LEA may fulfill the demands for efficiency, cost, and fuel flexibility [22]. Some of the main advantages of the LEAs are structural simplicity, low frictional losses, high thermal efficiency, and fuel flexibility [23].

### 2.1 Linear Devices

For on-site electrical power generation to be effective, an internal combustion engine that used natural gas with a thermal efficiency of 40% was targeted [8]. To meet the 40% efficiency, a novel LEA was proposed that took advantage of the free-piston, linear motion to minimize or eliminate frictional losses due to piston skirt side thrust, the crankshaft, and the wrist pin found in conventional slider-crank engines [24, 25]. Linear engines, also referred to as free-piston engines, have received interest since the 1920s, and applications have included gas compressors, hot gas generators, or combined with linear alternators for power generation. More recently, reviews were completed by Achten in 1994 [26], Aichlmayer in 2002 [27], Toth-Nagy and Clark in 2004 [28], Mikalsen and Roskilly in 2007 [23], and the most recent review in 2015 [29]. Linear engines have been designed for a variety of configurations and have used conventional liquid (gasoline and diesel) and gaseous (natural gas) fuels. Linear engine configurations have included dual opposed pistons for inward compression and dual and multi-cylinder configurations for outward compression. A schematic of different configurations is shown in Figure 5. Prior work examined spark-ignited (SI) and compression-ignited (CI) engines fueled with gasoline and diesel fuel, respectively [24, 30]. Linear engines may be two or four-stroke while a two-stroke combustion scheme presents further simplification, durability, and lower cost. For end-user electrical power generation in this type of application, the LEA was designed for continuous operation at full load.

To enhance the overall efficiency of the linear devices, higher axial deflection, and a higher natural frequency of the flexures is advantageous. In the case of a linear alternator, greater axial deflection leads to higher compression ratios and thus increased efficiency [31, 32]. In the case of a natural gas linear alternator, natural gas is more knock resistant and benefits from flexures with higher strokes and higher compression ratios than gasoline. Moreover, because of mean piston velocity is lower for linear engines compared to larger crank driven engines, small two-stroke engines tend to show their peak efficiencies at higher speeds, thus requiring higher frequencies. Overall, in the case of a NG driven two-stroke engine design for 1 kW gas-to-electric the flexure springs need to be designed for higher frequencies and higher compression [33, 34].

### **2.1.1 Cylinder-Piston Arrangement**

Cylinder-piston arrangement is one of the main classifications of linear machines. In this regard, the common linear machines can be classified into three main categories: Single piston, double-piston (dual or opposed configuration), and four-piston (dual, opposed, or complex configuration) [35]. A schematic of each category is shown in Figure 5. The simplicity, lower weight, and cost are the advantages of the single-piston designs; however, the force balance and stability is an issue in such designs. Figure 6 shows a prototype of a linear generator introduced by Mikalsen and Roskilly [36]. The machine included a cylinder and piston for combustion, an alternator, and an air bounce chamber. The air volume was controlled by valves to control the dynamics of the system. In Figure 7, another single-piston machine is shown. The main difference is the energy restoration system where the bounce chamber was replaced by mechanical springs [37]. In 2014, Kosaka et al. developed a single-cylinder linear generator [24]. A schematic of their design is shown in Figure 8.

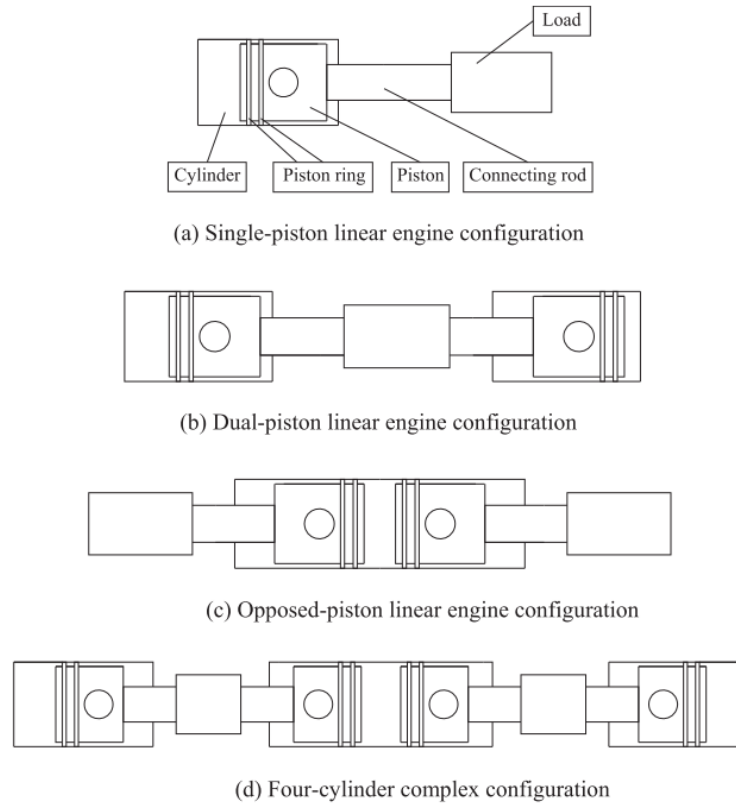


**Figure 5. Free piston piston-cylinder arrangements [35].**

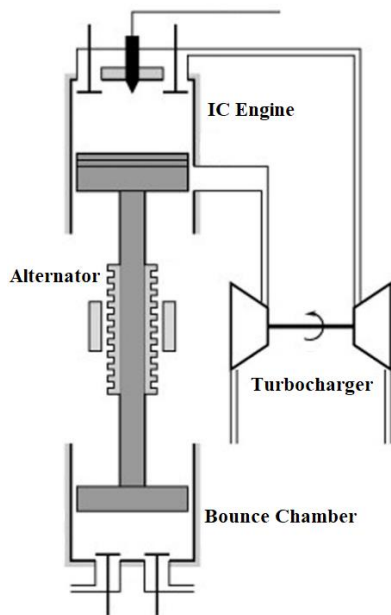


**Figure 6. Single piston linear alternator with turbocharger [35].**

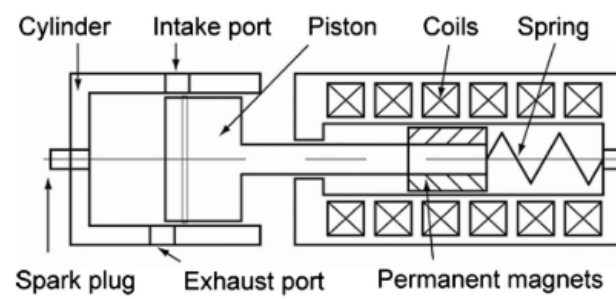


**Figure 7. Single piston linear alternator with mechanical springs [37].**

On the other hand, dual and opposed piston designs take advantage of better force balance and their system dynamics are easier to control. Figure 9 and Figure 10 show examples of dual and opposed piston designs, respectively. In the opposed-piston design, the first piston-cylinder is surrounded by a second cylinder which has a cooling water chamber around it. The cooling system is a known issue of the opposed piston designs. One main advantage of the opposed-piston engines is the reduced combustion heat loss due to the application of the shared combustion chamber. More examples of opposed-piston machines were provided in [35].

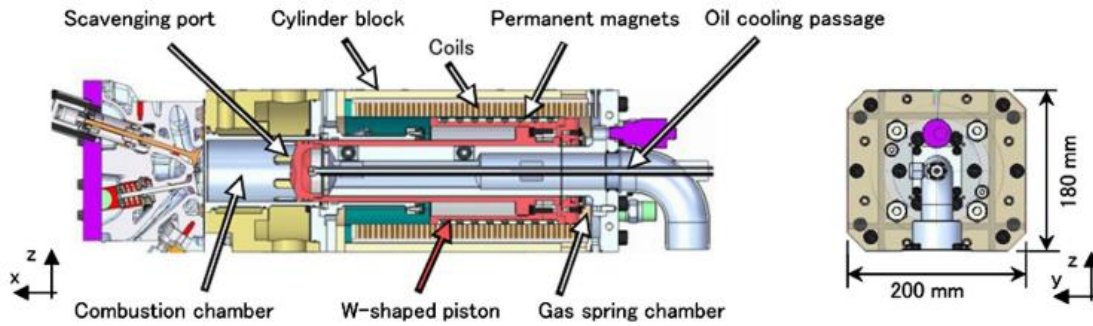


**Figure 8. Linear alternator with permanent magnets [24].**

In dual-piston design, the combustion occurs in two separate chambers with 180 degree phase difference. This feature leads to a simpler mechanism and higher power density [38]. Compared to opposed-piston engines, the combustion control is more complex due to the variability of compression ratio in two chambers which are connected mechanically. Although each cylinder's combustion stroke can be used for the compression stroke of the other cylinder, the application of the springs can increase the system's stiffness and frequency [39]. Another usage of the mechanical springs is to prevent the collision of the piston to the cylinder head [40, 41]. Dual-piston cylinder-piston arrangement has been widely studied in the literature [42, 43].

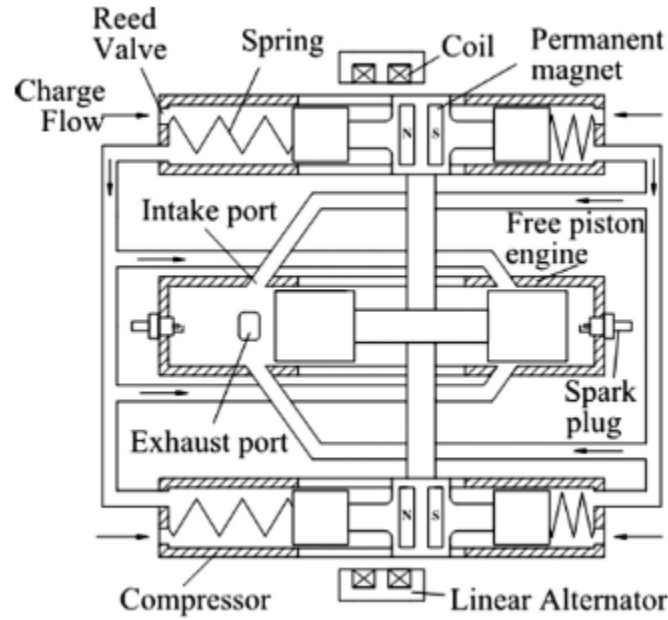


**Figure 9. Dual-piston linear alternator [44].**



**Figure 10. Opposed-piston linear alternator [45].**

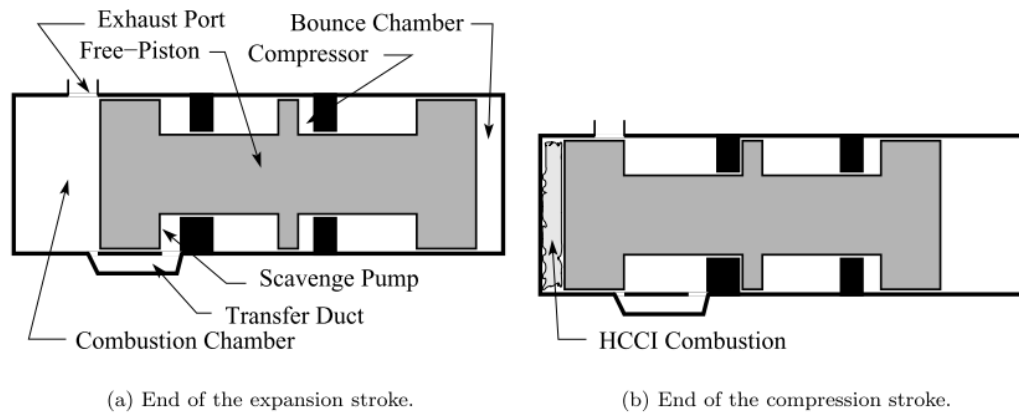
## 2.1.2 Applications

Free Piston linear machines have been used for several applications specifically where the linear motion of a piston is intended such as compressors, pumps, and actuators. In this section, four main applications of the free-piston linear mechanisms were reviewed and some of the successful examples were introduced.

### 2.1.2.1 Air Compressor

The air compressor was one of the early applications of the linear motion mechanisms. Figure 11 depicts the main parts of a linear compressor with a homogenous charge compression ignition (HCCI) combustion chamber, bounce chamber, and compressor. Usually, in linear compressor

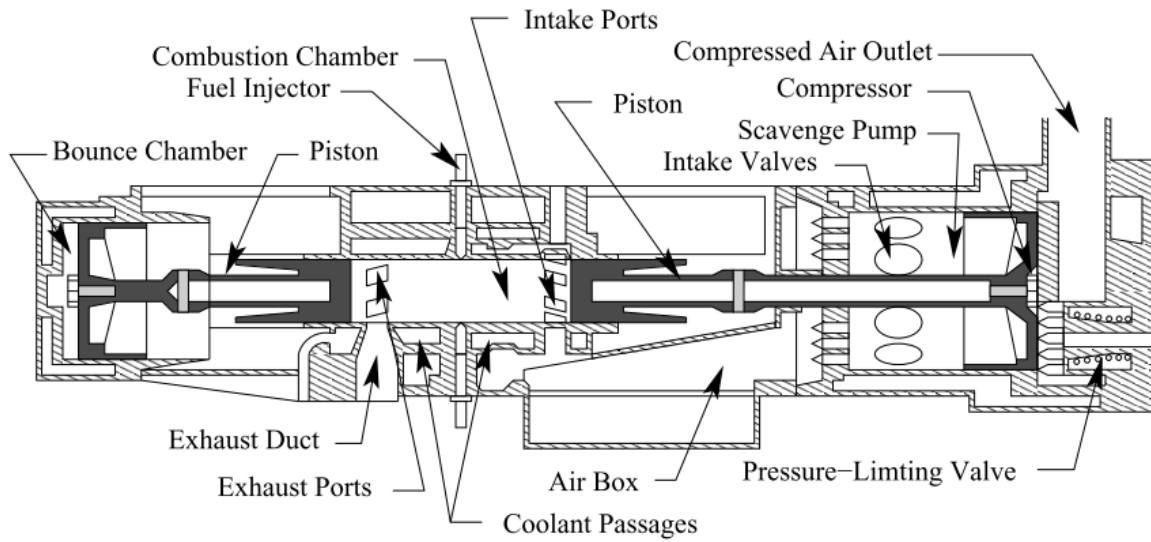
design, the load and system's stiffness, and hence the frequency, is assumed constant. This is one of the reasons that the application of the linear compressors are more common amongst other applications. This will lead to reduced control strategies required [27].



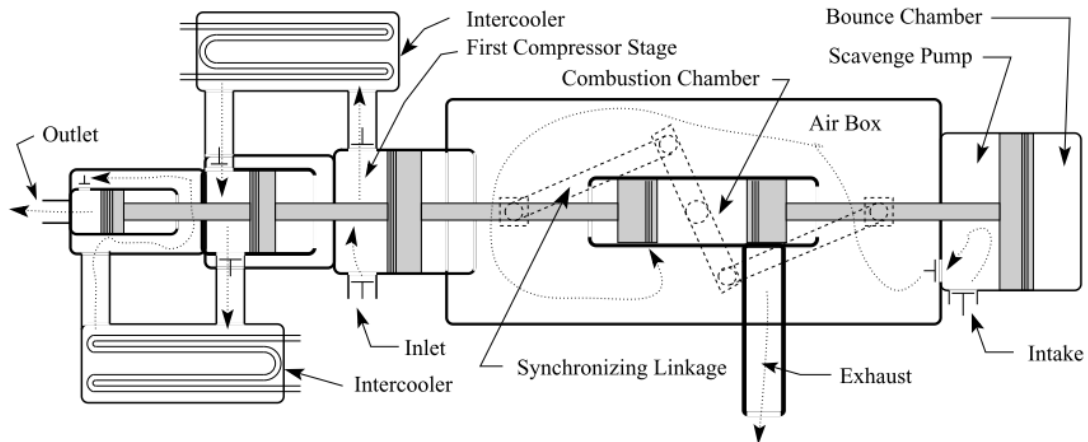
**Figure 11. HCCI free-piston air compressor [27].**

Figure 12 shows a linear free-piston compressor developed by Farmer in 1947 [46]. He started developing the free-piston concept machines in 1925 and tested machines using spark ignition and later in 1928 with diesel compression ignition combustion. His design was a single-stage compressor with main parts as the combustion chamber, bounce chamber, air compressor, and a linkage between pistons. The air delivery ranged between 30 to 100 cube feet per minute (cfm) at a nominal pressure of 100 pound per square inch (psi). For higher pressures, he used a multi-stage compressor machine. A schematic of his design is shown in Figure 13. In this design, three compressor stages were implemented to increase the output pressure.





**Figure 12. Single-stage air compressor [27].**



**Figure 13. Three-stage air compressor [27].**

Another successful example of a linear compressor is shown in Figure 14. The four-stage compressor development was started by Neumann in 1912 [47, 48]. The nominal air delivery was 70.5 cfm at 2950 psi. The design employed a two-stroke diesel engine. Compared to other designs and configurations with electric motors, the compressor was very compact in dimensions [49].

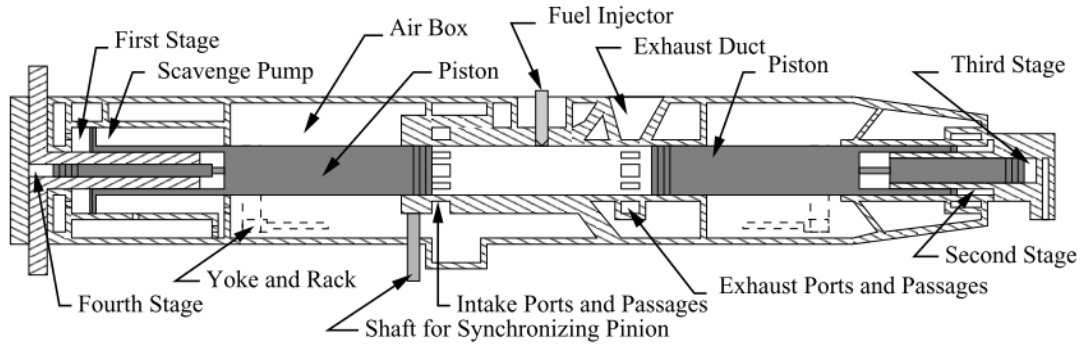


**Figure 14. Four-stages air compressor [27].**

In 1973, Braun and Schweitzer introduced an air compressor with spark ignition combustion, single-piston, and air cooling system [50]. A schematic of their design is shown in Figure 15. The control system was designed in such a way to use the piston velocity for the combustion ignition, rather than the piston displacement. The control system also was able to start and stop automatically.

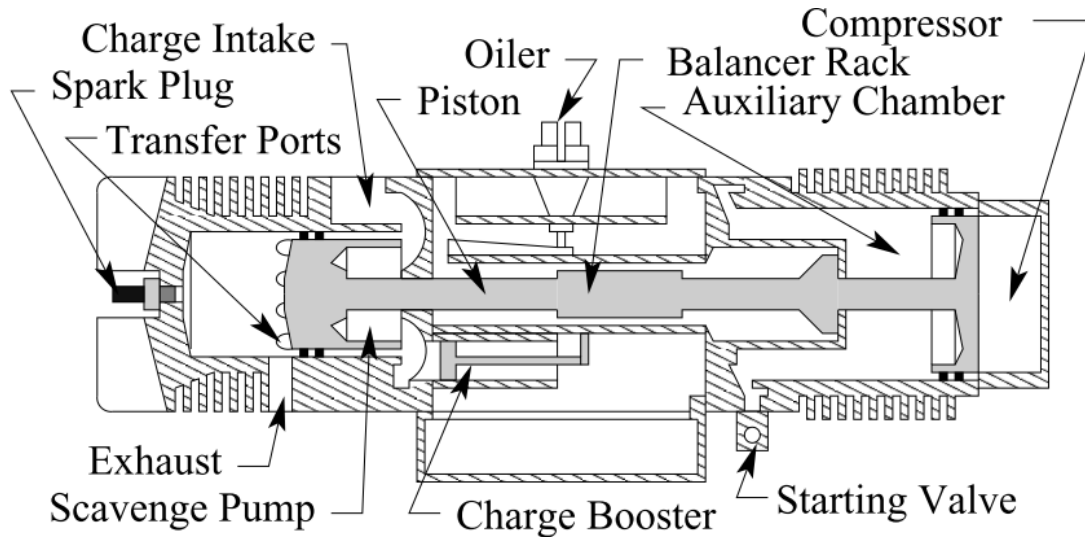


**Figure 15. Braun linear air compressor [27].**

#### 2.1.2.2 Hydraulic Pump

The main difference between the linear air compressors and linear hydraulic pumps is that the working fluid is not compressible in the hydraulic pump. This results in a smaller package of the machine but at the same time, the instability of the operations increases. This requires a more complex control system. Because the hydraulic fluid is not compressible, the energy cannot be

stored and hence it cannot be used for increasing the machine's natural frequency. Accordingly, using other methods to add stiffness to the system is essential. In 1988 Li and Beachley developed a linear hydraulic pump where the design fundamental was similar to the air compressors [51]. Their design is depicted in Figure 16. The pump had a bounce chamber and a hydro-pneumatic rebound circuit. The main unique feature of their design was lower irreversibilities and adjustable compression ratio by controlling the valves. The control system in their design played a key role so that the pump could work under a wide range of pressure demands while the engine could work continuously at its peak efficiency.

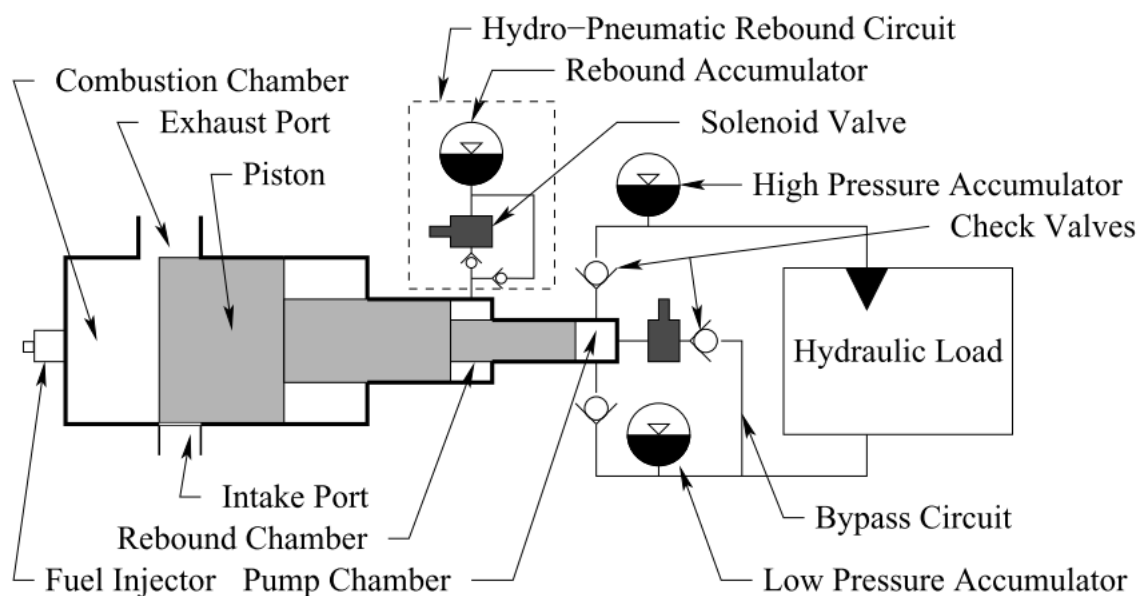


**Figure 16. Free-piston single-stage hydraulic pump [27].**

Other examples are the design developed by Heinz [52] and Tikkanen [53]. The configurations of both designs were similar and used a single-piston, dual diesel combustion chamber. The pump capacity was variable depending on the amount of fuel used in the combustion chamber.

### **2.1.2.3 Gas Generator (gasifier)**

Gas generators and gasifiers are referred to as the devices that use energy to produce combustion products or combustible gases at high temperature and pressure to be delivered to a turbine or turbine combustion chamber to generate mechanical work or electricity [27]. There are two main

types of free-piston linear gas generators: inward and outward. The two types are shown in Figure 17. The principles of free-piston gas generators are similar to the air compressor where, instead of delivering compressed air, the working fluid to be used is hot burnt gas. The high-pressure air is directed to the combustion chamber and supercharged combustion occurs and the products go to a turbine. As shown in Figure 18, the inward design is more compact, but they need relatively larger bounce chambers to provide energy for both pistons. One advantage of the outward configuration is that the pumping losses are lower because the compressed air directly enters the combustion chamber instead of the airbox [27]. The free-piston gasifiers are usually compared to the diesel engines in power generation in terms of thermal efficiency. One main advantage of the free-piston gasifiers, over diesel engines, is that they can reach higher compression ratios. Figure 19 shows a diagram of the free-piston linear gasifier invented by Pescara and developed by a Swiss organization in 1948 [54].

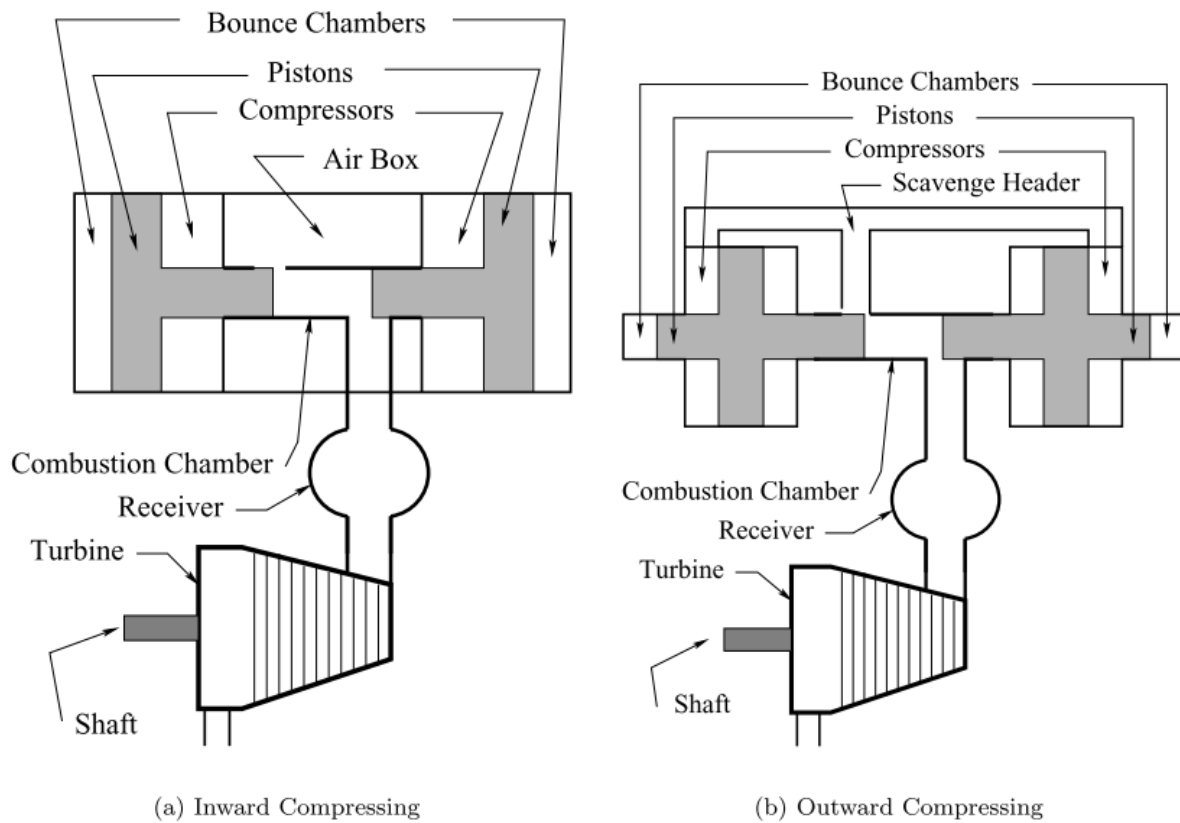


**Figure 17. Schematic of free-piston gas generators [27].**

Their invention was one of the most successful gasifiers ever developed. The technology used an in-ward compression scheme and at full load was able to deliver 3.65 kg/s of exhaust gas at 343 kPa pressure and 780 K. The thermal efficiency of the machine was reported to be 41%.

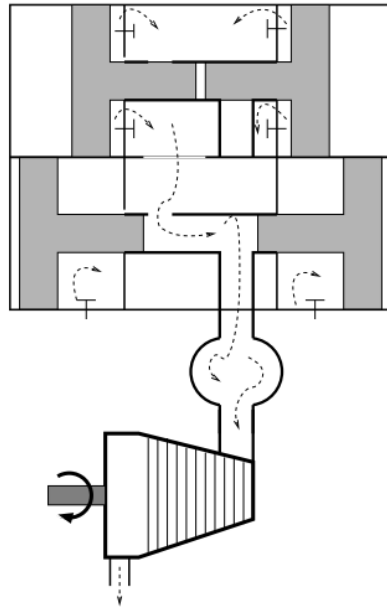


**Figure 18. Inward gas generator basic operation [27].**

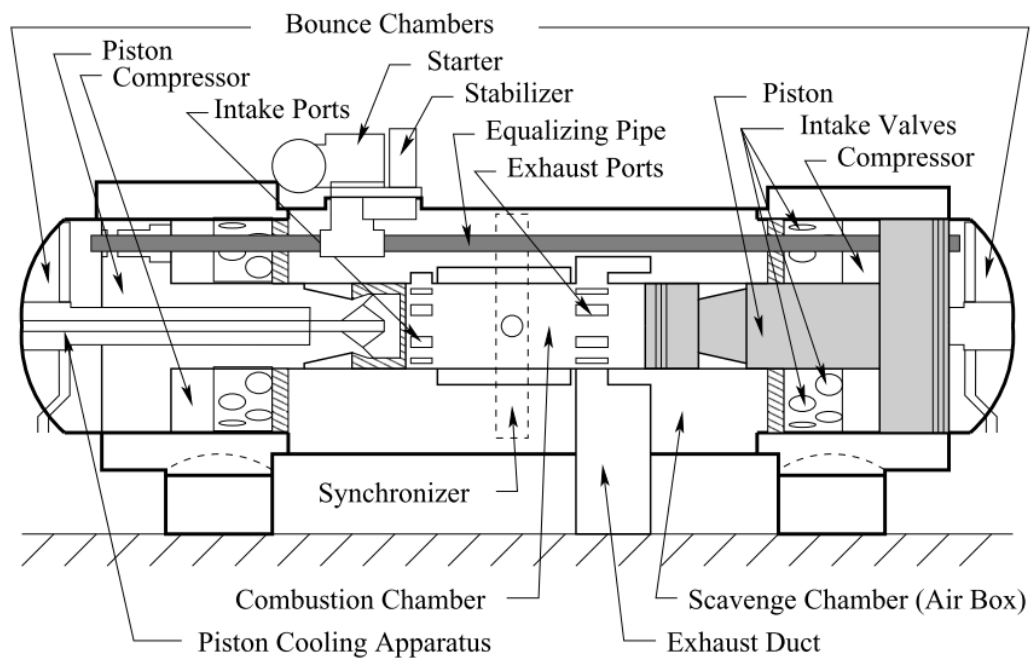


**Figure 19. Pescara's gasifier design [27].**

#### 2.1.2.4 Electricity Generator

Linear free-piston alternators or LEAs are considered as the latest application of the free-piston technology [27]. Being used in hybrid vehicles is one target application of such machines. Figure 20 shows the alternator invented by Van Blarigan, et al. in 1998 [55]. The combustion regime was HCCI and the target output power was 30 kW generated by a linear alternator. They found improved efficiency and reduced emission by implementing the HCCI combustion. This specific design remained at conceptual phases and was never commercialized. More research was performed on the same design later in 1999 by Goldborough and Van Blarigan [56].

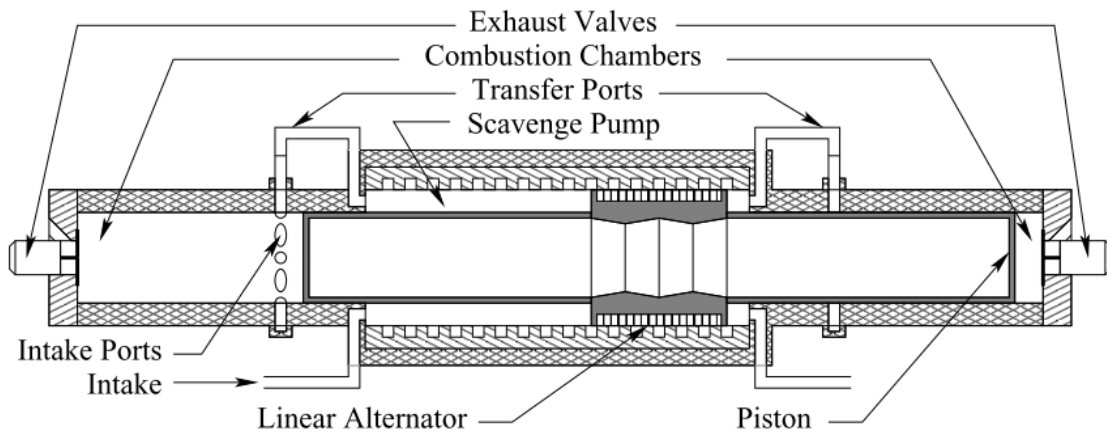


**Figure 20. Sandia linear alternator early design [27].**

In [27], Aichlmayr summarized the mentioned four applications by comparing the basic characteristics of each category. The results have been updated and are shown in Table 1. As the focus of this research is on LEA design, it is discussed in more detail in the next section. The early introduction, its development, and the main components are reviewed.

**Table 1. Summary of free-piston applications [27].**

Application	Delivery	Bounce Chamber	Control	Speed
Air Compressor	Fixed/Variable	Optional	Fuel Only	Fixed
Hydraulic Pump	Fixed/Variable	Required	Fuel and Stroke	Variable
Gas Generator	Variable	Required	Bounce and Fuel	Variable
Electricity Generator	Variable	Optional	Fuel Only	Fixed

## 2.2 Linear Engine Alternator

Typically, in oscillating free-piston LEAs, there is only one moving component (single and dual cylinder configurations). The moving component is the engine piston, shaft, flexure springs, and the magnets as the assembly. The linear motion of the system is driven by the combustion in the two-stroke engine. Flexure springs act as the energy restoration components – the same functionality as a flywheel in rotary engines. Magnets are placed on the shaft and reciprocating motion through the windings generates electricity. Flexure springs dominating the frequency of the oscillation. In this case, the stiffness of the springs can be varied to achieve the desired system dynamics. A schematic of a dual cylinder free-piston LEA is shown in Figure 21. The main components are two piston-cylinder at two sides, a connecting shaft, and the alternator which consists of windings and permanent magnets mounted on the shaft.

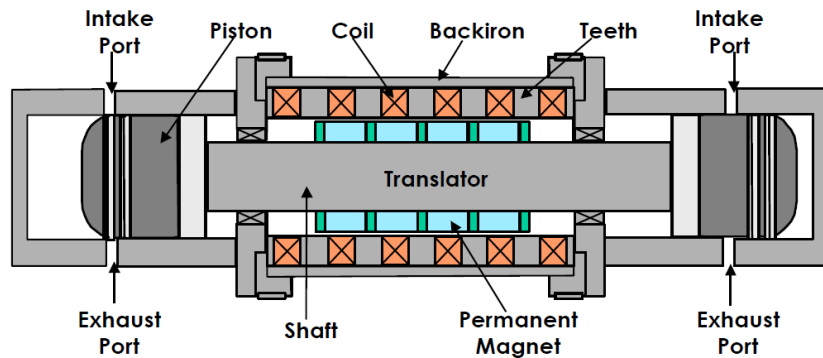


**Figure 21. Schematic of tubular brushless permanent magnet linear engine alternator [57].**

The term free piston in the proposed design means that the stroke length of the system is not restricted and can vary cycle by cycle. This unique feature makes the system more flexible to the operating conditions and power output as well as versatility on the fuel and reduced emissions. On the other hand, not having defined stroke limits makes the control system, and hence the sustainability of the system, very complex.

Spring-assisted LEA's have been developed and studied in a variety of configurations and applications. Aichlmayr extensively reviewed linear technologies [27]. Mikalsen and Roskily also studied LEA's in more detail [29]. In the recent 20 years, efforts have been focused on electricity generation compared to the mechanical drive in the past. The significant advantages of linear technologies, including robustness and lower friction, have attracted researchers from around the

world. One of the first examples was the free piston LEA developed at the University of Texas at Austin in 1995, a project funded by Southwest Research Institute to be used in hybrid electric vehicles [58].

Later in 1998, similar projects were started by research groups in Sandia National Laboratories (SNL) and West Virginia University (WVU). The machine designed and developed by SNL was a free-piston LEA with an HCCI combustion regime (Figure 22). One of the main features of their design was constant volume combustion [55]. They also investigated HCCI combustion in the model for higher performance and power output [56]. Continuation of their work on the optimization of the machine and combustion efficiency was reported in [59]. From their study in [60], the cyclic variation of the combustion behavior and, more specifically, the engine breathing was too significant from combustion stability and sustainability. SNL has continued the research toward the application of the opposed piston configuration and gas chambers as energy restoration components [61].

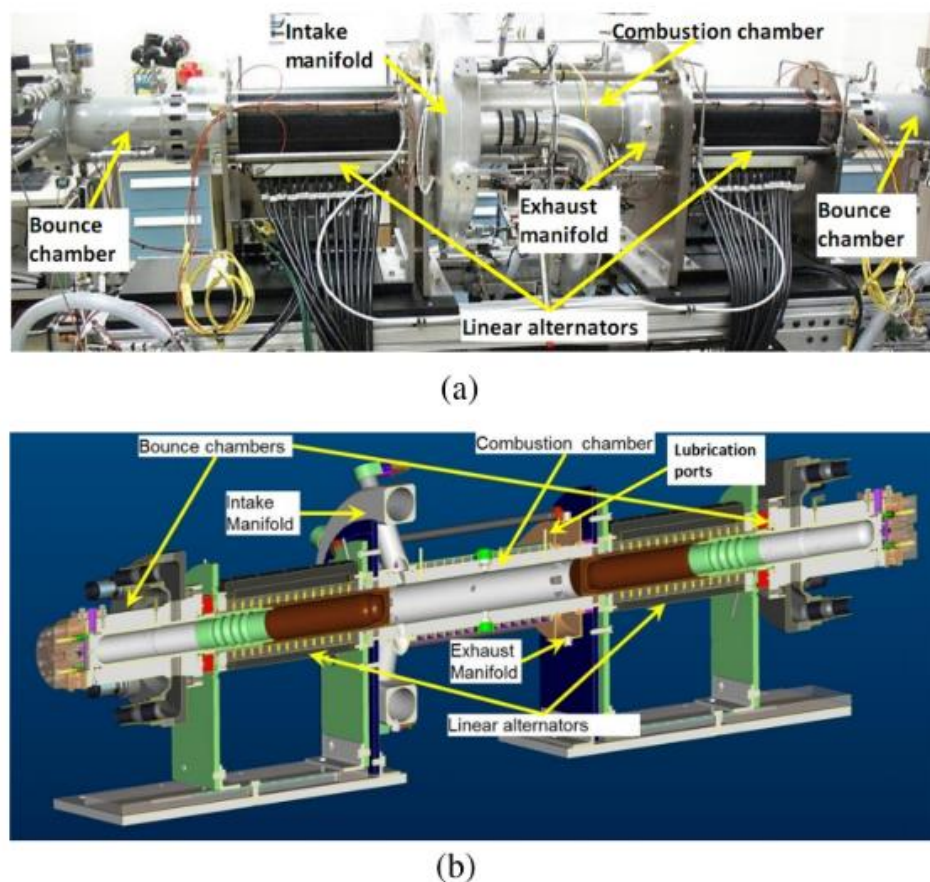


**Figure 22. Sandia National Lab opposed-piston linear alternator [62].**



The research at West Virginia University included both experimentation and modeling. The numerical model was developed in order to validate the experiments and enable optimization. A schematic and picture of the test bench is shown in Figure 23. The engine performance and energy release due to combustion with cyclic variation were well-studied. Gasoline fuel was primarily used and it was found that the combustion stability highly depended on the ignition timing and heat release. The electricity output of the machine was reported to be 309 W. From the numerical model, a sensitivity analysis was performed to investigate the combustion parameters including heat release, compression ratio, peak pressure, and combustion duration. The dynamics of the oscillating translator with variable moving mass was also investigated.

Further efforts were performed in WVU to develop a more advanced LEA machine using advanced methods such as artificial intelligence. In the second version of LEA prototyping, fuel flexibility, the air-fuel ratio in the engine, frictional losses, and the resonant frequency of the machine were studied [63]. The developed LEA used diesel fuel and operated between 50-60 Hz [19]. As a key finding of the research, the importance of the application of higher frequency through the application of the stiffer system to boost the output power was understood.

In 2004, a review paper was published with the latest technologies in LEA developments [28]. In [64], the working conditions of a diesel LEA prototype were investigated and studied. The authors analyzed the HCCI combustion regime behavior and found improvement in overall efficiency, resonant frequency, and power output with increased fuel and advanced injection timing. A researcher from WVU in 2014 published fundamental analyses of a dual-piston opposed linear engine [60, 61]. In a later study, they also numerically studied a spring assisted single cylinder linear engine alternator [6].

Research has been carried out at Newcastle University to design a linear engine with a single cylinder and bounce chamber. A picture of their prototype is shown in Figure 6. They comprehensively reviewed the challenges within the linear engine design with an HCCI combustion. Their study showed performance under different operating conditions and combustion regimes [23, 36, 65]. They have also extensively worked on the improvement of the control and dynamics of the system [40, 41].

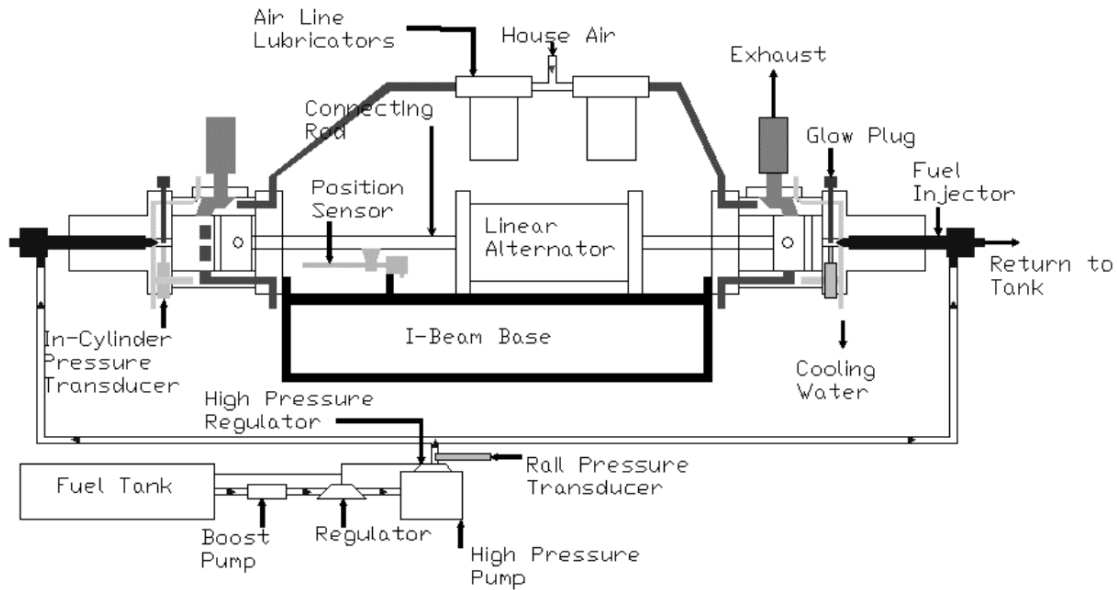
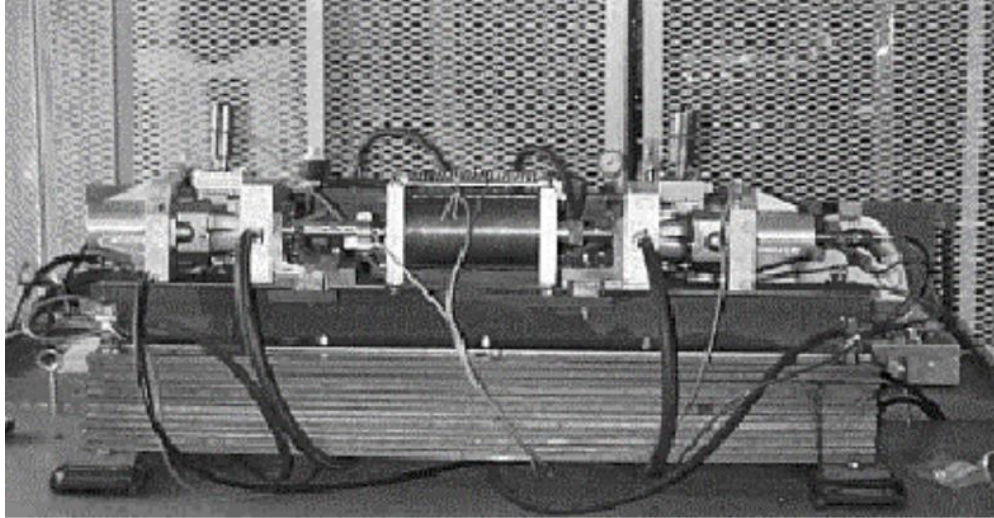


**Figure 23. West Virginia University free-piston LEA [66].**

Recently they have issued a review paper on linear technologies and commercial feasibility [30]. According to their review, there are some challenging criteria that have slowed the rate of linear engines down including the control system and translator motion, vibration, combustion stability, and engine lubrication.

Another research group that has been working on linear free-piston technology was the Beijing Institute of Technology. In [67], they reported the early results of their design of a single-cylinder free-piston engine for hydraulic pump applications. In their design, the engine piston is connected to the hydraulic pump piston and bounces due to the oil pressure to complete the combustion cycle.

The group used Simulink<sup>TM</sup> for a parametric study of various variables and the results were validated by a series of tests [68]. Through their studies, the engine compression ratio and injection timing were considered on the combustion performance. They have also performed a zero-dimensional analysis along with providing non-dimensional parameters to develop a free-piston LEA [69].

They showed that thermal efficiency highly depends on the ignition timing. It was shown that an optimum ignition timing can be obtained when the minimum negative work due to the increased pressure during the compression stroke occurs. In another study, they reported the effects of fuel on the steadiness of the combustion [70]. Their work continued toward the LEA's start-up procedure and using the alternator as a motor as the engine started [71].

Their validation showed that the numerical models can be useful, specifically for the few initial cycles of the operation. Later, the researchers at the Beijing Institute of Technology collaborated with researchers at Newcastle University in order to develop more advanced LEA technologies [72]. In one report, they provided a design with a single-cylinder, spark-ignited LEA [73]. They reached the maximum power output of 25.9 W with an overall efficiency of 13.5%. They also worked on the system dynamics of a dual cylinder LEA with diesel fuel [74].

The researchers at the German Aerospace Center (DLR) developed a free-piston engine with a power rating of 8 kW with a single cylinder. They used mechanical springs and their machine operated at 20 Hz. The study used a hydraulic actuator to control the motion of a piston [75]. In another work, they used a two-stroke engine and gasoline fuel to be used in a linear mechanism [76]. They continued their effort toward the optimization of the alternator seeing higher energy transformation rates [77, 78]. In their latest achievement, they designed a generator with 10 kW output operating at 20 Hz. The main obstacle remained the complex controlling of the system and its variation cycle to cycle. The overall efficiency was reported 17.9% with the combustion inefficiencies as the main reason [25].

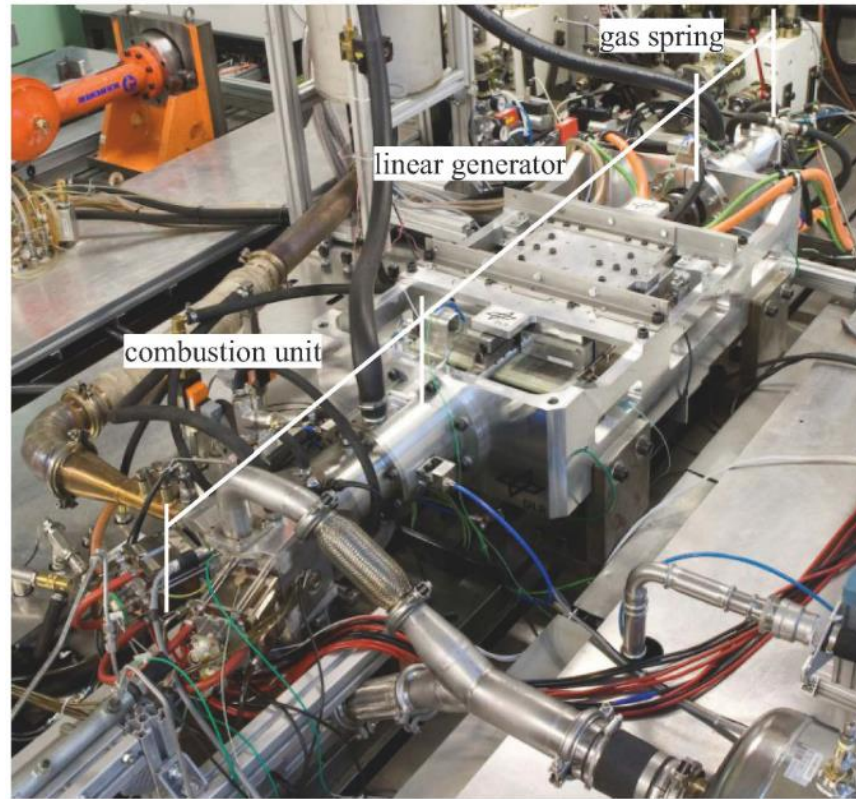


**Figure 24. German Aerospace Prototype [25].**

Other than these distinguished works, there are more studies on the design and development of LEAs from researchers around the world. A review of the LEAs for commercial applications can be found in [30]. A conceptual design was introduced by Pempek Systems which contained an assembly of three linear engines [79]. A study at Chalmers University was performed and investigated the flexibility of the dual piston linear engines through simulation [80]. In another numerical simulation by the IFP group in France, it was shown that enhancement in the engine's compression ratio and application of an exhaust gas recirculation (EGR) can increase the indicated efficiency by up to 50%.

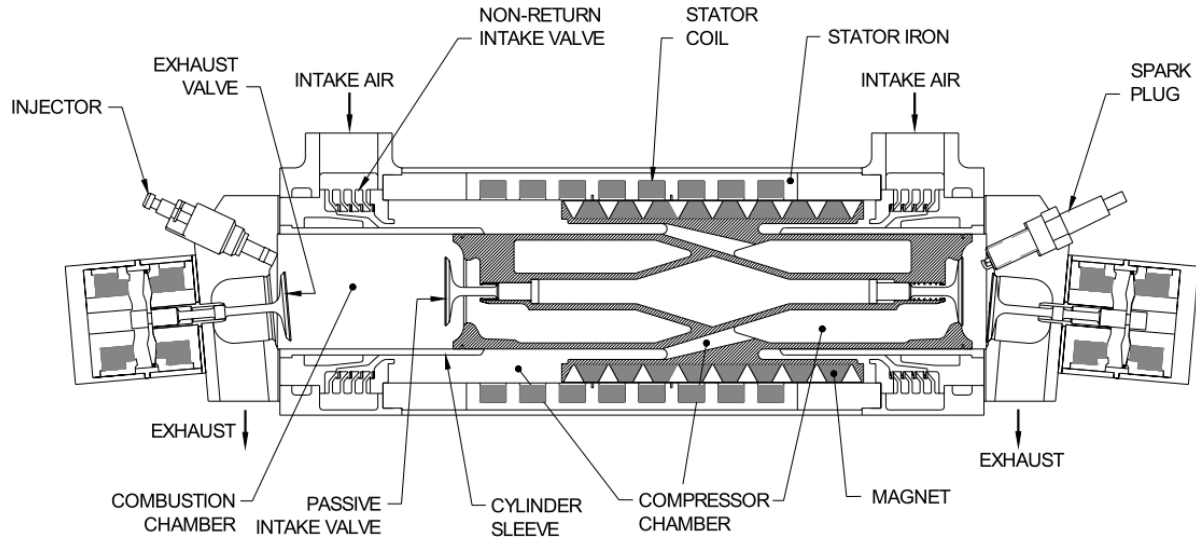


**Figure 25. The layout of the Free Piston Power Pack [79].**

Toyota has also performed extensive research on linear engines. Their design is a single-cylinder linear engine with the power output targeted to 10 kW to be used in hybrid vehicles [24, 81].

Researchers at Ulsan University have worked on the control of spring-assisted free-piston LEA and results reported in [82]. Their design consisted of a dual cylinder combustion configuration using propane as the fuel. They examined the combustion regime with both spark ignition and HCCI. The effects of spring's dynamics on combustion was reported in [83]. In their experiments, they tested the increased spring's stiffness which increased in an operational frequency ranging from 35 to 47 Hz. Increased frequency of the assembly improved the thermal efficiency from 6 to 7.22% and the overall efficiency by 25%.

In reviewing the research in recent years the utilization of springs illustrated the key role they serve in the stability, efficiency, and output power of free-piston mechanisms. Springs dominate the system's dynamics directly and affects the combustion regime and the electromagnetic electricity generation. Hence the spring design and its effects on the design are very important and challenging. In the following chapters, the spring design and analysis will be presented.

Single-cylinder LEAs commonly consisting of three main parts and include the engine, electricity generator, and rebounding components (springs). The proposed design consists of the same main parts and the literature is studied for each in the following sections.

### 2.3 Current GENSETS Free-piston LEA project in WVU

The WVU research group has been working on the ARPA-E GENSETS project since 2015. The main targets of the project were continuous and maintenance-free operation, 1 kW electricity generation using natural gas with a thermal efficiency of more than 30% (80% when used combined heat and power) [84]. The WVU free-piston LEA used a single-cylinder, two-stroke engine configuration, a linear alternator, and flexure springs. Figure 26 shows the images of the new design. The group has achieved significant improvement in the application of the flexure springs to increase the resonant frequency, the predictability of the combustion, and the control system. The control system, as mentioned in previous sections has been one of the greatest challenges in the development of the free-piston devices. However, the improvement in durability and overall thermal efficiency is still ongoing.

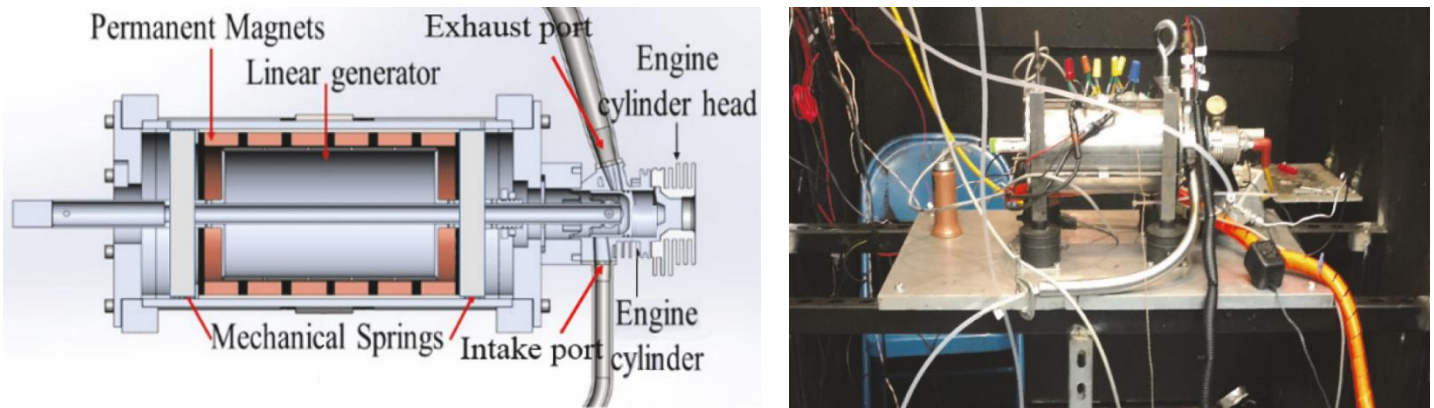


**Figure 26. WVU free-piston LEA-Alpha prototype.**

The prototype used a two-stroke cycle combustion strategy to ensure sustainable motion without intervention because each reciprocating cycle has a power stroke. This also allowed for a simple port configuration, rather than a complex cam-less valve control system. The mechanical losses in the linear engine environment are limited to pin and ring friction, which were estimated at around 2%, in strong contrast to the high losses in a slider-crank system.

By adopting a single piston, the surface area-to-volume ratio heat transfer problem in the combustion chamber was reduced and the indicated efficiency of the engine operation was increased. This innovation would not be possible without the decision to include springs. The single-piston decision also reduces cost and complexity and improves assembly and

maintainability by providing ready access to the alternator. The two-stroke design supports both cost reduction and power density. The design is dedicated to un-throttled full-power operation, within a narrow control band, and thus eliminates throttling losses associated with most spark-ignition engines. One innovative feature of the engine design relies on scavenging the exhaust gases and feed fresh mixture into the engine using two tuned pipes, and employing resonance to operate the engine in a “power band.” The resonant scavenging keeps pumping losses to a minimum of around 3%.

For end-user electrical power generation in this type of application, the LEA was designed for continuous operation at full load. The rated speed of the small-displacement, two-stroke engine used was between 3600-5400 cycles per minute (60-90 Hz) and stroke length was 20-30 mm [30]. The ranges for the frequency and stroke length are due to the development of the different versions of the LEA machine. Research has shown that heat losses are lower and engine breathing and efficiency are higher for higher operating frequencies [85]. Due to the lack of a rotating flywheel, springs were essential to restore the required energy for the compression stroke at each cycle of the engine. The usage of flexure bearings is an effective method to maximize the stiffness of the whole system and maintain the minimum moving mass to achieve the target efficiencies.

Since 2015, the research group in WVU has published several journal papers, dissertations, and reports on different areas of the novel design. The Ph.D. dissertations [86 - 88], and a MSc thesis [89], have focused respectively on the overall performance analysis of the 1 kW LEA machine using a zero-dimensional Matlab model and experiments, the development of a high-efficiency two-stroke engine, and instrumentation and the controller of the proposed machine. The results of the research and the zero-dimensional model were also published in [90 - 92]. The mass-spring dynamic equations along with thermodynamic relations representing the combustion and also electromagnetic induction theory were used to model the performance of LEA with different configurations. The two-stroke engine studies and the results obtained from experiments were reported in [31 - 34]. Several studies were performed on the design and optimization of the linear alternator and the results were published in [93 - 95]. The author of the current dissertation has also published research papers on the design and development of the flexure springs for the LEA machine [96 - 98]. A literature review on the history of development and the state-of-art of the three main components of the current LEA machine is presented in the following sections.



### 2.3.1 Linear Alternator

Linear alternators or generators convert the reciprocating motion into electricity or vice versa. There are two main applications for the linear alternators to work as a motor or generator. The first case has been implemented in many studies and industrial examples for start-up purposes; however, the second case has become very significant in recent years. There are different configurations of the linear alternators available which are designed and used based on the specific applications. Chevailler explored the design and selection of the linear alternators in his Ph.D. dissertation in 2006 [99]. Some of the main examples are reviewed in the following sections.

Fundamental analysis of linear electric machines was studied and reported in [100]. In that study, the electromagnetic induction electricity equations were derived and solved. Further, the researchers built the first prototype using tubular design and permanent magnets [101].

Nassar's study was a beginning and a baseline for other researchers to continue improving the linear alternators concept. In 1988, Nassar and Chen performed an optimization study to improve their design with enhanced design targets [102].

There are several configurations of linear alternators based on different types and combinations of the stator and translator. One of the primary designs was the application of permanent magnets. One of the corresponding challenges was the introduction of the differential equations describing the free oscillations of the translator. One of the common simplifications that have been used in modeling of such machines was using an equivalent circuit.

This method was introduced and used by Nassar and Chen in 1987 [103]. One year later, Pai and Bolda used the equivalent circuit method for a linear motor design [104]. They provided a comparison between the model and experiments. A common approach in the equivalent circuit method is using empirical data from tests which were explained in detail in the mentioned literature.

The FEM has been a strong method for modeling electrical machines. One of the earliest applications of the FEM in electrical linear alternator design was introduced in [105]. Compared to analytical methods, FEM showed high levels of accuracy.

Improvement of the computational methods and commencements of high-performance computers have allowed more complex analysis and development of linear machines. In [106], a 3D-FEM



approach was implemented to model a three-phase tabular transverse flux permanent magnet linear generator. Different criteria were analyzed in the study such as electromagnetic flux density, leakage, harmonics, EMF, cogging forces, and power.

In [107], an equivalent circuit method was used to investigate the performance of a permanent magnet alternator and to find the geometrical dimensions of stator design. FEM was also used to validate the analytical results. In 2009, Lu implemented a transient FEM to design a tubular permanent magnet linear alternator. He used the results of the analysis to optimize the air gap requirements and the generation of the eddy current power [108]. He also compared the effects of the magnetic pole orientations along the linear direction. He reported better performance of the radial configuration.

Linear alternators/generators are specifically of interest where a linear motion exists/desired. Actuating and power generations are two main causes. Among these two, power generation has attracted more attention.

One of the earliest applications of the linear alternators was in a Stirling engine that was introduced by Nassar and Bolda. Later in 2010, a group of French researchers used this technology in a linear generator mover [109 - 111]. In their study, the linear system was analytically presented and simulated. They also performed a parametric study of their system in order to increase efficiency and to reduce cost. The application of the linear alternators in linear combustion engines was based on the same concept as the Stirling engine application.

Cawthorne, from WVU, performed a detailed study to design a linear alternator for a free-piston linear machine. In his research, a simplified model was used for other components including dual-piston engines. Both analytical and numerical approaches were used to identify the performance of the system and to further optimization of the geometrical parameters [57].

To friction related to the conversion of the reciprocation motion of the piston to rotary motion is relatively high, using a linear alternator has many advantages to lower the overall friction. Libertine FPE is one of the leaders in the development of high-efficiency linear alternators that have tested several prototypes successfully. One of the main challenges in developing the linear alternators is the cogging forces which have a negative influence on the dynamic of the motion and exerts negative power into the system. Some studies reported methods to reduce the effects of the cogging forces [112, 113]. Another challenge is the control system of the alternator which is

usually treated the same as the main linear machine. There are many geometrical parameters that interact with each other and make the design process very complex. Amongst the input and output criteria, the most important parameters are the moving mass, speed and acceleration, control system, power, cost, and efficiency.

### 2.3.2 Two-stroke Engines

Two-stroke engines have many beneficial features compared to four-stroke engines and include simplicity, higher power density, and lower cost; however, the main intrinsic drawback of these types of engines is the fuel short-circuiting during the scavenging process. Besides the fuel economy, the HC emissions will be also a significant concern [114, 115]. Two-stroke engines have been widely developed and studied in order to achieve higher efficiency and power [116 - 118]. Some of the main advantages and disadvantages were presented in [87] and are shown in Table 2.

**Table 2. Summary of advantages and disadvantages of two-stroke engines [87].**

<b>Two-stroke Advantages</b>	<b>Two-stroke Disadvantages</b>
<ul style="list-style-type: none"> <li>▪ Higher power density than four-stroke engines of the same displacement</li> <li>▪ Valvetrain not required except for uniflow design</li> <li>▪ No oil pump loss</li> <li>▪ Higher operating speeds versus four-stroke engine counterparts</li> <li>▪ Less output torque fluctuation per cycle than four-stroke engines [13]</li> <li>▪ More cost-effective to manufacture than four-stroke engines</li> </ul>	<ul style="list-style-type: none"> <li>▪ Increased hydrocarbon (HC) emissions due to typical carbureted engines scavenging with an air-fuel mixture</li> <li>▪ Higher heat flux near TDC causing increased heat losses</li> <li>▪ Pumping losses in the case of crankcase compression</li> <li>▪ Misfires at low speeds due to poor scavenging</li> <li>▪ Incomplete combustion</li> </ul>

The first criterion for the two-stroke engine classification is the scavenging strategy. There are various methods from simple to very complex which are designed based on the type of application and desired power and efficiency output while considering the emission limitations. Some common methods include cross-scavenging, uni-flow scavenging, loop scavenging, and reverse scavenging.

In [114], characteristics of different scavenging methods were analyzed and uni-flow was recognized as the most efficient method. However, for linear applications, uni-flow scavenging is not practical due to the lack of conventional actuation.

Conventional two-stroke engines mix and compress the charge flow before entering the cylinder in the crankcase. Piston dynamics cause the suction of the fresh charge from the intake manifold and direct it toward the ports to be the main cylinder volume. The piston motion increases the charge pressure and turbulence which can help better scavenging and a more homogeneous mixture of the fuel-air charge. In some engines, a specific type of valve or port is used to prevent the backflow from the crankcase to the intake manifold [119]. Using a reed valve results in higher trapping efficiency. If not properly designed, brake specific fuel consumption of two-stroke engines can be very high [120].

One of the advantages of free-piston LEA machines is the engine variable compression ratio capability. With the same engine configuration, the mass-spring system can be modified to change the engine working conditions e.g. stroke length and speed. The variable compression ratio is especially important as it enables flexibility in using various fuels. Dual (or multiple) fuel engines can provide higher flexibility under various operational and environmental conditions. To be used as dual fuel engine, some modifications might be necessary in configuration of the engine for better performance. In [121], a diesel engine was modified for SI combustion with a blend of gaseous fuels. The main purpose of the research was to study the effects of an alternative fuel on performance and emissions. A dual fuel diesel-natural gas engine was developed and tested by Yousefi, et al. They reported reduced NO<sub>x</sub> emissions over a range of operations [122]. In another effort, it was shown that using NG-diesel as an alternative fuel can reduce the CO and HC emissions by 38.3% and 34.7%, respectively, compared to single diesel fuel [123]. Navaro, et al. studied the dual-fuel combustion of natural gas and hydrogen. Using this fuel blend resulted in reduced CO<sub>2</sub> and enhanced engine power [124]. In [125], Diermouni studied the performance of an HCCI engine with NG fuel. The engine was equipped with a turbocharger and showed an improved exergy efficiency. Yang, et al. investigated the effects of injection timing on the NG engine with diesel pilot fuel and found an increased efficiency [126].

One of the key features of the free-piston engines is the variability of the stroke length and hence the compression ratio. The effects of the compression ratio on two-stroke engines have been widely studied. Researchers at Yamaha Motor Company achieved a 1-3% decrease in fuel consumption by increasing the compression ratio from 6.6 to 13.6 [127]. Another study showed that reduced penetration distance of the fuel jet and the consequent strong fuel mixture resulted from an increased compression ratio [128]. Kapilan et al. studied the effects of the compression ratio on a

two-stroke engine with methanol as fuel. They reported a CR of 8.56 corresponding with the highest BTE for a wide range of engine load [129]. In [80], different fuels, including diesel, hydrogen, NG, and gasoline were tested in a two-stroke engine. Except for hydrogen, other fuels showed increased thermal efficiency. They showed that improved CR resulted in higher power density. In another effort, Krishna et al. tested a two-stroke engine with gasoline direct injection under motoring conditions. The CR was increased from 7 to 8 and turbulence parameters turbulent kinetic energy and tumble ratio were measured and showed 13% and 26% reduction, respectively [130].

### **2.3.3 Flexure Springs (Bearings)**

Flexure springs are known for their long service life and maintenance-free operation, which are mainly due to the elimination of contacting parts [131]. There are several papers on flexure design and optimization, using FEA and experimental tests, and sensitivity analyses in order to identify an optimized design. However, most of these studies focus on lower displacements at much lower frequencies than targeted in this study.

The wide application of the flexure springs in power systems was initiated in the mid-1980s to the early 1990s focused mainly around linear compressors for cryogenic applications [132, 133]. Many researchers in these studies used FEA as a fast method to examine the effects of dimensional parameters on the performance of flexure springs. Gaunekar et al. developed an exact analytical technique to develop a design method of flexures for space cryocooler applications. They reported non-dimensional design curves for a range of sizes [134]. Lee conducted an analytical study that predicted the flexure spring behavior with different geometries. They considered radial and axial stiffness, fatigue stresses, and dynamic characteristics. They developed design charts used for the design margin and effectiveness of new spring designs [135].

Rawling et al. showed that the use of flexure springs reduced the price and doubled the life of small cryocoolers for military purposes [136]. Qui et al. studied a method based on FEA analysis for the design of flexural bearings that were used in Stirling engines for aerospace applications. They demonstrated the reliability of over 99% confidence level in their spring design. The models considered both the surge and rocking modes of the spring arms [131]. Chen et al. developed a generalized design procedure of flexure springs based on the location and orientation of spiral cuts

and also the spiral design parameters [137]. Simcock et al. investigated the fatigue failure of flexural springs for a linear Stirling cryocooler. They used strain gauges to validate FEA results [138]. Al-Otaibi et al. proposed the design of flexural springs for a reciprocating linear motor with just under 16 mm stroke at 42 Hz. Studies were completed on the effects of design parameters on stiffness and stress and the designed springs were evaluated experimentally [139].

Kavade et al. investigated the design parameters such as spiral sweep angle and slot width using FEA to reach a long fatigue life of flexures for linear compressor applications with the displacement of 5 mm [140]. Zhou et al. compared the performance of oxford and triangle flexure springs for linear compressor purposes using FEA. They found the triangle type flexures produced higher radial/axial stiffness and also higher natural frequency under the basic structures [141]. Rajendra studied the effects of the shape factor and end angles of arms in an eccentric configuration flexure with a 3 mm stroke that optimized the axial and radial stiffness [142]. Amoedo et al. carried a parametric study of flexure springs used in a Stirling engine with fixed axial displacement. They presented non-dimensional charts as design guides [143]. Peng et al. performed an analytical study to model both axial and radial stiffness of flexures using strain energy. They examined the effects of the width of arms and thickness on the axial and radial stiffness [144]. Khot et al. designed and performed the optimization of flexures for linear compressors. They used the Taguchi method for optimization and different materials were used for experimental testing and validations. They used Beryllium copper and steel as materials. They reported that dynamic strain was 8% higher than the static strain [145].

### 3 Design and Optimization of Flexure Springs

Flexural spring design is a multi-dimensional design optimization problem due to the interplay of spring geometry on displacement, frequency, and moving mass. Although in calculation of the resonant frequency of flexure spring, the moving mass is considered, however, regardless of its effects on the frequency, it plays an important role on the dynamics and vibrations of the whole assembly. This was investigated and the results are in the following chapters. Figure 27 provides a solid model representation of the geometric layout of the proposed spring design focused on for this study. As illustrated in this figure, the spring was characterized by an inner diameter  $b$  where a translator rod was affixed, an outer diameter  $a$  where the spring attached to the alternator housing, and helical-shaped cuts in the disk that provided the arms of the spring. The shape of each helical-shaped cut, the width of the gap between arms, number of arms, eccentricity of the spirals, the length of spiral cuts, thickness  $d$ , and material selection were amongst the design parameters.

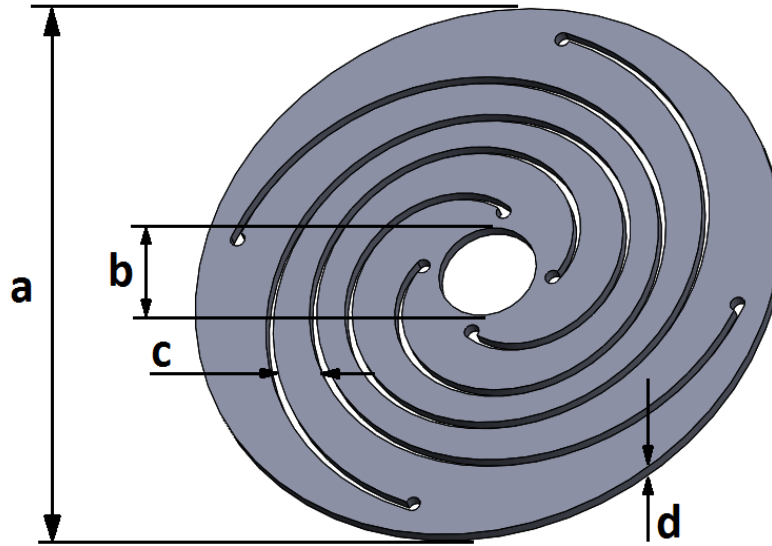
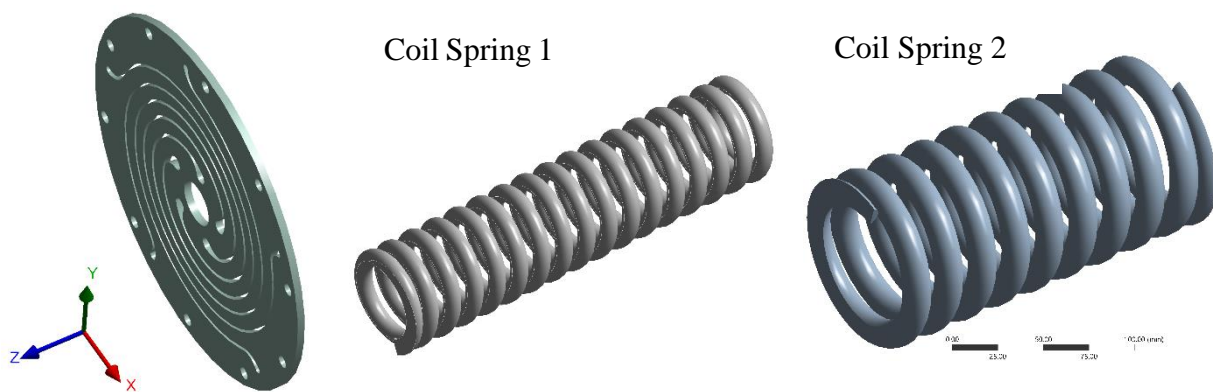


**Figure 27. Flexural spring geometry.  $a$ : outer diameter,  $b$ : inner diameter,  $c$ : arm width,  $d$ : thickness.**

#### 3.1 Flexure Springs vs. Coil Springs

While the application of the flexure springs for the free-piston linear machines is common, the feasibility of using coil spring can still be a question. There are key parameters that determine which rebounding component is appropriate for a specific application and include resonant

frequency; moving mass; stiffness in the axial, radial, and circumferential directions; fatigue strength; durability; higher mode resonant frequencies; bulk mass and volume; cost; and packaging feasibility. Some of these parameters are linked together. For example, stiffness and resonant frequencies are interacting directly; however, each of these parameters individually can influence the overall system's design and behavior. To obtain a general idea of whether or not the coil springs are practical to be implemented in linear machines, an FEA was performed and results of some of the above key parameters were compared to a generic steel flexure spring. The stress and fatigue life are not the subject of this preliminary analysis and for all cases evaluated, the same structural steel properties were used. For this purpose, two steel coil springs with high stiffness were selected from commercially available springs. In the selection of the coil spring, the first criterion was the ability of the spring to be maximumly compressed (elongated) equal or slightly greater than the maximum stroke length of the flexure spring (22 mm). The defined stroke length was selected by considering the simultaneous operations of the engine, flexure springs, and alternator and was increased to 30 mm in the upgraded prototypes. For such an application where durability is of significant importance, the compression coil springs were considered rather than tension coil springs. The second criterion for the spring selection was the spring rate. One coil spring was selected to have a stiffness of about the same as one flexure spring ( $\sim 35$  kN/m), and the second spring was selected to represent a pack of five flexure springs (175 kN/m). Figure 28 shows the relative sizes of the springs using the same scale factor.



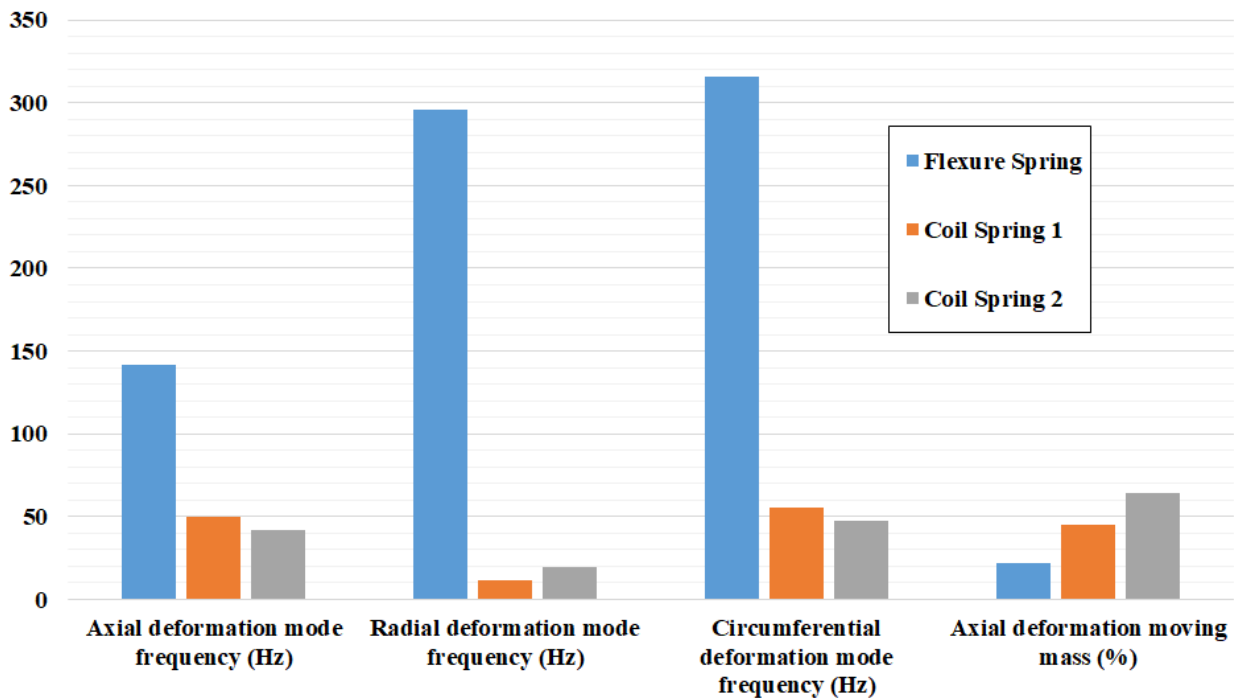
**Figure 28. Dimensional comparison of a flexure spring vs. coil springs.**

Table 3 compares the physical properties of the three springs. The preliminary comparison of the springs indicates that the coils springs are geometrically larger and heavier than the flexure spring.

**Table 3. Physical properties of flexure and coil springs.**

	Flexure Spring	Coil Spring 1	Coil Spring 2
Spring rate (kN/m)	35.5	37.6	178.6
Total Mass (g)	206	848	3960
Total Volume (cm <sup>3</sup> )	26.2	108.1	504.3
Bounding Box (x, y, z) (mm)	124 x 124 x 2.5	49 x 49 x 203	102 x 102 x 203

A basic modal analysis was performed via FEA to compare the stiffness of each spring in three directions: axial, radial, and circumferential. For a better understanding of the results, they were reported in the resonant frequency of the modes where the axial, radial, and circumferential deformations were dominant. The results of the mentioned frequency, and the percent of the axial moving mass, is shown in Figure 29, and the details are provided in Table 4. Results show that the flexure spring has remarkably better performance in terms of the dynamics of the system. In coil springs, the moving mass is the main parameter that influences the frequencies in all directions. For coil spring 2, which has the stiffness equal to five flexure springs or five coil spring 1, due to its large mass, the performance -stiffness and natural frequency - is lower than a single component of other spring types in this test. Results also show that the coil spring is very poor in bearing radial loads which would require use of additional bearing and lubrication systems. It means that using coil spring will result in additional components and cost.

**Figure 29. Stiffness and moving mass comparison of flexure spring vs. coil springs.**



**Table 4. Operational properties comparison of the selected springs.**

	Flexure Spring	Coil Spring 1	Coil Spring 2
Axial deformation mode frequency (Hz)	124	49.7	42.0
Radial deformation mode frequency (Hz)	296	11.6	19.5
Circumferential deformation mode frequency (Hz)	316	55.7	47.2
Axial deformation moving mass (gr)	45 (22% *)	386 (45% *)	2564 (64% *)

\* Numbers in the parentheses are the percentage of the total mass of spring.

There are other considerations regarding the assembly of coil springs and the attachment to the frame and translator. If the coil springs are used individually, it exerts a non-uniform radial loading to the shaft which will cause increased vibration and piston-ring friction in the engine. This is because the compression coil springs with high deformation should have a relatively large pitch distance. Having a larger pitch distance, the flat cuts on two sides of the spring will not form a complete (or near complete) circle shape. So, when a force is applied on one side, a torque is generated around the axis of the spring. This will exert a torque on the shaft.

This initial study showed that for a single-cylinder LEA similar to the current project, flexure springs provide higher natural frequency, and lower mass compared to the coil springs for a 1-5 kW linear power generator which requires the linear displacements of approximately 20-40 mm and a frequency of at least 40 Hz.

### **3.2 Flexure Springs vs. Gas Springs (bounce chamber)**

A gas spring or bounce chamber is another type of rebounding component that has been widely used in previous free-piston linear applications. Gas springs are usually designed and manufactured for a specific machine and hence they are not available as a commercially-available off-the-shelf component for such applications. The gas spring uses a working gas (air in most cases) to absorb the energy from the work done by a moving engine piston in the form of increased pressure and releases the energy back to help the system to complete a cycle and provide the required energy for the compression stroke. Theoretically, a gas can be compressed to high limits. It means that by utilizing a gas spring, by increasing the compression ratio and minimizing the clearance volume, the system's frequency can be increased to very high levels. However, in practice, there are several obstacles in using gas springs that limit the operation of an LEA with bounce chambers. First, using a gas chamber increases the overall friction and further strategies

will be required for the lubrication. The piston-cylinder friction, and the compression of the air, increases the system's irreversibilities and decreases the overall thermal efficiency. If high frequencies (more than 50 Hz) are intended, a high air compression ratio (greater than 20:1) will be needed. Such a high compression ratio needs a small clearance between the piston and cylinder head at TDC and very efficient sealing strategies. It should be noted that for the current commercial seals used in hydraulic and pneumatic systems, the speed and number of cycles are critical to the endurance of the seals. For the current LEA machines at 60 Hz, the current mechanical seal technologies do not meet target life requirements. In addition, high precision assembly of the piston and cylinder is a key factor in the durability and performance of gas springs and causes leakage and additional friction.

There has been a successful application of the bounce chambers as mentioned in the literature review. However, they were mostly used for heavy machines running at low frequencies. In short, with the current technologies, for small power generation units, the application of the gas chamber at a low price is not feasible, and using flexure springs have more advantages.

### **3.3 Flexure Design Approach**

In this chapter, two main approaches were used for the flexure design and analysis. The main approach is FEA and the second is an analytical solution. The analytical method incorporates the basic solid mechanic equation to find a relation for the stiffness of the flexure springs. Due to the complex geometry of the flexure's arms, some simplifications were implemented. However, to compensate for reduced accuracy, a machine learning algorithm in Matlab<sup>TM</sup> was utilized to find the non-dimensionalized coefficients to be used in the equation. The details are provided in Section 3.5.

The other approach, FEA, was extensively used for different numerical modeling including static and transient structural, modal and harmonic analysis, and also coupled FSI analysis. The general FEA considerations are provided in the Appendix Section 9.1.2. In addition, depending on the type of analysis, specific details will be provided in each corresponding section.

### **3.4 Flexure Design**

The primary objective in the spring design for the overall LEA system was the spring rate and effective mass of the spring. The primary analysis requirement of the spring was to maintain a stress level low enough to ensure the required fatigue life of the system. When flexures are operated at high frequency, the order of importance of the objectives was lifetime followed by the resonant or natural frequency of the spring structure and the maximum stroke. In order to meet spring rate, displacement, and fatigue life performance requirements, multiple springs were utilized in parallel in the actual LEA design. In Figure 3, two packs of flexure springs on each side of the translator each containing four springs was shown. To meet the higher overall speed of the assembly, the resonant frequency of the individual spring was maximized to reduce vibration and improve system dynamics.

The flexure spring total mass, and hence the moving mass, is parabolically proportional to the diameter and linearly proportional to the thickness with a positive slope. The axial stiffness is inversely proportional to the diameter and directly proportional to the thickness [137]. The design required the maximum stress lower than the yield strength in order to avoid both static failure and lower than half of the yield strength, as a rule of thumb, to prevent dynamic failure (fatigue).

#### **3.4.1 Material Selection**

The selected material for the flexure springs was required to have high stiffness to maximize the spring constant, have moderate ductility, high fatigue strength, and low density to reduce the moving mass inertia. These five requirements resulted in a narrow selection of possible materials. An additional selection consideration included the manufacturing costs associated with the availability and as manufactured form (e.g. sheet, bar, or other stock forms). Table 5 presents several possible materials, which are all hardened steel alloys except for one titanium alloy.

One of the best performing materials found for the given application was a Sandvik 7C27Mo2 martensitic stainless steel alloy. Because this material is martensitic, there are several advantageous properties that include the presence of the endurance limit and the ability to harden the material by heat treating. This material was found to have good physical and mechanical properties (i.e. elastic modulus, strength, and fatigue), machining capabilities, availability, and

cost. Machinability and surface finish were also considered acceptable. For manufacturing purposes, it was preferred to have the raw material in sheet form.

**Table 5. Properties of high fatigue life materials currently available from suppliers\*.**

<b>Material - Trade Name</b>	<b>Specifications</b>	<b>Density (g/cc)</b>	<b>Elastic Modulus (GPa)</b>	<b>Yield Strength (MPa)</b>	<b>Ultimate Strength (MPa)</b>	<b>Reversed Bending Fatigue Limit(MPa)</b>	<b>Average No. of Cycles to Failure</b>
Steel Alloy - 7C27Mo2 [146]	UNS S42026	7.7	210	1300	1800	710	10 <sup>7</sup>
Steel Alloy - Cronidur30 [147]	AMS 5898	7.7	210	1850	2150	1141	3x10 <sup>6</sup>
Steel Alloy - XD15NW [147]	AMS 5925	7.7	198	1580	2350	1095	3x10 <sup>6</sup>
Steel Alloy - 100Cr6 [147]	AMS 6440	7.83	207	2033	2240	938	3x10 <sup>6</sup>
Steel Alloy - C300 [148]	AMS 6514	7.99	189	1971	2020	861	10 <sup>8</sup>
Steel Alloy - C350 [148]	AMS 6515	8.08	199	2316	2358	758	10 <sup>8</sup>
Steel Alloy - AerMet100 [149]	AMS 6532	7.88	194	1689	1965	945	10 <sup>7</sup>
Steel Alloy - AerMet310 [149]	AMS 6532**	7.97	192	1900	2170	1030	10 <sup>7</sup>
Steel Alloy - AerMet340 [149]	AMS 6532**	7.86	192	2160	2430	986	10 <sup>7</sup>
Steel Alloy - M50 [147]	AMS 6491	7.87	189	2200	2480	1010	3x10 <sup>6</sup>
Titanium Alloy - Ti-6246 [150]	UNS R56260	4.65	114	1120	1200	550	10 <sup>7</sup>

\* Data provided in this table belong to alloys with specific heat/surface treatment tested under specific conditions and shapes. The values must be used with caution for engineering designs.

\*\* There is no direct standard number available from the manufacturer datasheets. The standard number provided is the standard number of similar alloys that these materials were derived.

Figure 30 is the S-N curves of the selected 7C27Mo2 stainless steel material for 50% and 10% probability of fracture provided by the manufacturer. This material has a defined endurance limit, which is desirable for achieving near-infinite life from the flexure springs. A decrease in stress less than 10% can result in a decrease in the probability of fracture of approximately 40%. Extrapolating this finding using Equation 1, the requirement for fracture probability of less than 1% required a maximum stress below 726 MPa. In order to increase the factor of safety for this application, 700 MPa was selected as the maximum design stress.

*Confidence Interval Bounds:  $\bar{y} \pm E$*

$$E = Z_{\alpha/2} \sigma / \sqrt{n} \quad \text{Equation 1}$$

In Equation 1,  $\bar{y}$  is sample mean,  $\alpha$  is the type one error, E is one-half of the width of the (1- $\alpha$ ) confidence level,  $\sigma$  is variance, n is the number of samples, and Z is the random variable associated with the standard normal distribution which was found in the literature [151].

**Table 6. Statistical data of 7C27Mo2 fatigue test.**

Maximum Stress (MPa)	Fracture Probability	$Z_{\alpha/2}$ Factor
$\pm 845$	50 %	0.674
$\pm 785$	10 %	1.64
$\pm 726$	1 %	2.576

$$\begin{cases} \bar{y} - 0.674 \sigma / \sqrt{n} = 845 \\ \bar{y} - 1.64 \sigma / \sqrt{n} = 785 \end{cases} \rightarrow \bar{y} = 886 \text{ MPa} \quad \sigma / \sqrt{n} = 62.11 \quad \text{Equation 2}$$

$$\sigma_s = 886 - 2.576 \times 62.11 = 726 \text{ MPa}$$

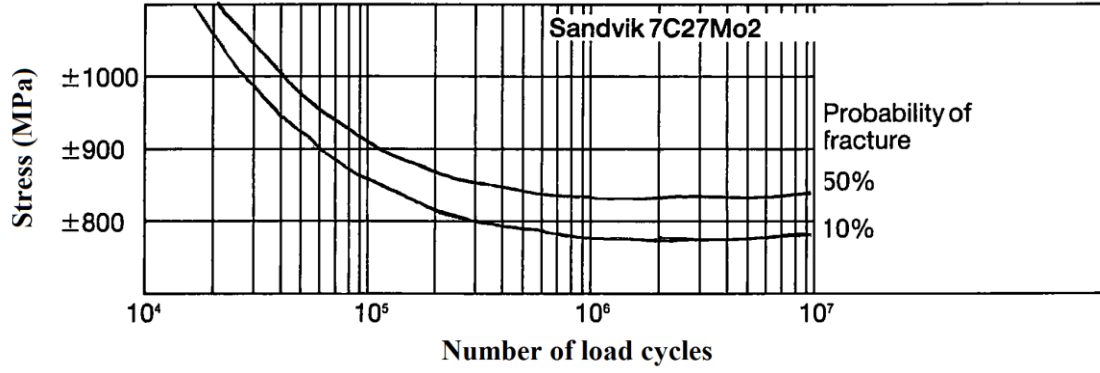


**Figure 30. S-N curves of 7C27Mo2 provided by the manufacturer [146]. At 700 MPa the probability of failure was extrapolated to be 1%.**

### 3.4.2 Flexure Arm Shape

There are several methods to describe a curve for spiral cuts [131], [135], [137]. In this study, the involute of circle was selected to describe the spiral geometry. Higher order equation of spirals and their mathematical properties are provided in section 3.5. The involute of circle provides a suitable equation for use in CAD software as a parameterized model. Such a CAD model was prepared and was updated automatically with communication between the CAD software and the FEA solver. Note that the concentricity of the spirals will lead to a change in the shape of arms and the loads on arms. Therefore, the arm geometry is a critical design feature of the flexure springs. To avoid geometrical failure during CAD updates, the concentric configuration of the arms was used, which required the start point of the spiral to coincide with the center of the flexure disk. The parametric equation of spiral profile in polar coordinates is [131],

$$R = (R_i + (R_o - R_i) * [t + f * \sin(2\pi t)]) * \cos(t\theta) \quad 0 \leq t \leq 1 \quad \text{Equation 3}$$

where  $R$  is the polar distance from the center of the flexure,  $R_i$  and  $R_o$  are the polar distance of the start and endpoint from center respectively,  $\theta$  is sweep angle and  $f$  is the shape factor. The shape factor controlled the radius of curvature as a function of the sweep angle. A zero value for the shape factor resulted in an involute of a circle.

### 3.4.3 Arm Shape Factor

To reduce the moving mass, it was desired to have the whole volume of the spring material equally stressed throughout the stroke. Figure 31 shows two different designs with the same dimensions except for the shape factor (see the previous section for the definition of shape factor). In both designs shown in Figure 31a and Figure 31b, the outer diameter is 124 mm, the inner bore diameter is 15 mm and the thickness is 2.5 mm. The shape factor changes the width of arms and was used to distribute the tensile and compressive stresses evenly throughout the arms. In Figure 31a, the shape factor value is 0.05 versus a shape factor of zero for Figure 31b.

The outer perimeter of the spring was fixed and the surface at the inner circle of the flexure had an axial displacement equal to 11 mm applied normal to the surface. To obtain the spring rate of the flexure, the reaction force was calculated at the fixed outer perimeter and was divided by the axial displacement. As illustrated in Figure 31, the stress was well-distributed for Figure 31a design, with a maximum value of 695 MPa but there were large stress concentrations near the outer diameter of spring for Figure 31b design with the maximum stress of 943 MPa. A well-selected value of the shape factor changed the width of arms around the middle point (Figure 31a). Reduced arm width helped ensure that the deflection occurred evenly along the length of the arm and reduced the stress concentrations at two ends of the spiral cut (Figure 31b). Based on the 700 MPa upper limit for the endurance, design *a* provided infinite life while design *b* lasted only for a few hours.

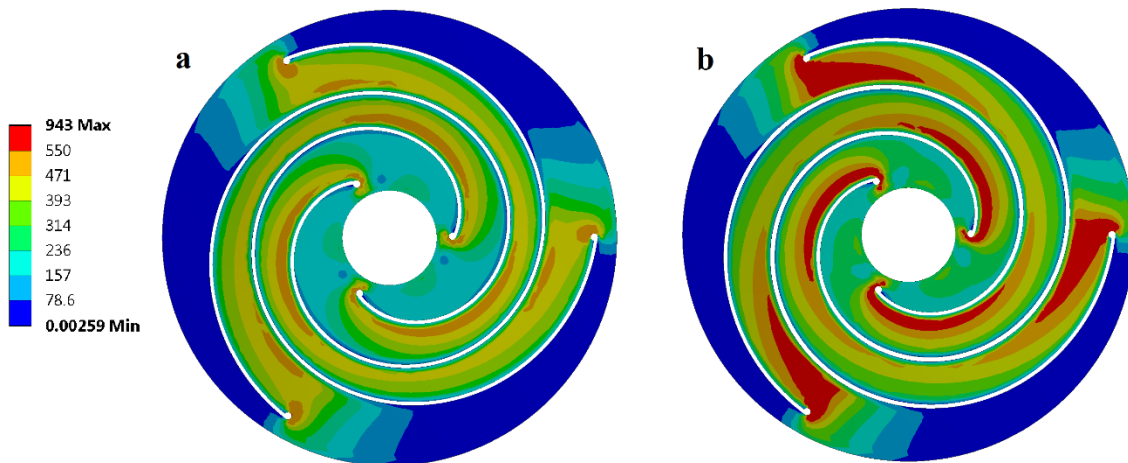


**Figure 31. Contours of the equivalent stress in MPa for two flexure designs with different spiral shape factor, a)  $f = 0.05$ , b)  $f = 0$ . The shape factor was one of the parameters used to control stress distribution within the arms. The objective was to distribute the maximum stress throughout the arms as shown for the left spring design compared to the right design.**



### 3.4.4 Modification of Arm Curves

The shape of the arm slots at the two ends resulted in an area of stress concentration. Multiple schemes were examined that used FEA to examine and reduce the stress at endpoints. Figure 32 shows three example designs from a radius-end with the same size as the slot in Figure 32a, to a variable geometry curved section in Figure 32c. As shown, the use of a greater radius of curvature led to a lower stress variation in the arms. A semi-circle end profile showed the highest amount of stress concentration (Figure 32a). A three quarter circle end profile improved the stress concentrations (Figure 32b). The profile improved by an increased radius of curvature and showed the minimum stress concentration (Figure 32c). It was noted that the end transition did not decrease the width of arms at the endpoints. Thus, the direction of cuts at each endpoint followed the slot angle and was directed towards the inner or outer diameter edges. From Figure 32a to Figure 32c, the maximum von-Mises stress was 536, 473, and 444 MPa, respectively. Based on fatigue life studies, the design in Figure 32c was estimated to last 100 times longer than the design in Figure 32a at a 1% probability of fracture. Thus, the endpoint geometry shown in Figure 32c was selected as the optimized endpoint. As discussed in subsequent sections, the endpoint geometry will not be modified beyond this geometry.

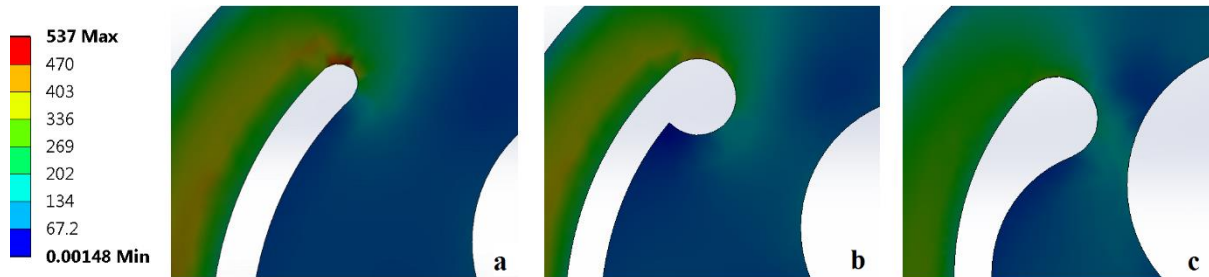


**Figure 32. Comparison of stress concentration in MPa at near center endpoints of a spiral cut with three different curve profiles. A tear-drop shape as illustrated in subfigure c significantly decreased stress concentration.**

### 3.4.5 Modal Analysis

Information on the frequency response of the flexure designs was obtained by conducting a modal analysis within the FEA software. The natural frequency of the flexures dictates the resonant frequency of the overall LEA operation. During the design process, higher modes of spring frequency were carefully considered so that the vibrational losses and probability of arm collisions were minimized. Figure 33 illustrates the first, second, third, and fourth modes of spring frequency.

These modes of frequency were found to be most critical in LEA performance and ignoring the frequency response was found to result in rapid failure. The first mode was the intended mode to operate, see Figure 33a. Due to the axisymmetric geometry of the arms, the second and third mode shapes were symmetric. The frequency of the second mode of deflection, due to its proximity to the resonant frequency, was responsible for most of the vibration. The fourth mode was called surge mode and the risk of collision between arms of two adjacent flexure was highest at this mode of vibration [131]. Collisions of two adjacent arms result in significant loss of energy, noise generation, and eventual failure. A minor modification in the design, such as slot width or shape factor, was used to change the arms vibrational frequency and reduce the potential of contact between neighboring arms. Modal analysis of the flexure springs will be studied in the following sections to consider the effects of the spring's higher harmonics on the vibration.

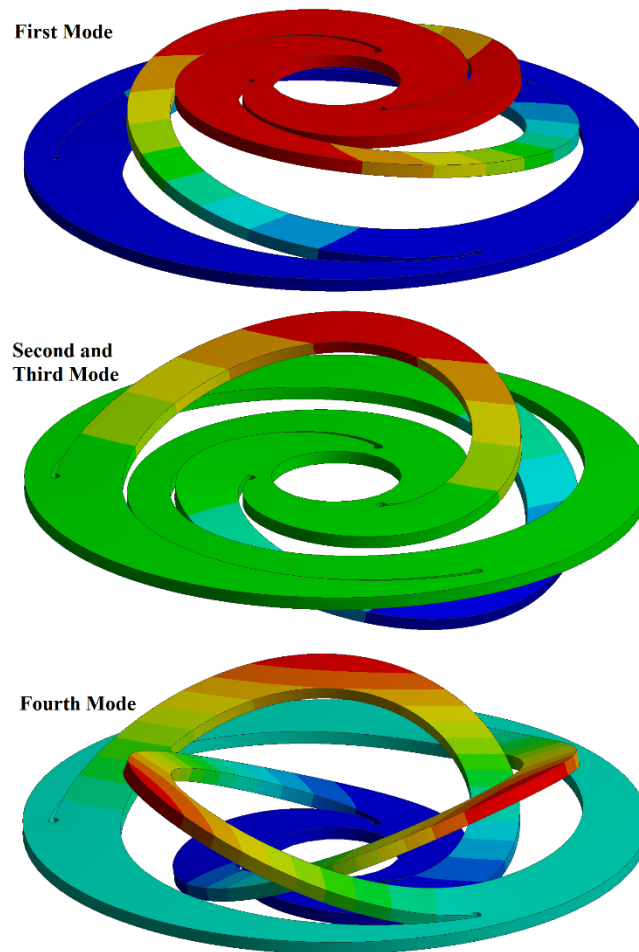


**Figure 33.** The first four mode shapes of a flexure. The contour colors correspond to a scaled displacement with red corresponding to the largest scaled displacement. The outermost radial edge was clamped ( $U_x=U_y=U_z=0$ ).

### 3.4.6 Moving Mass

The spring was designed to minimize the moving mass, provided that, when coupled to the LEA, the desired frequency was realized. For a dynamic system, the magnitude of moving mass was important as it affected the system response significantly. The acceleration and velocity of moving parts, reaction force at fixtures, and the natural frequency of the system were many of the most important parameters, which were a function of the effective mass of the system.

The effective mass for the flexure was obtained from a transient FEA simulation. The analysis calculated the kinetic energy of the spring, which considered a system with the total mass of the spring and maximum velocity of the inner edge and summed the kinetic energy of differential segments and their relevant velocity (Equation 4). With this method, the effective mass of 27.5% of the total mass was obtained. This value was close to the 26% value in literature [139]. The effective mass of helical coil springs ranged from between 33-40% and the results here highlighted the advantage of flexures over coil springs [152].

The effective mass was calculated using the following relationship,

$$\text{Effective Mass Percentage} = \frac{\sum m_i v_i^2}{MV^2} \times 100 \quad \text{Equation 4}$$

where  $m_i$  and  $v_i$  are mass and velocity of the differential segments, respectively,  $M$  is the total mass of a flexure spring, and  $V$  is the velocity at the center of the flexure. When using finite element,  $m_i$  and  $v_i$  are the mass and velocity of each element in the flexure body. It should be noted that the current formulation for the moving mass calculation also depends on the peripheral region of the flexure which is not being loaded. In the examples here, there is about 10 mm margin distance from the start and end of the spirals and the inner and outer diameters. Figure 34 shows the instantaneous moving mass of a titanium flexure spring within 5 cycles. The average value as mentioned above was 27.5%.

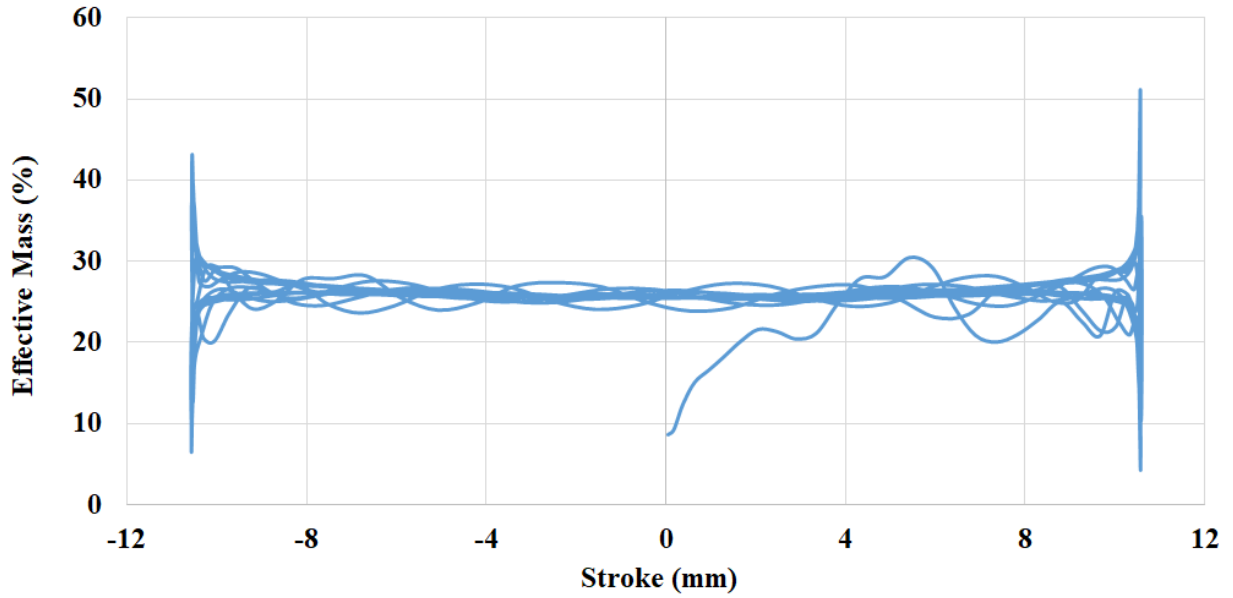


**Figure 34. Moving mass percentage.**

Based on primary alternator tests as a motor, a calculation was performed and it was estimated that the effective moving mass was 24% of the total spring-mass. This value was based on the total spring stiffness from experimental tests where the resonant frequency of the alternator was read from time-displacement graphs of the machine motoring tests. Then the percentage of moving mass was calculated using Equation 5. One reason for the difference in moving mass percentage from the LEA assembly experiments was the uncertainty in the stiffness of flexures under dynamic conditions. In Equation 5, while the frequency  $f$  and  $m_1$  was measured, the stiffness  $k_{total}$ , was the measured values from static tests. In other words, it was assumed that only moving mass of the flexures,  $m_2$ , was responsible for the changes in machine's operating resonant frequency versus the calculated static resonant frequency.

$$f = \sqrt{\frac{k_{total}}{m_1 + zm_2}} \quad \text{Equation 5}$$

where  $f$  is the machine resonant frequency,  $k_{total}$  is the total machine stiffness,  $m_1$  is the moving mass other than the springs mass e.g. rod and translator mass,  $m_2$  is the total mass of the springs and  $z$  is the fraction of springs moving mass.

### 3.5 Analytical Solution

An analytical approach also was implemented to obtain the stiffness and resonant frequency of the flexure springs. The CAD/FEA method as was explained in the previous sections are useful for the detailed analysis and verification of the final product, however, the analytical method can provide important information regarding the non-dimensionalization and parametric study of the flexure springs. As a drawback, because the mathematical equations and partial differential equations must be derived and solved, there are some limitations on the complexity of the geometry for the analytical solutions. Therefore, a simplified geometry will be used in this study.

There are different equations representing a curve for the spiral cut for a flexure spring. Here, three examples are presented. The first equation is the one stated in Equation 1. This equation is especially convenient for the parametric study using CAD/FEA. For the design space exploration, the geometric model needs to be updated in the CAD software at each iteration automatically and it is important that the curve has the ability to be updated using a mathematical representation and be connected to other flexure dimensional parameters easily. So, in this case, the original equation in [131] was updated to enforce the inner and outer diameter to the spiral equation. It should be noted that this equation is only an involute of a circle only when  $\theta=2\pi$ . However, this equation is useful as it directly uses the shape factor parameter and contains the inner and outer diameter parameters.

$$\begin{aligned} x_i &= [r_i + a + (r_o - r_i - (a + b))(t + f \sin(2\pi t))] \cos(t\theta) & 0 \leq t \leq 1 \\ y_i &= [r_i + a + (r_o - r_i - (a + b))(t + f \sin(2\pi t))] \sin(t\theta) & 0 \leq t \leq 1 \end{aligned} \quad \text{Equation 6}$$

Where  $x$  and  $y$  are the Cartesian coordinates of the spiral points,  $r_i$  and  $r_o$  are the inner and outer circle radius, respectively,  $a$  and  $b$  are the margin distance of the start and the end of the spiral from the edges of the inner and outer circles, respectively,  $t$  is the normalized length of the spiral,  $f$  is the shape factor, and  $\Theta$  is the sweep angle of the spiral.

Chen et al. provided a more detailed equation of the spiral equations with more parameters to control the starting and ending angle of the curve [137]. Although having more control could be beneficial for a better design to reduce the maximum stress concentration, these equations are

complex for an analytical solution and also the automatic geometry updating cannot be completed properly with having this many parameters in the equations. The equations are,

$$R = R_i + (R_o - R_i)(A_1\theta^1 + A_2\theta^3 + A_3\theta^5 + A_4\theta^7) \quad \text{where} \quad \text{Equation 7}$$

$$A_1 = S_i$$

$$A_2 = -\left[\frac{1 + 2F_M^2}{F_M^2}\right]S_i - \left[\frac{F_M^2}{2(F_M^2 - 1)}\right]S_o + \frac{F_M^2(5F_M^2 - 7)}{2(F_M^2 - 1)^2} + \frac{1}{F_M^2(F_M^2 - 1)^2}$$

$$A_3 = \left[\frac{2 + F_M^2}{F_M^2}\right]S_i + \left[\frac{(F_M^2 + 1)}{2(F_M^2 - 1)}\right]S_o + \frac{(7 - 3F_M^4)}{2(F_M^2 - 1)^2} - \frac{2}{F_M^2(F_M^2 - 1)^2}$$

$$A_4 = \frac{-S_i}{F_M^2} - \frac{S_o}{2(F_M^2 - 1)} + \frac{(3F_M^2 - 5)}{4(F_M^2 - 5)(F_M^2 - 1)^2} + \frac{1}{F_M^2(F_M^2 - 1)^2}$$

Another effective method is to directly use the involute of a circle in Cartesian coordinates.

$$x_i = r(\cos(\theta) + \theta\sin(\theta))$$

$$y_i = r(\sin(\theta) - \theta\cos(\theta))$$

$$\text{Equation 8}$$

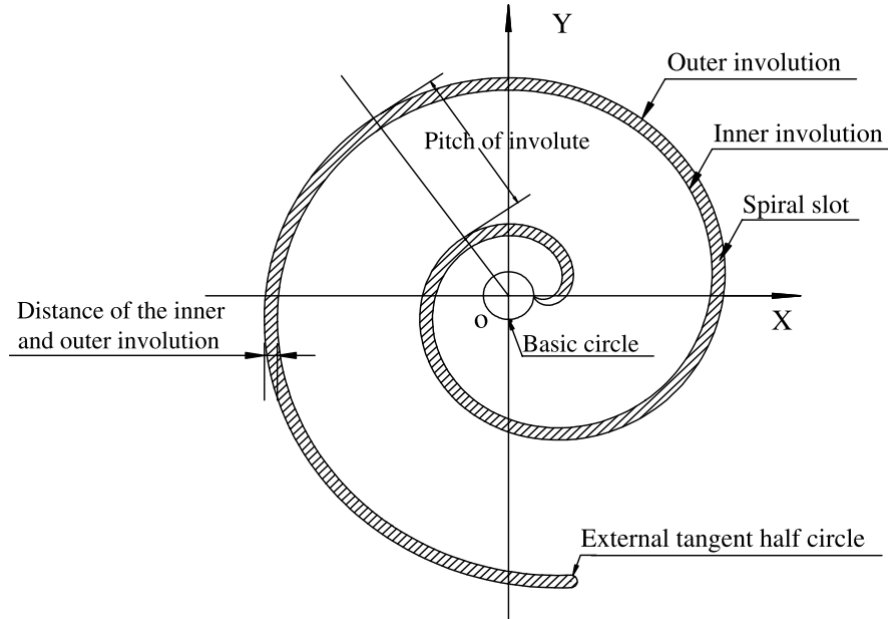


**Figure 35. Involute of a circle [137].**

This equation is very simple to use for the development of mathematical algorithms and analytical solutions. Using Equation 8, the curve will be an involute of circle and further equations related to characteristics of the curve can be used such as the pitch distance, curve length, and radius of curvature [137]. Although these set of equations are very easy to use, using shape factor parameter is not as straightforward as in Equation 6 and the outer diameter parameter cannot be controlled directly from the equation and hence the sweep angle are limited to the outer diameter, unlike the first method where any sweep angle of arms could be accommodated in a certain outer diameter of a flexure spring. For deriving the stiffness equations and non-dimensional numbers, this set of equations will be used.

$$\text{Pitch of the involute} = 2\pi a \quad \text{Equation 9}$$

$$\text{Radius of involute} = a\sqrt{1 + \theta^2} \quad \text{Equation 10}$$

$$\text{length of involute} = \frac{a\theta^2}{2} \quad \text{Equation 11}$$

From Equation 9, using uniform width arms (shape factor = 0), the width of each arm is

$$\text{Width of flexure's arm} = \frac{2\pi a}{n} \quad \text{Equation 12}$$

where n is the number of arms. The moment of force F applied to the center axis of the flexure on an infinitesimal segment of an arm is shown in Figure 36. The distance of the center axis and mid-point of the neural surface of the segment is R, at sweep angle  $\theta$ , starting from the center. The moment  $M = R \times F$  is decomposed into X and Y elements, parallel and normal to the top surface of the segment. The X element of the moment cause the arm torsional deformation and the Y element result in bending deformation. Each segment is considered as a small cantilever beam.

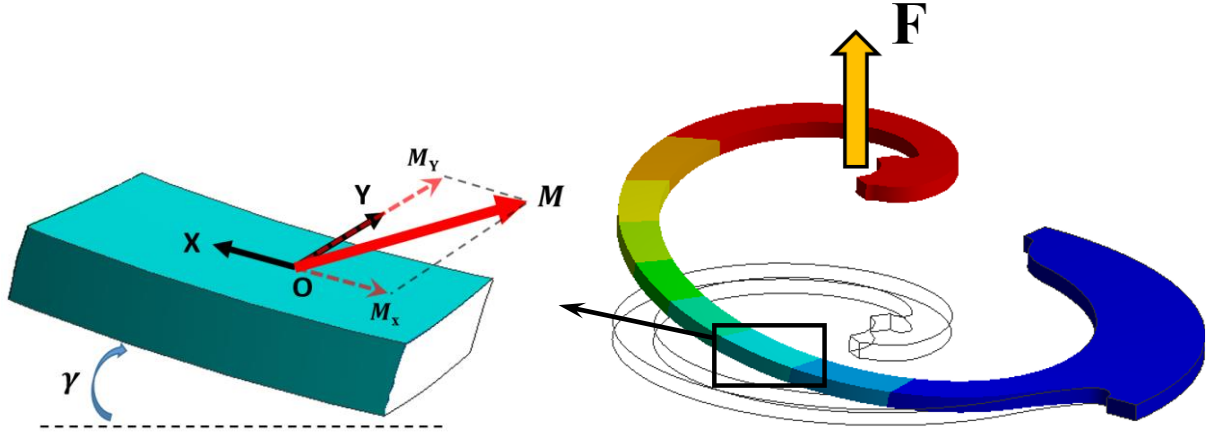


Figure 36. Force and moments on flexure arms.

The bending and torsional moments can be written as,

$$\text{Torsional Moment} \quad M_x = FR \cos(\gamma) \quad \text{Equation 13}$$

$$\text{Bending Moment} \quad M_y = FR \sin(\gamma) \quad \text{Equation 14}$$

The angle  $\gamma$  is called the helix angle and is the angle of the flexure arms after deformation with respect to the horizontal axis. The Z element of the main moment is negligible and hence  $M_z = 0$ .

The energy equilibrium equation for the work done by the force F and strain energy stored due to two moments,

$$\frac{1}{2}F\delta = \frac{1}{2}M_x\theta + \frac{1}{2}M_y\sigma = \frac{1}{2}[\{FR\cos(\gamma)\}\theta + \{FR\sin(\gamma)\}\sigma] \quad \text{Equation 15}$$

where  $\delta$  is the center deflection of the flexure,  $\theta$  is the twist angle, and  $\sigma$  is the slope angle. The internal strain energy in a cantilever beam subjected to bending is

$$dU = \frac{M(s)^2}{2EI} ds \quad \text{Equation 16}$$

Also, the external work due to moment M is

$$dW = \frac{M}{2} d\sigma \quad \text{Equation 17}$$

Writing the equilibrium of energy for the infinitesimal element, the bending rotation is found



$$d\sigma = \frac{M(s)}{EI} ds \quad \text{Equation 18}$$

It is assumed that the cross-section profile of the arm remains rectangular during the deformation. For the element shown in Figure 36 subjected to the torque T, the shear stress is

$$\tau = \frac{G\theta}{l} \frac{2A}{s} = \frac{2G\theta bh}{l} \quad \text{Equation 19}$$

The torque on a rectangular beam is calculated as

$$T = \int_0^{h_s/2} 4bh\tau dh = \int_0^{h_s/2} \frac{G\theta}{l} 8bh^2 dh = \frac{1}{3} bh_s^3 \frac{G\theta}{l} \quad \text{Equation 20}$$

Then the internal energy equation of the beam is written as,

$$dU = \frac{1}{2} \frac{\pi^2}{G} dV = 2G \frac{\pi^2 h^2}{l^2} dV = 18 \frac{T^2 h^2}{b^2 h_s^6 G} DV \quad \text{Equation 21}$$

And the external work on the beam is

$$dW = \frac{T d\theta}{2} \quad \text{Equation 22}$$

Writing the equilibrium equation, the torsion angle of the beam is

$$d\theta = 9 \frac{T(s)}{h_s^3 b G} ds \quad \text{Equation 23}$$

Substituting Equation 18 and Equation 23 into Equation 15 results in

$$Fd\delta = Td\theta + Md\sigma = \frac{9(Fa\sqrt{1+\theta^2}\cos\gamma)^2}{h_s^3 b G} ds + \frac{(Fa\sqrt{1+\theta^2}\sin\gamma)^2}{EI} ds \quad \text{Equation 24}$$

Integrating Equation 24 over the length of the curve, the axial displacement of the arm at its center is

$$\delta = \frac{FR_o^3}{4h_s^3 b} \left( \frac{9\cos^2\gamma}{G} + \frac{12\sin^2\gamma}{E} \right) \theta \quad \text{Equation 25}$$

The above formula was simplified by assuming the term containing the sweep angle is calculated as  $\sqrt{1 + \theta^2} \approx \theta$  for large sweep angles. Considering the definition of the linear spring's stiffness rate  $F = Kx$ , the final equation of the spring's stiffness is

$$K = \frac{1}{\left[ \frac{R_o^3}{4h_s^3b} \left( \frac{9\cos^2\gamma}{G} + \frac{12\sin^2\gamma}{E} \right) \theta \right]} \quad \text{Equation 26}$$

For most of the practical cases, the average spiral angle is less than 5 degree and can approximate  $\cos^2\gamma \approx 1$  and  $\sin^2\gamma \approx 0$ . Hence Equation 26 can be further simplified to

$$K = \frac{1}{\left[ \frac{9R_o^3}{4h_s^3bG} \theta \right]} \quad \text{Equation 27}$$

To obtain Equation 27, many simplifications have been used. To calibrate the equation, a machine learning scheme was used to find the coefficients related to the  $R_o$ ,  $h_s$ , and  $b$ . To start the calibration, initially 150 design points in a range of arm outer diameter, width, and thickness were selected and generated in CAD software and solved using FEA to find the stiffness. Results of stiffness from FEA and Equation 27 were compared and three coefficients were generated so that the error between the FEA and equation was minimized. The range of each parameter is shown in Table 6.

**Table 7. Design explorer parameters' ranges.**

Parameter	Lower limit (mm)	Upper limit (mm)
Spiral angle	$\pi$	$3\pi$
Arm width	1	6
Arm thickness	1	4

The initial comparison of the results of stiffness between the FEA and Equation 27 is shown in Figure 37. For the majority of the cases, the analytical approach underestimates the stiffness with about 70% error. It should be noted that the design points in Figure 37 were sorted based on the spiral angle on the x-axis. For a certain number of cases where the torsion of the arm was much higher than its bending the analytic formula over predict the FEA results. In these cases, conditions such as low spiral angle (about 90 degrees), narrower arm width, or a high ratio of the thickness/width existed. So, for an improved calibration of Equation 27, the values of 60 design

points where their dimensions were not practical to use in this application were omitted from the pool of data and the rest of them were used for machine learning study.

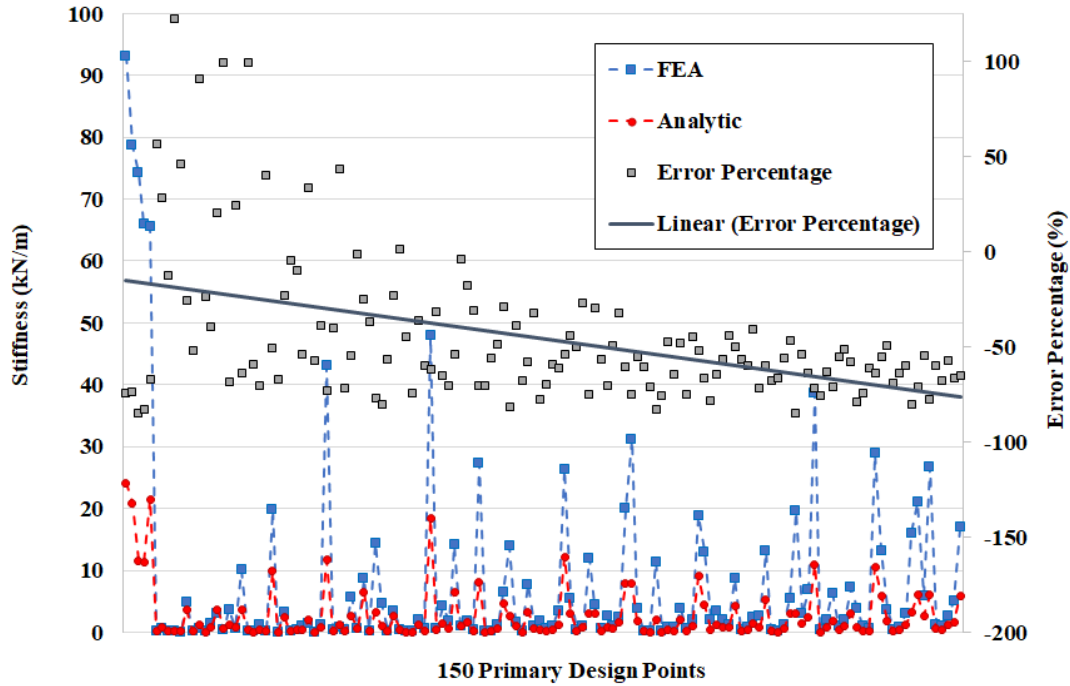


**Figure 37. Comparison of the stiffness results of FEA and initial analytical solution.**

In Equation 27, there are four places that require coefficients. It is important to continue the process step by step for one coefficient at a time. At each step, a variable that shows the best correlations in terms of goodness of the fitting is selected and the selected coefficient is applied to the equation and then proceed to the next variable. For each step, different combinations of the variables were examined to assure if the best correlation was obtained using a combination of coefficients to reduce the operations and the number of added coefficients to the final equations. However, the study showed that in all steps, using only one coefficient resulted in the best fit. In addition, for each step of the process, the input(s) and output (cost function) parameters should be selected. For the cost function, two parameters were available, the percentage of error and the ratio of two stiffness values from FEA and Equation 27. Using the ratio of the stiffness was more convenient because the percentage of errors was very high for some of the design points with low stiffness values in the denominator of the fraction. For the input, an array of different parameters were examined at each step, and then the one was selected that showed the best correlation between the input and output. Before going to the next step, the obtained value(s) of the coefficient was applied

to the selected parameters and the modified stiffness and then the modified ratio was calculated to be used as the cost function in the next step. In this case, the process was repeated three times and the order of input parameters was spiral outer diameter, thickness, and width. The details of the curve fitting results are provided in Appendix 9.3. Figure 38 shows the results of the three coefficients for the selected range of the parameters. Finally, Equation 27 is changed to Equation 28 that contains the coefficients.

$$K = \frac{1}{\left[ \frac{9(C_r * R_o)^3}{4(C_{th} * h_s)^3 (C_w * b) G \cdot \theta} \right]} \quad \text{Equation 28}$$

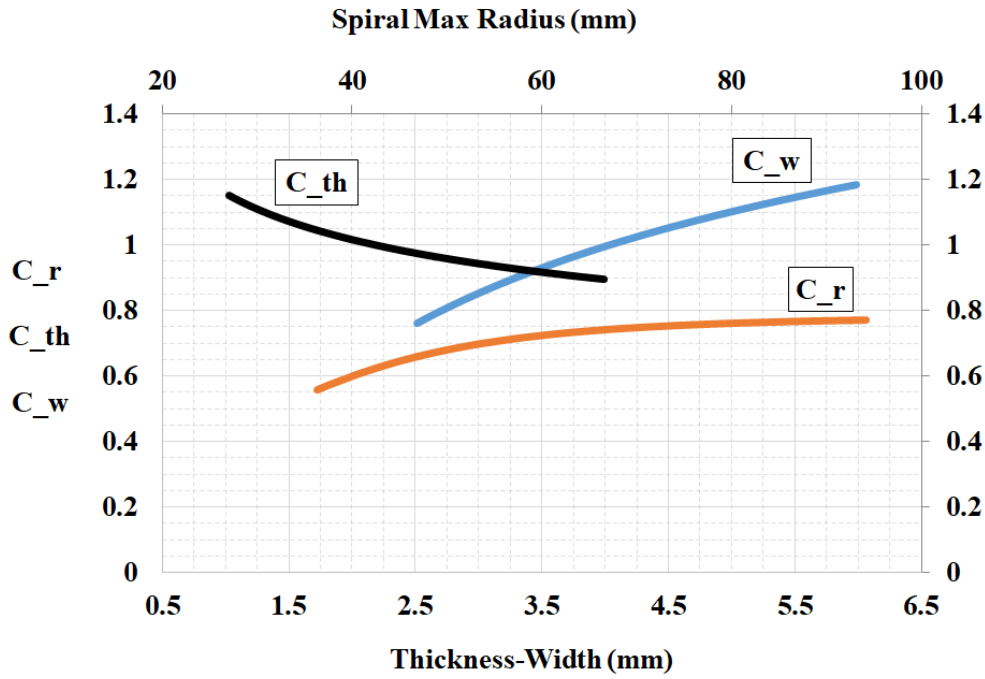


**Figure 38. Coefficients of spiral radius, thickness, and width for the analytical equation.**

Applying the coefficients shown in Figure 38, the error of the stiffness estimation by Equation 27 was improved significantly. Figure 39 shows the ratio  $K_{FEA}/K_{Equation}$  after every round of modifications. The design points on the x-axis were sorted based on the spiral sweep angle with the lower number on the left. Using coefficients in Figure 38, the average absolute error for all design points was 5.7%.

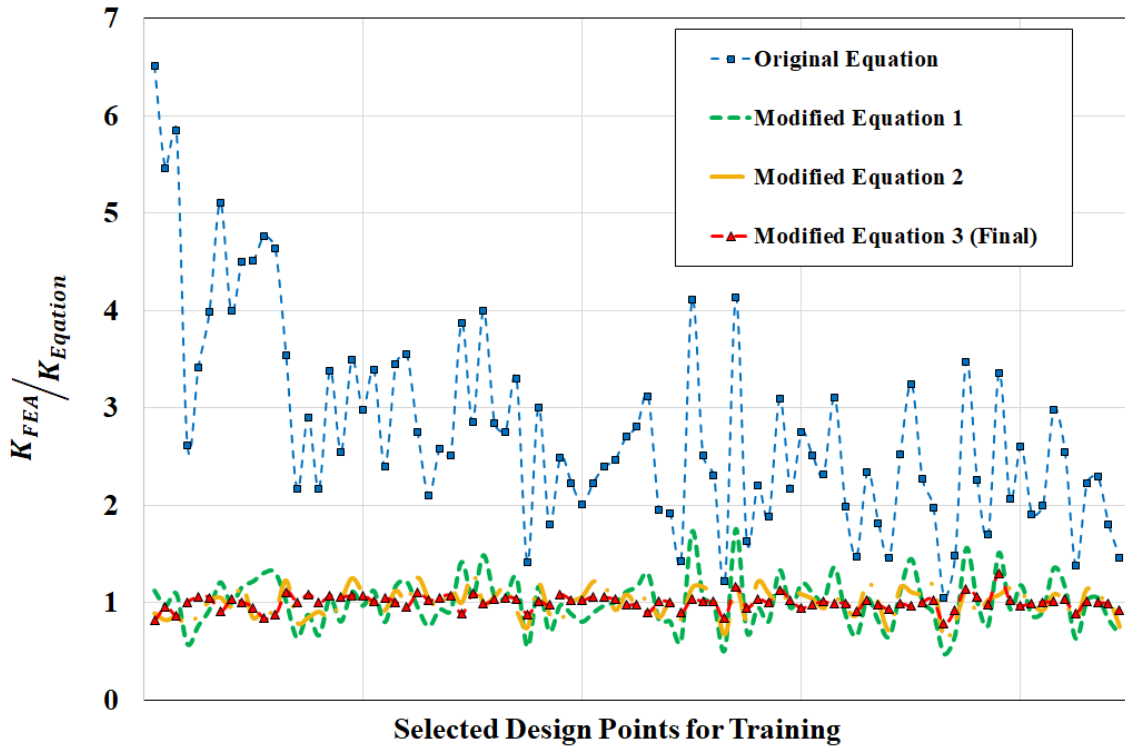


Figure 39. Improvement of the analytical equation in the prediction of one arm's stiffness.

### 3.6 Design Optimization and Sensitivity Analysis

The spring design was refined and included an analysis for a 10-year life span through a parametric study, which used the ANSYS software package. A fully parameterized model was first prepared in SolidWorks and then imported in ANSYS, which was subsequently solved via static structural and modal analysis solvers [153], [154]. A greater depth of the solid, FEA, and other models are provided in Appendix 9.1.3.

The geometric variables that defined the parametric model included the outer diameter, sweep angle, thickness, and the number of arms. Initially, an optimal space-filling method of design of experiment (DoE) was used to define an initial set of 1500 design points, which were calculated using FEA. The bounds of the design space were selected to be broad with a large number of initial design points to capture any non-linearities in the design space. Table 8 provides the ranges of the variables.

**Table 8. Independent variable ranges used for the presented design study.**

<b>Variable</b>	<b>Lower Bound</b>	<b>Upper Bound</b>
Outer Diameter	70 mm	150 mm
Thickness	1 mm	3 mm
Number of arms	3	8
Sweep angle	180°	540°

Using these initial design points, a neural network (NN) method was employed on which a response surface technique was used to determine the optimal design. The total number of design points for the NN was increased to 6000 design points. The inputs were similar to the initial design points and the outputs were maximum equivalent stress and resonant frequency. The NN algorithm was then trained based on these inputs and then outputs were calculated to determine the weight functions of the hidden layers associated with the neurons [45]. For the flexure springs for high-speed and high-stroke applications, the most common materials are steel and titanium alloys. Other materials are either not as strong as steel or not as light as titanium. The combination of these two properties makes steel and titanium alloys suitable candidates, specifically for prototyping and low-volume productions as the cost of raw material for titanium alloys are higher than steel alloys [150]. So, in this study, the design exploration was performed for these two materials in a similar way.

### **3.6.1 Optimization of Steel Flexures**

Figure 40 shows two designs of springs that are defined by the lower and upper bound provided in Table 8. Note the ends where the kerf slot begins and ends were not parameterized. Thus, the ANSYS-SolidWorks interface did not optimize this area of the spring. The effect of endpoint curves on the reduction of stress was accounted for via the definition of the allowed range of maximum stress. The defined ranges for the input parameters design points were created automatically in the ANSYS optimization tool.

Performance criteria such as spring mass, spring stiffness, natural frequency, and maximum stress were obtained and analyzed with the surface response tool in ANSYS. Using the response surface tool in ANSYS, the interaction of different design parameters on outputs, and the rate of their effects was examined. This allowed the most important design parameters to be identified. Figure 41 and Figure 42 show the variation of the resonant frequency and maximum equivalent stress of a

single spring as a function of the outer diameter, thickness, sweep angle, and the number of arms. For the surface graphs, only two of the input parameters were varied at a time while the other two remained constant at their mid-range based on Table 8.

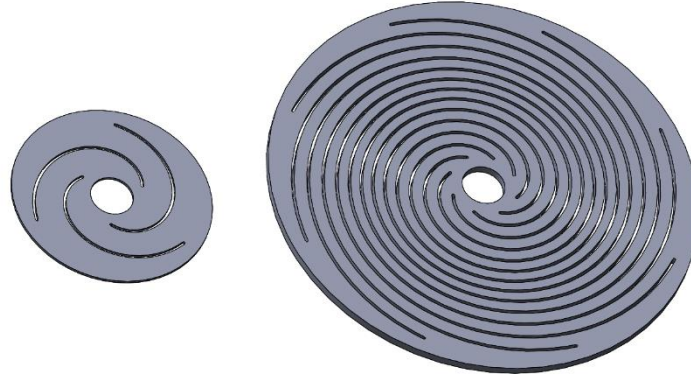


**Figure 40. Illustration of two fully parameterized models, left: design using the lower bounds, right: design using the upper bounds.**

The results were obtained based on the steel material properties as provided in Table 8. Design points with very high-stress values were eliminated; however, the maximum stress in some cases was still greater than the yield strength of steel alloys, which would ultimately result in failure. A few of these designs were retained since additional optimization of the spiral cuts and endpoint profiles, and shape factor was shown to reduce the maximum stress by average 20%. The maximum allowable stress level for most of the commercialized materials for high cycle applications was below 1000 MPa (see Table 5).

**Table 9. Material properties of the steel used in the simulation to evaluate geometric influence.**

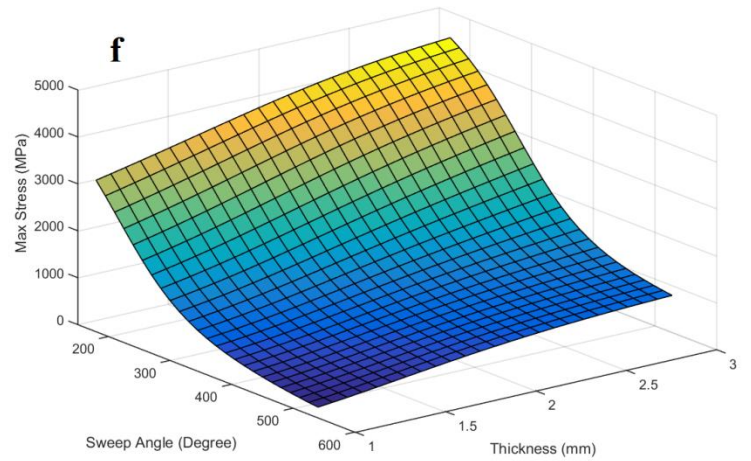
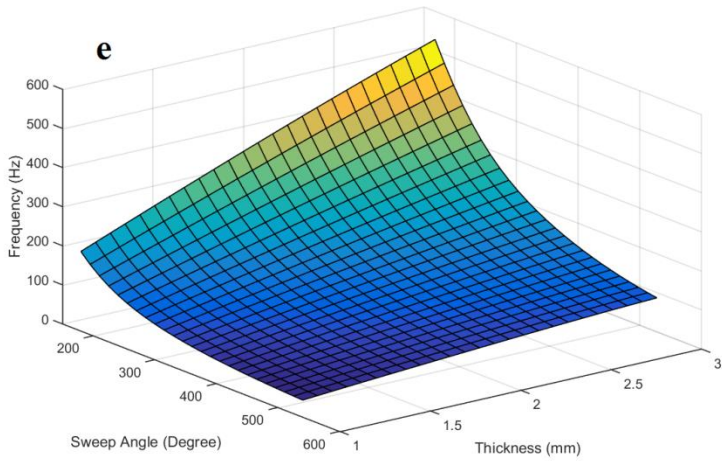
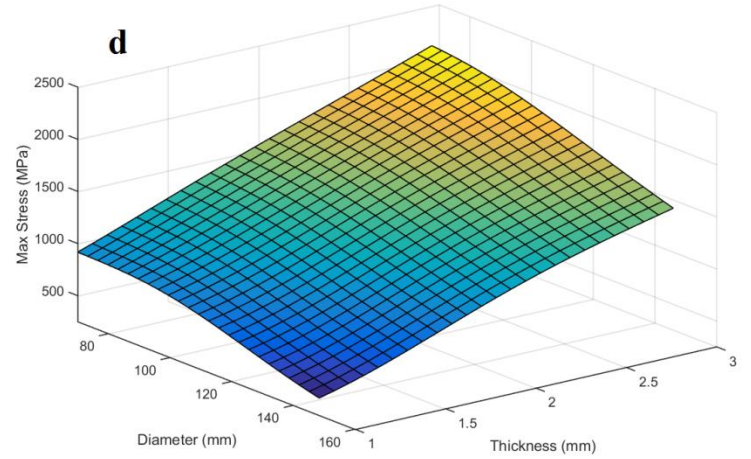
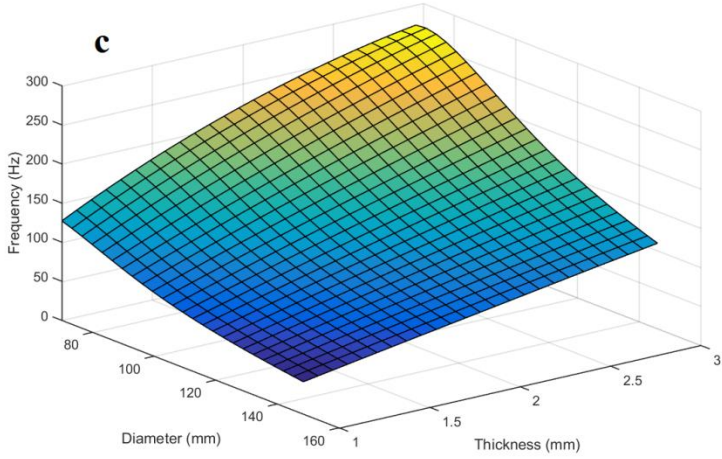
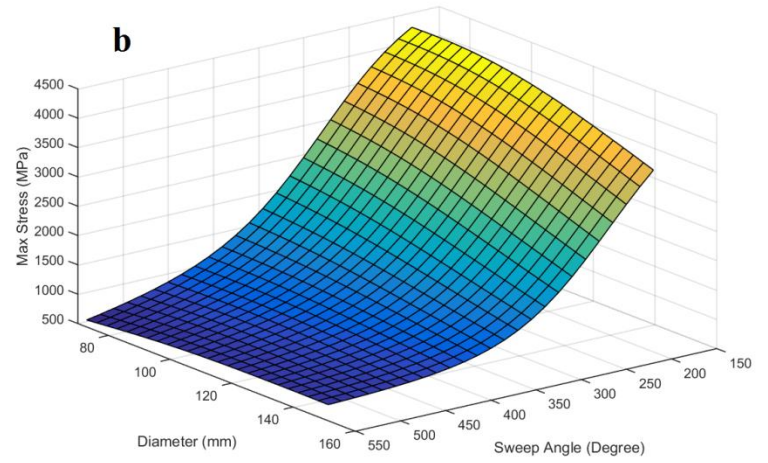
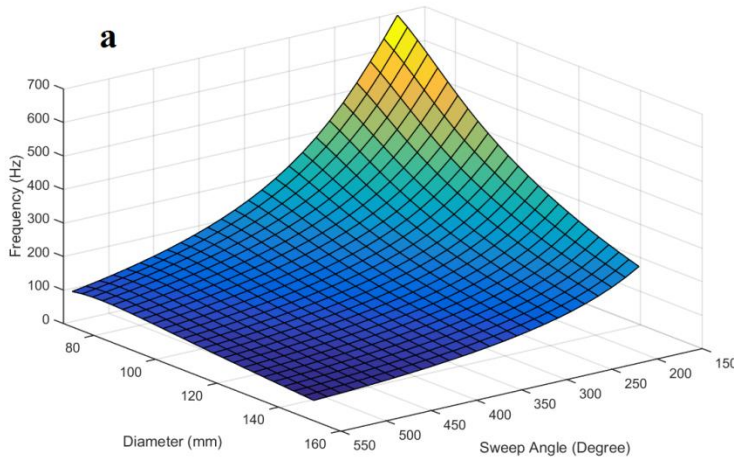
Property	Value
Density	7.7 g/cc
Elastic Modulus	210 GPa
Poisson's Ratio	0.3

Compared to the sweep angle and thickness, the outer diameter demonstrated greater influence on both frequency and stress (Figure 41a-Figure 41d). It was also determined that for a reduced sweep angle, the increase in the rate of stress was higher than the increase in the rate of frequency (Figure 41a, b, e, and f). Thus, to improve stiffness and life of a flexure, a modified sweep angle was not the first choice as its detrimental effects on stress were more than its favorable effects of frequency. The effects of increasing thickness showed almost a linear behavior and increased with both frequency and stress. However, the rate of increased frequency from increased thickness was

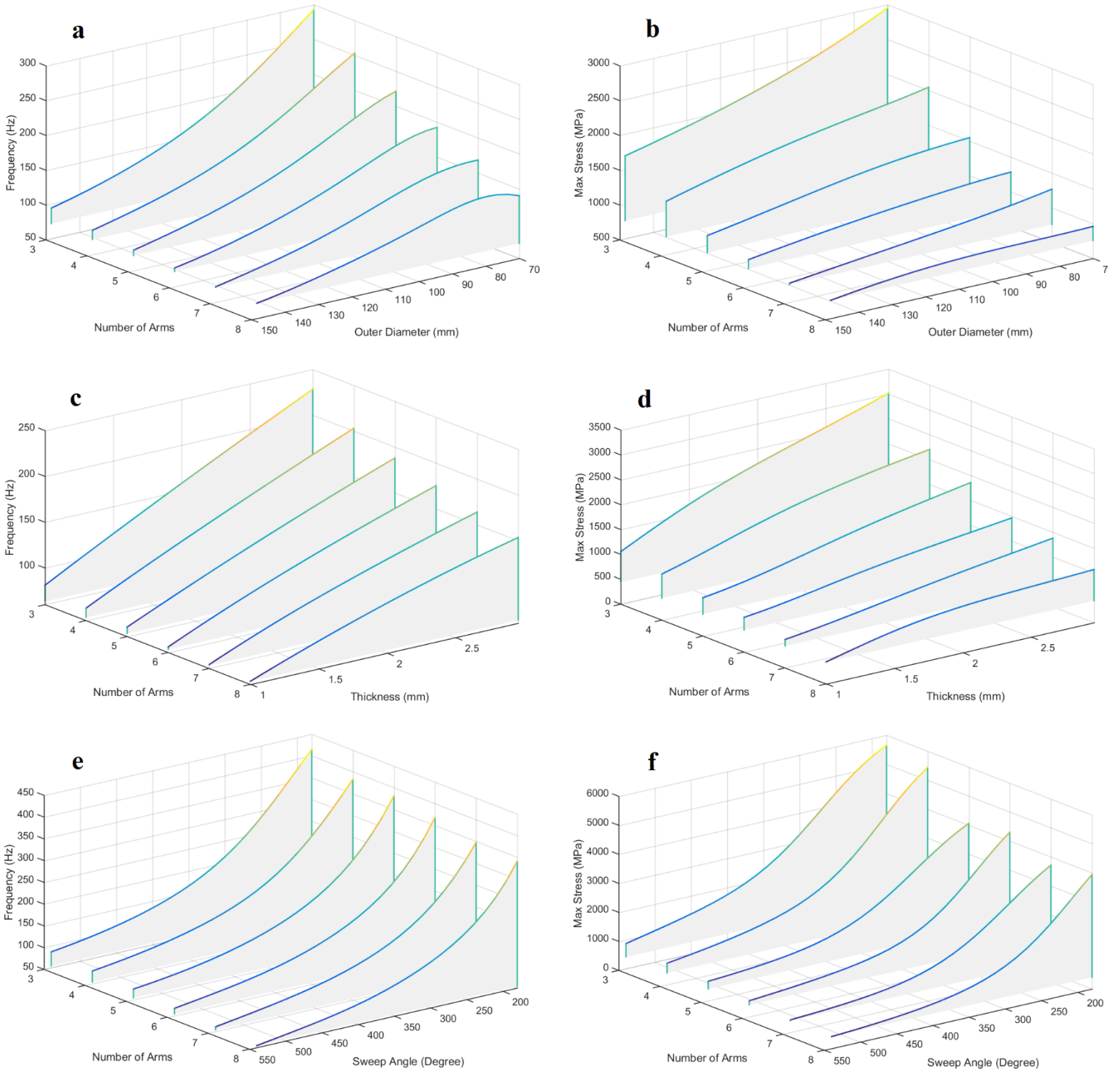
elevated at lower values of outer diameter and sweep angle (Figure 41c-f). The interactions of the number of flexure arms and the other three parameters are illustrated in Figure 42a-f. For high stroke applications, use of three or four arms yielded high stresses on the flexure and was not feasible for dynamic applications. In addition, it was found that in designs with seven or eight arms, the reduced diameter of less than 80 mm had negative effects on the resonant frequency of the flexure (Figure 42a). The effects of thickness on frequency were nearly linear in the whole range of the number of arms (Figure 42c). Figure 42e shows that when the diameter and thickness were constant, a reduced sweep angle increased the frequency of all designs with a different number of arms in the same manner.

Figure 43 depicts the sensitivity of the input parameters on the outputs for a different number of arms from four to seven. Each graph includes a segmented circle and ring. The circle at the center depicts the maximum equivalent stress and the outer ring shows the resonant frequency. Each of the colored segments is one of the three input parameters including thickness (blue), diameter (orange) and, sweep angle (grey). The rate of the sensitivity of performance criteria to design inputs is shown in each segment. The larger area of a color (the greater percentage) implies the greater importance of that specific parameter. The figure shows that the sweep angle of the springs was the most significant design parameter and the thickness was the second most important. Figure 43 yields useful information at a certain design point (mid-range) by which other parameters were tuned. For instance, with the current set of inputs shown in Figure 43, a reduction in the outer diameter was the most suitable parameter to change in order to increase the frequency with minor negative impacts on stress level. Another case was when a design was at the desired frequency but the stress level was still high – the case where a designer required lowering the stress level without considerable changes to frequency. In such circumstances, the sweep angle was the primary variable to change, which yielded the desired effect. It was found that the thickness had nearly the same influence on both the frequency and the stress.





**Figure 41. Response surface of interactions of outer diameter and sweep angle on frequency (a) and maximum equivalent stress (b), interactions of outer diameter and thickness on frequency (c) and maximum equivalent stress (d) and interactions of sweep angle and thickness on frequency (e) and maximum equivalent stress (f).**



**Figure 42. Response profile of interactions of number of arms and outer diameter on frequency (a) and maximum equivalent stress (b), interactions of number of arms and thickness on frequency (c) and maximum equivalent stress (d) and interactions of number of arms and sweep angle on frequency (e) and maximum equivalent stress (f).**

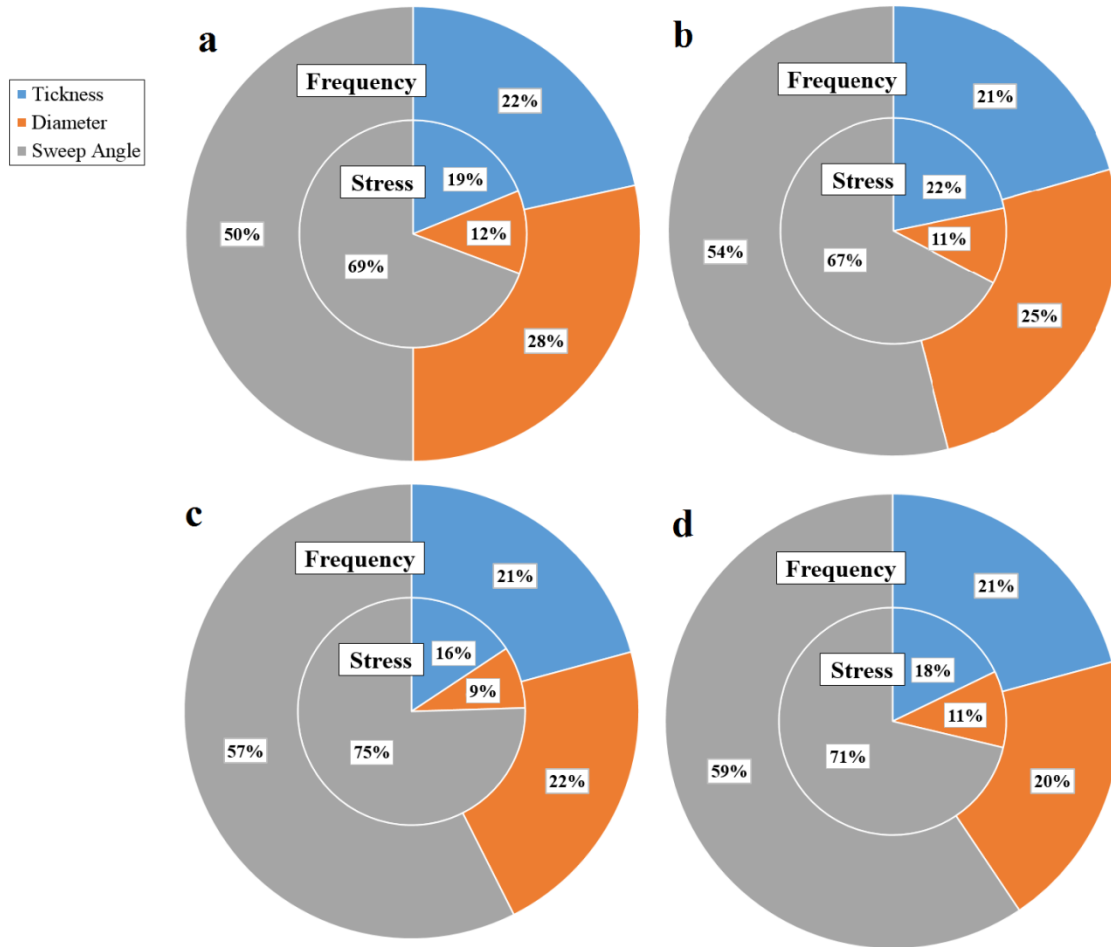


**Figure 43. Sensitivity charts for design parameters of a flexure with, a) 4 arms, b) 5 arms, c) 6 arms, d) 7 arms. The inner circles are associated with stress and the outer circles are associated with frequency. Sweep angle is demonstrated to have the most influence on both stress and frequency.**

The optimization tool identified possible candidates amongst all design points based on the design constraints for spring mass, resonant frequency, and maximum equivalent stress. Figure 44 shows the scattered distribution of all design points in a frequency/stress chart for the Sandvik steel material. Each point in the chart is a design point consisting of specific values for diameter, thickness, sweep angle, and number of arms. Steel alloy materials depend on the fatigue limit; therefore, a proper value for maximum allowed stress can be selected on the horizontal axis and the design point that produced the maximum frequency can be found by picking the top point. Using this chart, the best design was identified based on the material properties and operational limitations due to fatigue. Application of constraints on output parameters narrowed down the

choices and final design points and input values were selected from the chart. As mentioned above, modification of the shape factor and endpoint profiles reduced the stress concentration by average 20%. For instance, Figure 44 was used to determine the maximum achievable resonant frequency for a flexure spring made of C300 steel alloy (based on Table 5 fatigue limit value). The estimated value was 155 Hz when stress reduction possibilities by shape factor and slot profile modifications were considered.

Observing all design point scatters in Figure 44, a linear relationship between the maximum frequency and the maximum equivalent stress was identified. This linear relation is shown with a red dashed line in Figure 44 and is written in Equation 29 as a rule of thumb of flexure design using steel alloys.

$$f = 0.133 \sigma + 25 \quad \text{Equation 29}$$

where  $\sigma$  is the design maximum equivalent stress for a certain steel alloy (equal to the fatigue limit) in MPa and  $f$  is the highest achievable resonant frequency in Hz. This equation can be used to design a flexure with the same displacement boundary condition (BC)-deflection amplitude length of 11 mm.

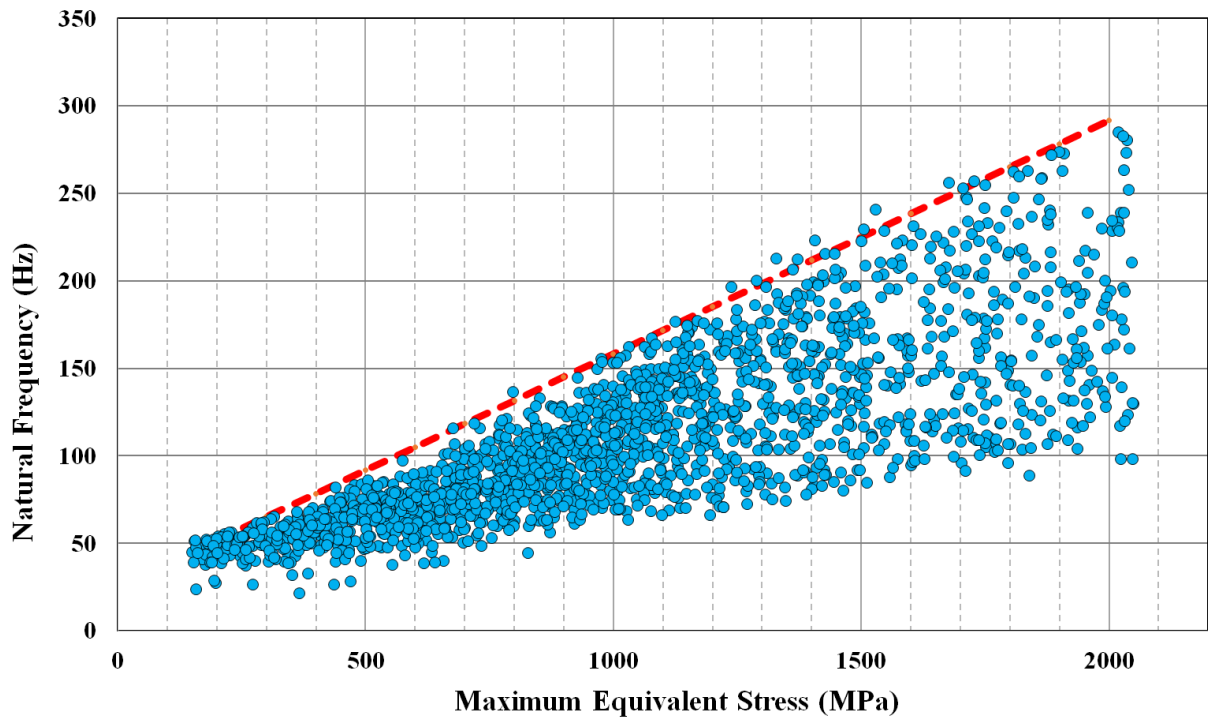


**Figure 44. Scattered distribution of design points in frequency/stress chart for a single steel spring.**



### 3.6.2 Optimization of Titanium Flexures

The same approach was taken for the titanium material. The results of the effects of the geometrical dimensions on the outputs, and also the sensitivity charts are presented in Appendix 9.4. To compare the steel and the titanium materials, the trade-off chart is shown in Figure 45. Same as the procedure for the steel material, the red dashed line in the figure represents the linear relation between the maximum stress level and the maximum achievable resonant frequency of an individual flexure spring. Equation 30 is the formula of the line.

$$f = 0.15 \sigma + 65$$

Equation 30

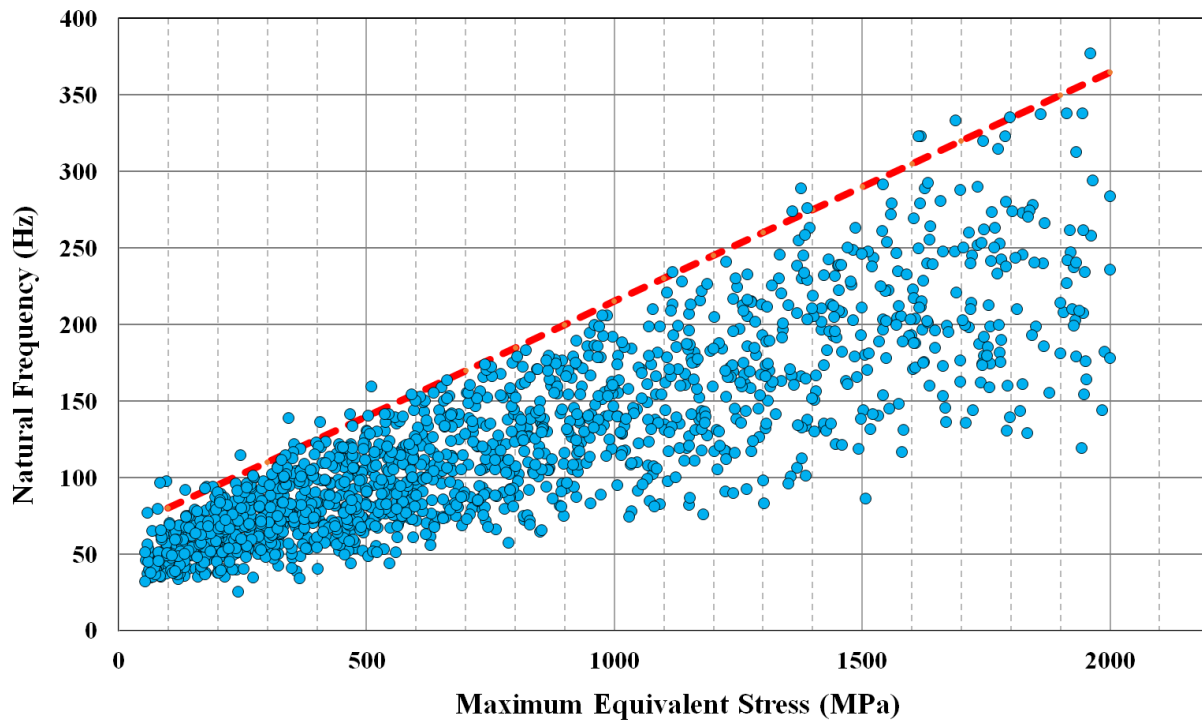
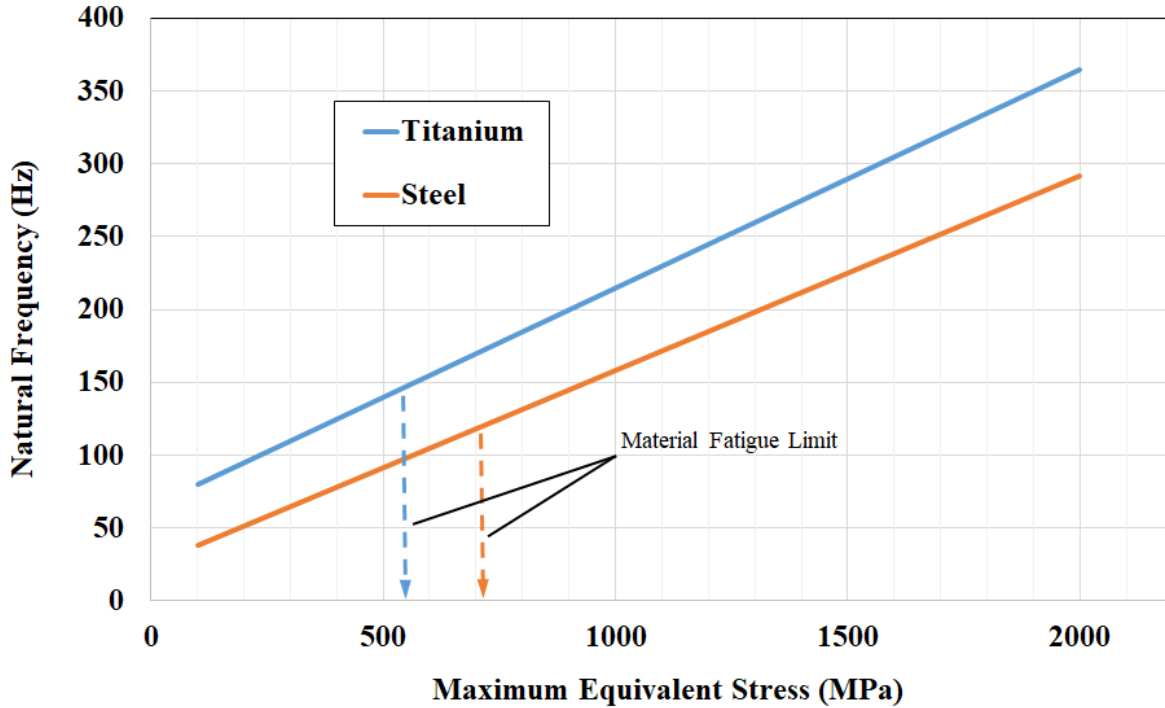


Figure 45. Scattered distribution of design points in frequency/stress chart for a single titanium spring.

To better understanding the difference between the maximum capacities of the titanium and steel materials, the two different upper limits are shown separately in Figure 46. As expected, the maximum frequency, with the same level of the stress, is higher for the titanium material. Also, the slope of an increase in the frequency versus the stress is slightly higher for the titanium material. In using Figure 46, the fatigue limit of the materials is the main factor. For example, if a resonant frequency of 150 Hz required for a single flexure, according to Table 5, steel alloy Aermet100, and titanium alloy Ti-6246 can be used. However, the maximum stress at this

frequency is very close to the fatigue limits, 550 and 945 MPa of the titanium and steel alloys, respectively. So, other factors such as cost, availability of the raw materials, machining properties, and performance should be considered. In general, if high performance and LEA machine's thermal efficiency are the main factors, then the titanium alloy is a better choice, but for high-volume production and cost, the steel alloys may provide a better option.



**Figure 46. Comparison of the maximum resonant frequency of titanium and steel flexures.**

To validate the applicability of the design charts presented in section 3.6 for the designs with different stroke lengths, a study was performed in FEA to check the linearity of the stress at different locations on the flexure's arm. As shown in Figure 47, 51 points from the inner to outer of an arm were selected in 17 rows, each having three points located at the left, right, and middle of the arm width. The results of the maximum equivalent stress are shown in Figure 48. Because each of these points is loaded differently, the slope of the stress level versus displacement is different. Hence for better representation of the linearity of the stress at all points in one graph, a log-log scale was used in Figure 48. It can be seen that stress is varied linearly with the displacement on a log-log scale. It means that the design charts in these sections can be used for other displacements, by scaling the stress values with respect to the original 11 mm displacement. For the locations that the stress is higher – e.g. the outer end of the spiral or the thinnest part of the

arm near the middle – the top lines cross each other at some locations, but the non-linearity effect is very low and negligible. It should also be noted that the analysis was performed statically as a ground for the preliminary flexure design using the design charts. However, in actual application use, the dynamics and higher harmonics of the flexure will exert some percentages of the non-linearity in stress levels at some critical locations.

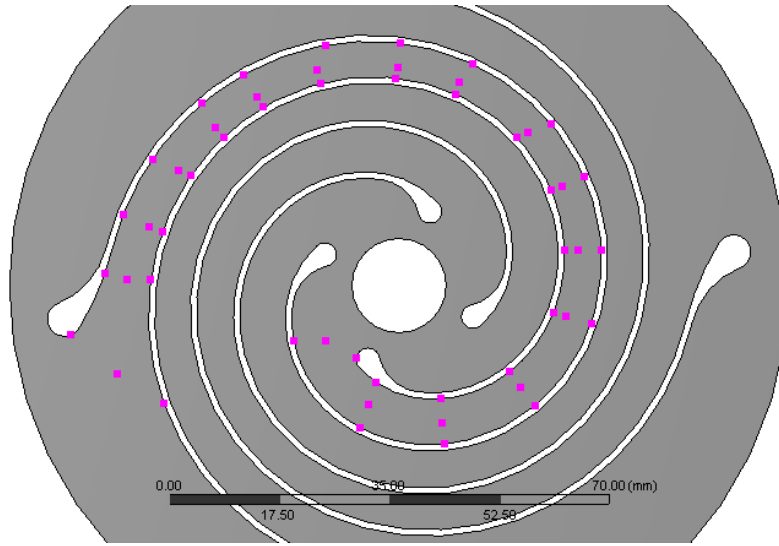


**Figure 47. Selected points on the flexure arm.**

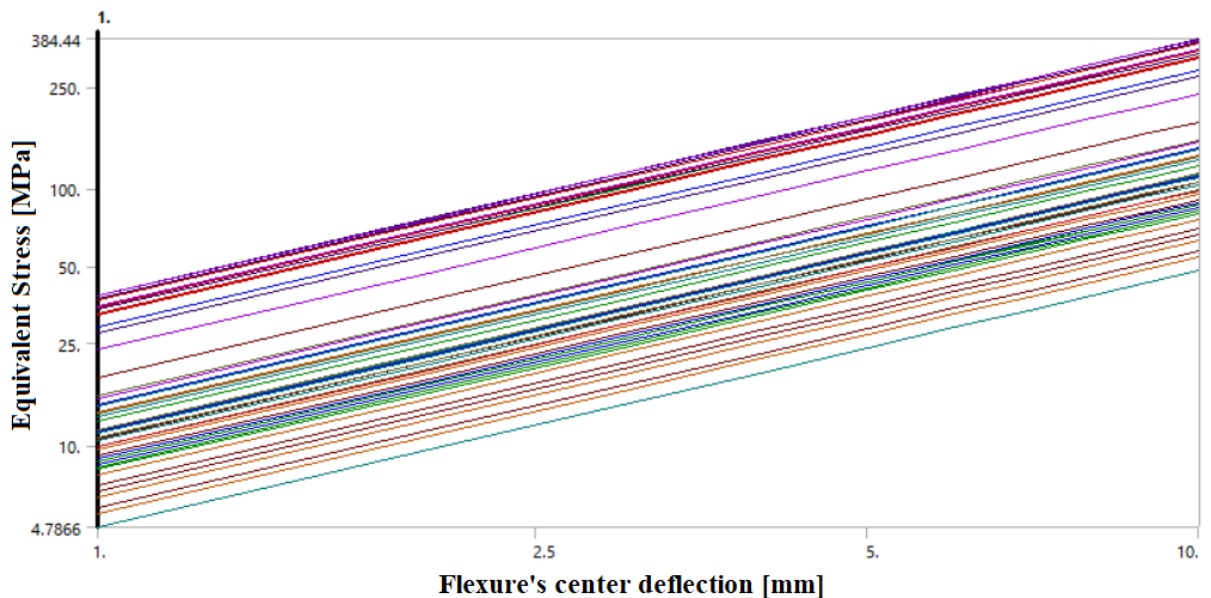


**Figure 48. Log-log diagram of stress linearity at points along the flexure's arm length.**

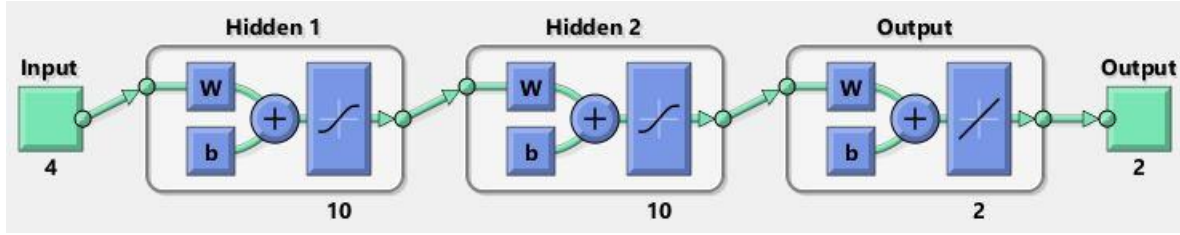
### 3.6.3 Design Points Data Analysis

Figure 44 and Figure 45 are the primary design tools for the steel and titanium materials, respectively. These graphs each include over 4000 design points where each point contains values of the four geometrical parameters. Although the 3D surfaces (or profiles) and sensitivity charts provide valuable information about the interactions of parameters and their effect on the outputs, they might not be very effective when it comes to the selection of the parameters for a specific flexure design. To enhance the usage of generated data from the design exploration, two approaches were implemented. The details are provided in the following subsections.

#### 3.6.3.1 Matlab™ Function

A neural network algorithm in Matlab™ software was used to find the correlation between the inputs and outputs of all selected design points shown in Figure 44. Two training algorithms, with a different number of hidden layers, were used to find the best method with better performance and lower errors. The methods studied were Leveberg-Marquardt and Bayesian Regularization with two hidden layers and neurons number ranging from 1-10 [155]. Two hidden layers were used because both methods reached their maximum performance and there were no benefits in increasing the number of layers beyond this point. Also, both methods showed improvement by increasing the number of neurons but not a very significant change at ten neurons and after. So ten was selected for the final solution. A matrix of values for the four parameters including sweep angle (in radian), outer diameter (in mm), number of arms, and thickness (in mm) was used as the NN input, and a matrix of two vectors of stress (in MPa) and frequency (in Hz), for the corresponding inputs were imported as the NN output. In the model, 85% of all data were used for the training, 10% for the validation, and 5% for testing of the NN function. Both NN methods showed satisfying performance and low error values, with slightly better results by using the Bayesian Regularization. The performance and error results of the training are provided in Appendix 9.5. To create the final Matlab program the Bayesian method was used. The schematic of the model is shown in Figure 49.





**Figure 49. Schematic of the neural network model.**

From the result of the NN algorithm, a Matlab function was generated and is provided in Appendix 9.6. To use the Matlab function, the name of a row vector including four design parameters should be used as the only argument of the function. The output of the function is a row vector including the maximum stress and the frequency corresponding to that design parameters' values. The order of inputs in the vector and their units must be according to what was stated above. An example is provided in the comments section of the function.

It should be noted that the final design of a flexure requires several modifications of the arms such as endpoint curves, using shape factor, and spacer's contact area modifications. In most cases, the final design will have a lower stress value than the predicted number by the Matlab function. By average, a 20% reduction in the maximum stress from the function output is achievable.

### 3.6.3.2 Design Charts

To better show the large data generated during the parametric study that can be used for finding the geometrical dimensions of a flexure, a series of design charts were produced that show each of the parameters on an axis. The best correlation between parameters was obtained when a ratio of "stress/thickness" was used to sort all design points. Figure 50 shows all design points for steel material in one graph with "stress/thickness" on the Y-axis, "sweep angle" on the X-axis, and separated with colors for the number of arms. In Figure 50, there is overlap between the six color bands which indicates that for a specific "stress/thickness" ratio, there are different possible designs with combinations of sweep angle and the number of arms.

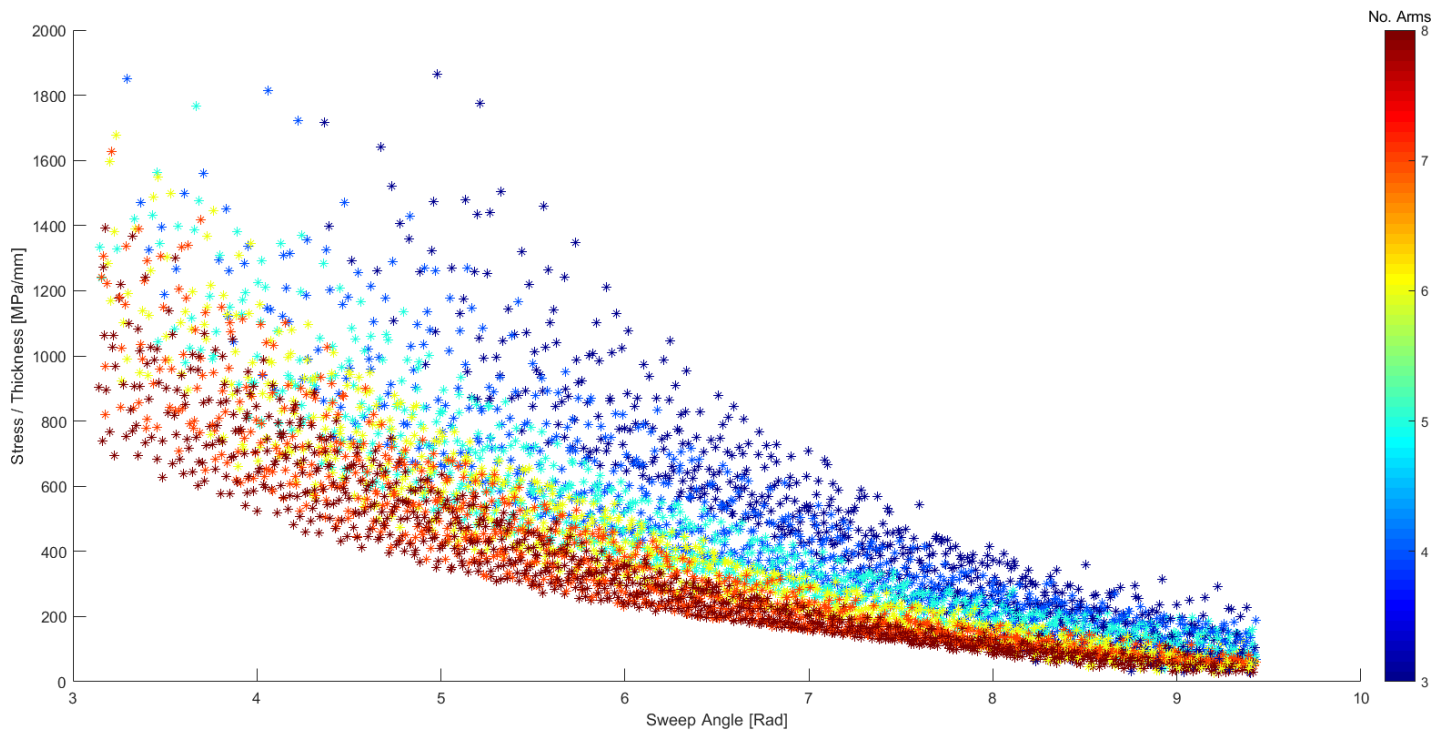


**Figure 50. All steel flexure design points pool sorted by the design parameters.**

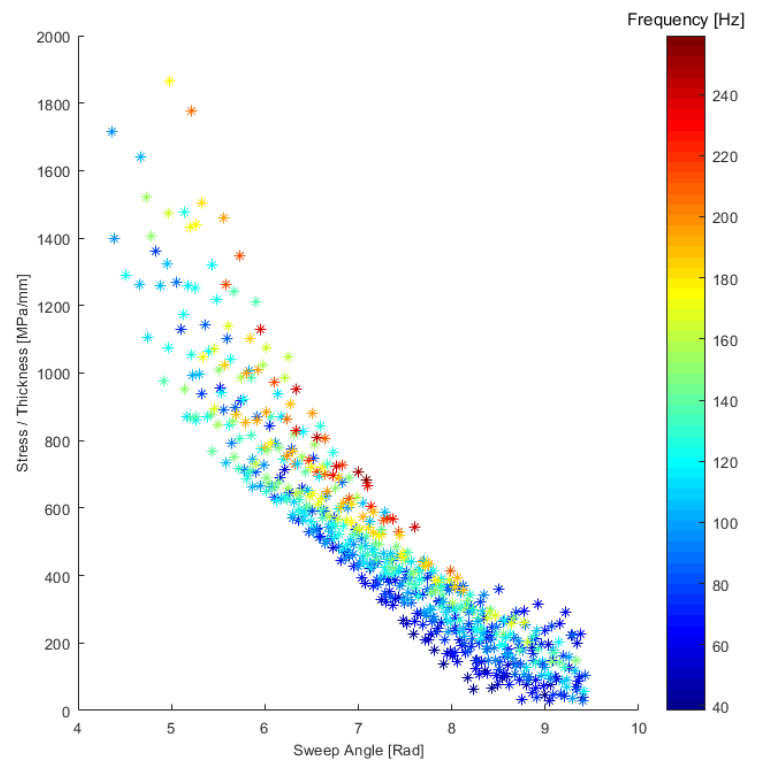
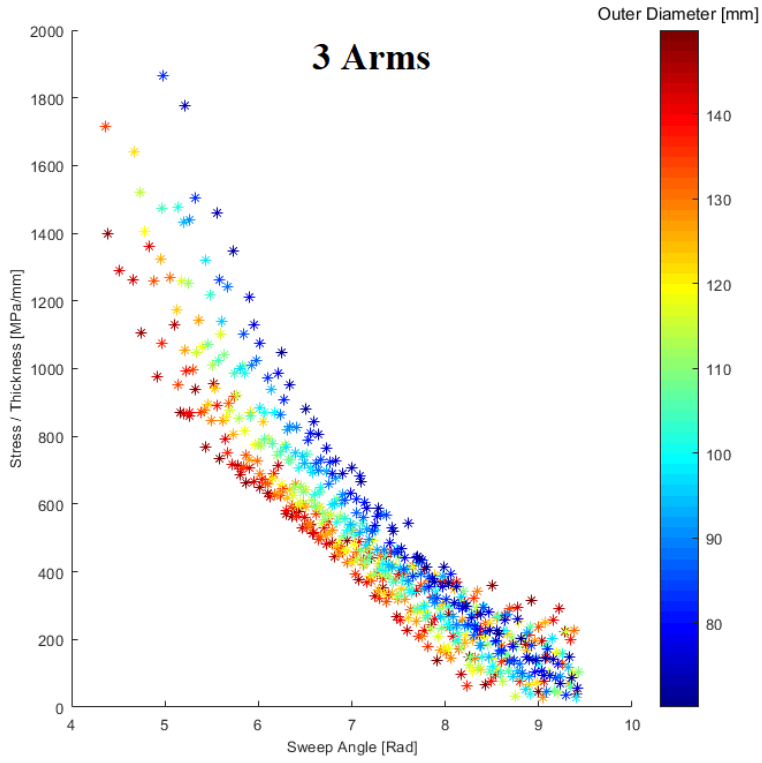
The parameter selection will be a step-by-step process starting with knowing the material properties, specifically the maximum stress allowed. For static or dynamic applications, considering the factor of safety, the maximum allowed stress is a fraction of yield or fatigue strength, respectively. The next step is the thickness selection. Depends on the flexure's raw material form, the thickness might be unchangeable, for instance, if the material form is a metal sheet. Figure 51 has separated the design points in Figure 50 into a set of six charts based on the number of arms. Each row is for a specific number of arms wherein on the left picture, points' color show the outer diameter, and on the right picture, colors correspond to frequency.

The steps for using the design charts can be written as follows.

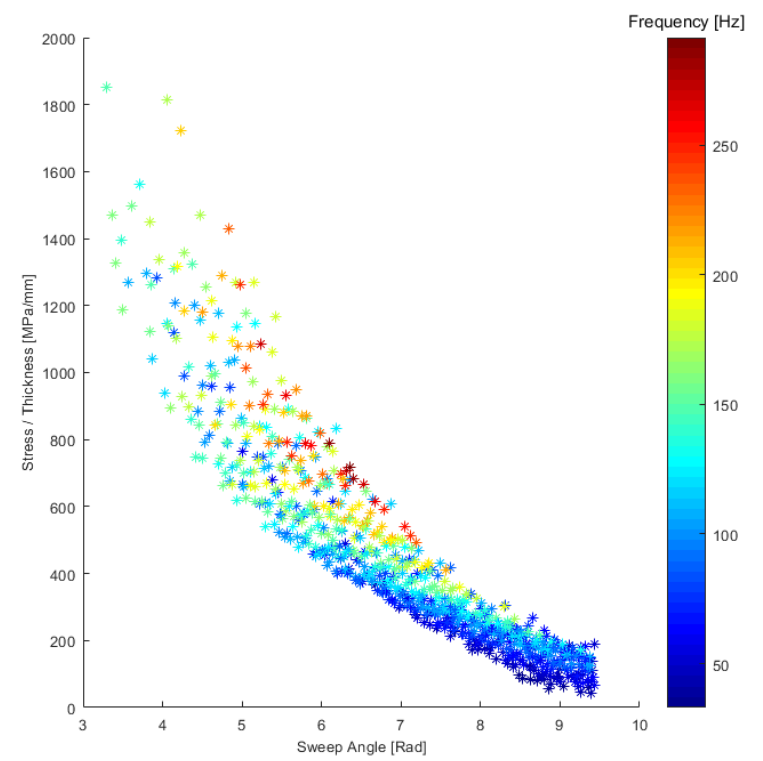
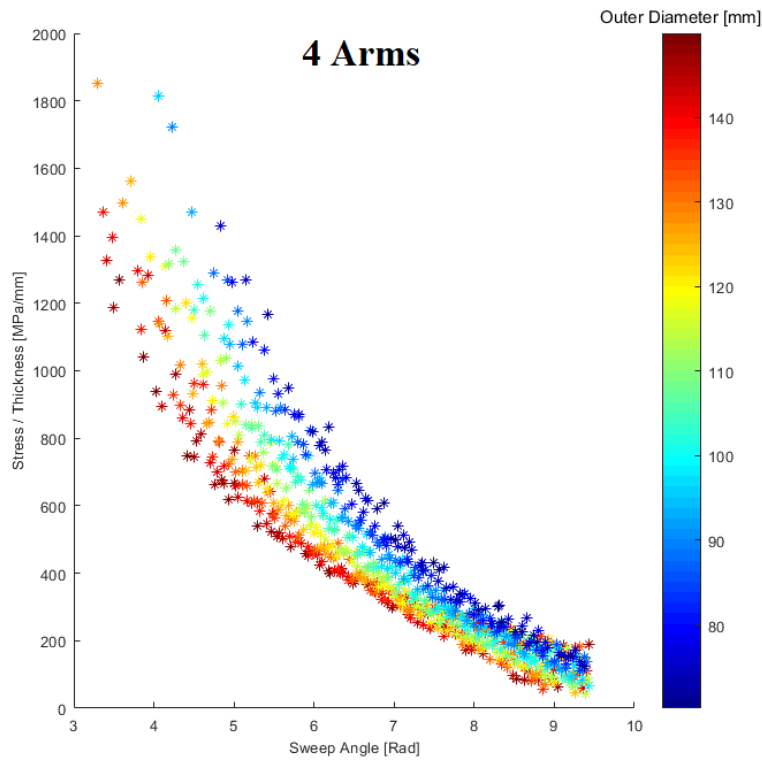
- 1- Select the material and define the maximum stress allowed in MPa unit.
- 2- Define/assume a material thickness in mm unit and calculate the "stress/thickness" ratio.
- 3- Use Figure 50 and find what combinations of the sweep angle and number of arms are available for the given "stress/thickness" ratio.
- 4- Use pictures in Figure 51 to find the appropriate outer diameter of the flexure.

It should be noted that for any stress/frequency requirement, multiple designs are possible. In this case, the geometrical limitations, such as the maximum diameter or thickness will narrow down the selection pool. In addition, as mentioned before, the provided design charts are meant to be used for the primary design numbers and further modifications will be required for the final design.

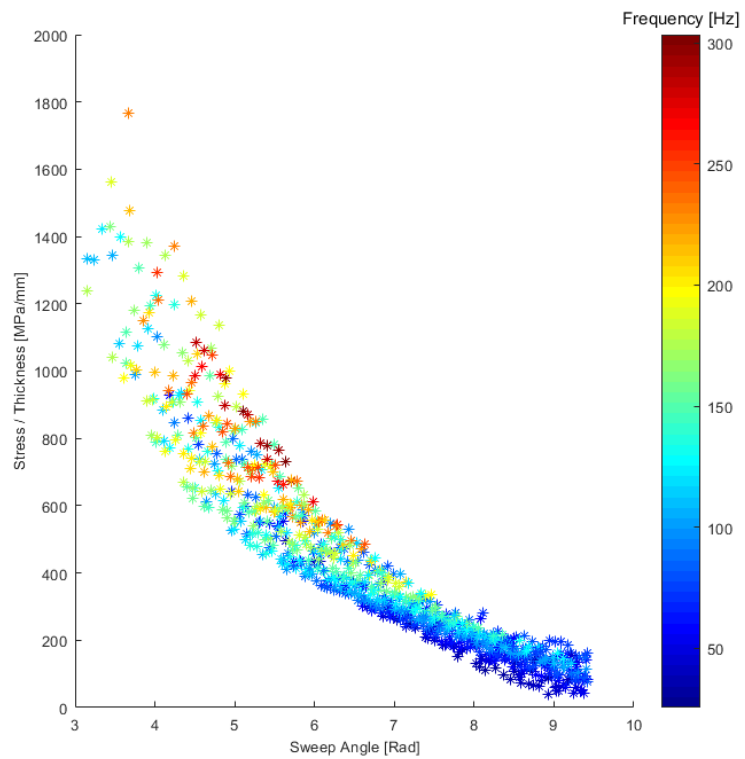
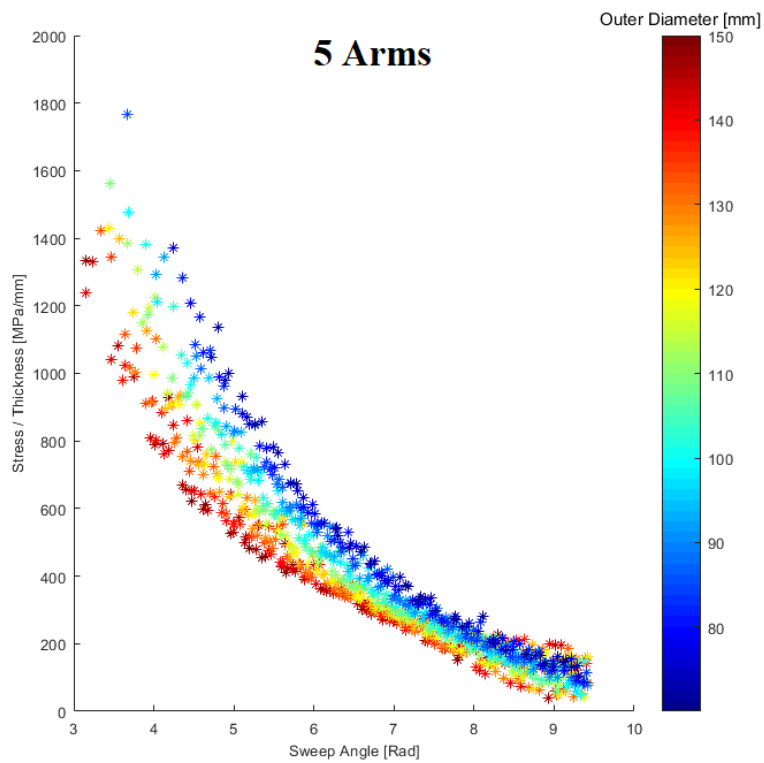
### 3 Arms



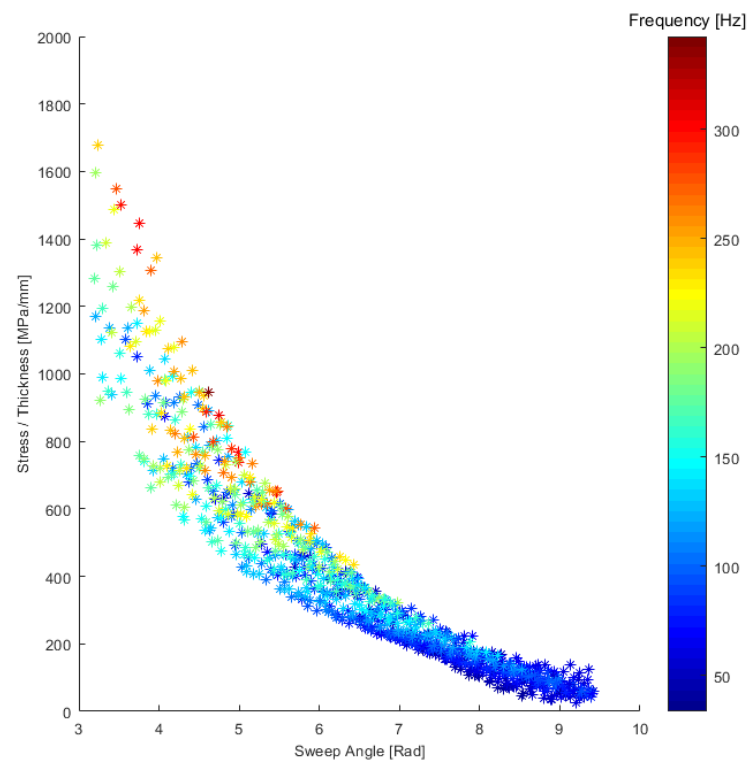
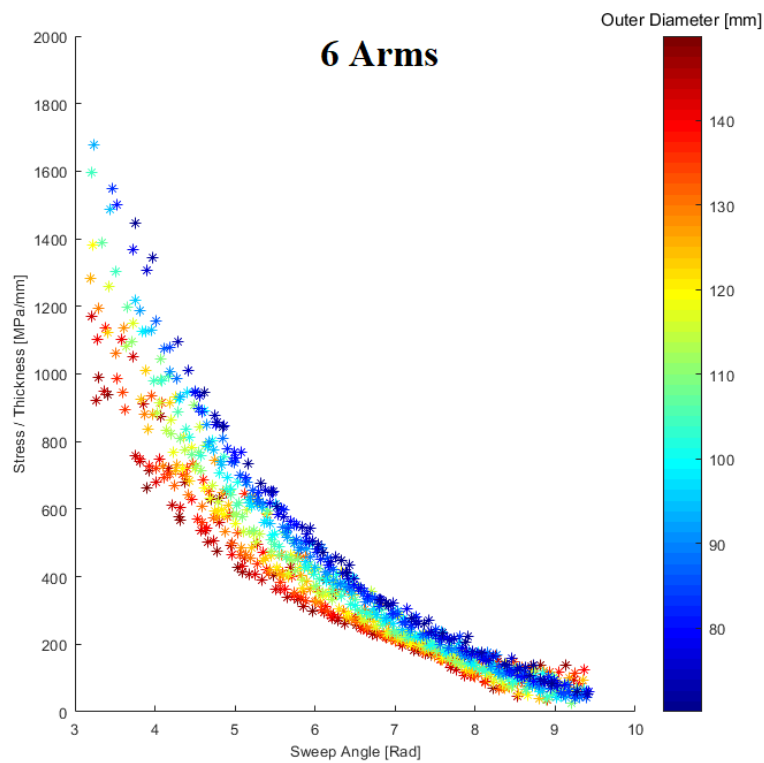
### 4 Arms



## 5 Arms



## 6 Arms



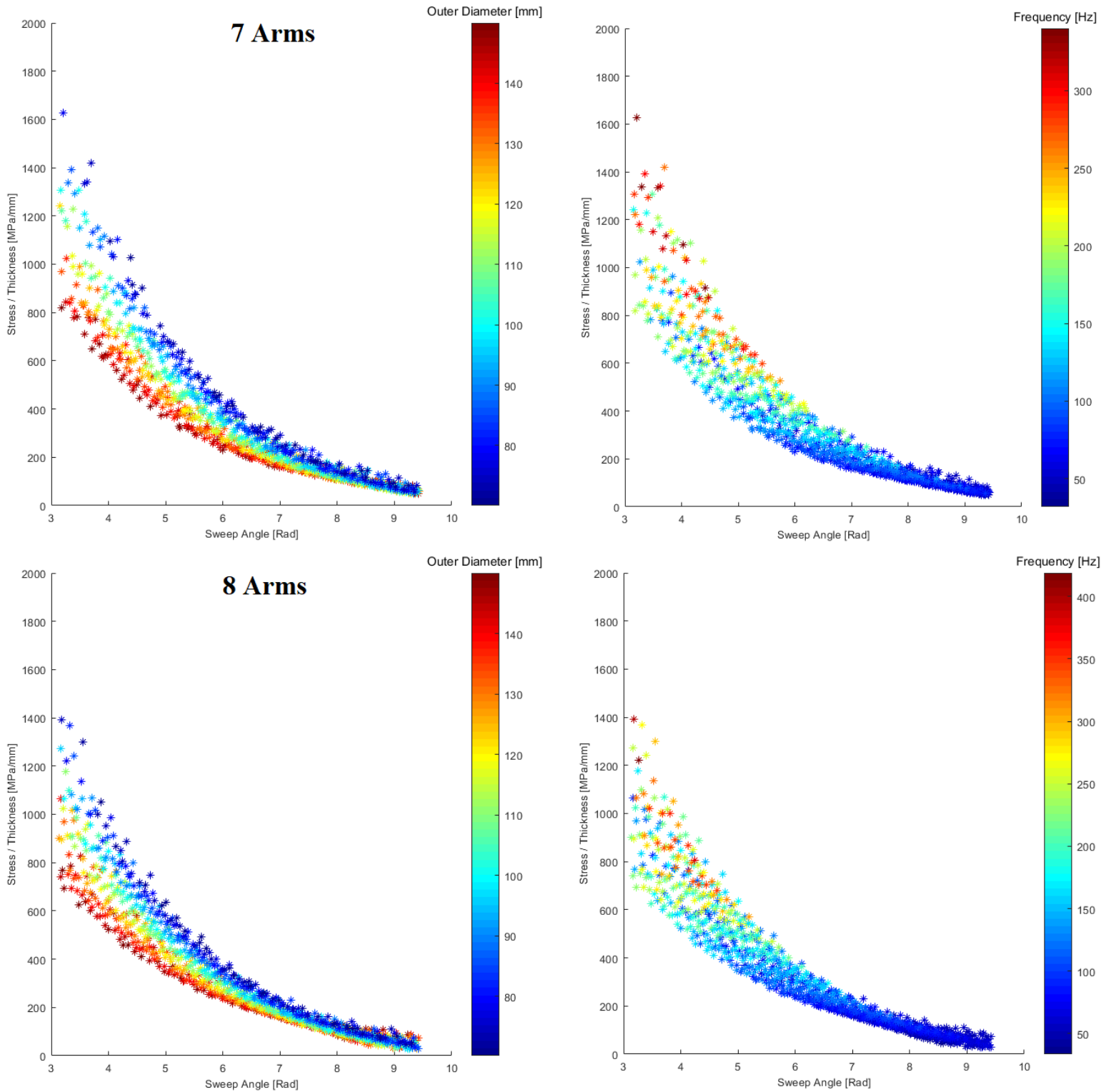


**Figure 51. Steel flexure design points vs. number of arms. left: colored by outer diameter, right: colored by frequency.**

### 3.7 Experimental Verifications

Following the design stated in Section 3.4, outer diameter 124mm, inner diameter 15mm, thickness 2.5mm, and shape factor 0.05, the geometrical dimensions were selected and the flexure springs were manufactured using a waterjet process. More details about the manufacturing process is provided in Section 4. A test rig was designed and manufactured with the capability of static testing up to five springs using a 10 kN Shimadzu AGS-X compression/tensile test machine [156]. Additional details are provided in Appendix 9.2. Figure 52 shows the test rig and flexure. The manufactured springs were tested statically and were used to compare the stiffness and spring arm strain with the FEA results. The spring rate from the tests was obtained from the instantaneous slope of force variation over a fixed pre-defined displacement of 10 mm with a rate of 5 mm/min. The sampling rate was 1 Hz. From the experiments, the spring rates and the linearity of a set of springs were compared to FEA results. Moreover, to ensure the results of equivalent stress from FEA simulations, three axial strain gauges were used on each side of the spring and arranged in a half-bridge configuration in different locations of arms with possible higher stress. Figure 52c depicts the strain gauges installed on one side of the spring. As shown, gauges were mounted near the start point, endpoint, and in the middle of an arm.

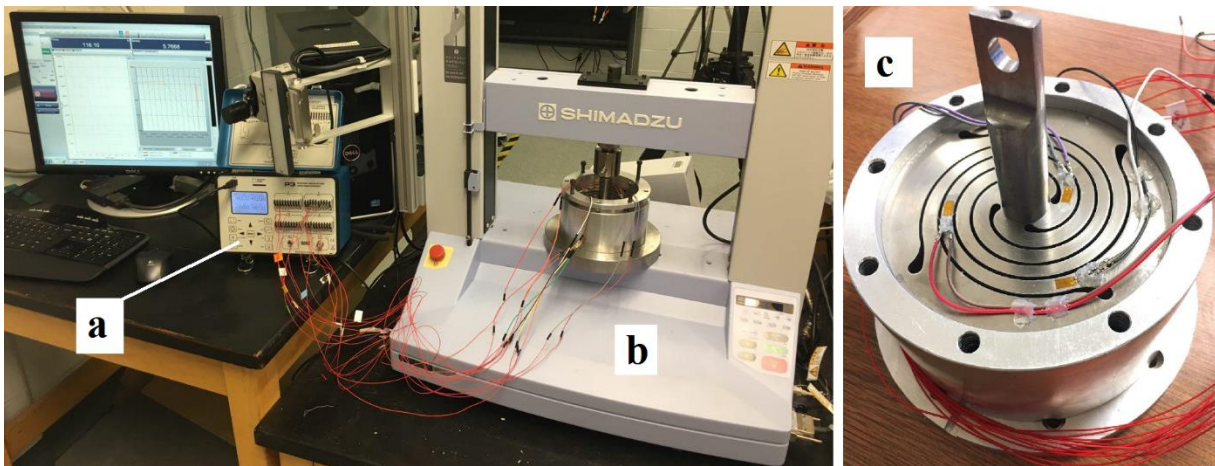


**Figure 52.**Static test rig with a custom fixture. Label a) is the signal processor, b) is the Shimadzu load frame, and c) is the flexure and fixture. Figure c depicts the placement of strain gauges on the arms of the flexure spring.

Results of static force/displacement tests showed good agreement between FEA and experimental tests. The FEA under predicted the stiffness results at higher values of displacement. The average differences between stiffness values from the experimental test and FEA of all deflection points were measured to be less than 5%. The error was assumed to be rooted in the measurements and



manufacturing uncertainties. Figure 53 provides a comparison of FEA and test results. Because of the non-symmetric and non-uniform geometry of the flexure spring, at different deflection points from the neutral position to maximum deflection, the infinitesimal elements in the body of the flexure were loaded in a different manner. This is the reason that the spring rate is not uniform with the deflection. Experimental tests showed higher rates of stiffness non-linearity compared to FEA results, specifically after 6 mm of deflection. The non-linear properties of the materials in the real-world were found to be a possible reason for the stiffness non-linearity, which was not considered in the current FEA. Also, the attachment conditions between the flexure and fixture may not have been simulated in FEA appropriately. The relative displacement between the parts at contact, and also deformation of the test rig can change the results.

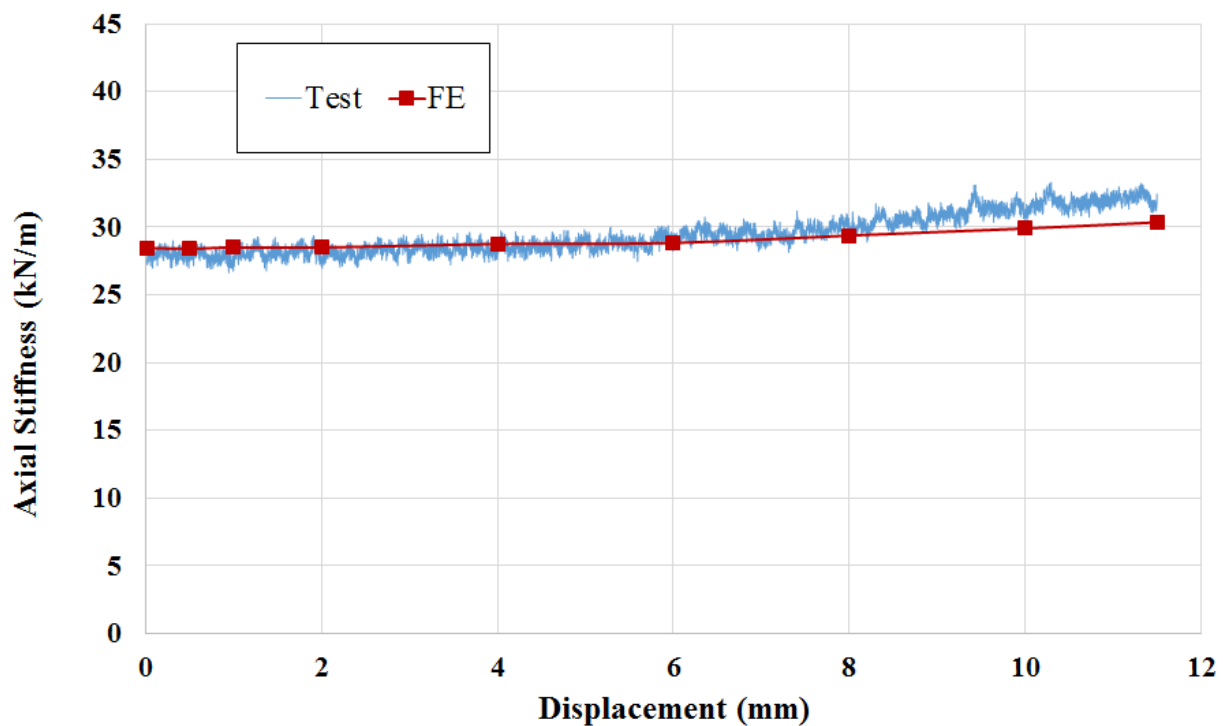


**Figure 53. Comparison of FEA and Experimental results of the flexure stiffness as a function of displacement.**

The combination of one to five springs was tested to check the stiffness linearity of the assembly – see Figure 54. Axial stiffness compares the stiffness of an assembly with two, three, four, and five flexures. Results indicated the theoretical assumption of linearity was valid.



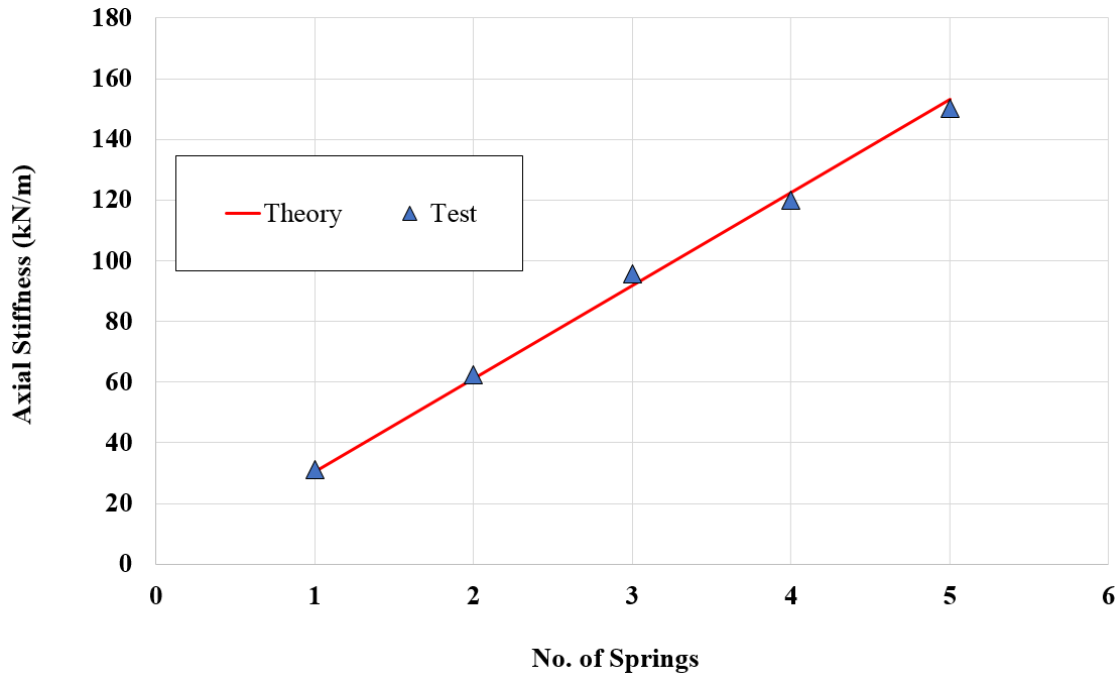


**Figure 54. Stiffness linearity of a spring assembly (more than one spring in series).**

Figure 55 shows the normal strain results from strain gauges. The solid lines are experimental results while dashed lines show the FEA results. The solid red line shows the force input line for the tests. As shown in Figure 52c, the inner end strain gauge was located near the inner circle of the flexure, the middle strain gauge was located at the middle of an arm, which had the narrowest width, and the outer end strain gauge was located near the outer diameter of the flexure. The strain gauges measure the first principal strain in the longitudinal direction where they were positioned. Results showed good agreement between numerical and experimental results. It was observed that strain rates under static conditions changed quite linearly with the linear axial force applied. This linear behavior demonstrated that the arms of the flexure strings are in nearly pure bending. As was predicted, the two endpoints of spiral cuts were the locations of the highest normal strains along the length of arms. These results highlighted the importance of curve modifications at the slot endpoints. One of the reasons for the slight differences of the strain results between experimental test and FEA was due to the imperfections in the installation of the strain gauges and the substrate surface roughness. As mentioned above, the difference between the BCs in FEA and the experimental tests could be another reason for the differences. The FEA solution procedure and used BCs are explained in Appendix 9.1.

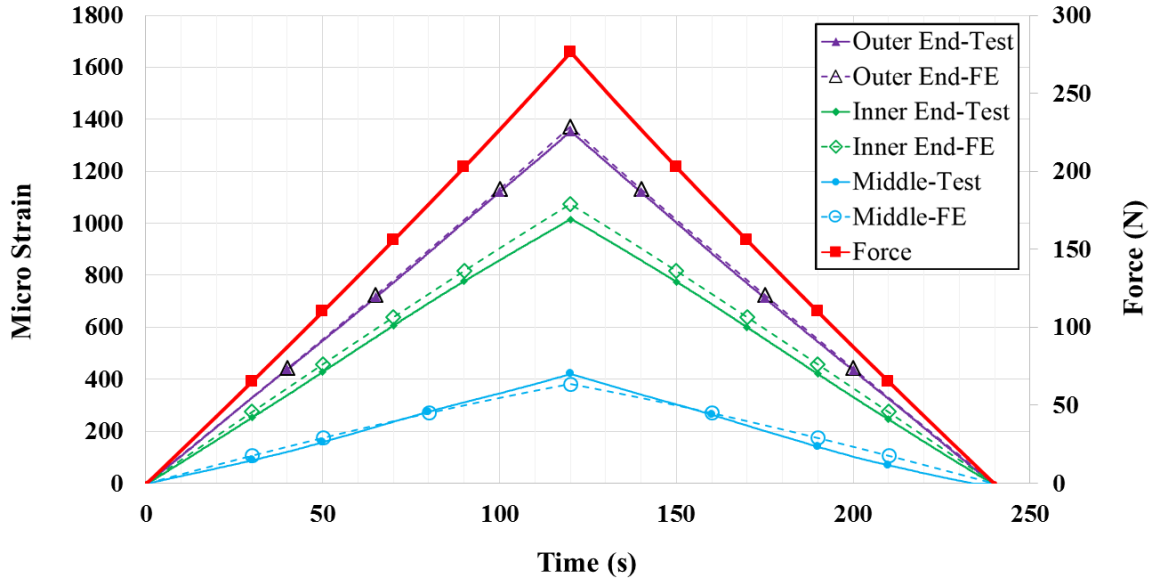


**Figure 55.** Strain gauge measurement at selected locations (see Figure 12c) compared to FEA results of strain at fixed velocity deflection test. Solid lines denote experimental values and dashed lines correspond to FEA values.

From both Figure 54 and Figure 55, the FEA predicted the static results of the stiffness linearity versus number of flexures and strain on different locations of an arm. In Figure 54, the root mean square of error between the experiments and theory was 2.45%. In the strain comparison graph, the FEA predicted the experiment values with high accuracy. The maximum absolute error value was observed on the strain at the middle point at the maximum deflection point and was measured about 50 microstrain, or 5.6% error compared to experiments. The average of absolute error for all three locations was 15 microstrain, equal to approximately average 2% error at all deflection points. The accuracy of the results at the outer endpoint was the highest which specifically is important as the maximum stress occurs in this area and the whole flexure spring design process is planned according to the stress value at this point and using FEA as a reliable tool will help to achieve better designs.

## 4 Manufacturing Methods and Statistical Analysis

In this section, the manufacturing methods and their influence on the design of flexure springs were studied. As discussed earlier, material selection is one of the most important factors in the flexure spring design. The whole design of an LEA machine is influenced by the flexure spring performance limits, which itself is initiated by the material properties of the flexure spring. After the material was selected, the next step is the manufacturing of the flexures. Depending on the form of the available material, there are three main methods for the manufacturing including 1- waterjet, 2-CNC machining, and 3- electrical discharge machining (EDM) due to the relative hardness of the selected materials. For all methods, the material in flat sheet form with ground and polished surfaces is preferable. However other forms of the material can be used such as bars and plates. Using other forms of material may increase the final cost. Figure 56 shows the flexure springs made by using wire EDM and waterjet methods. In general, for manufacturing one flexure spring, waterjet is the fastest and most cost efficient method, while CNC is the most expensive, and takes a longer time. However, for using EDM, multiple number of metal sheets can be stacked together and cut at the same time. This option is available for waterjet too, but because of the kerf angle issue (see Figure 60), the maximum thickness is more limited compared to EDM. The manufacturing setup and machining of a single flexure as shown in the picture below takes about 1-2 hours with a waterjet, 2-3 hours with wire EDM, and around 100 hours using a regular 3-axis CNC machine. The characteristics of the three different manufacturing methods were compared in Table 10. According to

Table 10, for high volume production, both water jet and wire EDM machining are good candidates. Considering the machining accuracy, if both long service life and high thermal efficiency of the LEA are higher priorities than cost, the EDM is a better method.

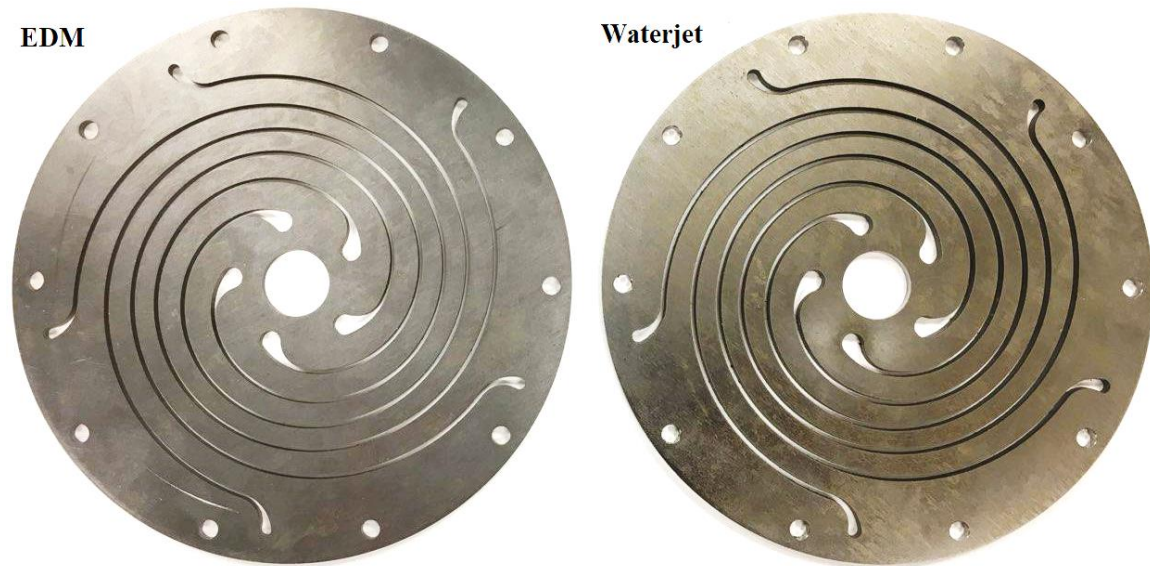


**Figure 56. Flexure springs made using EDM (left) and waterjet (right) methods.**

**Table 10. Comparison of manufacturing methods.**

<b>Machining Method</b>	<b>Waterjet</b>	<b>Wire EDM</b>	<b>CNC</b>
<b>Accuracy</b>	low-medium	high	very high
<b>Setup Time</b>	low	low-medium	medium
<b>Machining Time</b>	low	medium	very high
<b>Machining Cost</b>	low	medium	very high

The flexure springs for the GENSETS project were made of different materials with titanium and steel bases. Amongst several available steel alloys with desirable mechanical characteristics, Sandvik 7C27Mo2 material was selected. The main reason for selecting this material was the availability of material sheets in small quantities for prototyping. For manufacturing, the waterjet method was used. Using waterjet as the cutting tool exerted inaccuracies which are analyzed here.

#### **4.1 Material Properties**

Before starting to analyze the effects of manufacturing on flexure springs, the metal sheets received for the prototyping were tested. This test was performed to check the accuracy of the material properties provided in the supplier's datasheets. The reason for this was first because the datasheet numbers were reported from the tests on standard specimens and usually in other dimensions than the received material forms. In this case, the datasheet material properties of Sandvik steel was for

the specimens of up to 1 mm, but the sheet that was used for the waterjet cutting was 2.5 mm thickness. The second reason was the fact that sometimes the mechanical properties of the metal sheets are different in lateral and longitudinal directions. This is because of the metal forming processes and commonly the sheets in longitudinal direction have a higher mechanical strength [157]. To do tests, six standard specimens were cut using the same waterjet machine used for flexure manufacturing. Three of the specimens were cut along the lateral direction of the sheet, and three were cut in the longitudinal direction. The specimens then were used for a standard tensile test in an MTS<sup>TM</sup> machine. The waterjet and MTS machines are shown in Figure 57. To check if the edge quality of the surface affects the mechanical properties and strength of the specimens, one of the three specimens of each group remained unfinished on the sides. The other two were sanded according to the ASME standard recommendations [158]. Figure 58 shows the manufactured specimens and the detailed view of the surface finish on the sides.



Figure 57. MTS machine (left), Waterjet machine (right).



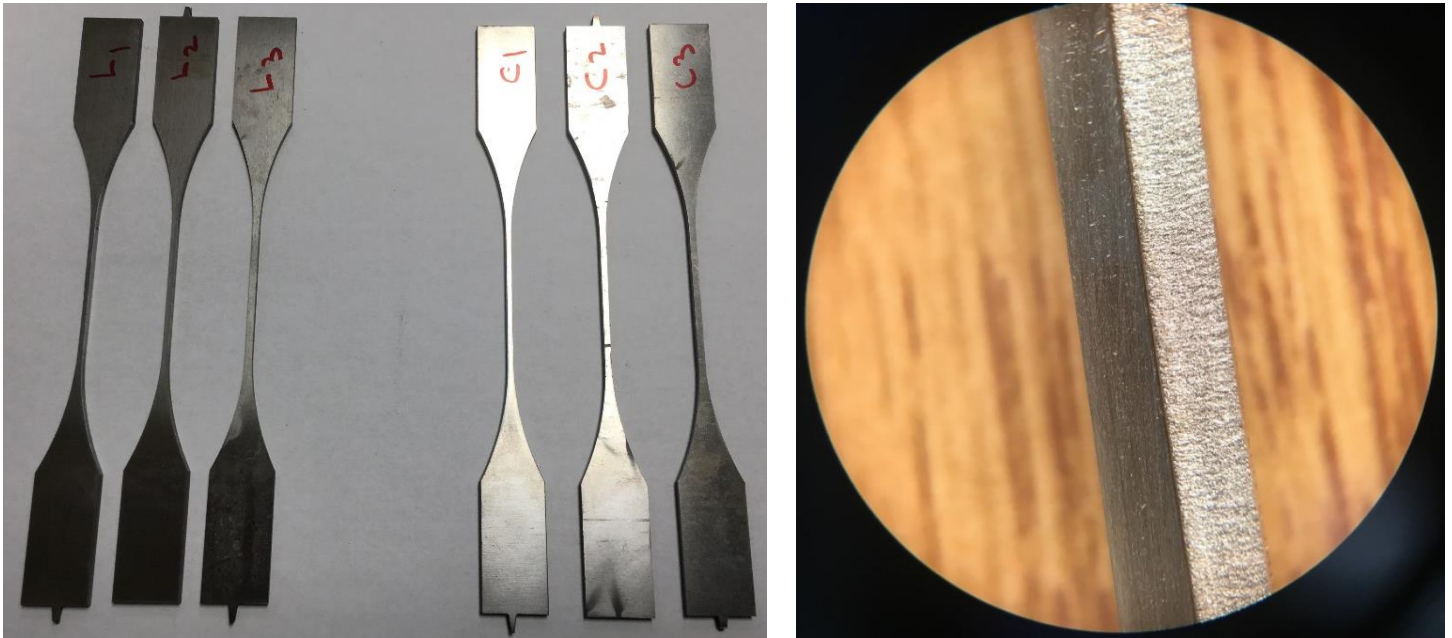


**Figure 58. Manufactures specimens, finished and unfinished surface (right).**

The results of the tensile test are presented in Figure 59. The 0.05% and 0.2% proof line showed around 50 MPa lower in material strength values compared to the 1300 and 1450 MPa from the supplier's datasheet [146]. This is an important result that should be carefully considered when the fatigue limit of the material is considered for the spring design. From the figure, it was also understood that finishing the side surfaces had no significant influence on the test results. In addition, the specimens cut from different directions showed almost the same behavior with the parts in the longitudinal direction having a slightly better elongation at fracture, about 8%.

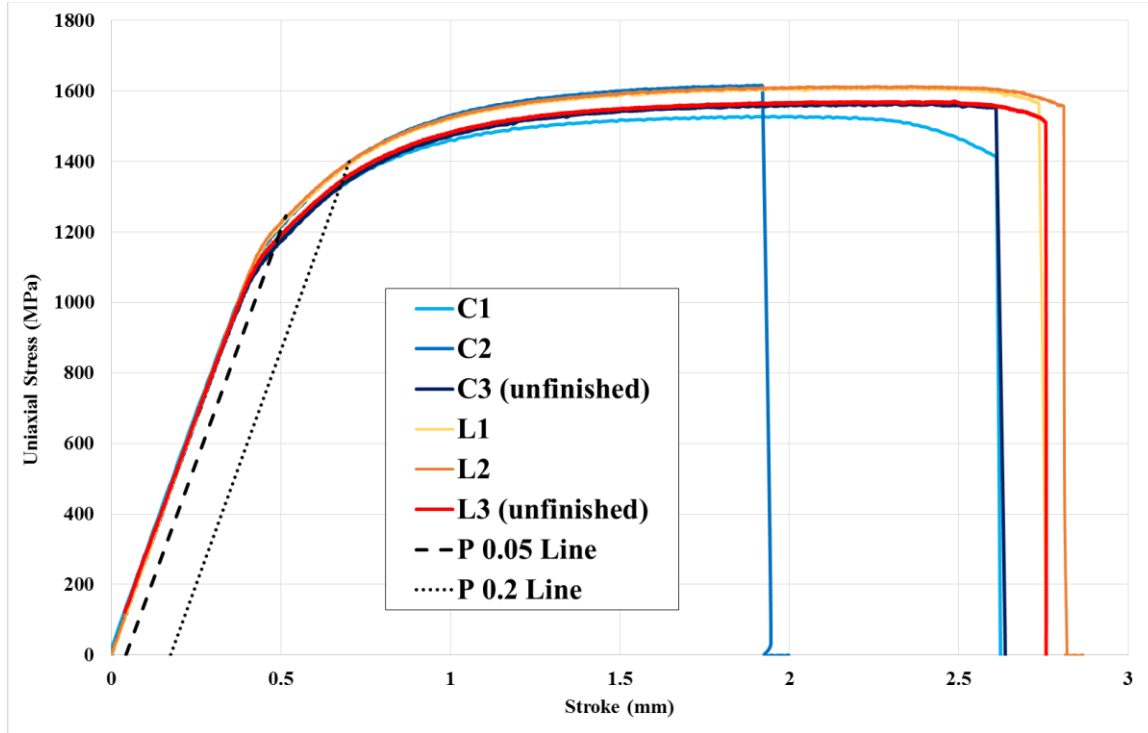


**Figure 59. Sandvik material tensile test results.**

## 4.2 Machining Accuracy

One of the issues in cutting using waterjet is the kerf angle. Kerf angle, or bevel, refers to the dimensional difference between the top and bottom of the cut cross-section. Cutting too fast will result in a wider kerf width at the top of the cut cross-section and a narrower kerf width at the bottom of the zone [159]. Figure 60 shows an example of cutting speed effects on the kerf width on an aluminum piece. Although slower cutting results in reduced kerf angle, it will degrade the surface finish and its quality which will result in stress concentrations at microcracks created by the waterjet abrasive particles.

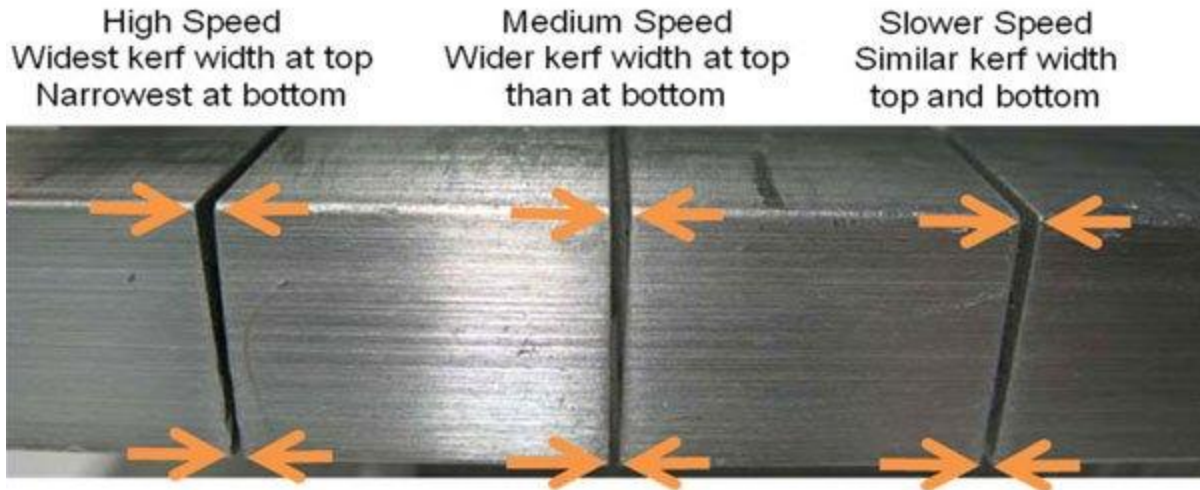


**Figure 60. Waterjet kerf angle effect [159].**

Another influencing factor in the cut quality is the nozzle height. A nozzle too far from the piece can result in unequal cut width on two sides of the metal sheet, the same effect as the kerf angle. Figure 61 shows this effect in detail. So, for each material and the specific dimensions of the piece, there is a trade-off between the waterjet cutting factors to obtain the best results. The machining specifications can be extracted from the waterjet machine's datasheets and recommendations.

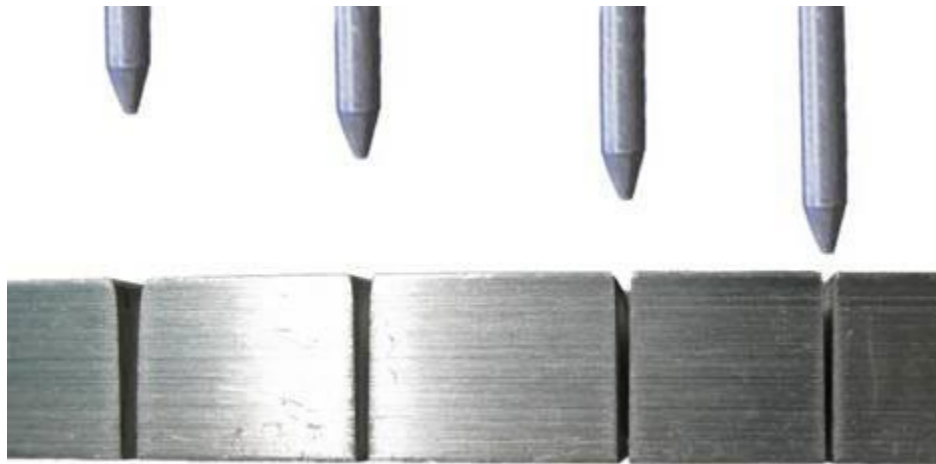


**Figure 61. Waterjet nozzle height effects [159].**

The kerf angles were generated in both steel and titanium flexure springs. It was observed that the magnitude of the cut width difference on the titanium material was more than steel material.

To investigate the effects of the kerf angle and other manufacturing deficiencies, a statistical analysis was performed on 12 flexure springs for each material to test the axial stiffness statically. The first evaluation was testing the stiffness of the two sides of a spring. The test was repeated two



times for all 24 springs, each time one side was faced up where the pushing force from the Instron machine was being applied. Figure 62 and Figure 63 shows the flexure's spring rate for the Sandvik steel and titanium materials, respectively. The blue line shows the stiffness when the face with narrower cut width was up. From the figures, it can be seen that the kerf angle effects less significant in the steel flexures, while larger differences in the two sides' stiffness were observed in the titanium springs. The difference in the stiffness of springs should be considered when assembling them into the LEA machine.

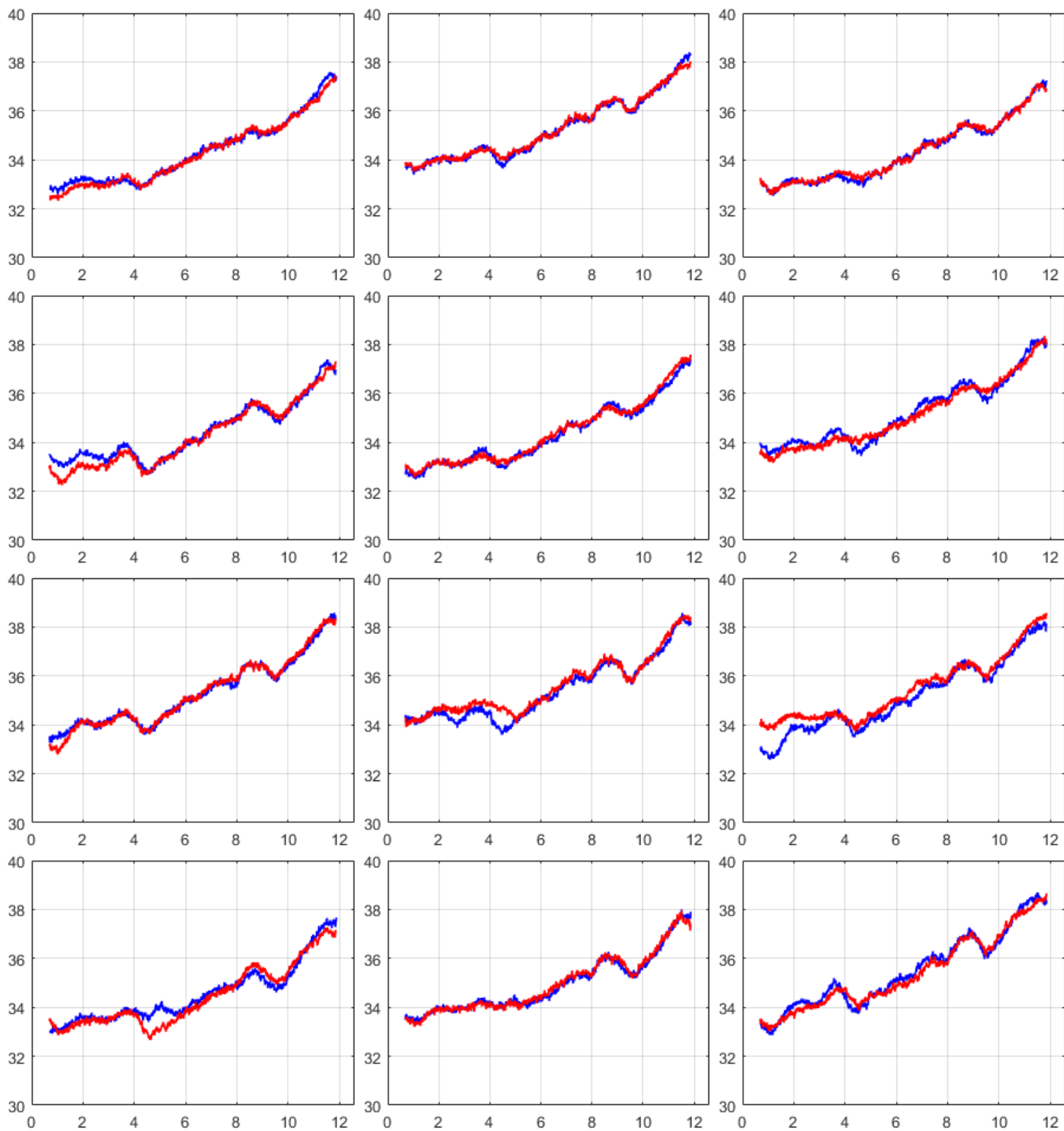


**Figure 62.** Comparison of directional stiffness of twelve Sandvik flexures, blue: side 1, red: side 2. X axis is deflection in mm and Y axis is the stiffness in kN/m.

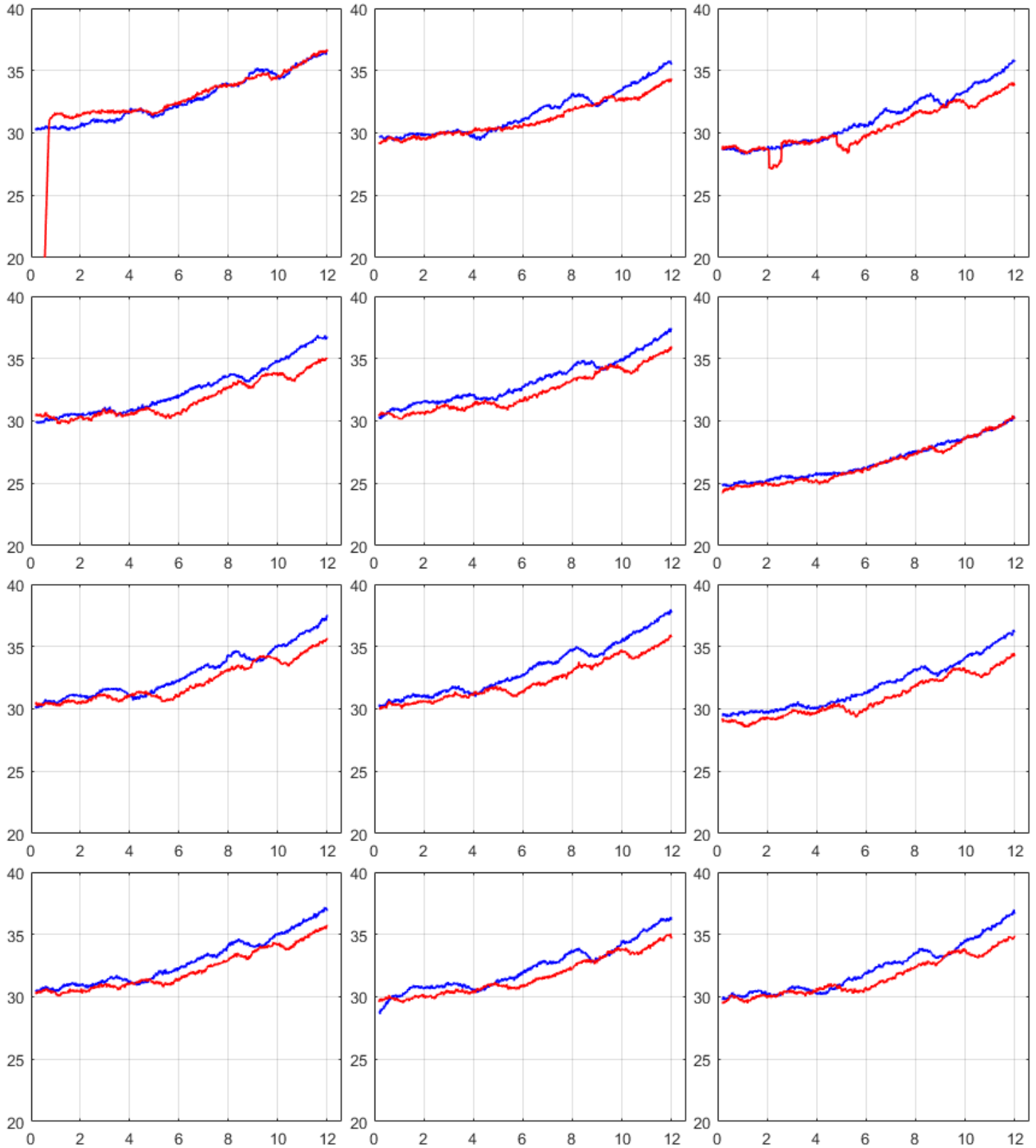


**Figure 63.** Comparison of directional stiffness of twelve titanium flexures, blue: side 1, red: side 2. X axis is deflection in mm and Y axis is the stiffness in kN/m.

In the next step, all of the springs' stiffnesses were compared in one graph for both materials to compare the deviation of stiffness from the average. According to Figure 64, with the same design pattern of the arms, after manufacturing, there was about a 6% difference in the stiffness of flexure springs. All flexures showed a similar non-linearity pattern.

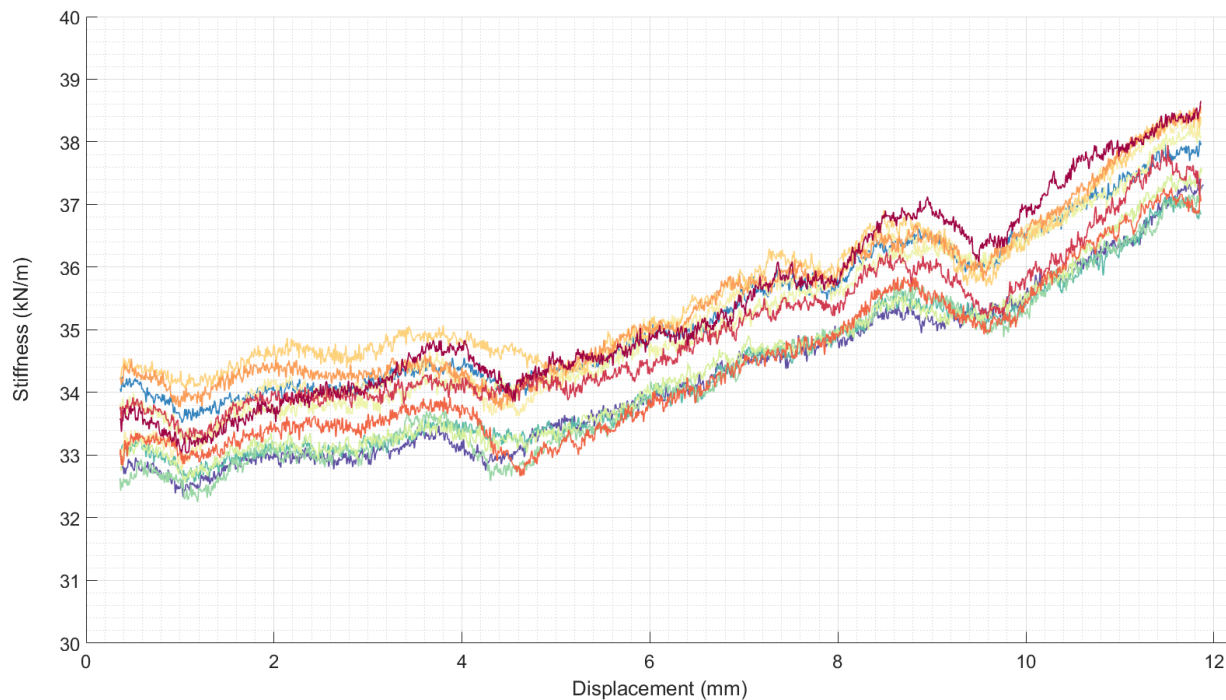


**Figure 64. Sandvik steel stiffness variations with displacement.**

Figure 65 is the stiffness results of the titanium flexure springs. Compared to the steel material, the averaged difference in the stiffness was slightly higher, about 8%. There was one spring with obvious machining issues that was considered as an outlier and was not counted in the statistical analysis. From both figures of the statistical analysis, the spring rate of the flexures showed a second-order relation with displacement.

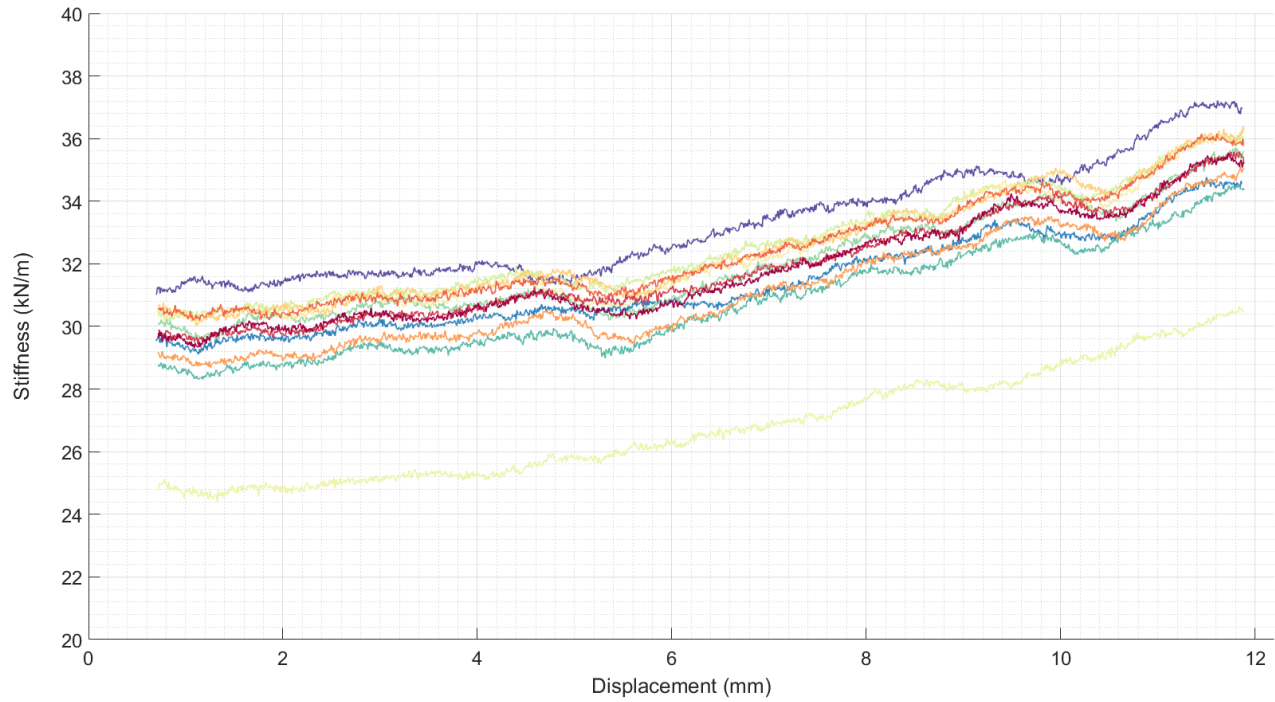


**Figure 65. Titanium stiffness variations with displacement.**

### 4.3 Packaging Conditions Analysis

To achieve the desired total stiffness and frequency of the LEA machine, multiple flexure springs should be stacked together. In Figure 54, it was shown that the total stiffness of the spring pack varies linearly with the number of springs. To improve the system performance, a spacer was designed to increase the contact surface which helped to reduce the stress concentrations in critical regions. Figure 66 compares the equivalent stress on a flexure spring when two different spacer designs were used. With the same packaging force, using wider spacer reduced the maximum stress on the flexure spring from 823 MPa to 742 MPa. The contact status contours on the left column indicated larger sticking region compared to the thin spacer.

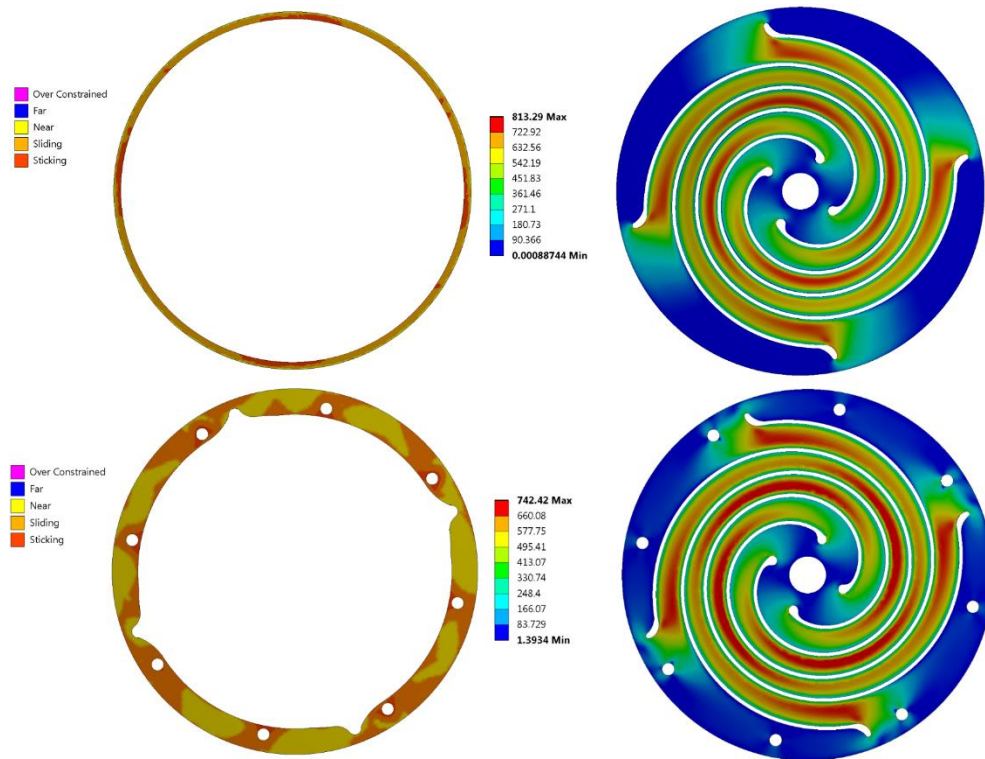


**Figure 66. Spacer geometry effect on Von-misses stress.**

Here, the conditions of the attachment of the flexure to the rod were examined to examine how it affects the stiffness of the spring, as it was deemed the most important parameter in the spring design. For this test, one steel spring was selected. The test consisted of four steps. Two conditions of the rod movement were considered, one when the rod was free to rotate in contact with the pushing arm (well-lubricated contact), and the other when the rod was fixed between the arms grips. For each of these conditions, the other side of the rod where it passes through the flexure's inner circle experienced two conditions itself. One that it was fixed to the rod via a bolt designed underneath the flexure and other condition when it was free to move and lubricated. The test setup is shown in Figure 67.

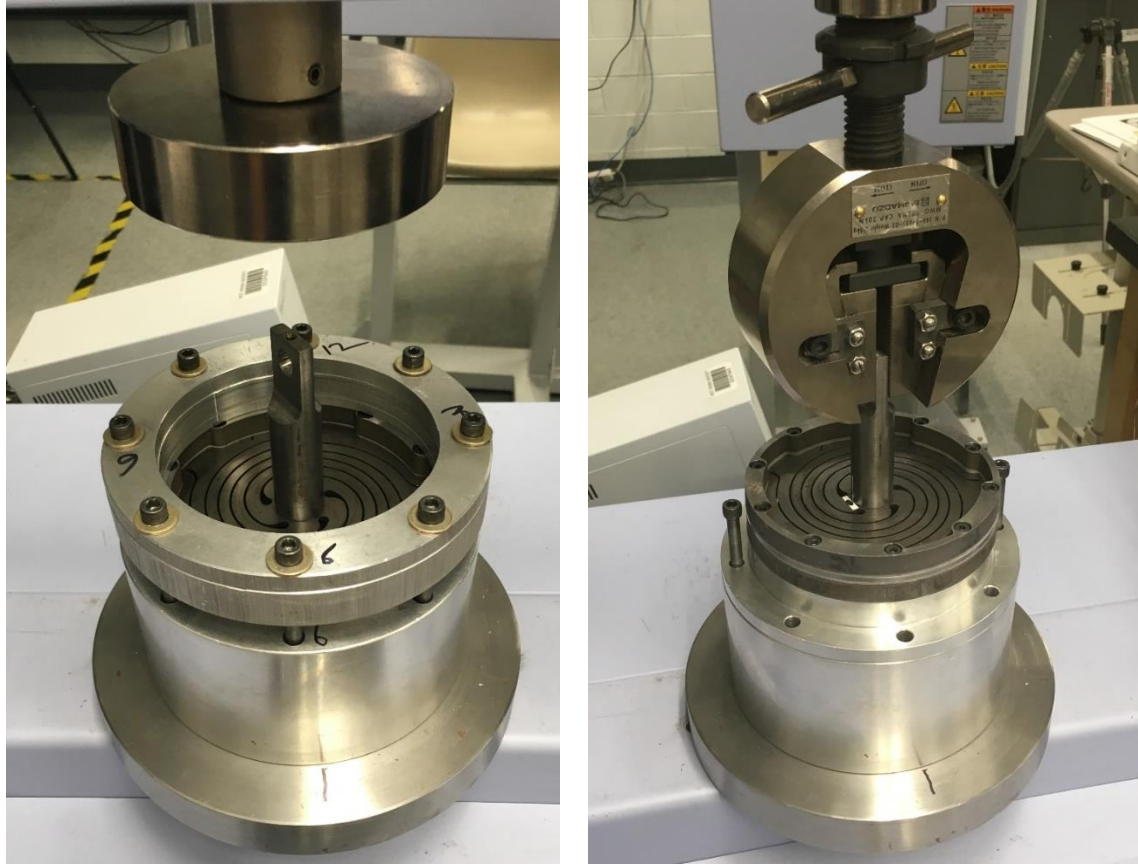


**Figure 67. Flexure-shaft connections variations experiment.**

The results of the four experiments are provided in Figure 68. It was found that the attachment of the flexure and rod had negligible effects on the results. However, the fixed rod in the Instron machine's grips resulted in large fluctuations in the stiffness. From the results of this test, it was found that such attachment lets the flexure inner circle freely rotate on the center rod, resulting in the more stable performance of springs. It is also important that such behavior in the spring's stiffness can increase the stress in the flexures.



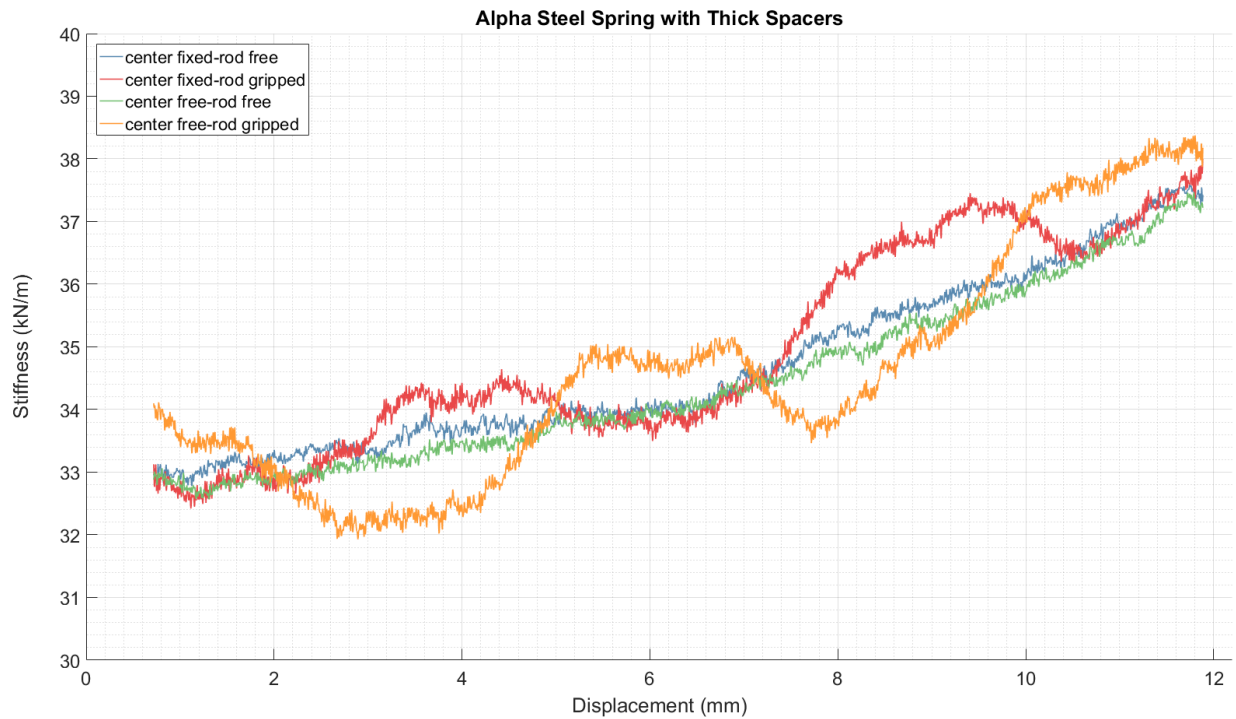


**Figure 68. Stiffness results vs. shaft connections conditions.**

#### 4.4 Packaging Force Experiments

The flexure springs were packed in two assemblies which were then located on the two sides of the alternator in the LEA machine. To achieve high frequencies, the number of flexure springs were commonly between 4-10 on each package. Using a high number of springs in each package resulted in high force reactions at the outer fixture. In the updated design, the flexure packages used eight 4 mm bolts to apply the required packing force to the flexures. Loosen bolts influences the stiffness and performance of the spring. To examine the effects of the packaging force on the spring's behavior, a series of tests were performed on a package of one flexure spring attached to the fixture with two different spacer designs: a 3 mm width spacer (tested for both titanium and steel flexures) and a wider spacer with bigger contact area (only tested for the steel flexure). The bolts of the package were tightened with the torque values ranging from 5-110 in.lb (0.5-12.4 Nm). The results are presented in Figure 69 to Figure 71.

Figure 69 shows the results of the titanium spring. The titanium springs were designed in a way that only thin 3-mm spacers could be used with them. Results showed around 5% increase in the stiffness by increasing the packaging force, specifically at higher displacements. The change in the



stiffness was reduced after the 35 in.lb torque. It should be noted that these numbers are only for one spring and for a pack containing multiple springs, the number should be multiplied as well. Eight bolts of 1/4" size were used in the titanium spring pack.

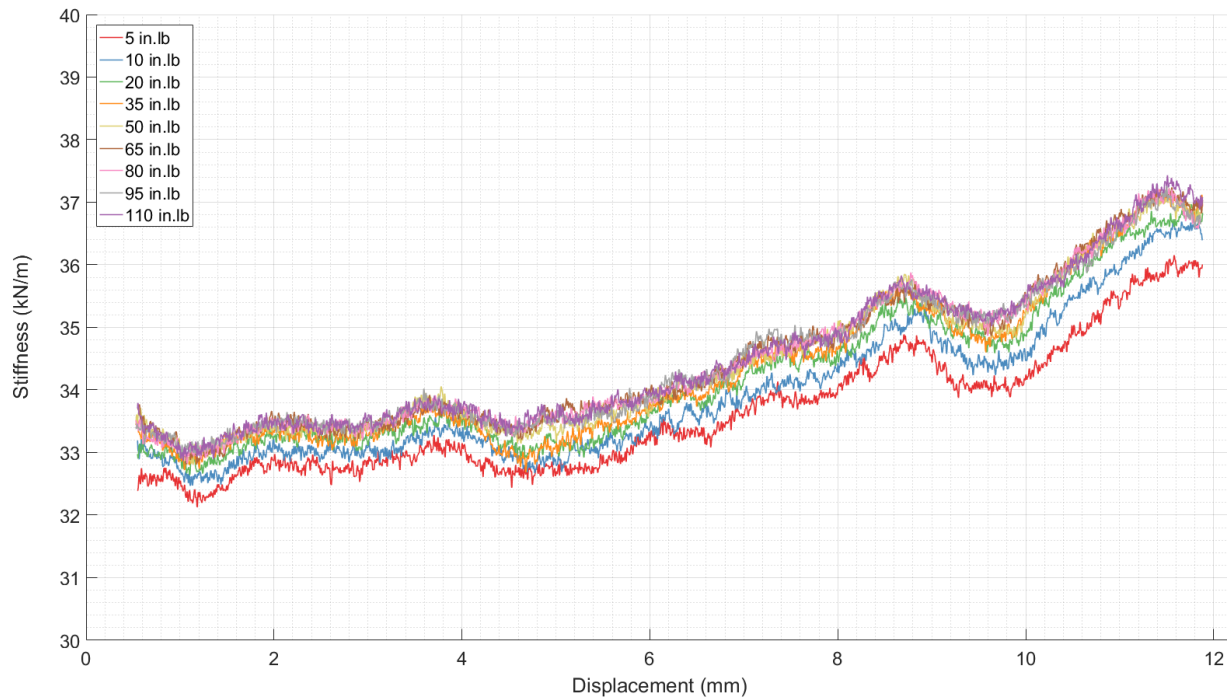


**Figure 69. Bolt torque comparison – titanium springs, thin spacers.**

For the steel spring pack, two spacer types were used. The thin spacers were similar to the titanium package – a 3 mm width spacer - and the wider spacers designed to increase the contact area and reduce the stress at spiral endpoints. For the steel package, ten 4-mm bolts were used. Results of the thin spacer in Figure 70 are similar to the titanium results with fewer deviations from the average. Similarly, it was observed that for one spring, a bolt torque up to 35 in.lb increased the stiffness and with no significant differences after this value.

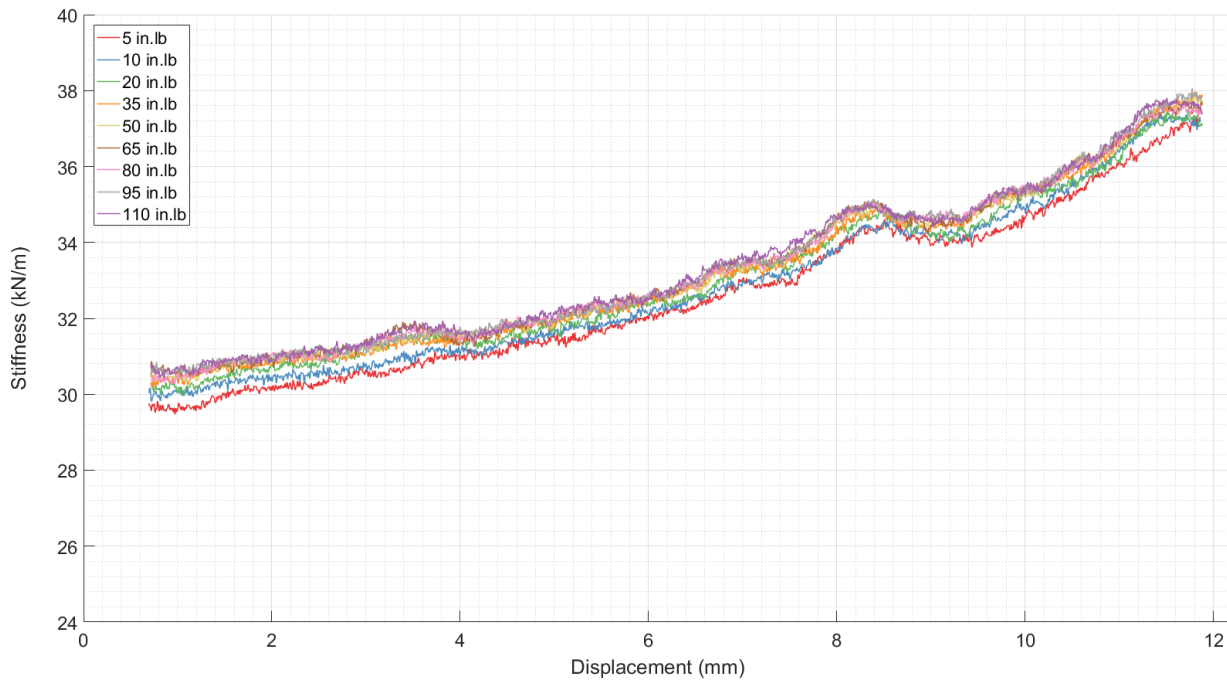


**Figure 70. Bolt torque comparison – steel springs, thin spacers.**

Figure 71 shows the results of the same steel spring with wider spacers. Having more contact areas helped the springs to be supported at the outer perimeter and, hence, the effects of the bolt torque were reduced. It can be seen from 2 in.lb torque to the maximum 50 in.lb, the changes were not very significant. The bolts tightened with 2 in.lb torques could be loosened by hand. This graph shows the importance of using wider spacers that will be helpful for such high-frequency dynamic systems where the vibration may loosen the bolts frequently.

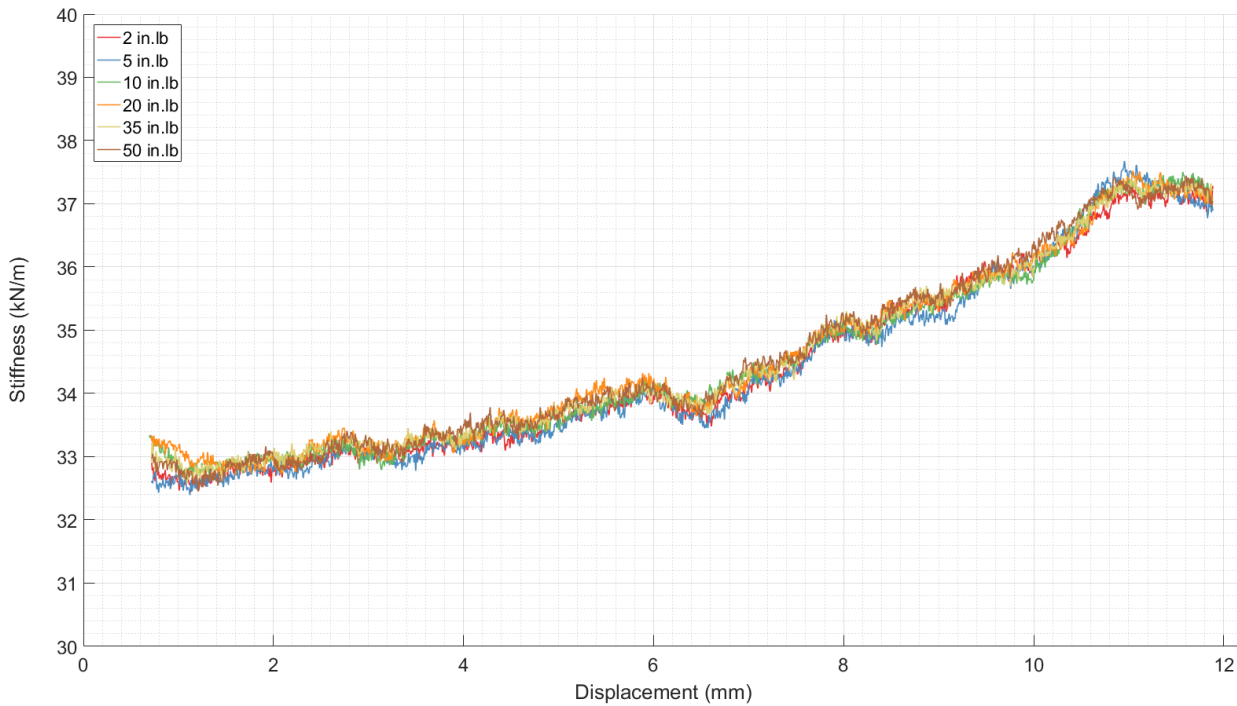


**Figure 71. Bolt torque comparison – steel springs, thick spacers.**

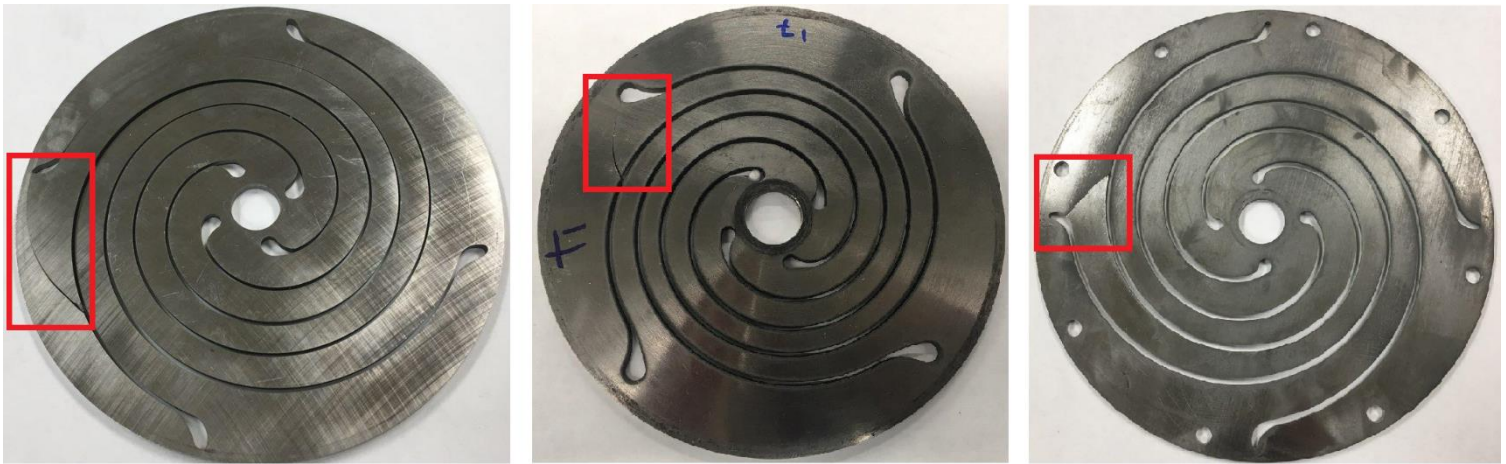
## 4.5 Fatigue Fracture

Flexure springs in the LEA machine are under high loads ( $> 500$  MPa) at a very high frequency ( $> 60$  Hz). As mentioned in the material section, the fatigue is the main risk for the life of the springs. Although the design of the spring was in such a way that the maximum stress is relatively lower than the fatigue limit (about 100 MPa), the dynamics of the systems and vibration cause additional stress concentrations, specifically at the curved locations near the outer end of spirals. Under the cyclic loading with the maximum stress magnitudes of below the yield strength, a crack begins to form at locations with high stress concentration. With continued cyclic loading, the crack grows and propagates perpendicular to the tensile stress. When the crack has grown a certain distance that the rest of the cross section cannot resist the load, the final rupture occurs [160]. In general, fatigue failure occurs in the following steps:

- Cyclic plastic deformation before crack initiation
- Initiation of microcrack(s)
- Propagation of microcrack(s) (Stage I)

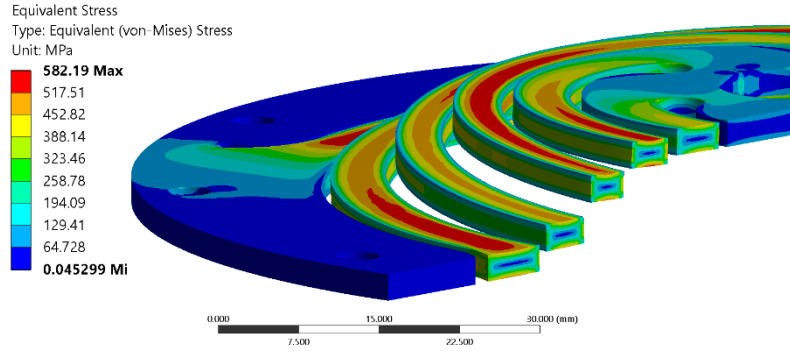
- Propagation of macrocrack(s) (Stage II)
- Final rupture (overload) [160]

Figure 72 shows flexure springs made from three different materials. As shown, in all three cases the fracture occurred in the same location. Other than the system's vibration and higher harmonics, there are other reasons that increase the stress magnitude on the flexure springs. Some of them are material imperfections, material properties uncertainty, and manufacturing method issues. The first cause is rooted in metallurgical processes and is out of the scope of this research. The second cause was discussed in the previous section. In this section, the third reason is discussed.



**Figure 72. Fractured flexures, left: Sullivan steel, middle: titanium 6246, right: Sandvik steel.**

The flexure's arm is under bending and torsion loading at the same time. However, the main portion of the stress is due to the bending. Figure 73 shows FEA stress on a cross section of an arm in different locations along the length. In each cross section, the stress on the top and bottom surfaces is maximum, and at the middle is minimum, near to zero. Also, the stress on the side surfaces is considerably lower than the top and bottom surfaces which indicates the higher amount of bending load at the cross sections.



**Figure 73. Cross section view of Von-misses stress on flexure's arms.**

With such maximum stresses on the top/bottom surfaces, the final finish becomes very important. Cracks from high-stress locations initiate and propagate in the material and cause a fracture. The small notches on the surfaces, specifically near the edges are amongst the common places for the crack initiations.

The most distinct characteristics of fatigue failure are beach or clam shell markings on the fractured surfaces due to the cyclic loading. It should be noted that such marks may not be visible on all materials failed by fatigue. Also, another reason for no beach marks is a very fast rupture. Guides for interpreting fatigue fracture markings have been shown schematically in Figure 74 for rectangular cross sections [160].

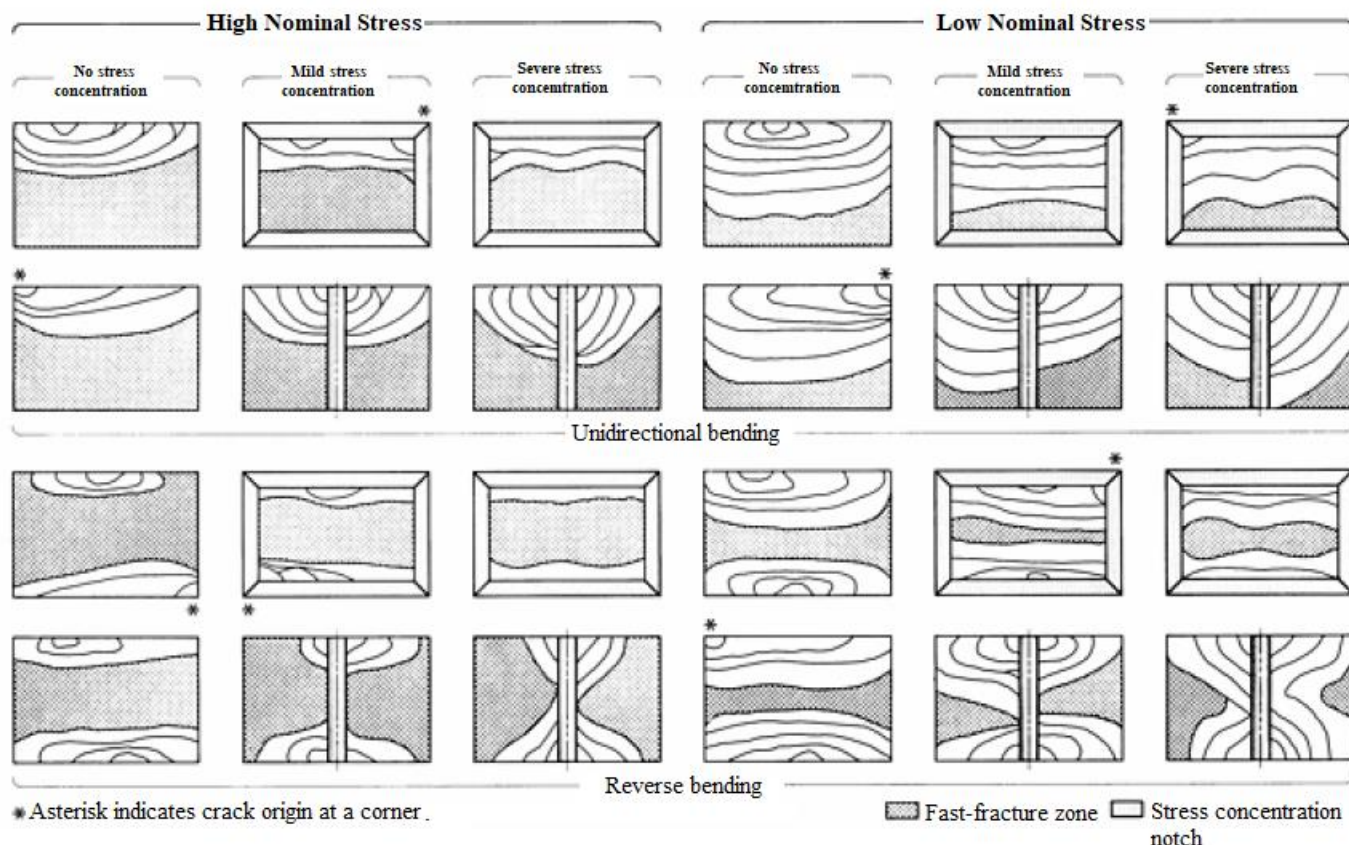


**Figure 74. Schematic representation of fatigue fracture surface marks produced in square and rectangular components and in thick plates under various loading conditions [160].**

When a flexure's arm breaks in the LEA machine testing, the frequency drops and most of the time, a loud noise is generated which is due to the collision of the broken arm to the adjacent flexures. After the fracture, the broken arm could experience hundreds of oscillations and due to this, not many of specimens with clean-untouched fractured surfaces was readily available. Most of the fracture surfaces were rubbed and the patterns may have been removed.

Figure 75 contains the cross section of the fractured surface of three flexure springs from left to right, Sandvik steel, Sullivan steel, and titanium material. In most cases, beach marks are concave to the failure origin. However, the notch sensitivity of the material and the residual stress patterns can influence crack propagation to produce beach marks in notch-sensitive materials that are convex to the origin, although such cases are rare [160].



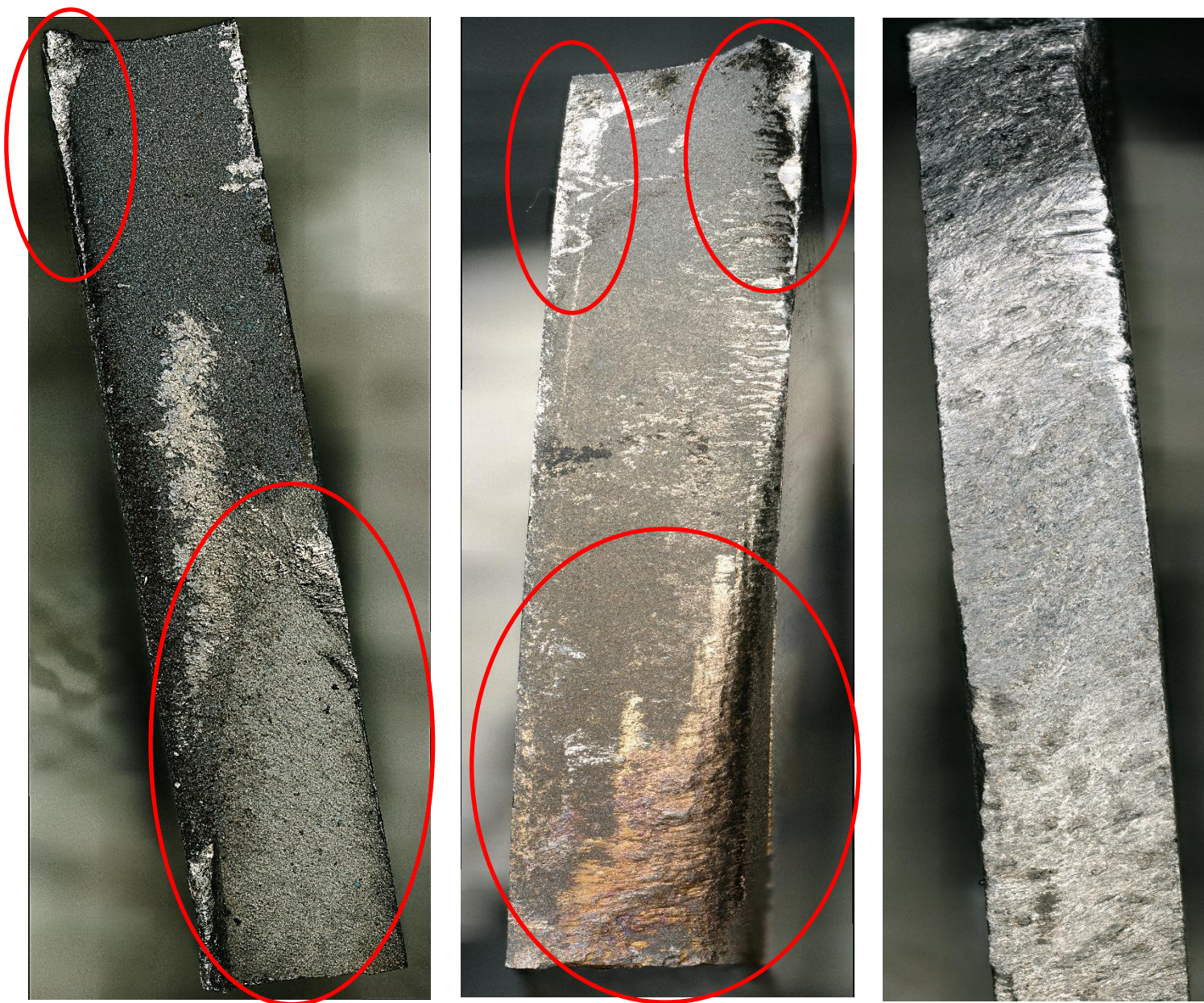


**Figure 75. Fractured surface of left: Sandvik steel, middle: Sullivan steel, right: titanium flexure springs.**

In Figure 75, the beachmarks for the two steel materials are visible, but it is not distinguishable for the titanium material. On the bottom right corner of both pictures, the curved line of grown cracks are visible in the lighter gray color. Also, there are smaller regions of the crack growth at the top corners. The darker gray area is the overloaded regions after rupture. Comparing the left two pictures in Figure 75 with Figure 74, the patterns are similar to the cases with low to medium stress concentration and unidirectional bending loading. The larger area of crack growth on one side of the flexures indicates that the bending loading was not constant over a cycle of LEA's operation.

The stress at the critical areas of the spiral arm is simultaneously under bending and torsion stresses. According to Figure 69, the crack initiated from the bottom right corner that for both specimens it was the location of the highest stress concentration near the spiral end.

#### **4.6 Surface and Edge Quality**

Fatigue cracks can be initiated at a wide variety of features, such as scratches, abrupt changes in cross section, tool marks, corrosion pits, inclusions, precipitates, identification marks, and weld configuration defects. In some cases, microcracks may be present before loading begins for example, grinding cracks, quench cracks, or hot or cold cracks from welding. All these problems increase the likelihood of early failure by fatigue, assuming the presence of alternating stresses of sufficient magnitude. The absence of surface stress raisers, smoothly polished surfaces and a very low inclusion content will not prevent fatigue if the alternating stresses are of sufficient magnitude and are applied long enough, but these factors are all desirable features for long life [160]. In the current LEA design, the flexure springs were manufactured by waterjet. There are various surface finishing methods that can help to improve the quality of the edges and surfaces. Figure 76 shows the side surface of four different springs. The descriptions of the processing methods and the material are provided through the labels and caption. In the pictures, the jet direction was from right to left. It can be seen that on the side where the water started cutting the material, the surface roughness was larger in size, and more material was removed. The surface roughness will be possible places for the cracks to initiate and grow until the fracture. The third and fourth pictures, show two surface improvement methods. In picture c, both the top and bottom surfaces of the flexure spring were polished for 24 hours in a vibratory tumbler machine. The sanding material was silicon carbide of grit 800 in size. It should be noted that although only the top and bottom surfaces were effectively in touch with the sand grits, the side surface quality was significantly improved as well. In the picture, both edges were enhanced in quality, and the size of the surface roughness and density of sharp edges were removed. This will decrease early fatigue risk. Picture d demonstrates a flexure spring that was exposed to shot peening. Collisions of the tiny metal shots cause additional compression residual in the material which helps the strength of the material under tensile stresses. Again comparing the shot-peened edges and the untouched edges, the sharp corners were reduced and the edges have more curved shaped than angled.



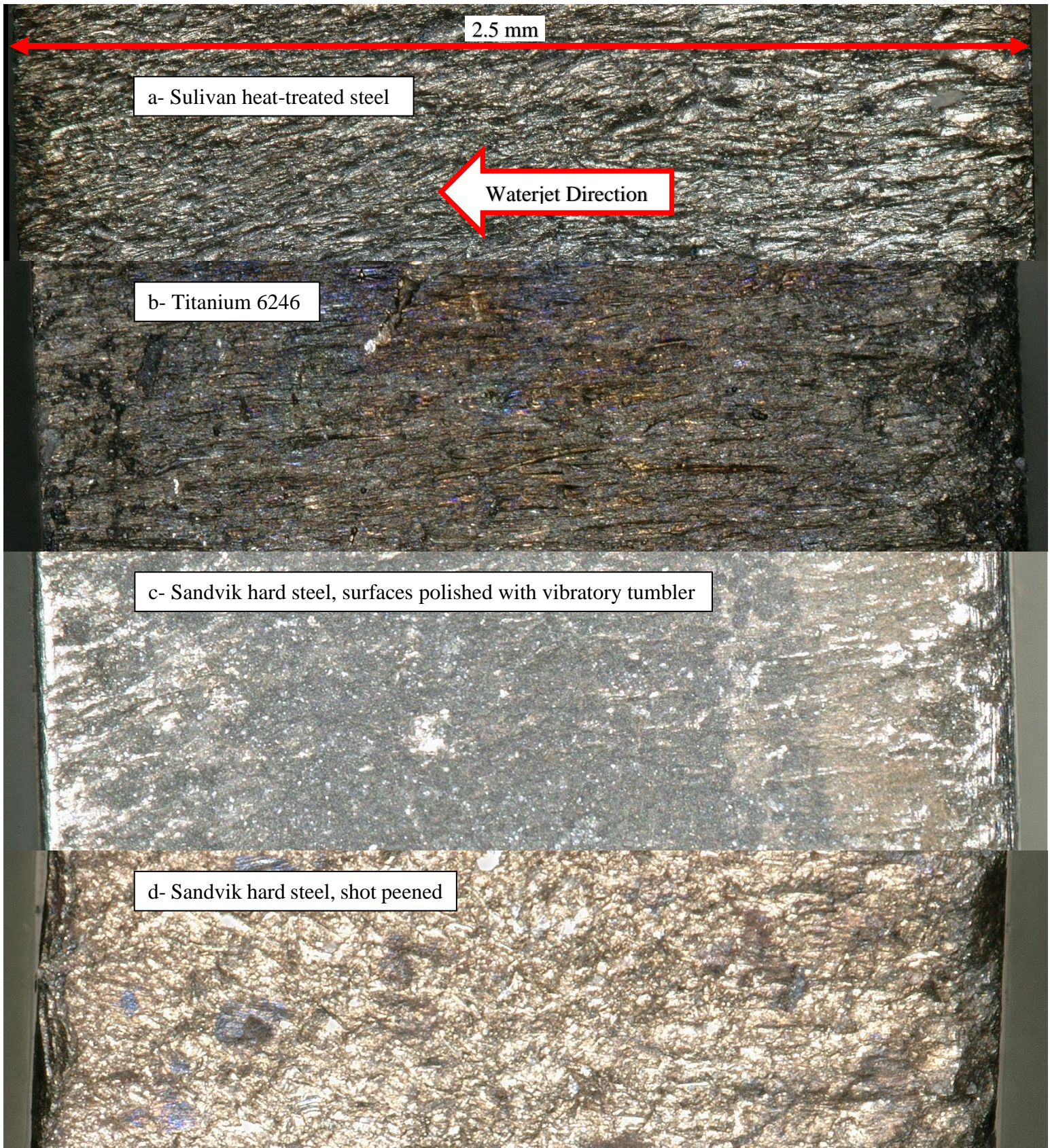
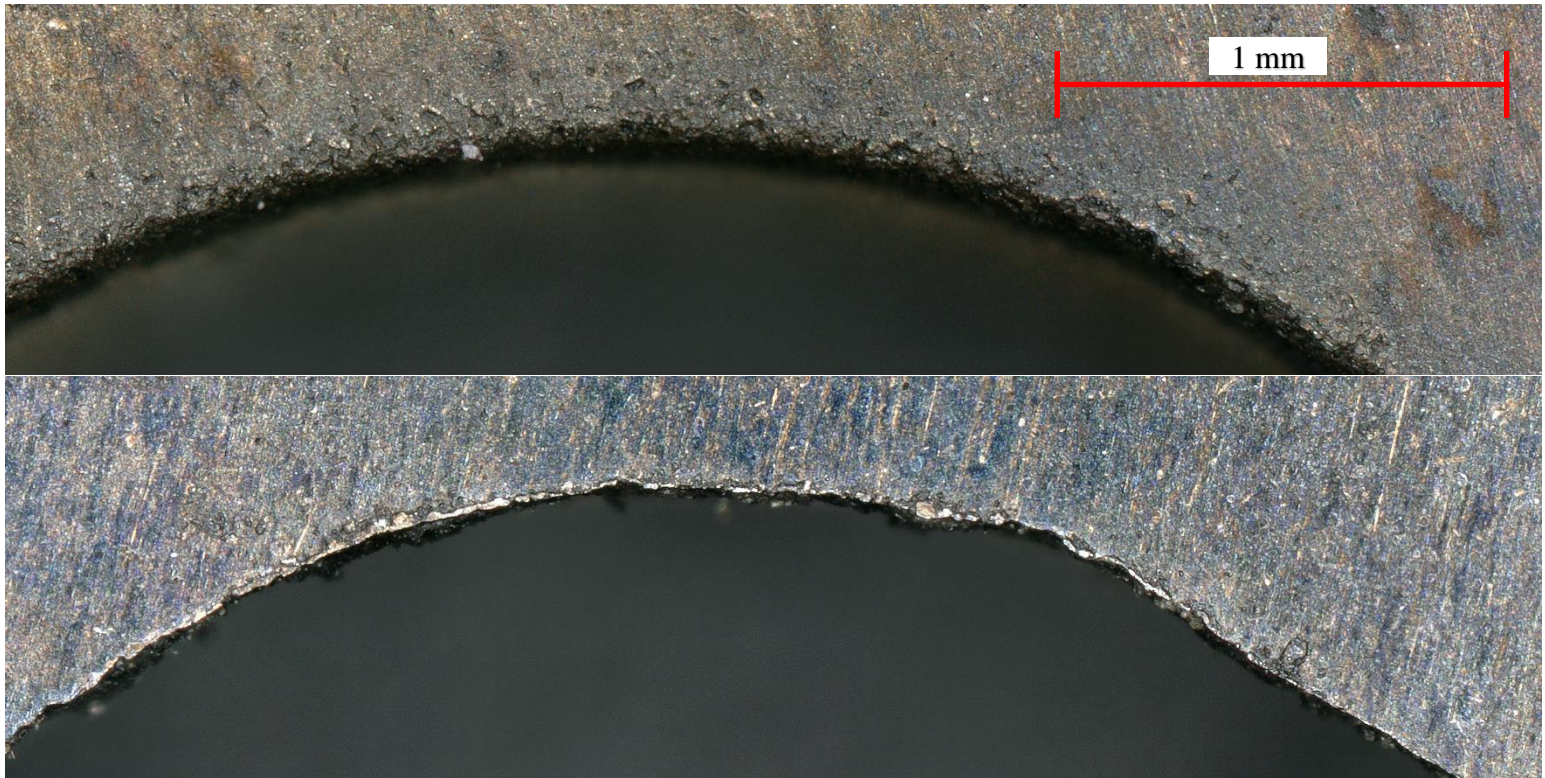


Figure 76. Water jet cut quality of side surfaces: a) Sandvik steel, b) Sullivan steel, c) Sandvik steel-tumbled, d) titanium.



The kerf angle was introduced in a prior section and it was shown it had negligible effects on the stiffness of the two sides of the springs. However, the side that the water starts cutting the material is more exposed to the abrasive, and a portion of the jet at lower speed contacts the top surface and leads to greater material removal. Figure 77 shows the two sides of the same spring, at the same location near the high-stress curved region at the end of the spiral arm. The top picture is the waterjet starting side and the bottom picture is the below side. It is shown that the top surface has significantly higher roughness compared to the bottom surface. Although the bottom surface is not perfect as illustrated with many sharp corners and edges and non-uniform radius of curvature, the edge and surface quality point appear better than the other edge and has a lower risk of crack initiation.



**Figure 77. Two sides of a titanium flexure at the same location.**

Three common methods of flexure manufacturing are waterjet, electrical discharge machining (EDM), or milling (CNC). These methods were compared in Table 12. The edge quality of both side surfaces of flexures with these three methods were compared in Figure 78. The edge quality of both top and bottom surfaces of flexures made by EDM and CNC were both satisfying and



minimum surface/edge finishing was required. However, according to Table 12, the CNC method is not practical, even for prototyping. So, it remains only the EDM as an alternative to the waterjet.

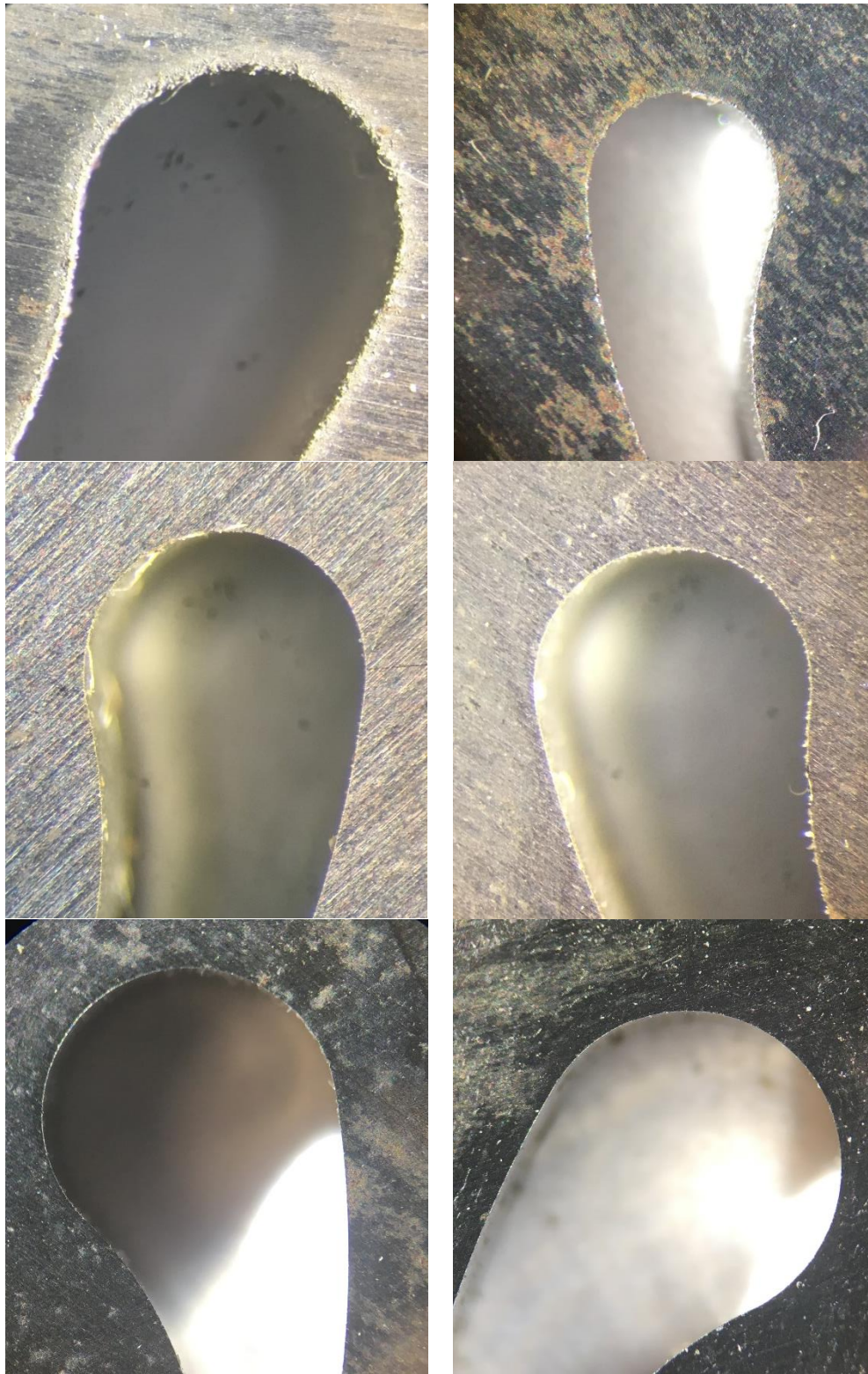


**Figure 78. Two sides of a steel flexures made by top: waterjet, middle: EDM, bottom: CNC.**

It should be noted that if the waterjet is used, additional surface processing is necessary that will increase the final manufacturing cost. So there is a tradeoff between the initial higher cost of the EDM and the cost of surface modifications of the waterjet machining. Overall, EDM is a good candidate for the manufacturing of the flexure for both prototyping and mass production. Further study is needed to calculate the final cost of each method and also the required fatigue failure associated with each of them.

## 5 Energy Performance Analysis

In this section, the performance of an individual flexure spring is studied. Specifically, criteria related to the energy conversion of the spring between kinetic (KE) and potential (PE) energies, under the real operating conditions are considered. In LEA machines, the output power and the thermal efficiency have a direct relationship with the oscillating frequency of the machine, which itself depends on the resonant frequency of individual flexure springs. In general, increasing the resonant frequency is one of the main methods to improve the performance of the LEA. However, higher frequencies cause issues that influence the energy loss mechanisms of the flexure springs and their durability. As a dynamic system, generally, there are three sources of energy loss, which are referred to as system damping. Damping is an energy dissipation mechanism that converts the energy of the system into other non-useful forms of energy e.g. sound and heat. These energy dissipation mechanisms in a dynamic system mainly depend on two factors, material and velocity. There are three main categories of energy dissipation mechanisms: 1- structural damping (or hysteretic damping), 2- viscous damping, and 3-Coulomb damping (or dry damping) [161].

The first category – structural or material damping – is the energy loss at the molecular level inside the volume of a material. It is also referred to as the internal friction of the material. The energy loss at this level depends on the material properties and the type of loading.

The second category happens when a fluid exists in the system. The changes in the velocity of the layers of the fluid (in contact with the solid surfaces) generates resistive shear forces and reduce the energy of the system. In the LEA, the oscillation of the flexure springs moves a relatively large volume of the air adjacent to the side surfaces and generates drag forces. The effects of the phenomenon are specifically important at higher frequencies.

The last category of damping, Coulomb damping, is very well known as sliding friction. The nature of the sliding friction is also behind the electrostatic bonds at the molecular level of the contacting surfaces, methods exist to simulate and quantify this energy dissipation mechanism.

Calculating the internal friction of material is very complex from a theoretical standpoint and is not the focus of this research. However, the parameters that will influence it will be examined. Instead, the drag force analysis, vibration, and the friction of the flexure spring system are

considered in this section. The drag forces and friction are two of the three damping categories, and the vibration influence all three categories which were studied here.

### **5.1 Air Drag Viscous Damping**

The disk-shaped geometry of the flexures at high stroke length and frequencies inside of the enclosed alternator frame, if not properly designed, would work similarly to a small air pump. Therefore, considering the large surface area of flexures, the drag force can be a significant source of power loss and must be carefully controlled. Moreover, sharp edges at the spiral cuts of the flexure arms, at high velocity, may generate sound waves that are dissipated in the enclosure. The airflow inside of the flexure housing caused by the flexure's oscillations increases the advection heat transfer mechanism and could be used to transfer the heat generated due to electrical resistance losses in the coils and permanent magnets [162]. This depends on the air velocity and the gap width between the flexure arms. In addition, the generated vortices behind and ahead of the flexures increase turbulence and pressure gradient which affects the engine side where the scavenging chamber is attached [163], [164]. It is recognized that the flexure area air could be evacuated to eliminate, or reduce, the air to reduce the viscous drag. However, this was seen as an additional cost and was not investigated as a possible mitigation strategy.

The losses due to the air drag force effects (also known as windage losses) are categorized as viscous losses or viscous damping. There are several physical mechanisms that influence the viscous energy loss and includes the interaction of the pressure waves reflected from the moving flexure surfaces and/or fixed enclosure walls, the pressure gradient between two sides of flexure surfaces while oscillating, the viscous forces acting on the lateral surfaces of the spiral cuts, and the flow and discharge coefficients of the air flowing through the slits. The shape of a flexure spring arms continuously changes during a cycle of oscillation and, hence, the openings between arms of the flexure change in shape and area. Due to the complexity of the dynamic behavior of a flexure spring and the involvement of viscous loss mechanisms, the application of analytical and theoretical methods are near impossible. In such cases, numerical simulations and experimental tests serve as valuable surrogates to improve the understanding of these losses.

To examine the effects of the aerodynamic drag force on a flexure's dynamic behavior and quantify drag force losses, a CFD solver has been utilized to investigate the fluid-structure interaction (FSI) between the solid spring material and ambient air. To generalize the drag force effects on flexures, a parametric study was performed to determine the effects of the most significant parameters. The analysis included the diameter, gap width, stroke length, and operational frequency. After determining the drag force coefficient from the CFD analysis, the drag force is calculated from Equation 31.

$$F_D = \frac{1}{2} C_D \rho A V^2 \quad \text{Equation 31}$$

where  $F_D$  is the overall drag force,  $C_D$  is the overall drag coefficient (a single drag coefficient to account for all of the abovementioned viscous loss mechanisms),  $\rho$  is the air density,  $A$  is the surface area of the flexure and  $V$  is the effective relative velocity [165]. A closed cylindrical domain which represents the physical boundaries of the domain that the flexure is located in, one flexure was prepared in ANSYS design modeler for simulation. The fluid domain contained 150,000 tetrahedron cells and solid domain incorporated 8000 cells. The structural solver sent the deformation information to the CFD solver and the drag force was returned to the solid surfaces. Figure 79 shows the solid and fluid domains and sequence of force/displacement transfer between these domains. More details were provided in Appendix 9.1.4. Due to the high frequency vibration of the arms, careful selection of the mesh size/type and time step was required to avoid a negative cell volume error during the dynamic meshing. A full cycle sinusoidal reciprocating motion was modeled via coupled FSI simulation.

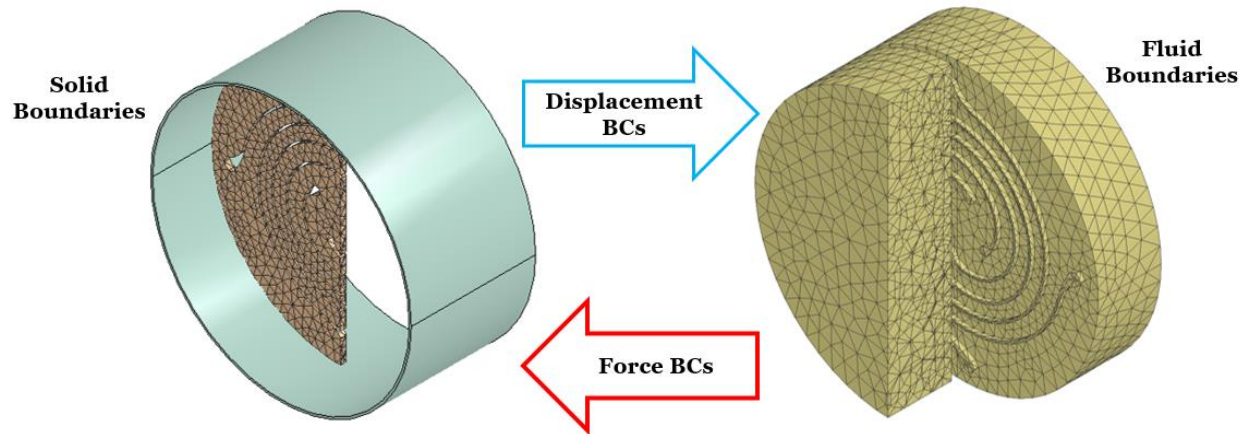


**Figure 79. Solid and fluid domains in fluid/structure modeling.**

Figure 80 shows the CFD results of streamlines and vectors of flow velocity oscillating in a closed volume. The time written on top of each picture is the normalized time of one cycle from  $t = 0$  to  $t = 1$ . Contours show a turbulent flow with high velocities near the center and also the spiral cut ends where more open areas exist for the flow to escape from one side to another side.



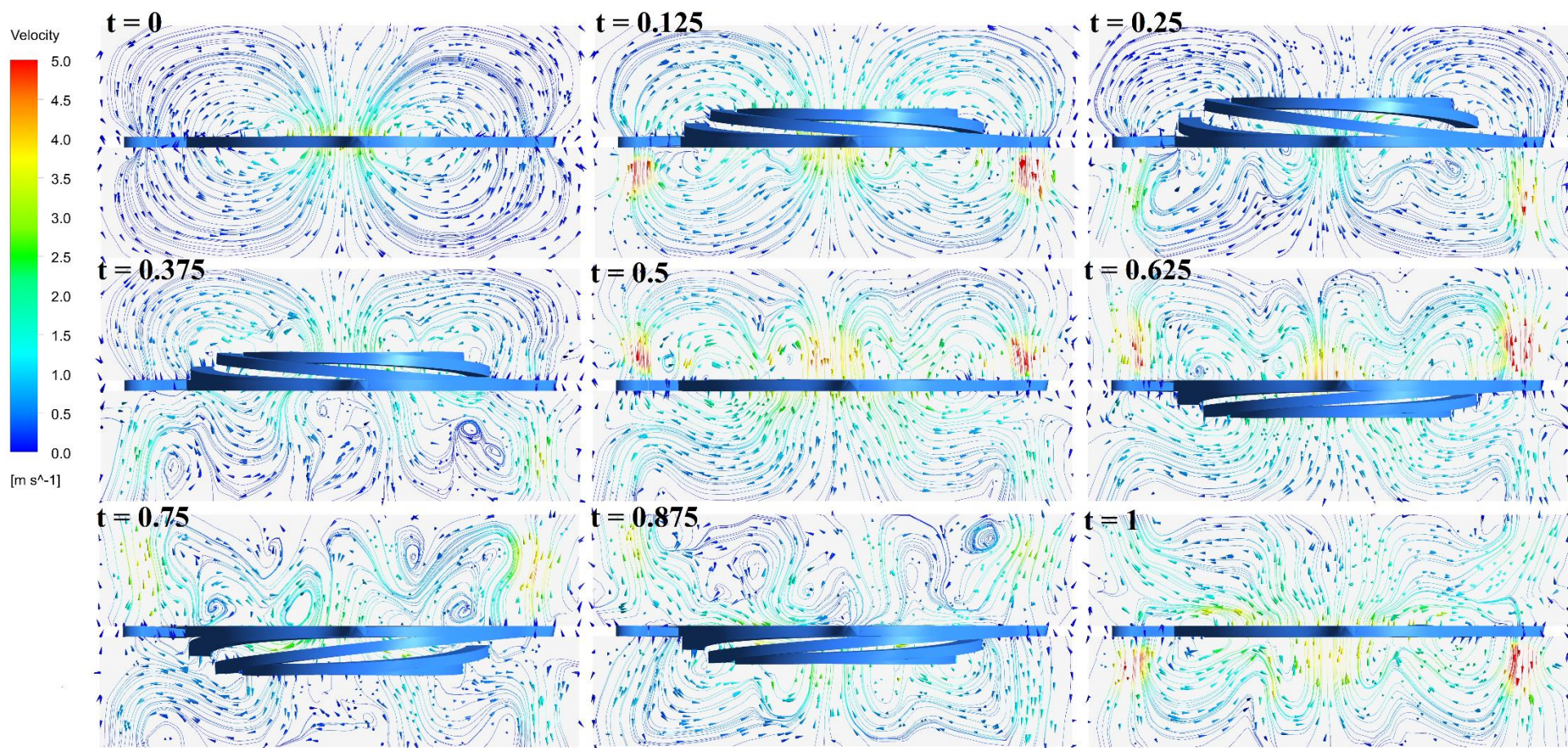


**Figure 80. Flow velocity streamlines and vectors around one oscillating flexure spring ( $t$  is normalized time during one cycle of oscillation).**

Figure 81 through Figure 84 show the variations of the drag force coefficient within a full cycle versus flexure diameter (OD), gap width, stroke length, and frequency, respectively. The fluctuations of the drag coefficient is because of the higher frequency modes of the spiral arms. At the onset of the motion, the ambient air is stationary and inertia forces lead to the higher amplitude of the drag coefficient compared to steady state operation. Based on the defined positive direction of the drag force, if the overall drag force is in the reverse direction – which happens if the flexure experience vacuum conditions on the surfaces – then the drag coefficient will be a negative value.

As can be seen in Figure 81 through Figure 84, the drag coefficient value peaks at the middle of the cycle where the flexure has the maximum velocity. Under a fixed stroke length of 22 mm and a frequency of 65 Hz, as the outside diameter of the flexures increased from 85 mm to 160 mm, the peak of the drag coefficient increased non-linearly. Figure 82 shows how increasing the gap width can significantly reduce the drag coefficient. The influence of gap width on drag force is important when the two sides of the alternator frame are completely closed and the gap between arms is the only air pathway. Figure 83 shows the effects of stroke length on the drag coefficient. At the fixed frequency of 65 Hz, increased stroke length yielded a higher peak velocity, and based on Equation 31, will result in higher drag forces. Figure 84 shows the effects of operational frequency at a fixed stroke length of 22 mm where an increasing frequency resulted in a higher drag force on the flexure surfaces.

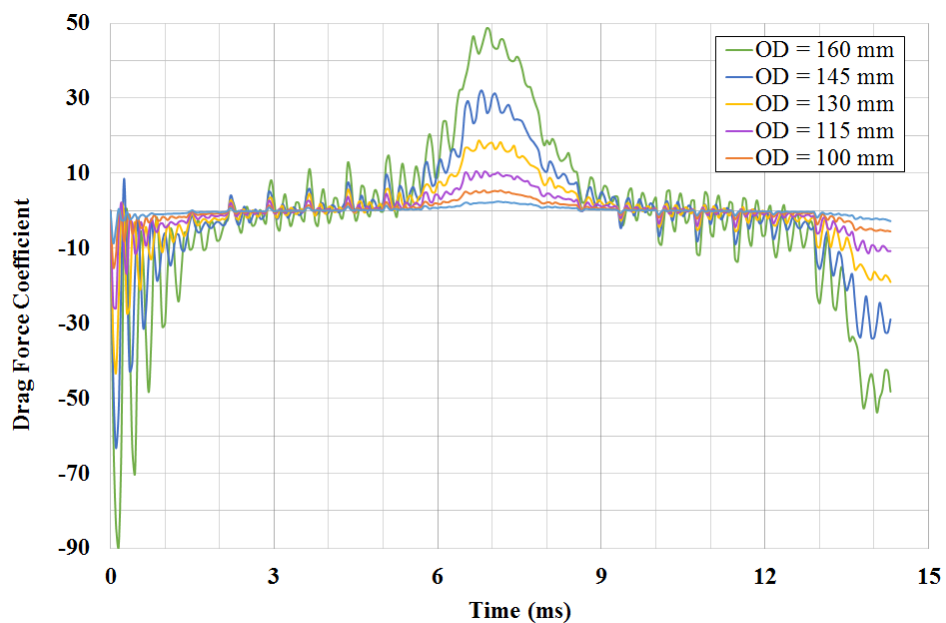


**Figure 81. Cyclic variation of drag coefficient vs. outer diameter of flexure.**

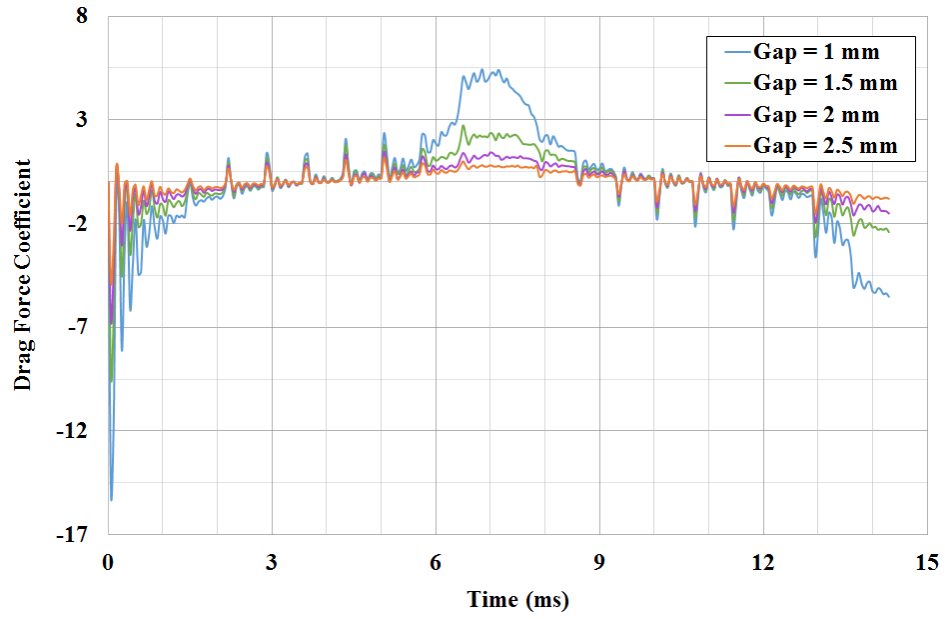


Figure 82. Cyclic variation of drag coefficient vs. gap width of flexure.

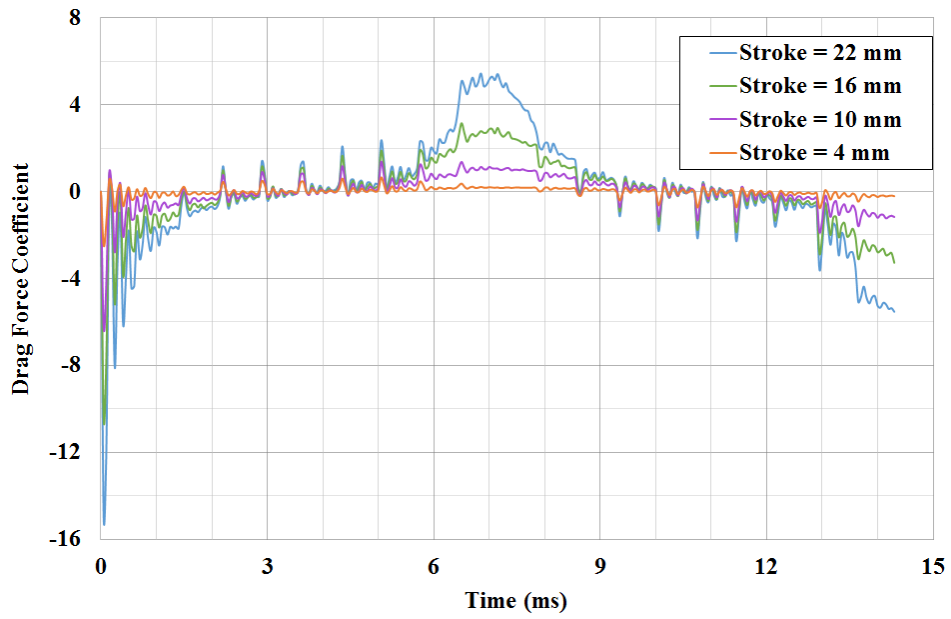
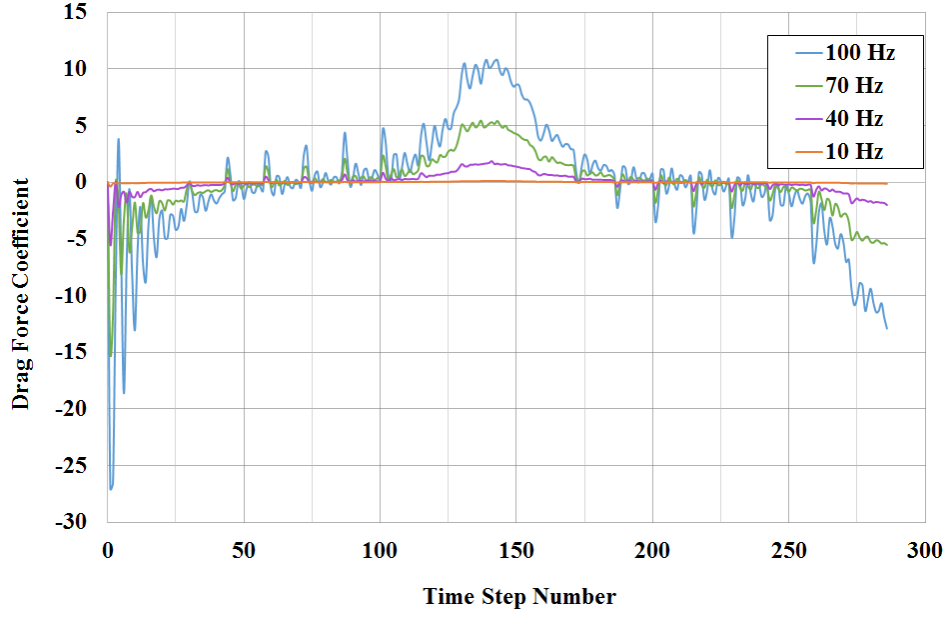


Figure 83. Cyclic variation of drag coefficient vs. stroke length.





**Figure 84. Cyclic variation of drag coefficient vs. oscillating frequency.**

To determine the drag force, the local velocity of the spring must be determined. Because of the non-linear deflection of flexure arms, the velocity along the length of arms is non-linear. To estimate an effective velocity, the spring was divided into 20 equally spaced integral ring sections based on two different approaches: a mass average-based and a kinetic energy-based. The equations are provided in Equation 32 and Equation 33, respectively.

$$V_{eff} = \frac{\sum_{i=1}^n m_i v_i}{M} \quad \text{Equation 32}$$

$$V_{eff} = \sqrt{\frac{\sum_{i=1}^n m_i v_i^2}{M}} \quad \text{Equation 33}$$

where  $V_{eff}$  is the effective velocity of the flexure,  $n$  is the total number of the segments,  $m_i$  and  $v_i$  are the mass and velocity of the  $i^{th}$  segment, respectively, and  $M$  is the total mass of the flexure spring. Figure 85 shows the variation of these calculated velocities during the cycle. The figure also shows the maximum velocity of the center of the flexure compared with the effective velocities. The effective velocity was used in Equation 31 to find the drag force.

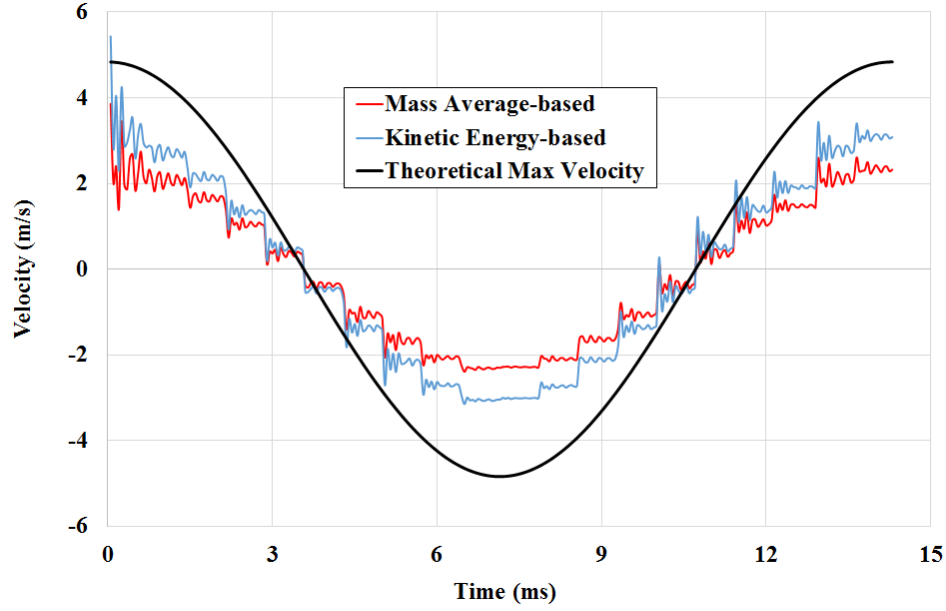


**Figure 85. Effective velocity.**

To calculate the energy loss due to the drag force, the displacement of the centroid of one arm of the flexure was obtained and then the energy loss was calculated using the Equation 34.

$$dW_D = \vec{F}_D \cdot d\vec{s} \quad \text{Equation 34}$$

where  $F_D$  is the vector of drag force and  $ds$  is the displacement differential vector. The calculated drag force losses using Equation 34, as depicted in Figure 89, was compared with the experimental test results explained in the following section.

In an LEA machine, multiple flexure springs were assembled into spring packages to increase the overall stiffness and hence the resonant frequency of the machine. To avoid the collision between the adjacent flexure springs, they were separated using one or multiple spacers. In the experiments, the distance between two flexures varied between 1-5 mm. To consider the effects of the distance between adjacent flexures on the drag force, a CFD study with similar domains as shown in Figure 79 was used with two flexure springs at the middle. The gap between flexures was varied between 1 to 10 mm. Figure 86 shows the net instantaneous drag force on all surfaces of one of the springs and Figure 87 shows the integration of the drag force over one cycle of oscillation of the same spring. As can be seen, the cyclic sum of the drag force was increased by the gap distance between flexures. Increased gap distance, caused higher flow volume and pressure change in the volume between flexures and increased the drag force.

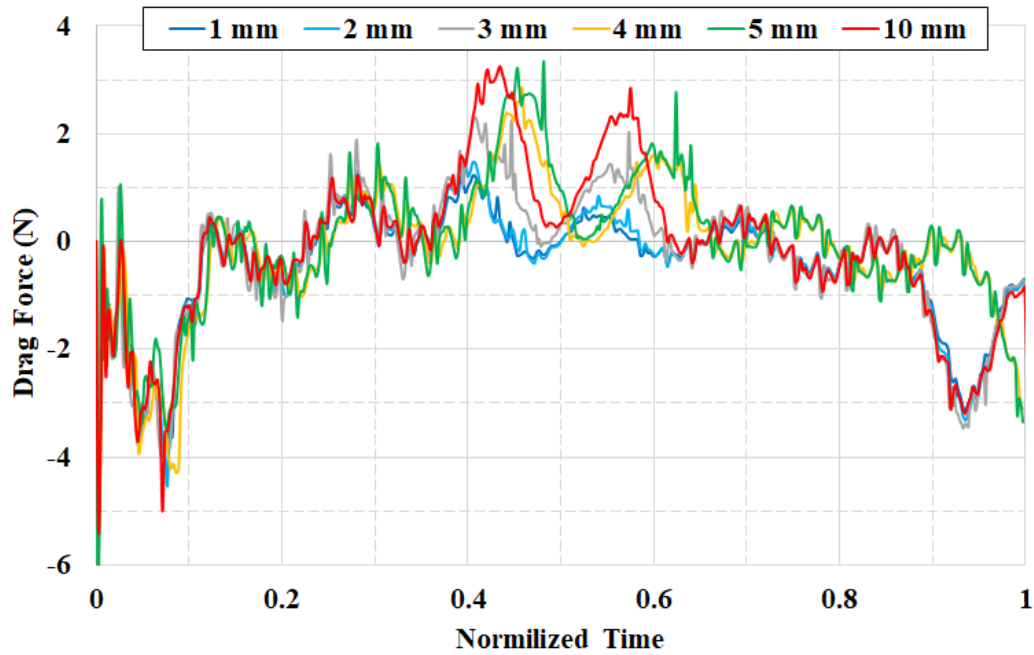


Figure 86. Variation of drag force versus distance between two adjacent flexure springs over one cycle.

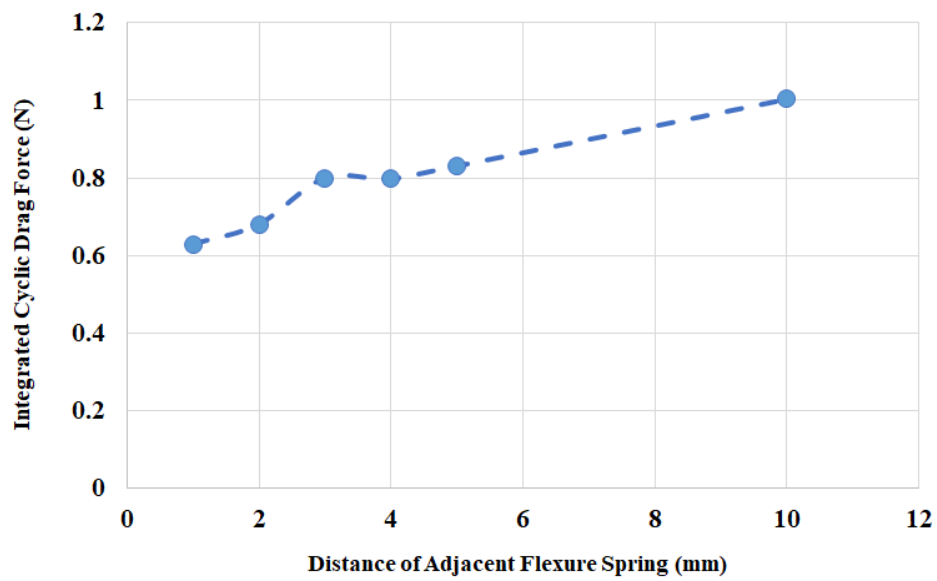


Figure 87. Integrated drag force on one flexure spring over one cycle.

## 5.2 Experimental Validation

A series of tests in a vacuum chamber was designed for the linear alternator to eliminate windage losses in the system. Two tests were performed – one inside the vacuum chamber at vacuum equal to 28.6 inches of mercury and one at ambient pressure in Morgantown, WV, so that windage losses could be determined by differencing. Figure 88 shows the test setup for the vacuum test. The test setup consists of a Yokogawa power analyzer to measure the input power and estimate of the power losses, an oscilloscope to monitor the displacement and frequency, and a control unit (Texas Instrument digital signal processor (TI DSP) and inverter board) to power the machine.

For the vacuum chamber test, to reduce the number of unknowns in energy balance calculations, the linear alternator was run as a linear motor. The linear motor was powered at the spring's resonant frequency. This resonant frequency of the spring was determined by the control unit (TI DSP). An oscilloscope was used to measure the stroke length of the linear alternator. Using the Yokogawa power analyzer, the power delivered to the linear motor, as well as voltage and current, were measured.

In the current method, the total mechanical energy loss was calculated by subtracting the electrical loss from the total input power. When a linear alternator works as a motor, at steady state, the total input power is equal to the total losses. Knowing the electrical losses due to the winding's resistance, an estimate of the total amount of the mechanical losses can be made [166]. The mechanical losses obtained were due to both windage losses and vibrational/frictional losses. To distinguish these two mechanisms, the vacuum tests were performed to isolate the effects of air drag force. The energy balance of steady-state motoring tests are shown in Equation 35 and Equation 36 for ambient pressure and vacuum condition tests, respectively.

$$[P_{input}]_{ambient} = P_{copper} + P_{windage} + P_{vibrations} \quad \text{Equation 35}$$

$$[P_{input}]_{vacuum} = P_{copper} + P_{vibrations} \quad \text{Equation 36}$$

where  $P_{input}$  is the power delivered to the machine,  $P_{copper}$  is the copper loss,  $P_{windage}$  is the viscous power loss due to windage effects and  $P_{vibration}$  is the losses due to structural and frictional damping. Under the same operational conditions, the difference between Equation 35 and Equation 36 will result in  $P_{windage}$ . To identify the structural damping losses from Equation 35, the  $P_{copper}$  can be obtained from Equation 37.

$$P_{copper} = RI^2$$

**Equation 37**

where  $R$  is the electrical resistance of windings and  $I$  is the current measured by the power analyzer.

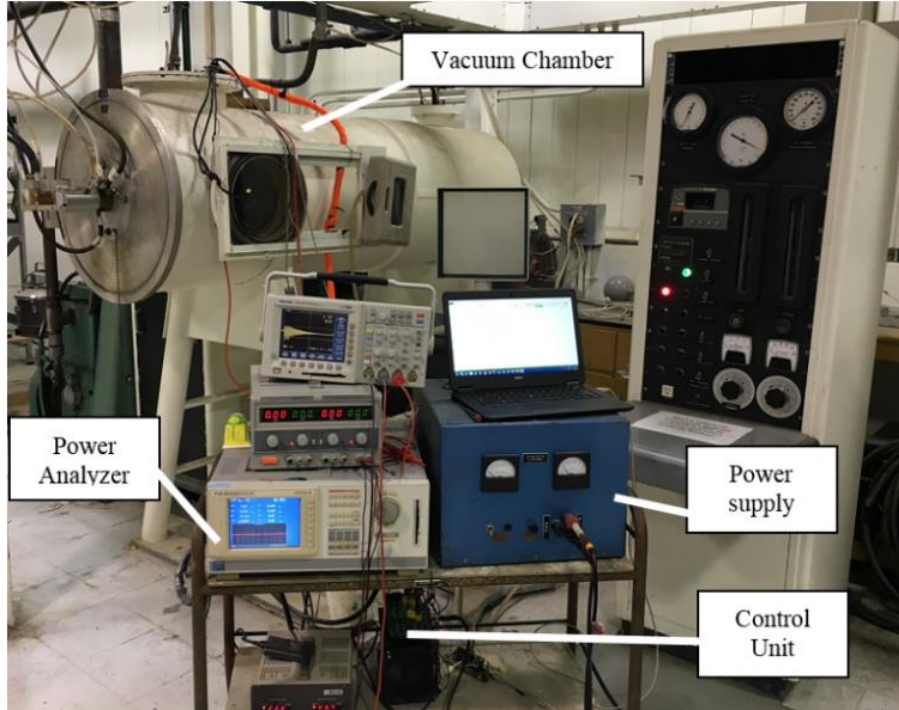


**Figure 88. Vacuum test cell.**

Figure 89 illustrates the windage power loss estimated by CFD compared to experimental results for six springs. Increased power losses were observed as the displacement was increased. As illustrated in this figure, the upward trend of the power loss with stroke length was predicted in CFD modeling. The difference between the two graphs increased as stroke length increase. This is due to the non-linearity of flexure spring stiffness which was not considered in the CFD simulation.



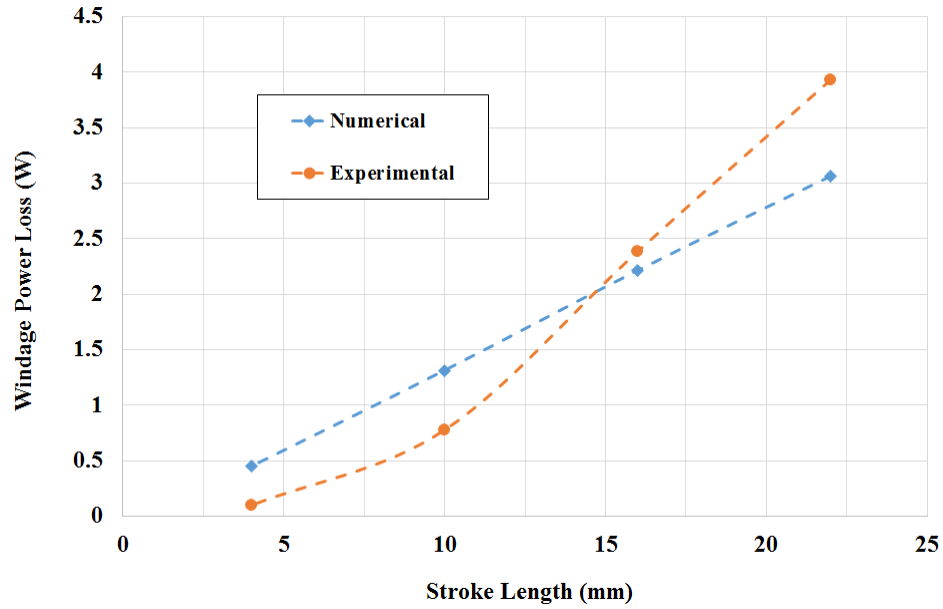


**Figure 89. Windage power loss.**

The percentage of contribution of windage loss was obtained from a comparison of the total power loss with and without the presence of ambient air while the alternator was running. The results of vacuum chamber tests showed that between 10-15% of the total mechanical energy loss was from windage effects while the input power was between 70 – 75 Watts and the electrical power loss was measured around 40 Watts.

### 5.3 Vibration

The vibration of flexure arms is another potential source of energy loss. The vibration increases the frictional losses at any contacting surfaces. In addition, the local deflections due to vibration increase the total amount of damping losses, e.g. viscous damping losses and structural damping losses (hysteresis losses). The source of vibration is rooted in higher modes of frequency than the resonant frequency. Figure 90 shows the first four vibrational modes of the frequency obtained from FEA. Due to geometrical symmetry, the second and third modes are similar. These modes are within a factor of five of the resonant frequency of 65 Hz for this design which resulted in the first four modes causing local deformation of the arms. Results of FEA showed that fifth and higher

modes of vibration of the flexures are far enough from the operating frequency (more than 500 Hz) so that their effects on the amplitude of vibration were negligible.

When the assembly resonates at a certain frequency (the major natural frequency of the whole system) higher frequency modes of the flexures increase the amplitude of vibration proportional to the proximity of operating frequency and higher modes of frequencies [167]. Table 11 shows the FEA-derived values of the first four modes of frequency of the currently manufactured flexures.

**Table 11. Flexure's deformation modes frequencies.**

Mode Number	Frequency (Hz)
1	138
2	242
3	242
4	347

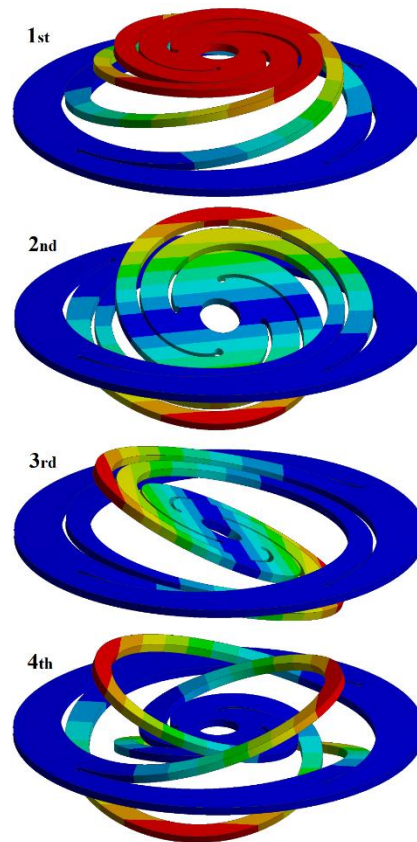


**Figure 90. Flexure's first four modes of deformation.**

Higher order vibration modes induce increased stress on the spring arms or increased the possibility of collision of two adjacent flexure arms. As such, a portion of input energy will dissipate into the surrounding air in the forms of heat and noise energy due to increased local deflections. To reduce the effects of losses due to vibration, the higher resonant frequency is desirable but the maximum frequency is limited to the maximum allowable stress level and fatigue failure considerations. Higher natural frequency resulted in a higher frequency of the assembly, lighter design, and higher output power. The second, third, and fourth modes of frequency were the most significant cause of unfavorable arm vibration that caused higher energy loss and reduced life. With the same geometry of the arms, both higher material stiffness and lower density will result in reduced vibration of the arms. To examine the severity of vibration at different locations on the flexure arms, with respect to their nominal displacement (static conditions), a transient FEA was performed for two spring designs as shown in Figure 91. Six equally spaced points were selected on one arm. The BC for the transient analysis was a sinusoidal displacement with a stroke length of 22 mm and a fixed outer perimeter. To capture the effects of the operating frequency on the vibration of the arms, several frequencies from the low bound 25 Hz to the resonant frequency of each flexure – 138 Hz for the titanium flexure and 122 Hz for the steel flexure – were examined.

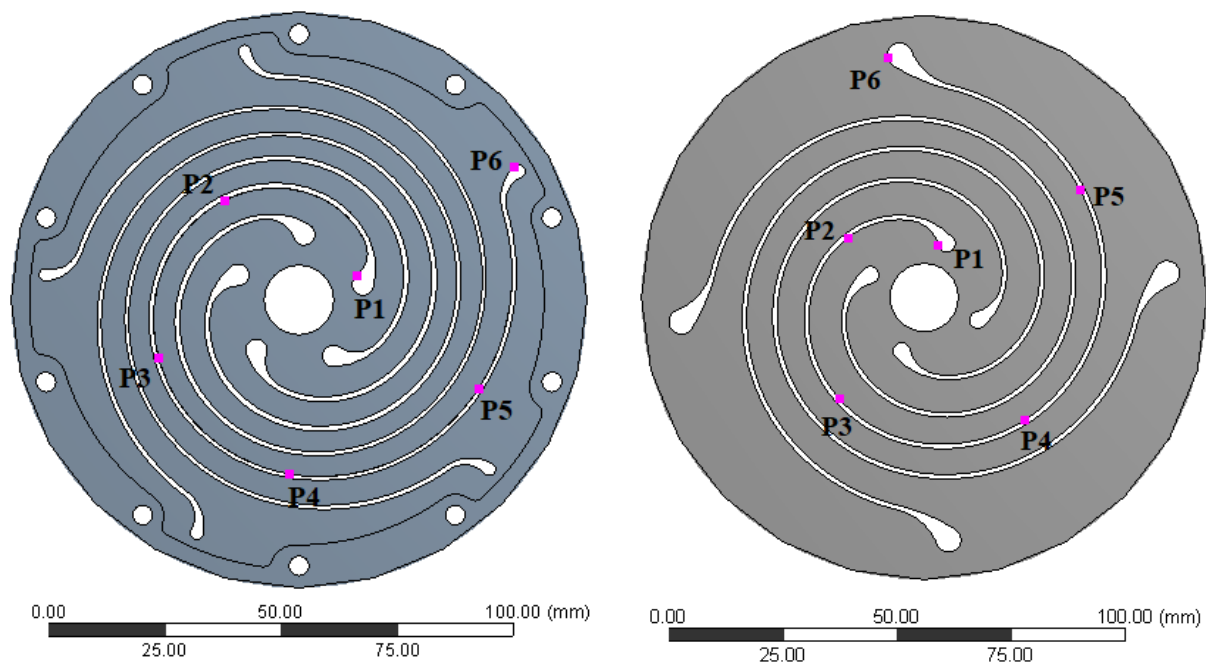


**Figure 91. Selected points on steel (left) and titanium (right) flexures.**

Figure 92 and Figure 93 show the displacement of selected points along the arm's length during one cycle of operation for the titanium and steel flexures, respectively. Point number 1 is located near the center of the flexure and has the sinusoidal-shaped displacement similar to the input boundary condition and point number 6 is located near the outer diameter of the arm which has the minimum displacement amplitude. Because different frequencies were used, for a better representation of one cycle of each frequency, the time on the x axis was normalized by the end time of each cycle. To compare the amplitude of the vibration with the non-vibrating arms, one case was solved with increased stiffness (1000 times higher), and reduced density (1000 times lower). In each graph, the black dashed line shows the near sinusoidal motion at that location.

For both designs, the vibration of P1 and P2 points are very low and negligible. The amplitude of the vibration increases as moving from the center toward the outer diameter of the flexure. It can be seen that the vibration at P3 and P4 caused the maximum amplitude of the oscillation to exceed the designed deflection of the spring in one direction which was 11 mm. According to Figure 90, the increased amplitude exceeding the center position is due to the 4<sup>th</sup> mode of deformation for the titanium flexure and 5<sup>th</sup> mode for the steel flexure. Regardless of the stress concentration, which is discussed in the following paragraphs, this mode of vibration causes the collision of the adjacent flexures in the assembly if a safe distance was not considered. One rapid solution to the collision problem could be increasing the distance between adjacent flexure, however, it also increases the overall length of the LEA machine and weight. One design aspect was to keep the distance between the flexure minimum, which in the LEA machine was 3 mm.

Despite the amplitude of the oscillation at point 6 is minimum amongst the other six points, the magnitude of the increase in the amplitude due to vibration at this point is maximum. Higher vibration result in increased strain energy and hence increase stress concentration at the endpoints of the spirals. This is the main reason that fatigue fracture at P6 locations is very common and the highest risk.

Another important observation from the results of the dynamic analysis was the effects of the oscillation frequency, or in other words, the frequency of the LEA machine versus the resonant frequency of individual flexure springs. As shown in Figure 92 and Figure 93, the highest magnitude of vibration occurs at the speed equal to the resonant frequency of the flexure springs. In practice, an LEA machine cannot work at this speed because there are other parts connected to

the center of the flexures via a shaft that reduces the machine's frequency due to increased mass (see Equation 5). Although increasing the LEA's working frequency will directly increase the output power and the engine's efficiency, a reduced operating frequency significantly increase the factor of safety and the overall life span of the flexure springs. The reduced frequency can be compensated by improving the alternator design (e.g. permanent magnets or windings) that naturally tend to increase the moving mass.

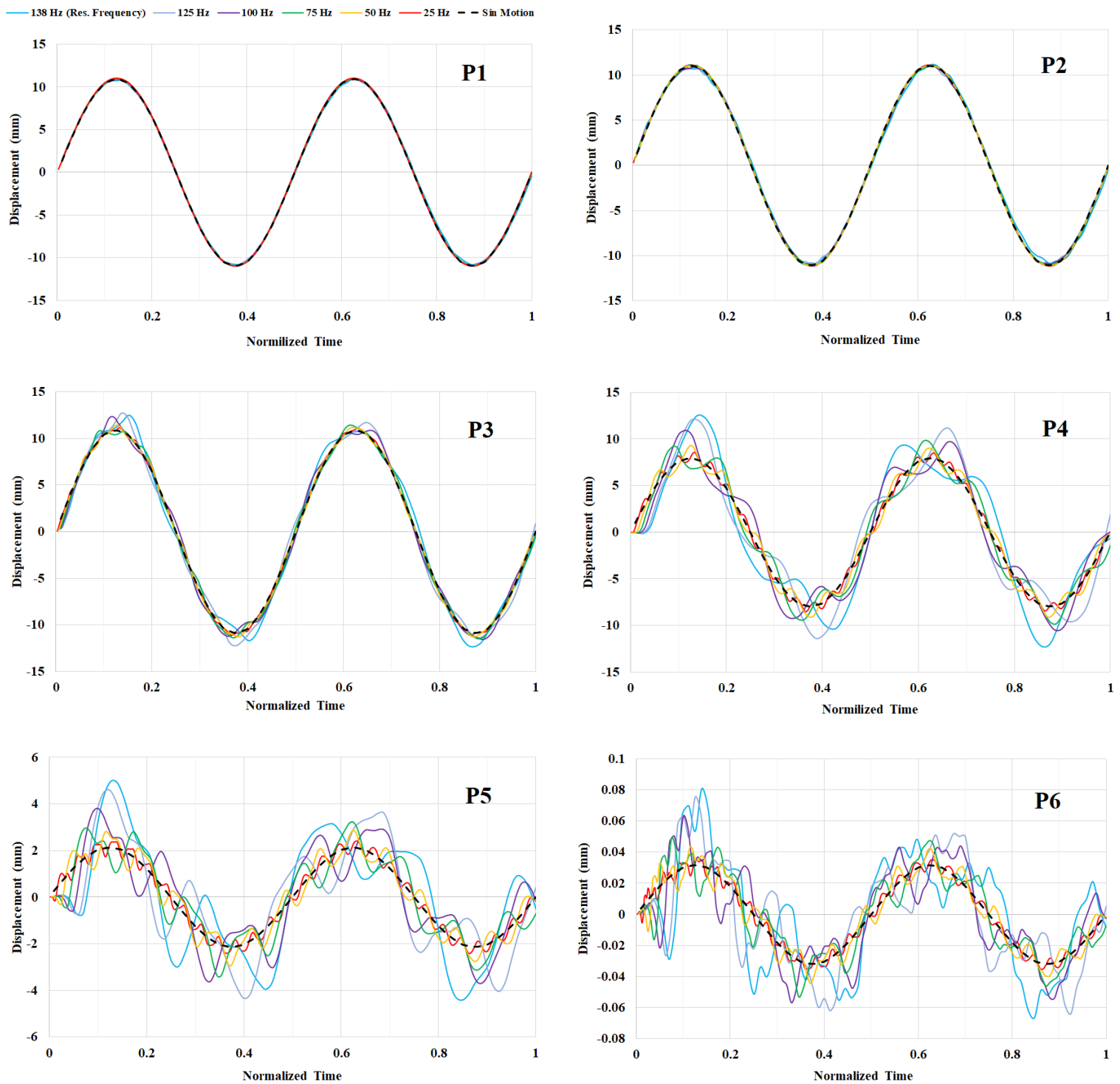


**Figure 92. Amplitude of displacement at different locations of a titanium flexure's arm.**

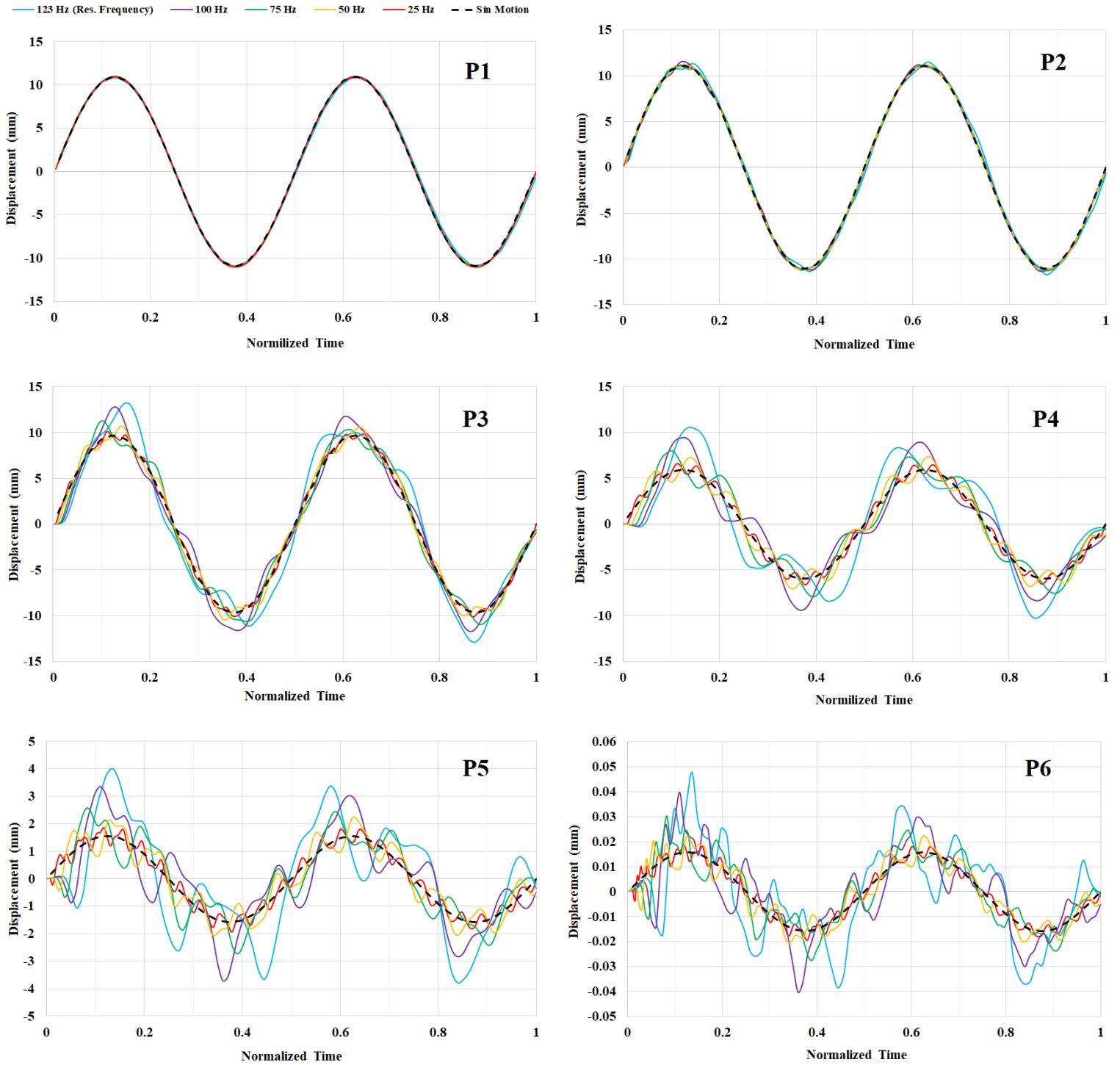


**Figure 93. Amplitude of displacement at different locations of a steel 'flexure's arm.**

In general, in mechanical mechanisms the vibration itself is not an energy loss, however, it is a phenomenon that boosts all of the loss mechanisms as mentioned at the beginning of this section. So, to have a quantified measure of the vibration, an energy approach was used to compare the PE

and KE energies of the flexure elements in dynamic conditions with different frequencies. Figure 94 and Figure 95 are the strain (potential) and kinetic energies of the whole flexure springs during two consecutive cycles for the titanium and steel flexure designs, respectively. Solid lines are the potential energy and dashed lines show the kinetic energy. In an ideal condition, both kinetic and potential energies must vary sinusoidally with a 90-degree phase difference. At the spring's neutral positions (0, 180, 360, 540, and 720 degrees), the kinetic energy is maximum and the potential energy is minimum, and vice versa at maximum displacement amplitudes (90, 270, 450, and 630 degrees). It was shown that the higher frequencies caused additional energies in the flexure body, both kinetic and potential.

For the potential or strain energy, generally, any added strain energy is not expected by an increased velocity. Compared to the static condition that the potential energy of a spring is calculated by  $PE = 1/2K(x-x_0)^2$ , the velocity should not influence the energy stored in the material at any location of the cycle. However, fluctuations from the sinusoidal variation of the strain energy is because of the vibration. The extra motion of the arms causes more strain at some locations which increase the potential energy that is not useful in the overall performance of the system. As mentioned in the discussions of the previous graphs, specifically the vibration of the P6, the additional strain energy increases the stress level and causes an unexpected fracture. The fluctuations of the strain energy was reduced at a frequency of 75 Hz and lower. At 25 Hz, the strain energy variation was very close to sinusoidal.

For the kinetic energy, an increase in the total energy of the flexure is expected to be influenced by the frequency. To generate Figure 94 and Figure 95, kinetic energy was calculated by  $KE = 1/2m_iV_i^2$  for all elements and the sum was reported for each time step. What was expected, however, was the linear variation of the total energy by frequency. In the figures, kinetic energy doesn't show a sinusoidal behavior. Also at the maximum stroke positions where the strain energy is maximum and kinetic energy should be zero, at higher frequencies, i.e. 138Hz and 125 Hz, there is a considerable magnitude of the kinetic energy. The increased kinetic energy due to the vibration of the arms increases the drag force losses, increases the sliding distance at the contacts between springs and spacers. Also, increased vibration of flexure arms could generate higher noise levels.



The additional kinetic and potential energy due to vibration are being converted to one another simultaneously. The extra strain energy at some locations leads to plastic deformation which is energy loss.

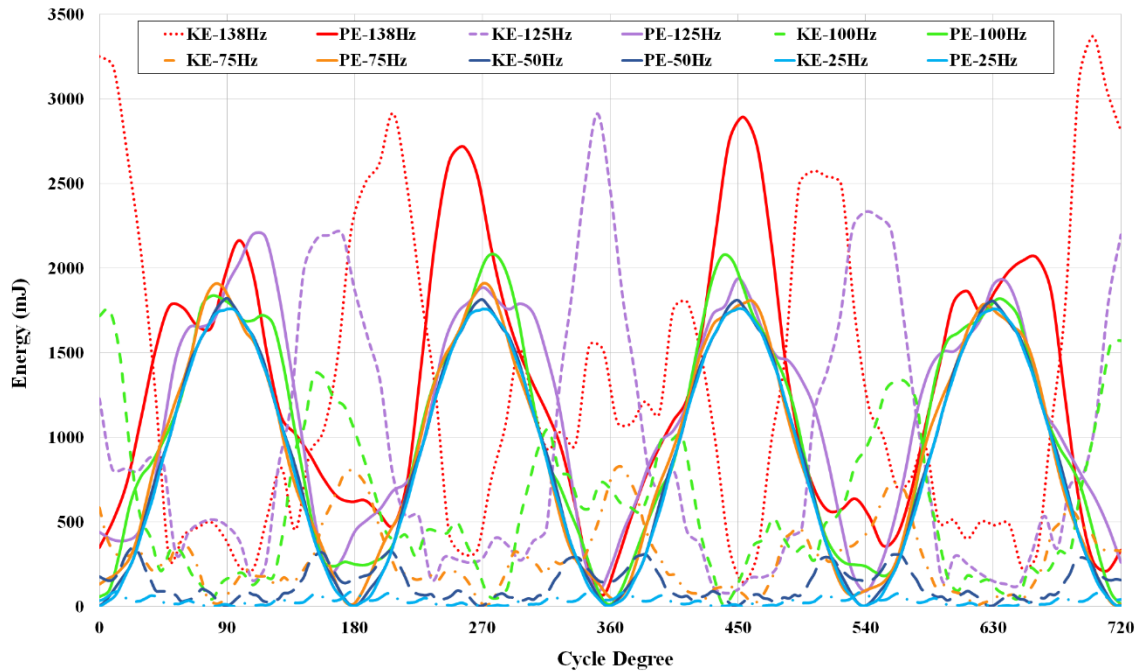


**Figure 94. Two-cycle conversion of potential energy (solid lines) and kinetic energy (dashed lines) - titanium flexure.**

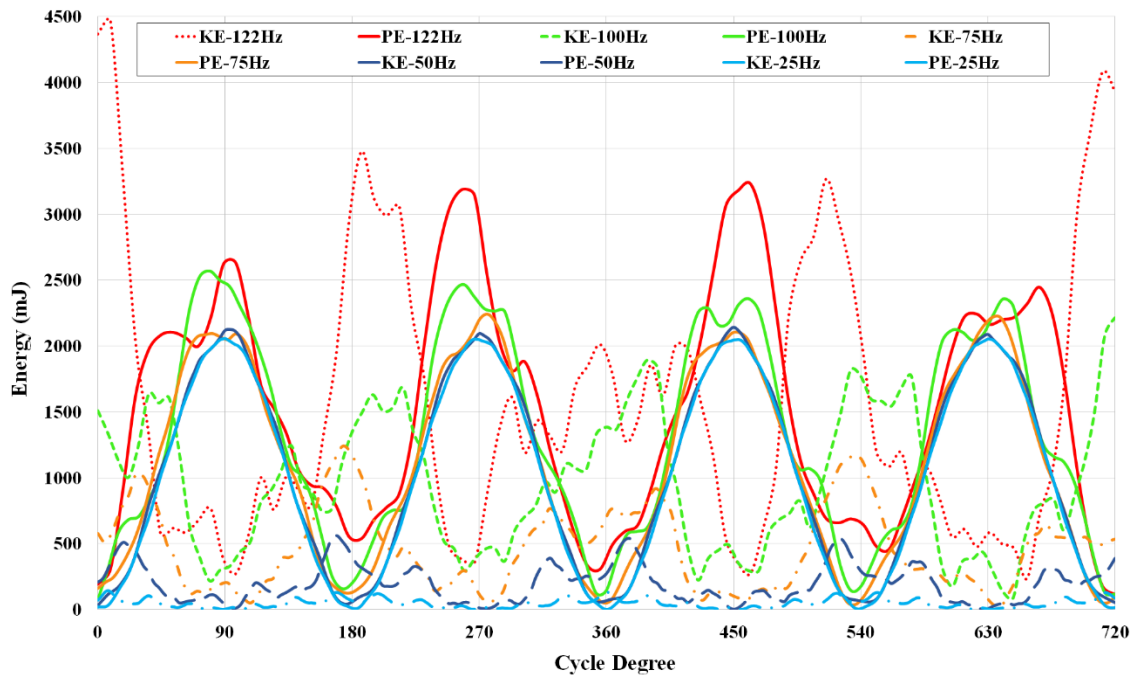


**Figure 95. Two-cycle conversion of potential energy (solid lines) and kinetic energy (dashed lines) - steel flexure.**

To calculate the change in the potential and kinetic energy of the flexures as a function of frequency, both PE and KE were integrated over five consecutive cycles for both titanium and steel material designs. The unit of the integrated parameters was mJ/Hz so the results for each frequency were multiplied to the corresponding frequency and then divided to the number of cycles to obtain the averaged mJ/cycle unit for PE and KE. The results are shown in Figure 96. As mentioned above, compared to ideal (static) condition, a fixed PE and constant slope (linear) KE lines versus frequency were expected. But the combination of higher modes of deformation and consequent vibration resulted in an increase in PE and non-linear change in PE curves. The increase in PE at higher speeds is harmful to the life of the flexure springs and increasing KE increases the energy loss and interferes with the cyclic energy balance of the machine. The PE or strain energy is directly related to the stress magnitudes of the flexure spring under loading. It can also be interpreted in this way that at higher machine frequency, more energy is stored in the springs that cannot be converted into useful work and is wasted via different loss mechanisms.

From 25 Hz up to the resonant frequency of the individual springs, the PE increase by around 50%. The consequent increase in the stress due to this excessive PE or strain energy was not uniform on the body of the spring and changed instantaneously due to combination of different modes of vibration. However, a slight increase in stress level at the regions with high stress such as the spiral end profiles could be deleterious and cause early fatigue. From the results of this study, it was concluded that a maximum safe operating speed range of a linear machine incorporating flexure springs was between 30-40% of the resonant frequency of a single flexure spring.

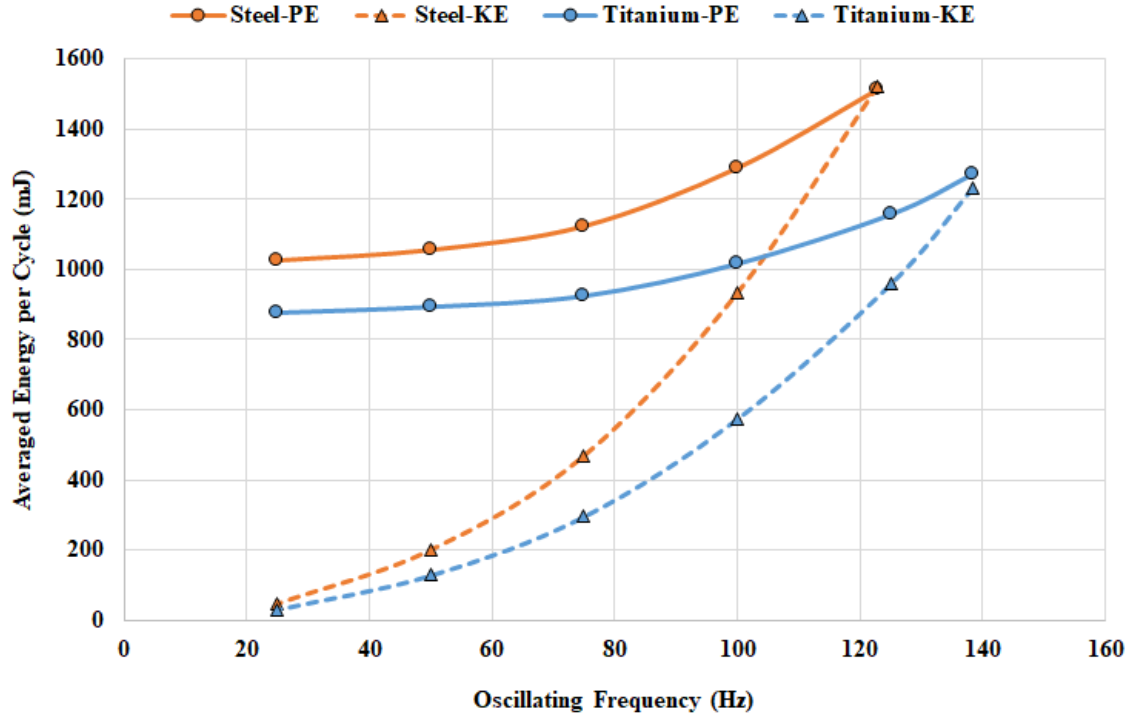
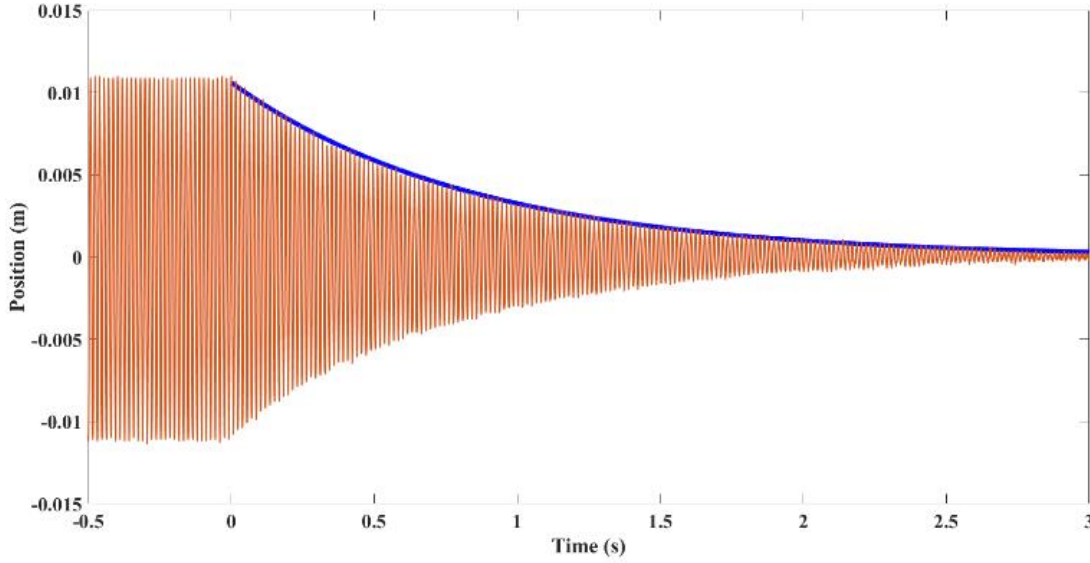


Figure 96. Averaged potential and kinetic energy-per-cycle for steel (blue) and titanium (orange).

## 5.4 Experimental Measurement

The mechanisms involving energy loss due to vibration can be found at both the microscale and macro scale. For the microscale level, higher fluctuations at high frequencies resulted in higher strain energy dissipation as heat, while for the macro scale, arm vibration generated sound waves that dissipated in the surrounding air [168], [169]. Also, vibration can increase the losses by increasing the sliding friction between contacting parts which is possibly the most significant energy loss mechanism in LEA flexures. To isolate the effects of the vibration on energy loss, a damping test was carried out in the vacuum chamber to mitigate windage and acoustic effects. The damping test is the same as the test for quantification of the windage losses except this time data was collected from transient shut-off cycles instead of steady-state operation. Figure 97 shows the damping of displacement of the assembly with six flexures at 22 mm stroke and 65 Hz. At  $t = 0$  s, the input power was switched off and the oscillations decayed until around  $t = 3.0$  s.



**Figure 97. Decay of displacement amplitude of oscillation.**

To find the decay of energy and damping factor an exponential curve was fitted above the damped curve. The fitted blue curve is shown in Figure 97. The equation of the exponential curve is:

$$x = 0.014124 e^{-1.181t} \quad \text{Equation 38}$$

where x is the peak position at each cycle. Compared to the motion of a damped harmonic oscillator as described in Equation 38 the damping ratio of the system can be found [166].

$$x = C e^{-\zeta \omega t} \sin(\sqrt{1 - \zeta^2} \omega t) \quad \text{Equation 39}$$

where C is a coefficient,  $\zeta$  is the damping ratio,  $\omega$  is natural frequency and t is time. The sine part in Equation 39 is equal to one because the data were picked at peaks. Comparing Equation 38 and Equation 39 the value of damping ratio can be found as  $\zeta=0.003$ .

The peak points are the location at the ends of oscillation cycles in which flexures store the maximum potential energy. The exponential equation of peaks position was used to find the decay of total energy of flexures based on the Equation 40.

$$PE = \frac{1}{2} K (x - x_0)^2 \quad \text{Equation 40}$$

where K is the total stiffness of the assembly for six flexures which was assumed a constant number. Using a derivative of energy over time the power loss was found during the decay period and is shown in Figure 98.

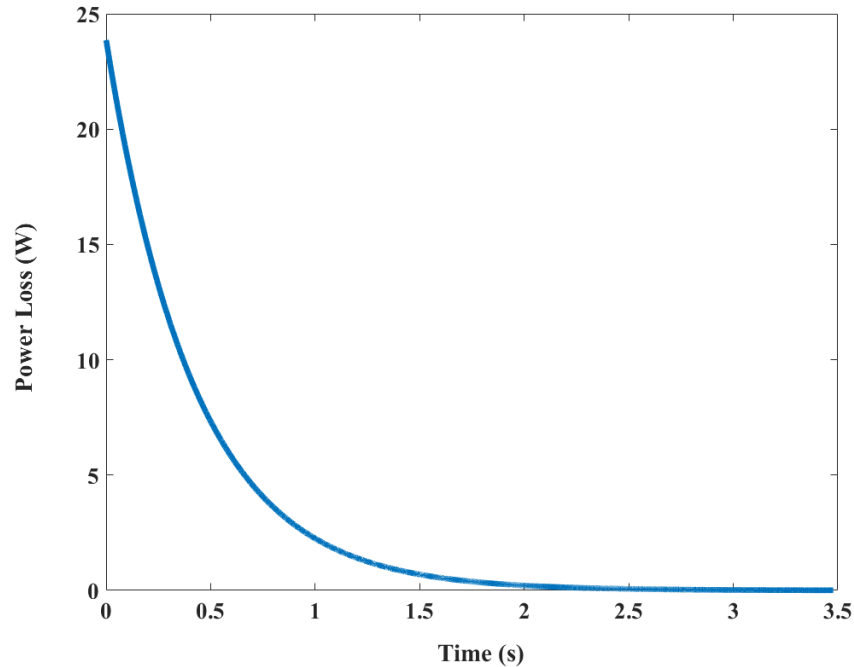


**Figure 98. Vibrational power loss of alternator vs. time.**

One reason for the reduction of the power loss by time under ambient conditions was the decreased amount of resistant drag force with the stroke length reduced which was directly proportional to the relative velocity (Figure 99). The other reason is the non-linearity of the stiffness and moving mass of the springs with displacement which will change the dynamic response of the system [170]. The first portion of the graph – between  $t = 0.0$  s and  $t = 0.2$  s - is nearly linear and indicates that the power loss changes directly with stroke length. The variation of the power loss with stroke length is shown in Figure 99. At  $t = 0.0$  s, there is 24 Watts of energy loss which is equal to the losses at steady state operation of the alternator with 22 mm stroke at 65 Hz. At steady state, the total input energy from power supply was measured 70-75 Watts. Thus, 32% of the total input power is considered as mechanical losses mainly due to the vibration.

The same procedure was implemented to quantify the effects of the LEA machine total stiffness (number of springs) and the frequency, under ambient and vacuum conditions. Figure 100 shows the results of the frequency for 2, 4, and 6 springs in the assembly. It is shown that under both ambient and vacuum conditions the frequency was increased, which was not linear as expected, because the constant moving mass of parts such as shaft and translator. The ambient pressure and the air resistive drag force caused a slight increase in the resonant frequency, about 0.25%.

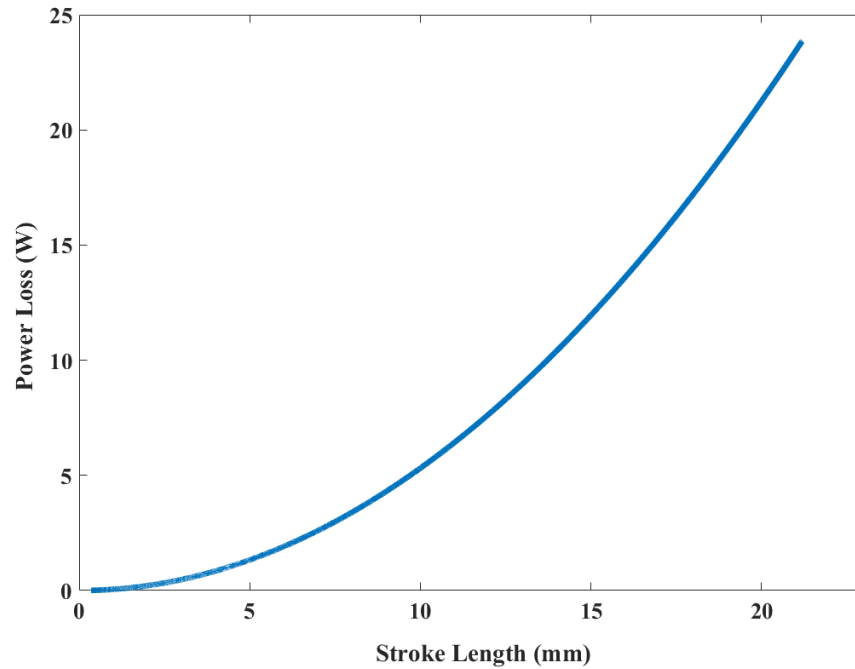


**Figure 99. Vibrational power loss of alternator vs. stroke length.**

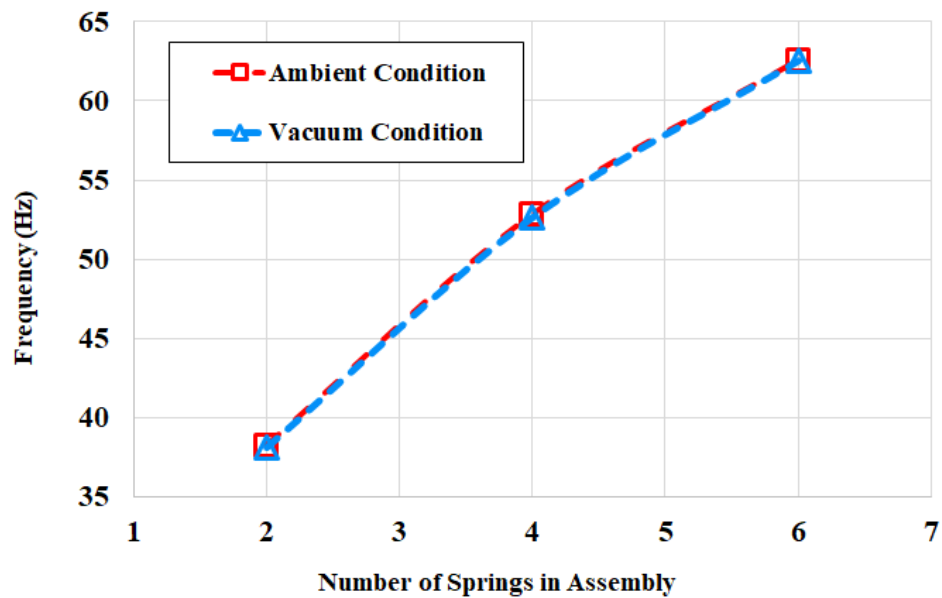


**Figure 100. Resonant frequency vs. number of flexure springs.**

The damping of the system was calculated from the damping tests and results are shown in Figure 101. The ambient pressure resulted in increase in the damping ratio of the system by an average value of 11.3%. The non-linearity of the damping ratio is because of natural frequency of the machine, when the damping tests were performed.

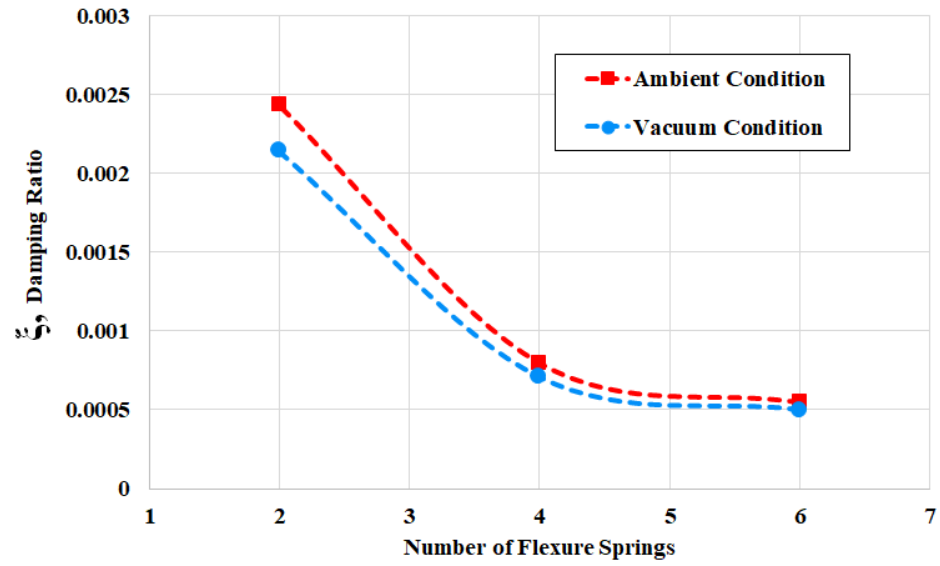


**Figure 101. Damping ratio vs. number of flexure springs.**

## **6 The LEA Assembly Dynamic Analysis**

Flexure springs are the core of the suspension system of the LEA and their performance dominates the overall operation of the assembly. The resonant frequency of the LEA, the oscillation's wave shape, and the efficiency of the alternator are all among the parameters that directly depend on the flexure springs. A flexure's performance highly depends on the assembly characteristics and the BCs. After the design and optimization of the flexure springs, it is important to examine the performance of the whole LEA system to analyze the effect of the flexure springs on the assembly and vice versa.

The main force input of the system is from the engine at compression and expansion strokes. In addition, the forces from the alternator assembly have significant effects on the alternator, specifically when the alternator is electrically loaded. Even in the absence of the loadings, the permanent magnets generate magnetic resistive forces that vary by the movement of the translator. The combination of the forces will influence the system dynamics. To study the effects of the assembly's mass, stiffness, and damping on the dynamics of the system, two types of studies were completed. The modal analysis was completed to study the first few resonating modes of deformations and their associated frequencies. The second study included a series of harmonic analyses to consider the effects of excitations from the load sources.

### **6.1 Test Setup**

To compare the results of the FEA modal and harmonic analyses and also to obtain the coefficients of the damping of the pack of flexure springs in the LEA machine and the frame through different mounting strategies, a series of experiments were performed. Figure 102 shows the test setup. In the right picture, the LEA machine is located on an aluminum plate with two position sensors to monitor the frame's vibration. The position sensors were oriented in axial and lateral directions. The aluminum plate was attached to a fixed table through four shear mounts. Figure 103 shows the different shear mounts. The blue one is more flexible and the black mount is stiffer. According to the datasheet, the stiffness for the blue and black mounts is 56.9 and 175.1 kN/m, respectively. The same tests were performed with the blue and black shear mounts to investigate the effects of the mounting strategies on the dynamic behavior of the LEA machine and also to extract the



damping coefficients needed for the FEA. In the left picture of Figure 102, other equipment for running the LEA machine and data acquisition is shown. The descriptions are provided in the caption.

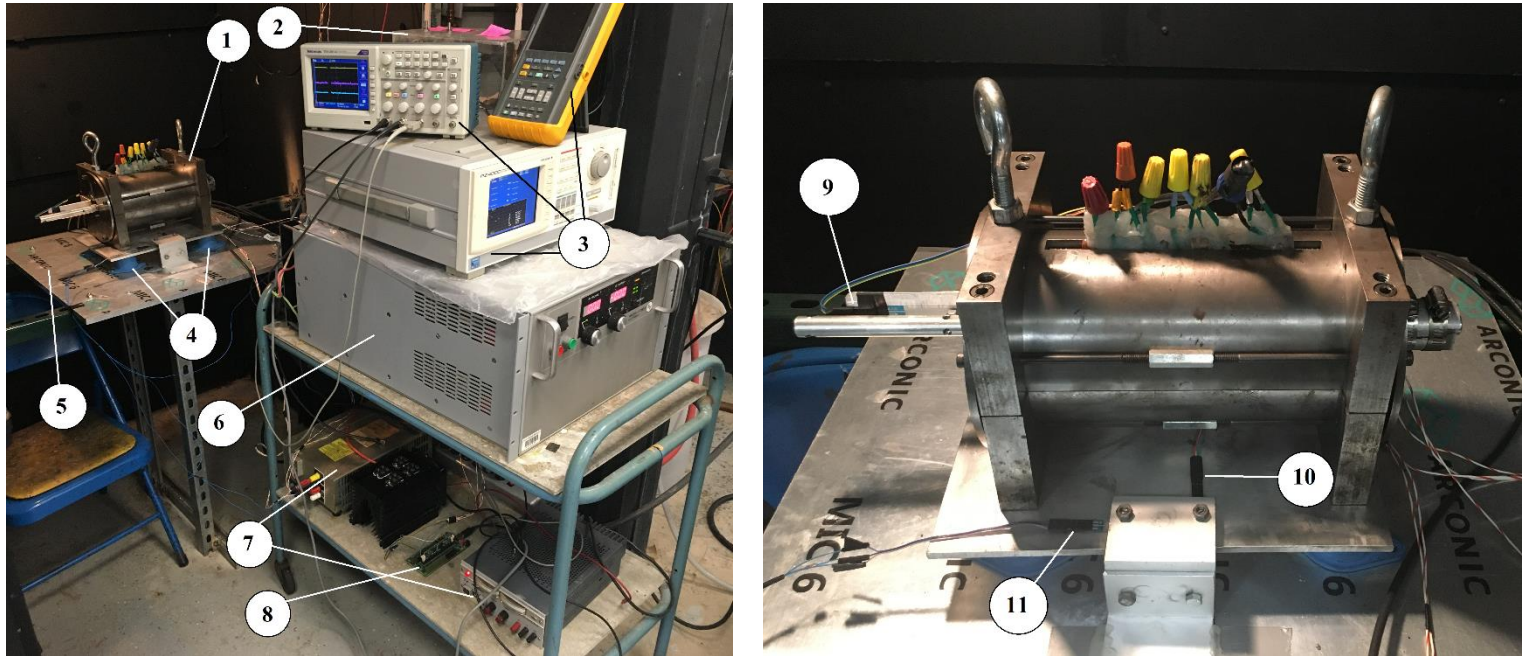


**Figure 102. Damping test setup: 1-LEA machine, 2-signal changing knobs, 3-scopes/power analyzer, 4-shock absorbers, 5-fixed table, 6-high-voltage power supply, 7-low-voltage power supplies, 8-microcontroller, 9-translator linear position sensor, 10-frame lateral position sensor, 11-frame linear position sensor.**

The tests were conducted primarily for validating FEA results. In this regard, different tests with 8, 6, and 4 springs were performed. Two spring packs with an equal number of springs were incorporated in the assembly. For each number of flexure springs, a dumping test was performed and the decay of the displacement amplitudes was recorded to calculate the damping ratio. This damping ratio is the combination of all damping mechanisms as mentioned before. What is needed for the FEA is the damping ratio for the two mass-spring systems, the translator, and the frame.



**Figure 103. Two types of shear mounts.**

Figure 104, is an example of a damping test with 8 flexure springs fixed on first, blue shear mounts (top picture), and second, black shear mounts (bottom picture). From the pictures, the oscillations were dampened faster when using the black shear mounts. In damping tests with translator's oscillation of 10 mm, it took about 2.5 s for the black mounted frame, and about 1 s, for the blue mounted frame to damp all of the frame's vibration. The amplitude of low frequency vibration of the frame also was higher in the first test. In the red curve, there are two different frequency modes. The higher frequency mode is the same as the translator's frequency and the lower frequency mode is the damping characteristics of the frame. In the second test with the black mounts, the lower frequency mode is less clear than the test with blue mounts. However, the amplitude of vibration at a higher frequency is higher in the second test compared to the first test. This is important as it was discussed in the analysis of vibration of a single flexure spring, the reverse direction of the force and displacement causes the loss of energy. So, in this case, the black mounts had a higher rate of energy dissipation, and hence, it lost more energy of the system.

A detailed view of the first 0.1 s is shown in the right corner of pictures in Figure 104. In both cases, it can be seen that the high frequency vibration of the frame and oscillations of the translator had 180 degree phase difference.

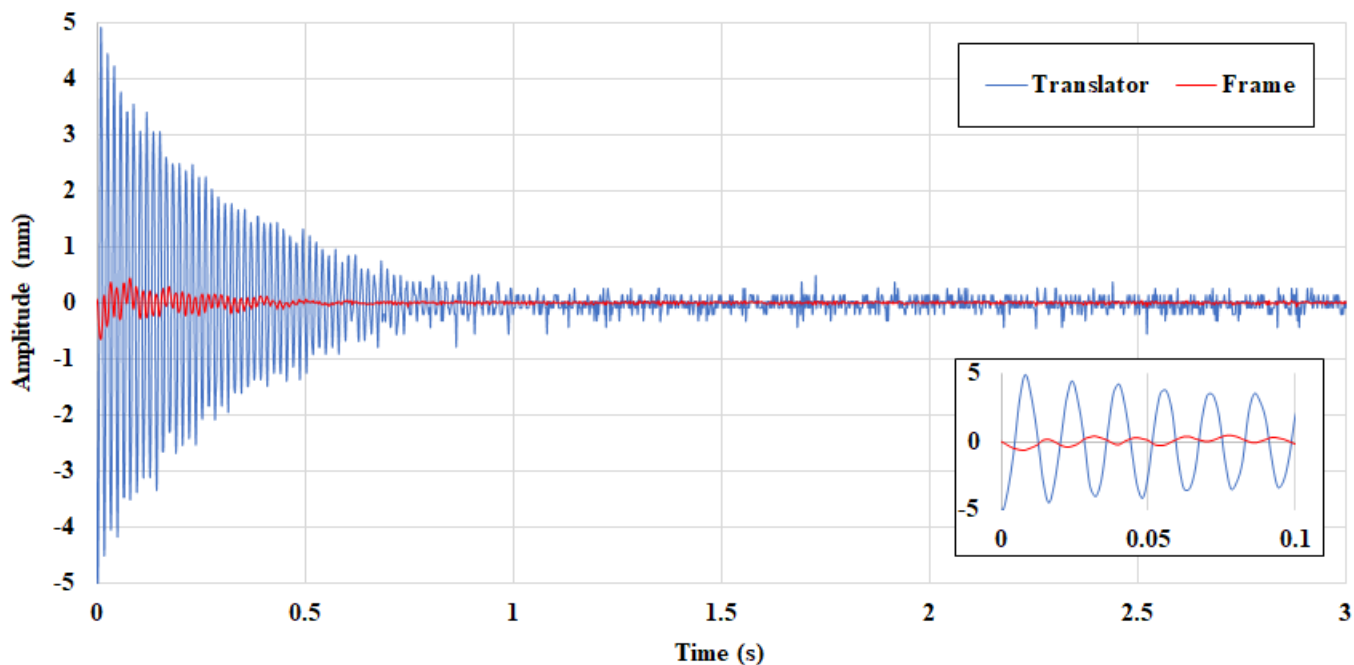
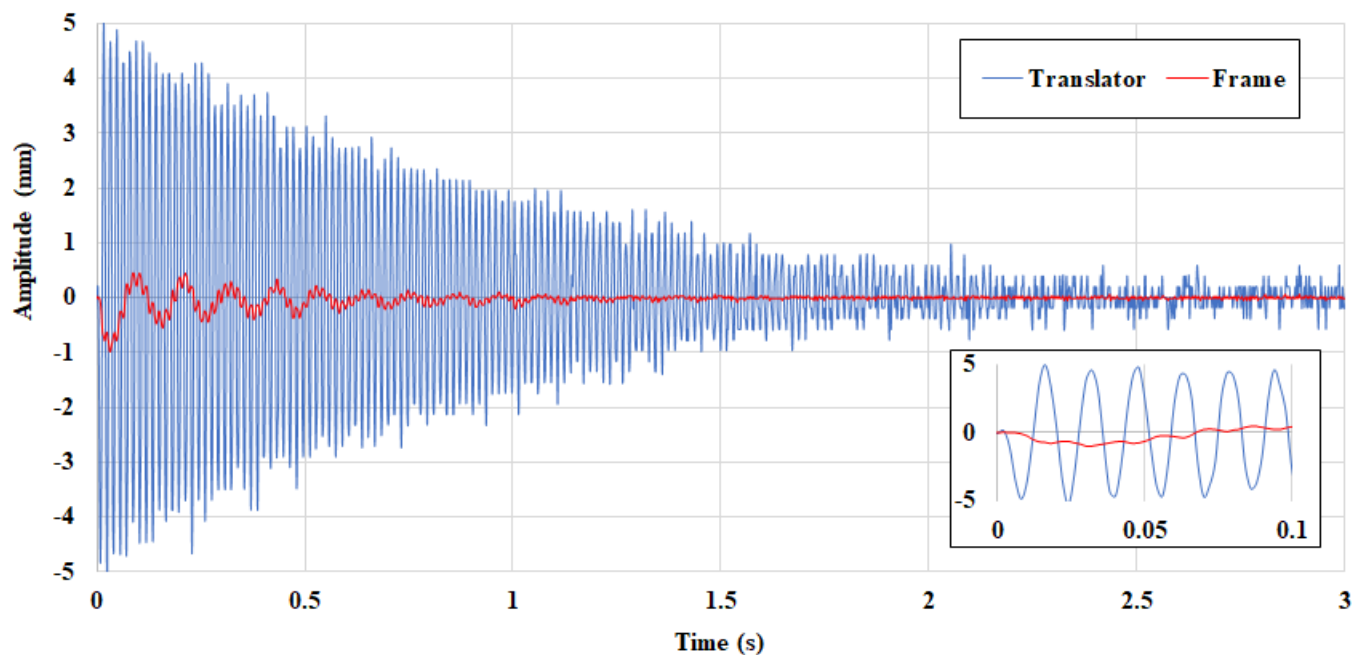


Figure 104. Translator vs frame vibration, top: 8 springs, blue mount, bottom: 8 springs, black mount.

## 6.2 System Damping and Stiffness

To calculate the frequency of the translator's oscillations and also the damping coefficients of the shear mounts, a Fast Fourier Transform (FFT) was used. Figure 106 and Figure 107 are the FFT

graphs. On the left side, the peak value is the translator's frequency, and on the right side, multiple peaks show the different modes of vibration. The highest frequency was the same as the translator's frequency, and the lowest number was low frequency damped vibration that was discussed earlier. In all repeated damping tests, there were another peak in the FFT graphs that had lower spectral density than the more obvious mode in Figure 104 red curves. This will be discussed in more detail in the following sections where FEA results are being compared.

To extract the damping coefficients from Figure 104, the same procedure in section 5.4 was used to first, find the damping ratio  $\xi$ . To be used in FEA, depending on the application, then the damping ratio can be converted into  $\alpha$  (mass) or  $\beta$  (stiffness) damping coefficients using the below equation.

$$\xi = \frac{\alpha}{2\omega} + \frac{\beta\omega}{2} \quad \text{Equation 41}$$

where  $\omega$  is the resonant frequency in rad/s. In real conditions, the damping ratio consists of both mass ( $\alpha$ ) and stiffness ( $\beta$ ) damping ratio. Defining the contribution of each of these damping coefficients in a system needs detailed experimental tests. In many cases, a common practice is to consider only one of the two terms on the right hand side of Equation 41 and convert the damping ratio in either of mass or stiffness damping coefficients. From experience of different FEA models, it was found that using the stiffness damping coefficients achieved better results in terms of predicting the experiments and numerical solution convergence. Figure 105 shows all three damping properties. As can be seen the damping of the frame decrease by the number of flexures in the LEA machine. The blue shear mounts showed lower damping coefficients than the black mounts for both frame and translator.

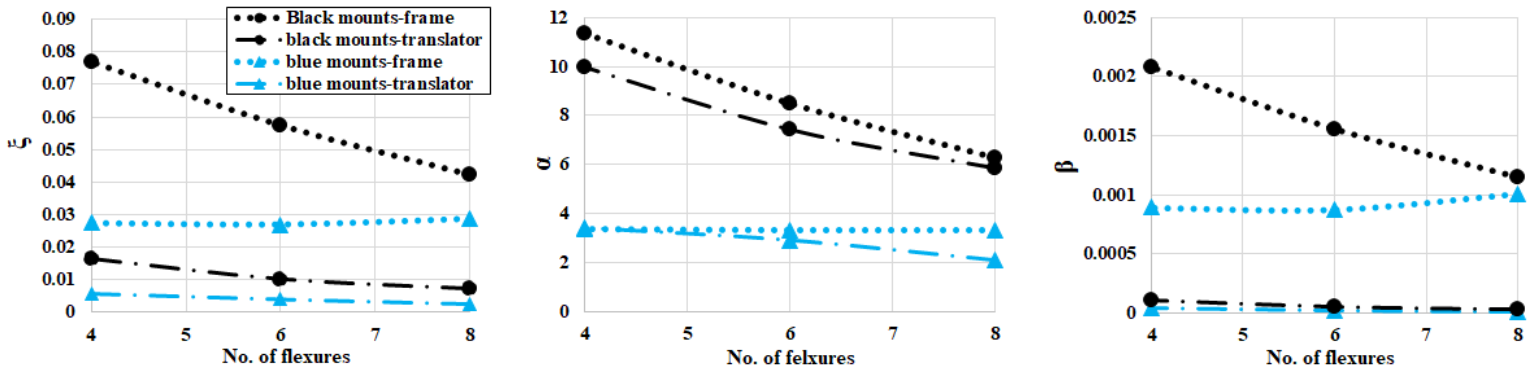
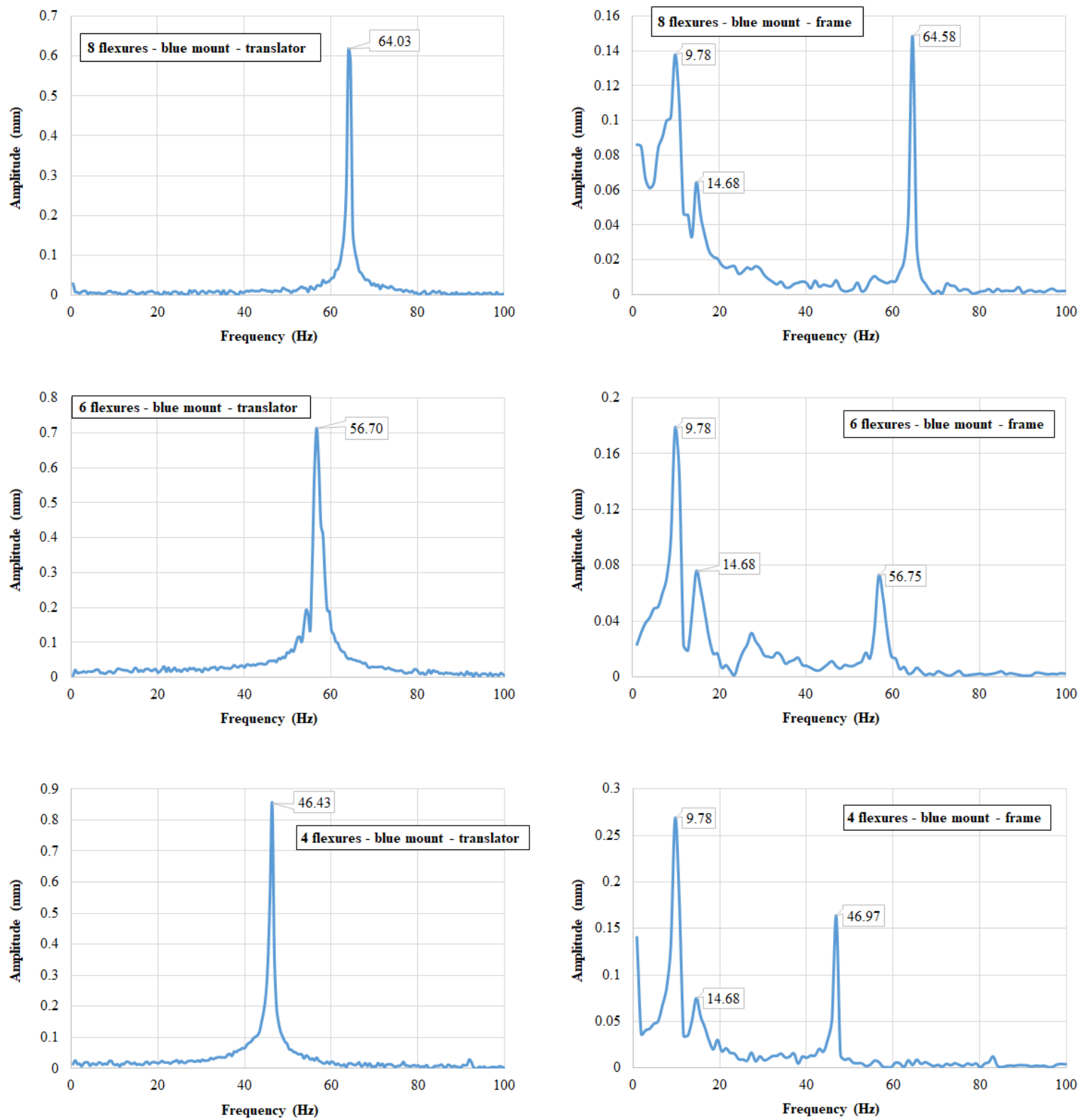
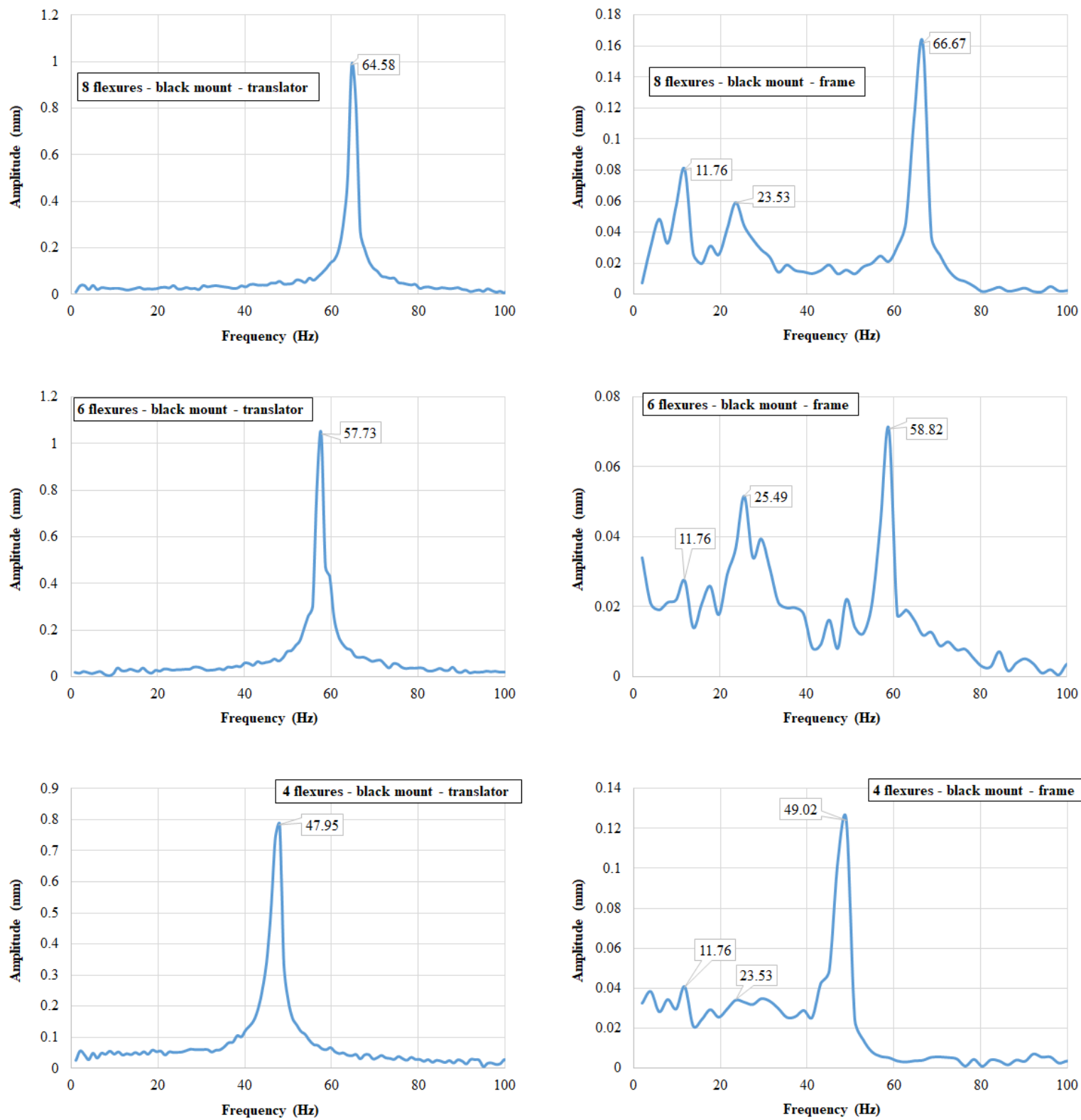


Figure 105. LEA damping characteristics, left: damping ratio, middle: mass damping ratio ( $\alpha$ ), right: stiffness damping ratio ( $\beta$ ).



**Figure 106. FFT Graphs of LEA with blue shear mounts vs. number of springs, left: translator oscillations, right: frame vibration.**



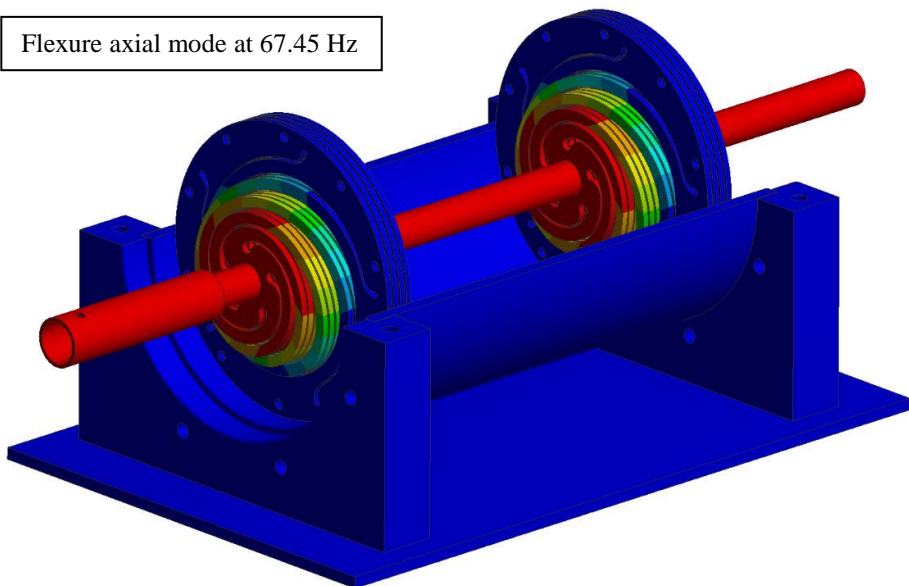
**Figure 107. FFT Graphs of LEA with black shear mounts vs. number of springs, left: translator oscillations, right: frame vibration.**

### 6.3 Modal Analysis

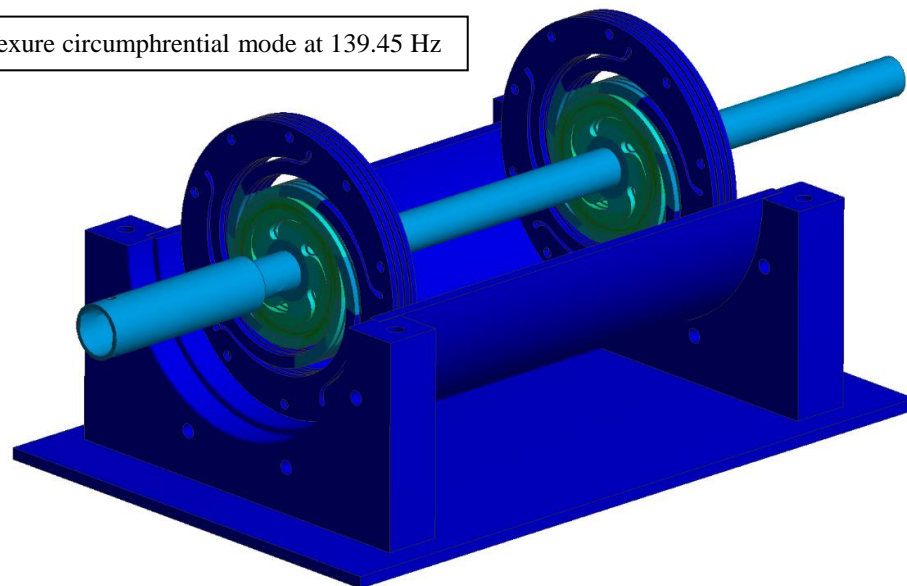
To perform an analysis of the whole LEA assembly, a modal analysis was first conducted in FEA. Modal analysis provides information on the modes of deformations, especially the first couple of modes, their deformation shapes, and their frequencies. Some of the deformation modes were desired and the machine was expected to operate with those modes; however, many other modes were unwanted and deleterious to the machine's performance. If the frequency of the unwanted modes is low, or close to the frequency of the excitation loads, the amplitude of vibration increases and will result in energy loss, noise, and mechanical failure. In the modal analysis, the first mode is the axial movement of the frame. In this section, only the mode shape of the LEA machine due to flexure springs' stiffness was considered and the effects of the mounting strategies and frame vibration will be mentioned in the next section. Different numbers of the flexure springs from two to eight were studied. Figure 108 shows modes 2-6 deformations from the lowest on top left to the highest on bottom right. Modes four and five are identical which are the radial deformation of the flexures. For this flexure design, the order of deformations mode is axial deformation of flexures, circumferential (twist) deformation of the flexures, radial deformation of flexures, and the tilting deformation of the rod. The order of these modes depended on the flexure design. For example, a change in dimensions of the arms or the number of arms may result in the circumferential deformation mode occurring after the radial deformation. Depending on the number of arms, some of the modes are repetitive, which in this case for the flexures with 4 arms, modes 4 and 5 are the same and only the direction of the deformation is different. Mode 6 is also the combination of the radial deformation of the spring packs on each side of the LEA. When the radial deformation of the left and right packs are in the same directions, the rod has a translational displacement. But when the radial deformation happens in a different direction at each side, it results in the planar rotation of the rod.



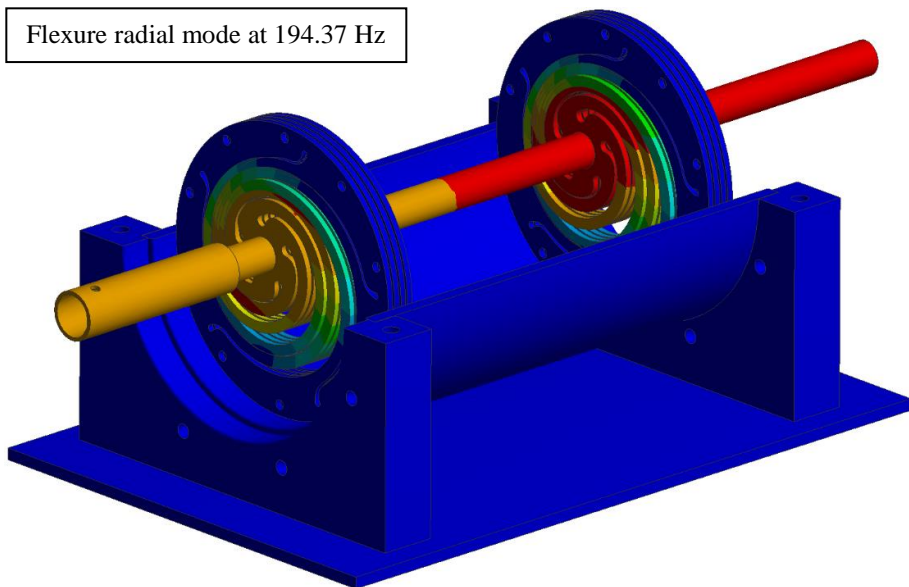
Flexure axial mode at 67.45 Hz



Flexure circumphrential mode at 139.45 Hz



Flexure radial mode at 194.37 Hz



Rod tilting mode at 218.50 Hz

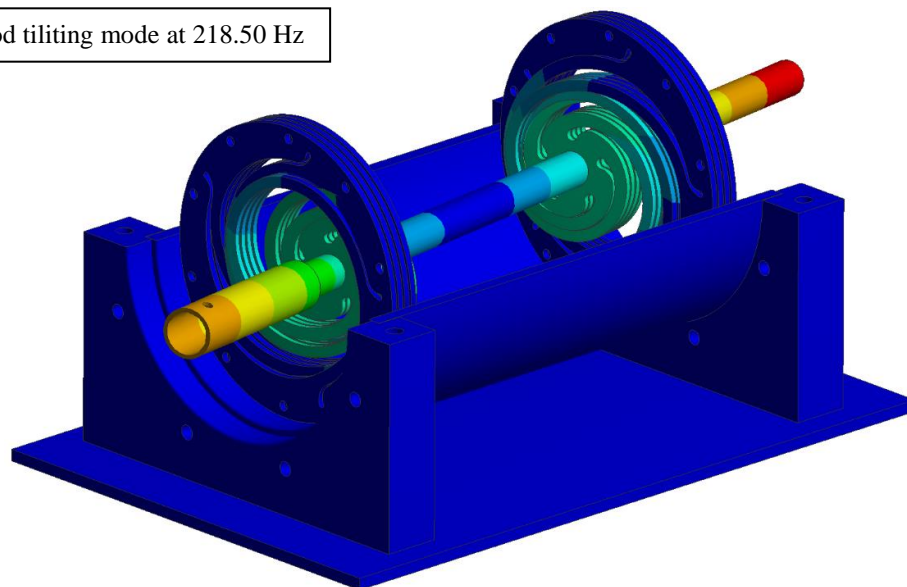
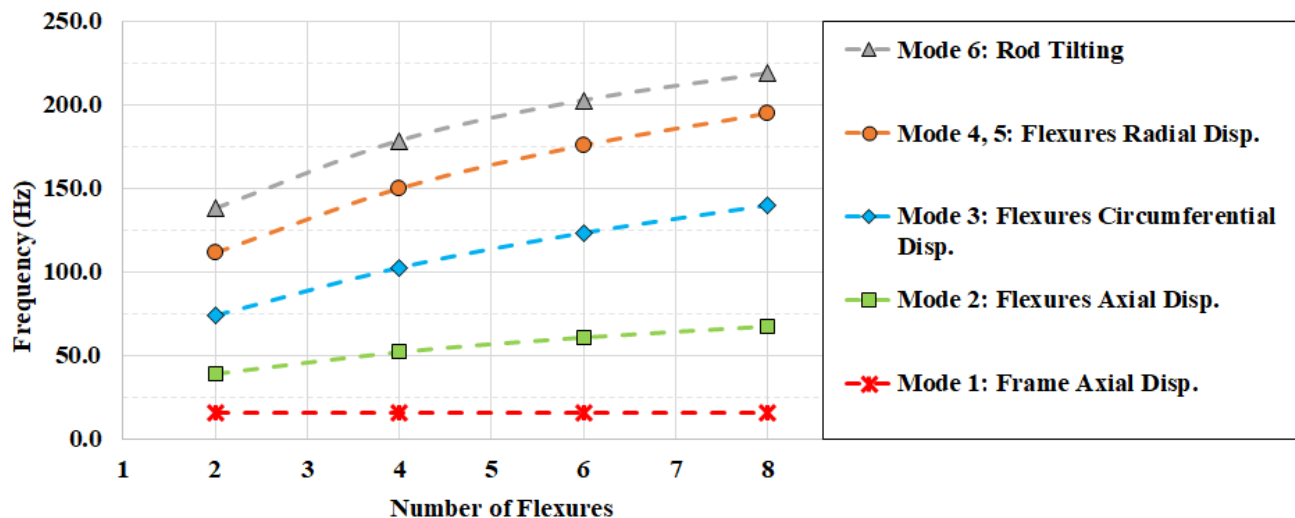


Figure 108. LEA machine resonating mode shapes.



The frequency of these four modes was calculated for an LEA with a different number of flexure springs to find the effects of the number of springs on each mode. The results are shown in Figure 109. As can be seen, the number of flexures doesn't illustrate any influence on the frame's vibration. The frame's displacement is a factor of the shear mounts stiffness and the total weight of the assembly. In fact, the weight of the assembly does change by reducing the number of springs; however, its effects were found negligible on the frame's vibration. The other four types of deformations directly depend on the flexures' stiffness in different directions. In all cases, the mass of the fixed moving mass of the magnets and rod is the reason that the relationship is not fully linear. The order of the non-linearity on the second mode, the flexures' axial displacement, is higher which is because of the variable moving mass of the flexures.



**Figure 109. Damping ratio vs. number of flexure springs.**

In the next step, the effects of the stiffness of the shear mount were considered. The deformation frequencies for both black and blue shear mounts are provided in Table 12. The first row is different mode shapes and their description and the second row shows the shear mount selection for each mode. Other than the first mode, which is the obvious results of the frame stiffness, its effect on the second mode were marginal and there was no influence on the other higher modes.

**Table 12. LEA's deformation modes resonant frequencies (Hz).**

Mode	Mode 1: Frame Axial Disp.		Mode 2: Flexure Axial Disp.		Mode 3: Flexure Circumferential Disp.		Mode 4, 5: Flexure Radial Disp.		Mode 6: Rod Tilting	
Flexure	Blue	Black	Blue	Black	Blue	Black	Blue	Black	Blue	Black
<b>2</b>	15.6	26.8	38.7	39.4	74.1	74.1	111.0	111.0	137.7	137.7
<b>4</b>	15.5	26.9	51.9	52.3	102.6	102.6	149.6	149.6	178.3	178.3
<b>6</b>	15.4	26.8	60.8	61.2	123.1	123.1	175.3	175.3	202.4	202.4
<b>8</b>	15.2	26.6	67.5	67.8	139.5	139.5	194.4	194.4	218.5	218.5

The effects of the shear mounts were compared with the experimental results. Tests were performed with 8, 6, and 4 springs. In Figure 110, the left picture is the translator's axial deformation (second mode), and the right picture is the frame's axial displacement. The blue and black lines are associated with the blue and black shear mounts, respectively. At first glance, it can be seen that the FEA over predicted the first (frame) and the second (translator) displacements. The error margin is less than 10% for the translator, almost the same order of magnitude for both of the shear mounts, and between 50-100% for the frame. The frequencies from experiments were extracted from the FFT charts. Looking at the FFT charts again, it can be seen that a frequency very close to the FEA results exist, however, they are not the most dominant frequencies at which the displacement waves were damped. Another possible explanation that has not been considered in the FEA that can cause such difference is the effects of the table which was assumed to be rigid. During the experiments, it was observed that the table also shakes, specifically with the black shear mounts. Designing a table is arbitrary and was not the focus of this research and calculating its stiffness and damping coefficients is very complex. So for this study, it was neglected in the FEA analysis. Another reason for such a difference could be the imperfection in the attachment of the shear mounts and the LEA machine. In the FEA model, the connections are considered ideal and all mounts act similarly in the same cyclic manner. However, in reality, any imperfection in dimensions and assembly of the mounts to the fixed table and the assembly frame will cause different stiffness and damping that the machine sense from. In the translator's frequency results, the connections were considered perfectly bonded for the sake of the computational cost and also non-linear modeling limitations. But again, in real conditions, there is friction between parts, specifically between flexures and spacers, which will damp the energy more, compared to the completely bonded surfaces.

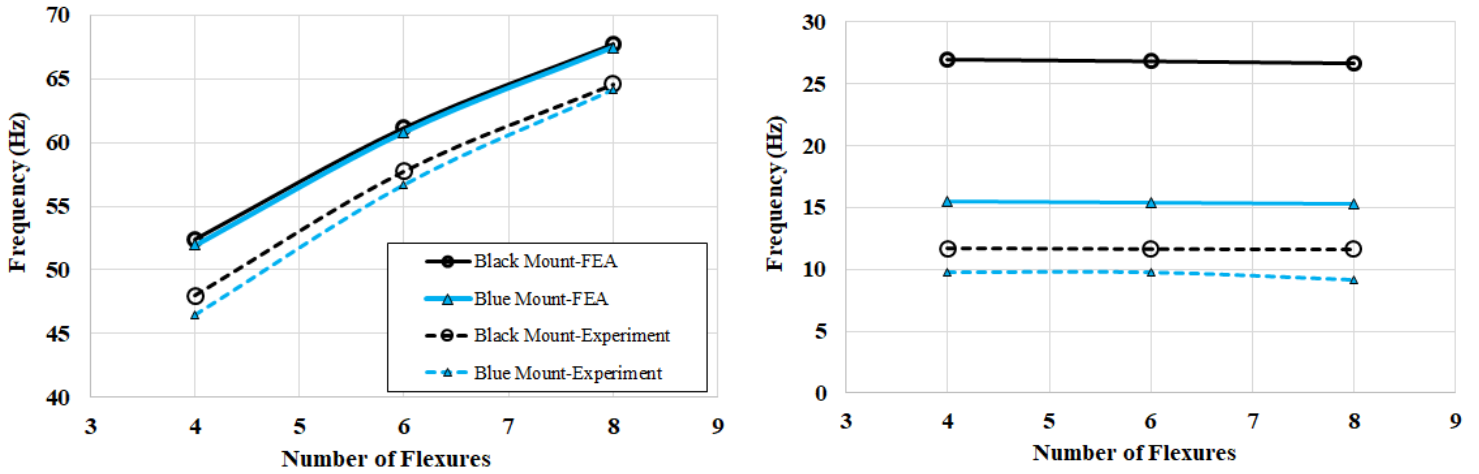


**Figure 110. Frequency vs. number of flexure springs, left: translator, right: frame.**

## 6.4 FEA Parametric Study

Using the experimental data of the stiffness and damping of both translator and the frame, a parametric study was performed to investigate the counter effects of each translator's and frame's dynamic parameters on the outputs. The study was performed on an LEA machine with four flexure springs and the variation of parameters including the translator's damping coefficients, frame's mass, stiffness, and damping coefficients. An FEA transient model was used for the analysis. To capture the high frequency oscillations of the translator, the time step should be small enough. At the same time, due to the relatively large scale of the problem size (about 2M nodes) and the consequent computational cost, larger time steps are desirable. For the LEA assembly parametric study, the effects of higher vibration modes of the flexure at time step size of  $2.5E-4$  s and smaller were neglected. Also, the frame was initially fixed and its vibrations was influenced by the translator's oscillations. For each case, the total simulation time was set to 1 s and the fixed time step was 0.001 s. Also, modifications were made to reduce the computational cost. Figure 111 shows the geometry of the LEA machine for the parametric study via transient analysis. The shear mounts were replaced by a coil spring element on each side of the LEA machine. Each of these spring elements represents two shear mounts. The stiffness of each of the spring elements was equal to twice the stiffness of each mount and its damping coefficient was the same. All parts in the assembly were changed to rigid except for the flexure springs and the rod which remained flexible. To account for more springs, the flexure's material properties (density and the elastic

modulus) were modified. As shown in the figure, only flexible parts were meshed and the number of nodes were reduced to slightly over 200,000 nodes. Also, only one flexure spring was considered on each side of the translator representing multiple number of flexures by scaling the modulus and density of the material.

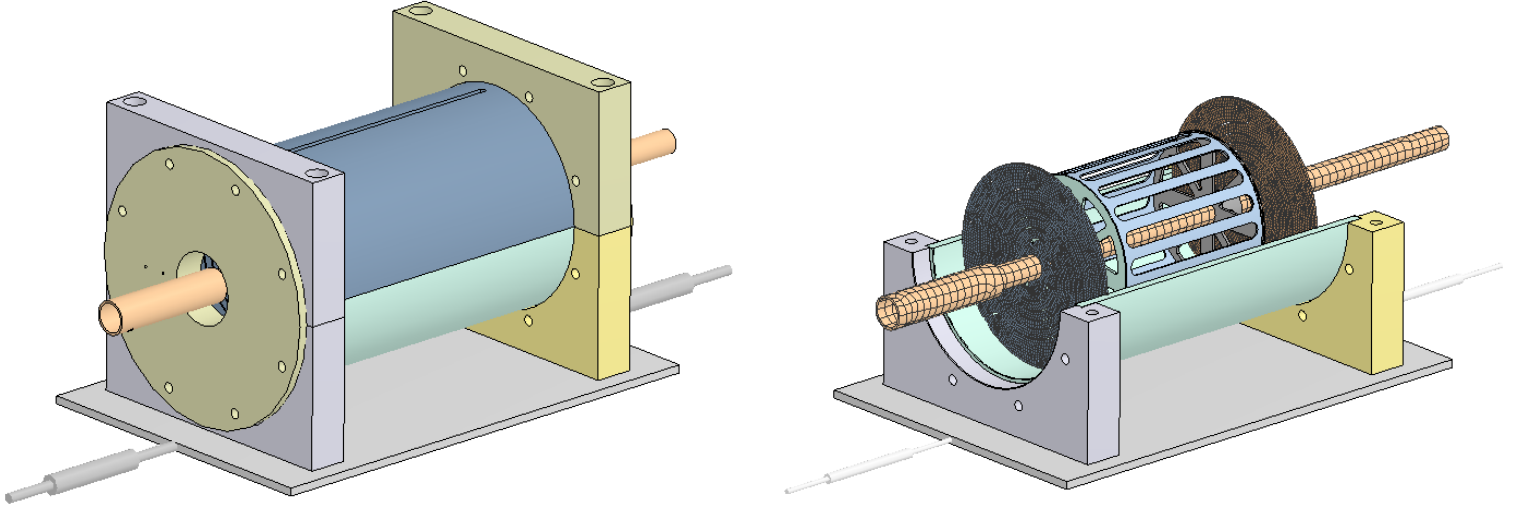


**Figure 111. Reduced geometry of LEA for the transient FEA analysis.**

For the FEA analysis, the damping coefficients can be used in different forms. For individual parts such as flexures, the damping can be input using the alpha or beta damping coefficients (see Figure 105). Using different forms showed improved results (numerical solution convergence) when the beta damping was used for the flexures. On the other hand, for the frame's spring elements the only way to consider the damping was to directly calculate the damping of the frame from the damping ratio. So by using the frame's  $\xi$  values for the corresponding shear mounts from Figure 105, the frame's spring damping coefficient,  $C_{frame}$ , can be calculated using the below formula.

$$\xi = \frac{C_{frame}}{C_{critical}} \quad \text{Equation 42}$$

where  $\xi$  is the damping ratio and  $C_{critical}$  is the critical damping of the shock absorber (spring element).  $C_{critical}$  is a material characteristic and can be calculated by using Equation 43.

$$C_{critical} = 2m\omega_n \quad \text{Equation 43}$$

where  $m$  is mass, and  $\omega_n$  is the natural frequency of the element. To calculate the natural frequency of the spring elements, springs (shear mounts) should not be considered as individual components. In fact, in Equation 43, the mass  $m$  is the portion of the LEA's mass that each of the springs is

attached to (12 kg) and the natural frequency is the frames low-frequency vibration (see Figure 110).

For each of the parameters three different values were considered: translator\_beta\_damping=[2E-5, 4E-5, 8E-5], frame\_mass=[24, 48, 96] kg, frame\_spring\_stiffness=[24, 48, 96] N/mm, and frame\_spring\_damping=[0.005, 0.01, 0.1] N.s/mm. The corresponding actual values for the LEA machine with four flexure spring was translator\_beta\_damping=4E-5 (with blue shear mounts), frame\_mass=24 kg, frame\_stiffness=96 N/mm (total stiffness with four blue shear mounts), and frame\_damping=0.04 N.s/mm (total damping with four blue shear mounts).

#### **6.4.1 Translator and Frame Damping**

In the first step, the effects of the translator (flexure) and frame damping were considered. The results of a different combination of these two parameters according to the values mentioned in the previous section are shown in Figure 112. It should be noted that the damping coefficients used were the cumulative value that accounts for all of the damping phenomena such as the different friction, drag, and material. In Figure 112, the frame's mass was 24 kg, and the frame's stiffness (each spring element) was 48 N/mm.

The translator and frame damping coefficients had a direct influence on the decay of the oscillation's amplitude of the translator and frame, respectively. Increasing the frame damping under fixed translator damping (pictures in rows from left to right), slightly decrease the translator's amplitude reduction. Also, as expected, the increase in translator damping reduced the high-frequency vibration of the frame (pictures in columns from top to bottom). Also, the frame damping had no effects on the damping of the high-frequency vibration of the frame.

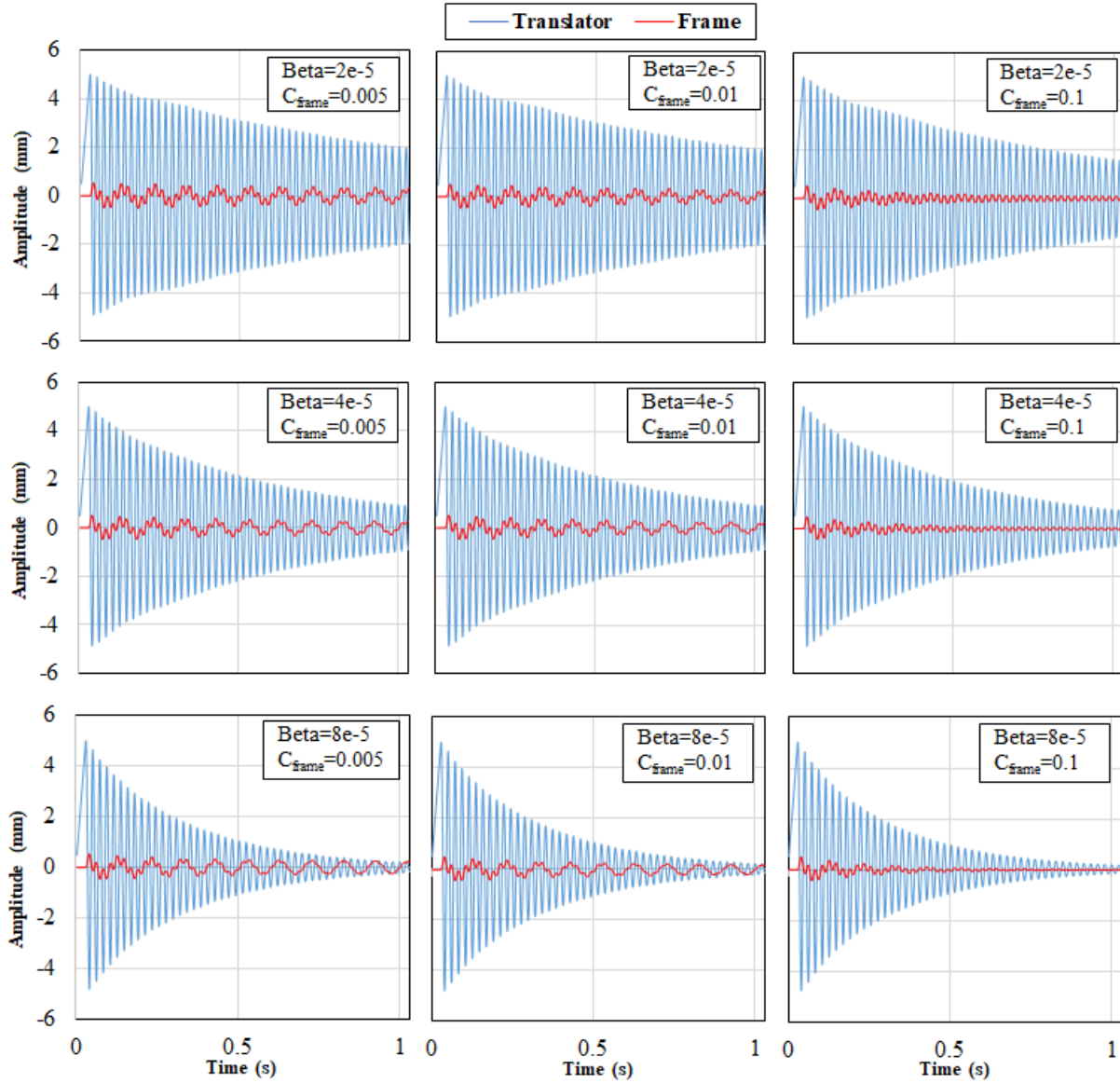


**Figure 112. Effects of translator and frame damping on the dynamic behavior of LEA.**

#### 6.4.2 Frame Stiffness

All of the nine cases shown in Figure 112 were repeated with three different frame stiffnesses. While using the blue shear mounts, the total frame stiffness was 96 N/mm, other scenarios where the total stiffness was 48 and 192 N/mm were also considered. Figure 113 shows the effects of the frame stiffness on the translator oscillations and frame vibration. In the results illustrated, the frame mass was 24 kg and the frame springs damping was 0.01 N.s/mm. As can be seen in the figure, the frame stiffness did not significantly influence the translator oscillations in terms of frequency and amplitude. Its effect on the frame vibration is important. There are two different modes of

frame vibration, a high-frequency mode – which is due to the translator’s oscillations – and a low-frequency vibration mode. Frame stiffness did not change the amplitude of the frame’s low-frequency vibration. However, as shown, the frequency of low-frequency vibration increased. On the other hand, the frame’s stiffness slightly changed the pattern of the high-frequency vibration of the frame. At lower stiffness values, the amplitude of the high-frequency vibration was higher and more uniform in time. Increasing the frame’s stiffness slightly reduced the amplitude of a portion of the high-frequency vibration. The higher non-uniformity in the vibration’s amplitude causes non-zero mean stress value that results in a higher risk of fatigue failure of the grounding mounts. Also, it should be noted that the damping and energy loss due to the shear mounts has a relationship with velocity. A higher frequency of the frame’s vibration could potentially increase the energy loss at the frame’s attachments to the ground. So, from the results of this study, ground attachments with lower stiffness are desirable.

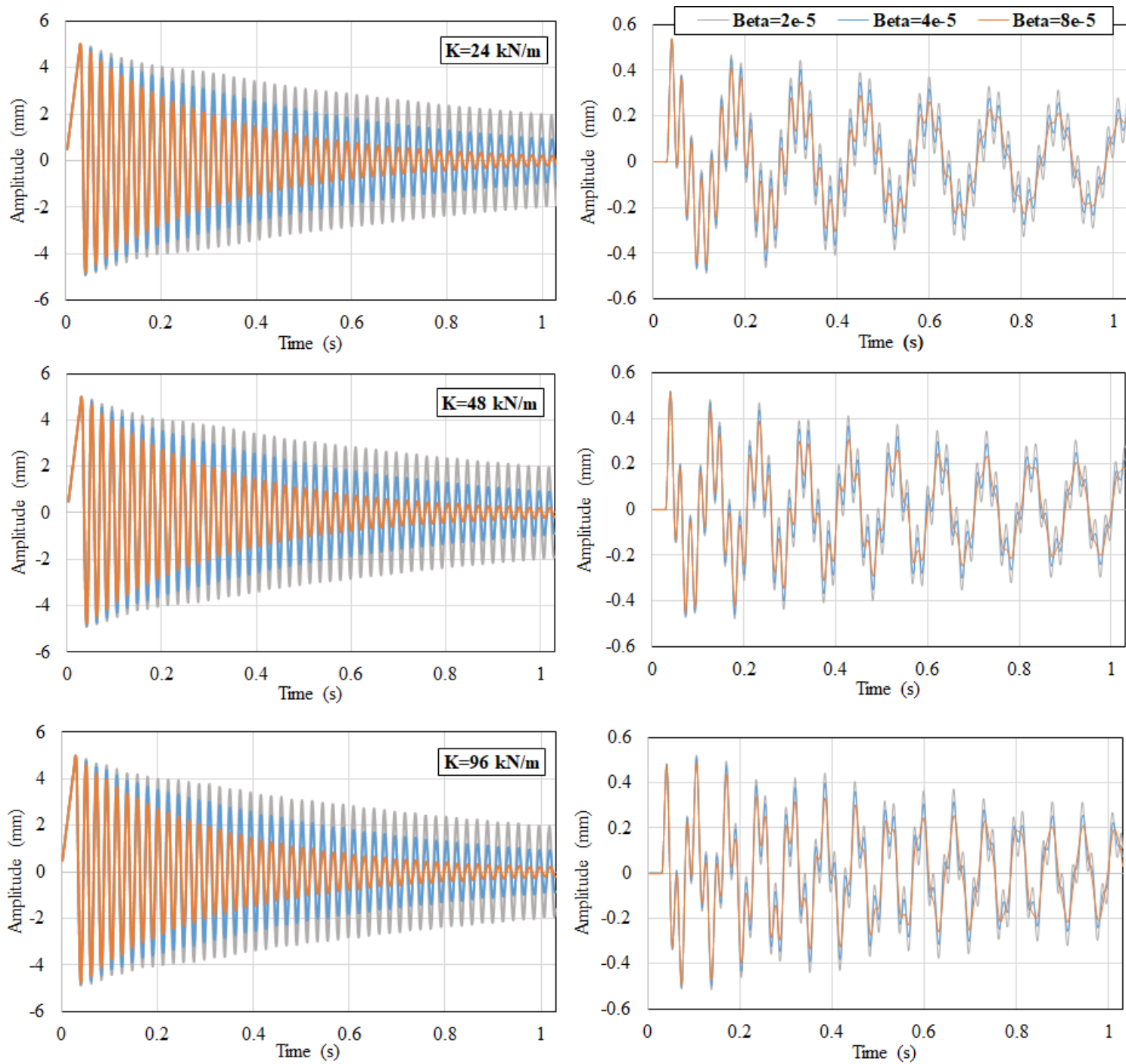


**Figure 113. Effects of frame stiffness on the dynamic behavior of LEA.**



### 6.4.3 Frame Mass

In the last step, the effects of the frame's mass (total assembly mass) were considered. In the modeling, the total mass was varied with different frame damping values while the translator damping (beta coefficient =  $4E-5$ ) and the frame stiffness ( $K_{\text{spring}}=48$  N/mm) were fixed. The effects of the frame mass on the translator were very low with a very slight decrease (less than 1 Hz) in the translator's frequency with an increase in the frame mass from 23 kg (actual value) to 96 kg. This artificially added mass was considered non-moving. The translator's amplitude of oscillations did not change with the frame mass. Figure 114 shows the frame vibration. As can be seen, the amplitude of low-frequency vibration of the frame reduced by an increased mass of about 30% reduction. Also, the amplitude of the high-frequency vibration reduced by an average of around 50%. As expected, the frequency of the low-frequency vibration reduced. From the results of Figure 114, it can be realized that increasing the frame mass is an effective method for the management of the frame's vibration. Lower vibration's amplitude can reduce the energy loss in dampers where the velocity and amplitude are two of the main factors for dissipating the energy. In addition, lower vibration amplitude is desirable as it will also enhance the life span and maintenance of frame parts and other components attached to it.

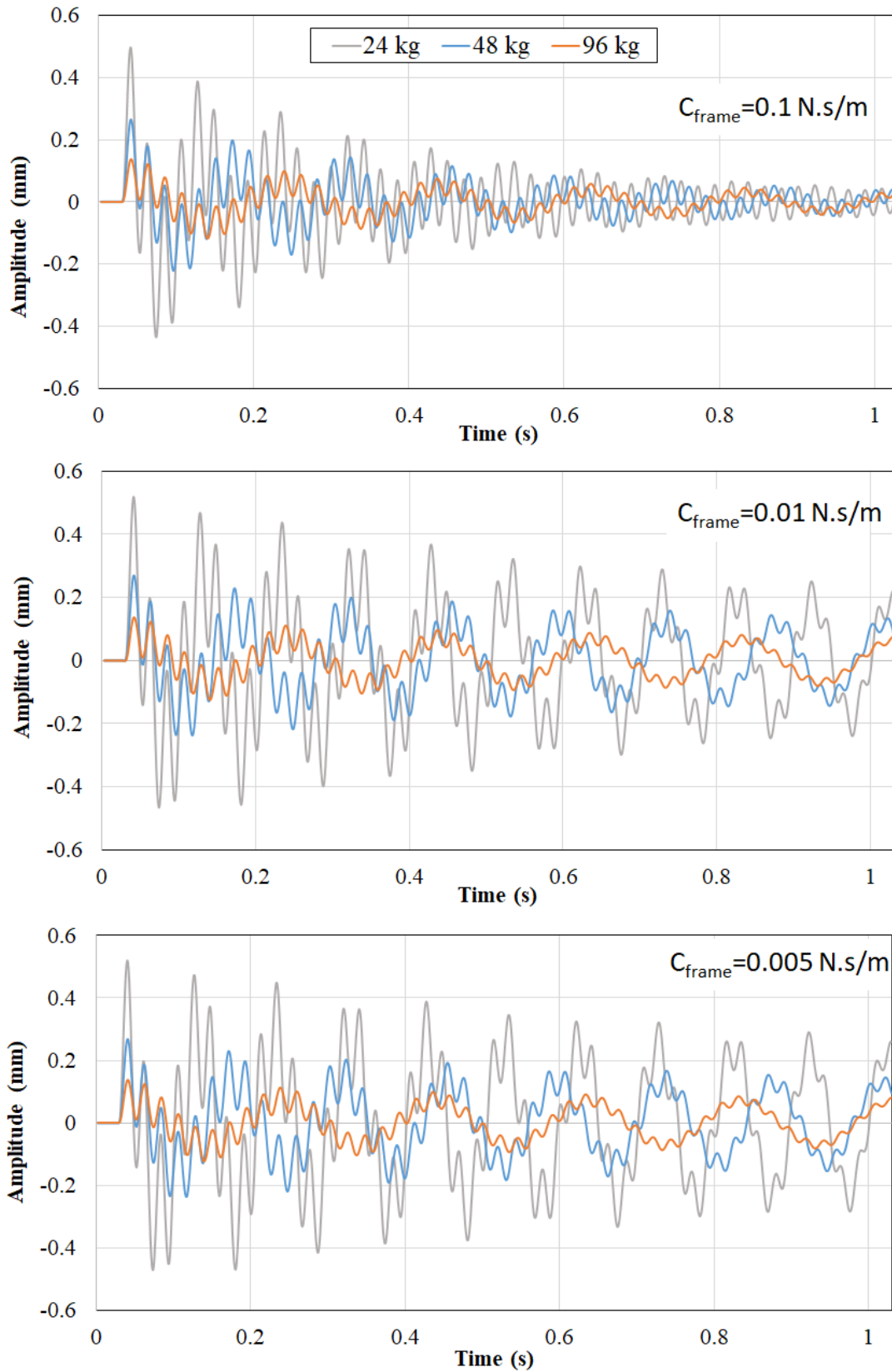


**Figure 114. Effects of frame mass on the dynamic behavior of LEA.**

## **7 Summary and Recommendations**

### **7.1 Summary**

As the main objective of this research, a spring system was developed to be used for a one-kW resonating free piston linear engine alternator (LEA) for the GENSETS program. Reviewing previous studies along with the experience of the research group in WVU in the past, the requirements of a rebounding mechanism were defined and the best method was defined to use flexure springs to serve as linear energy restoration system as well as linear bearings at the same time. To design flexure springs, two main approaches were introduced: Using FEA and machine learning to optimize a design, and an analytical solution. For the FEA, first, the main design parameters were defined. Then a sensitivity analysis was performed to find the influence of the design parameters, on maximum stress and natural frequency of flexures. The results of the parametric study was a pool of design points which was used to create a computer program for designing of flexure springs. Also, design charts were generated that can be used for the primary design of flexure springs for a wide range of outputs for the operation ranges of maximum 30 mm stroke length and 100 Hz frequency.

For the manufacturing, two of the possible materials were selected, a steel and a titanium alloy because of their high strength and fatigue limit, and also low density in titanium alloys. The manufactured springs were tested to validate the stress and strain relationships with the FEA results. Also, a statistical analysis was performed to find the manufacturing influence on the force-displacement results of springs of both types. Three manufacturing methods were considered and compared. Methods were used to enhance manufacturing quality and to reduce fatigue failure risks.

The energy performance of the flexure springs was analyzed using both experiments and FEA. Through experiments, the mechanical energy losses were quantified and methods were implemented to isolate the effects of drag force on resonating springs. Then 3D CFD was used to model the drag force effects on flexure's energy loss. Also a parametric study was performed in the CFD to identify the flexure's geometrical dimensions effects on the drag force. To study the effects of vibration on the dynamic performance of the springs, a series of transient FE modeling was completed.

The whole LEA machine dynamics was studied using FEA and experiments to quantify the vibration of the frame and its damping coefficients. Experiments were performed with a different number of springs and different mounting strategies. FEA was used to find the effects of mass, stiffness, and damping in the LEA machine and their influence on the overall performance of the machine.

## **7.2 Major Findings**

### **Spring Type Selection**

- A comparison between flexure springs and compression coil springs for the linear applications were performed and it was found that implementing flexure springs provides higher resonant frequency and hence power output for the LEA machine. The moving mass of a flexure spring was significantly lower than an equivalent coil springs' resonant frequency by about 30%.
- Comparing springs of the same stiffness, the coil springs were between 4 to 5 times heavier than the flexure spring. By using flexure springs, the overall weight of the LEA machine will be reduced and the energy density will increase.
- The radial and circumferential stiffness of the flexure and coil springs were compared and results showed a low stiffness of coil springs, specifically in the radial direction where flexure springs had very good stiffness.
- From the packaging versatility, flexure springs can be packed in an LEA machine in linear fashion but applications requiring multiple coil springs may require additional mounting considerations. Also, coil springs exert additional torque to the shaft while flexure springs marginal torque on the shaft.
- Compared to gas springs, for small residential CHP units, flexure springs have the advantage of providing higher frequencies, above 50 Hz. The mechanical challenges in the application of gas springs, such as thermal losses and mechanical sealing at high speeds, are the main reason for the selection of flexure springs over gas (or air) springs.

## **Flexure design**

- The main flexure design parameters were identified as outer diameter, arm's spiral shape, arm's length (sweep angle), number of arms, and thickness. The sweep angle and outer diameter were the most influential parameters on the outputs of the maximum natural frequency and maximum equivalent stress.
- The hardened steel alloys and titanium alloys were identified to be suitable for manufacturing the flexure springs for high-frequency, high-stroke length application, due to the high fatigue strength and spring rate for steel alloys, and high fatigue strength and low density for the titanium alloys. For lower cost and high volume production, steel alloy was a better candidate, whereas for prototyping and achieving the maximum resonant frequency, titanium alloy was a better choice.
- Different spiral arm shapes were studied and the involute of the circle was found as the desired geometry in terms of simplicity of manufacturing and automated design optimization process in CAD/FEA software.
- Modifications methods were introduced to reduce the stress concentration on the flexure's arms at the highest deflection point. Methods include using shape factor and using large-radius curves at the endpoints of spiral cuts and were shown to reduce the maximum stress by an average of 20% compared to unchanged flexures with constant arm's width and semi-circle shape at the endpoints.
- The maximum natural frequency of flexure springs with steel and titanium materials for one-kW LEA machine with 22 mm stroke length was calculated to be 124 and 138 Hz, respectively, while the fatigue strength of materials was considered for an extended lifetime of flexures.
- The modal analysis of flexure springs showed that the fourth and fifth modes of deflection result in unwanted vibration of the arms that increase the stress concentrations on the flexure's arms compared to the static (very low speed) conditions and also it increases the risk of collision of adjacent flexures' arm.

- The moving mass of a flexure spring for outer diameter between 70 to 150 mm was calculated between 20-25% under dynamic conditions. This moving percentage is comparable with the 45-65% moving mass of the compression coil springs.
- A sensitivity analysis of flexure springs was completed for steel and titanium materials for a range of four main design parameters and results showed the sensitivity of the outputs (stress and frequency) in order of highest to lowest to sweep angle, outer diameter, thickness, and the number of arms.
- Analysis of data of over 6000 design points generated by a machine learning algorithm showed a linear relationship between the maximum stress on flexure and the maximum achievable resonant frequency. The slope of increase in frequency with stress was about 12% higher for titanium material flexures.
- The linearity of the stress by flexure's center deflection was analyzed for 51 equally spaced locations along the length of one flexure's arm and results showed the linear increase by deflection distance for all locations under static conditions.
- A computer program was developed for the flexure design by training a neural network algorithm using all design point data generated during the parametric study. The software input four main design parameters and predicts the maximum stress and frequency. The fitness goodness of the NN algorithm was  $R^2 = 0.9999$ . The final stress and frequency values belong to the non-modified design in which the stress value can be reduced by an average of 20% by using the two modification techniques, modifying the shape factor and spiral ends radius.
- Data analysis was performed on the pool of data of all flexure design points to find meaningful correlations between the parameters to be used in 2-D design charts. Sorting the design points by the "stress/thickness" ratio versus sweep angle, the number of arms, and outer diameter showed the best results.

### **Experimental Analysis**

- Experiments were performed for the force-displacement and stress-strain validation. The results showed higher stiffness non-linearity – about 5% over the 11 mm displacement

range – in experiments compared to FEA where material non-linear behavior and test rig attachment condition were identified as possible reasons for such difference.

- The strain on three locations along the flexure's arm length showed a linear behavior and was in good agreement with FEA results.
- Experimental study of the stiffness of a package of flexure springs including up to five flexures showed a linear relationship with the number of springs.
- The mechanical properties of Sandvik steel material was tested using the ASTM tensile testing and results showed about 4% lower yield strength values compared to the supplier's datasheet. Increase in the thickness of the material resulted in reduced tensile and yield strength.
- Twelve water jet manufactured flexure springs of both steel and titanium material were tested for directional stiffness to examine manufacturing effects. The titanium material showed higher differences of stiffness between left and right side stiffness of the spring while the stiffness difference was marginal for the steel material.
- The differences range of flexures' average stiffness due to water jet manufacturing tolerances was ~1.38 kN/m for steel material (about 4% increase from the minimum value), and 2.5 kN/m for the titanium material (8.1% increase from the minimum value).
- The attachment of the flexure springs in the assembly was analyzed and results showed constant stiffness occurs when the rod could freely rotate on the springs. Rigid attachment showed high amplitude fluctuations (~3 kN/m for a steel flexure) in the stiffness results for static tests.
- Packaging force of springs was studied experimentally to investigate the tightening force of the package with one flexure spring, on the axial stiffness of the package. The torque applied to a threaded connector varied between 5 in.lb to 110 in.lb. Two spacer types were evaluated and the ones with increased contact area showed lower variation in the stiffness results and no significant changes after 10-15 in.lb torque per spring. Using thin spacers, at least 35 in.lb torque per spring was required to ensure consistent results.

## **Manufacturing methods**

- Three methods were considered as feasible manufacturing methods: waterjet, EDM, and CNC. The CNC machining showed the best accuracy while cutting the narrow spiral gaps was considerably time consuming and costly. Comparing the waterjet and EDM, there is a trade-off between cost and accuracy. Using waterjet was cost effective in terms of machining time, while the surface and edge roughness was larger in size. The EDM method resulted in high quality on the edges. The after-machining modifications are necessary for the waterjet, but minor modification was required for the EDM method.
- Using waterjet, the kerf angle effects caused about a 5% difference in the slot width on two sides of the flexures with a larger width on the side where the waterjet starts cutting the material.
- Two methods were identified effective for improving the surface and edge quality of the flexures made by waterjet: tumbling and shot peening. Both methods improved the surface roughness of the top and bottom surfaces. The tumbling of the flexures for 24 hours with finishing media of grit 800 removed a large portion of microcracks on the edges and also the side surfaces of the arms, where it was not easy to reach for shot peening.

## **Fatigue Fracture**

- In most cases, the fatigue fracture occurred at the endpoints of spiral cuts at the outer diameter.
- Fatigue fracture was the primary fracture failure criterion at the end locations of spiral arms. Manufacturing imperfections and resulted roughness on the edges can increase the stress concentration and increase the risk of microcracks initiation.
- The fractography of the cracked surfaces showed the crack initiation from the top (or bottom) surfaces near the spiral end curved profile. The beachmarks on the fractured surfaces indicated medium to high nominal stress concentration with loading patterns more similar to unidirectional bending than the reverse bending. A possible reason for such patterns can be either a fast rupture where there was no time for the cracks on the other



side to propagate enough distance or the flexure deflection was not equal in its left and right deflections.

### **Flexure's Energy and Loss Analysis**

- The resistive air drag force on the side surfaces of an oscillating flexure spring was found as a source of energy loss. The energy loss was quantified through experiments by comparing the losses under ambient and vacuum conditions. The drag losses contributed to 10-15% of total mechanical losses in the linear alternator design.
- The effective velocity of flexure springs was calculated using two formulations, mass-averaged calculation and KE-averaged formulation. The velocity according to mass-averaged formulation was 47.8% of the maximum velocity at flexure's center, and the KE-averaged formulation was 63.3% of the maximum velocity. The latter formulation was used in the calculation of the drag force loss.
- Vibration and energy conversion of a single flexure spring showed unwanted kinetic energy in one cycle of deformation, caused by higher modes of vibration of arms. The percentage of the amplitude of vibration was higher at the outer ends of spiral arms where most fatigue fractures occurred. This showed the extra stored strain energy at those locations that resulted in the stress value exceed the fatigue limit several times in the cycle. The high stress values eventually lead to early fracture of the arms.
- Vibration analysis of flexures at different operational speeds showed that for flexure springs with natural frequency in the range of 120-140 Hz, the operational speed of less than 50 Hz reduced the amplitude of the vibration and KE and PE curves had smoother shape (close to sinusoidal) without the additional strain/kinetic energies compared to the ideal sinusoidal motion of arms. So, from the results, the operational frequency of 30-40% of the natural frequency of the flexure is beneficial from both the energy conversion and life aspects.
- The result of KE-PE energy conversion in a single flexure spring showed that cyclic stored strain energy of a flexure had a second order relationship with the frequency of operations.

- The total mechanical losses of an LEA machine increase as a function of displacement with second order relationship.
- The ambient air had a marginal influence on the resonant frequency of the LEA machine.
- The ambient air drag force resulted in 11% increase in the damping ratio of the LEA machine.

### **LEA Assembly Analysis**

- An LEA assembly with 4, 6, and 8 steel flexure springs was tested to quantify the machine's frequency and the damping coefficients with two types of shear mounts. The resonant frequency of the linear displacements was compared to FEA results and experiments underpredicted the resonant frequencies by about 10%.
- Experiments showed a 1 to 2% increase in the LEA's linear displacement frequency by using the stiffer (about three times) shear mounts.
- The first modes of deformation of the LEA machine in order of magnitude was frame's linear vibration, flexure's linear deformation, flexure's circumferential deformation, and flexure's radial deformation.
- All deformation modes of the LEA, except for the frame's vibration, increased by increasing the number of flexure springs (LEA's total stiffness) non-linearly. The non-linearity was due to the constant moving mass of the translator.
- Results from the FEA parametric study on the LEA's dynamics showed that the mass and stiffness of the frame did not noticeably influence the translator dynamic behavior. Increasing the frame's damping reduced the amplitude of the translator's oscillations by 0.03% and 0.54%, respectively, for the damping coefficients of  $C=0.01$  and  $0.1$ , compared to the case where  $C=0.005$ .
- Reducing the LEA's frame stiffness will enhanced the uniformity of frame's high-frequency vibration mode shapes and also reduced the frame's natural frequency. Both of these changes could lead to reduced wasted energy in the frames shock absorbers and improve the durability of the components.

- Increasing the frame overall mass reduced the amplitude of both low-frequency and high-frequency vibration of the frame. Lower vibration amplitude of the frame could reduce the LEA energy loss and improve the life and maintenance of the LEA's components.

### **7.3 Recommendations for Future Work**

- The flexure design process using machine learning should be improved by including more design parameters such as shape factor, gap width, and spiral end closing methods, specifically for the automated CAD process. This should allow achieving a computer program with improved results for a wide range of applications.
- The analytical solution of the flexure's arm design can be rewritten with reducing the assumptions that were made for simplicity, and also another step is required to be added to the current solution to characterize the effects of the number of arms in the equation using FEA or experiments.
- In order to improve the flexure design for the linear application in terms of the frequency and stress, as the first step, additional materials should be identified with preferred material characteristics such as high fatigue strength, low density, high elongations, and high notch resistivity.
- The future design optimization should consider the effects of design parameters on the higher modes of deformation to reduce the unwanted vibration of the arms under dynamic conditions.
- Advanced surface finishing methods are required to enhance the surface/edge quality of the flexure's arm including mechanical, heat treatment, and electrochemical processes.
- A study is needed to consider using different materials and manufacturing methods in terms of overall LEA machine's cost, added value due to increased service life, higher LEA's frequency (power output), and higher thermal efficiency by using advanced materials/machining methods for manufacturing flexure springs.
- A test rig is required to monitor the force-displacement and possibly stress-strain behavior of the flexure springs while under normal working operation.

- A fatigue test rig is essential for testing flexure springs to study the effects of different designs, operating frequency, and materials.
- Further FE studies are required to investigate the fatigue life and crack initiation/propagation, considering surface roughness caused by different manufacturing methods and to estimate the flexure's regular service/replacement time intervals.
- A complete analysis using both experiments and FEA is necessary to characterize the frictional losses in a spring pack under dynamic conditions with different packaging methods.
- The effects of the zero-position biases should be studied for the dynamic response of the flexures as well as the flexure's life. The cycle-by-cycle variation in loading from the engine causes non-zero mean stress values on flexure springs that significantly affects the fatigue endurance of flexures and needs to be investigated.
- A sensitivity analysis is required to study the interactions between the translator's stiffness, mass, and damping, and the frame's stiffness, mass, and damping.
- Energy harvesting strategies can be investigated to convert the vibration of the frame into useful energy.
- Acoustic analysis of oscillating flexure is required to study the effects of design and operating parameters on the noise generation to minimize the noise for the residential applications. This can be completed by both experiments and FEA.

## 8 References

- [1] “The Plain English Guide to the Clean Air Act | Overview of the Clean Air Act and Air Pollution | US EPA.” <https://www.epa.gov/clean-air-act-overview/plain-english-guide-clean-air-act> (accessed Mar. 04, 2020).
- [2] “Energy Flow Charts - Lawrence Livermore National Laboratory,” 2015. <https://flowcharts.llnl.gov/> (accessed Mar. 04, 2020).
- [3] “U.S. Energy Facts Explained - Consumption and Production - U.S. Energy Information Administration (EIA).” <https://www.eia.gov/energyexplained/us-energy-facts/> (accessed Mar. 11, 2020).
- [4] “What is the Efficiency of Different Types of Power Plants? - FAQ - U.S. Energy Information Administration (EIA).” <https://www.eia.gov/tools/faqs/faq.php?id=107> (accessed Mar. 12, 2020).
- [5] “U.S. Energy Information Administration (EIA).” <https://www.eia.gov/> (accessed Mar. 04, 2020).
- [6] “ARPA-E | GENSETS.” <https://arpa-e.energy.gov/?q=arpa-e-programs/gensets> (accessed Mar. 04, 2020).
- [7] “ARPA-E | MOVE.” <https://arpa-e.energy.gov/?q=arpa-e-programs/move> (accessed Mar. 04, 2020).
- [8] “Learn About Natural Gas | American Gas Association.” <https://www.aga.org/about-natural-gas> (accessed Mar. 04, 2020).
- [9] “Electricity in the U.S. - U.S. Energy Information Administration (EIA).” <https://www.eia.gov/energyexplained/electricity/electricity-in-the-us.php> (accessed Nov. 08, 2020).
- [10] “Isometric Energy Vector Images (over 13,000).” <https://www.vectorstock.com/royalty-free-vectors/isometric-energy-vectors> (accessed Oct. 22, 2020).
- [11] A. Anvari, “Global warming mitigation using smart micro-grids,” *Glob. Warm. - Impacts Futur. Perspect.*, no. May 2012, 2012, doi: 10.5772/48204.
- [12] “About the CHP Partnership | Combined Heat and Power (CHP) Partnership | US EPA.” <https://www.epa.gov/chp/about-chp-partnership> (accessed Mar. 12, 2020).
- [13] A. Ondeck, T. F. Edgar, and M. Baldea, “A multi-scale framework for simultaneous optimization of the design and operating strategy of residential CHP systems,” *Appl. Energy*, vol. 205, pp. 1495–1511, 2017, doi: 10.1016/j.apenergy.2017.08.082.
- [14] M. Bianchi, A. De Pascale, and P. R. Spina, “Guidelines for residential micro-CHP systems design,” *Appl. Energy*, vol. 97, pp. 673–685, 2012, doi: 10.1016/j.apenergy.2011.11.023.
- [15] G. Vishwanathan, J. P. Sculley, A. Fischer, and J. C. Zhao, “Techno-economic analysis of high-efficiency natural-gas generators for residential combined heat and power,” *Appl. Energy*, vol. 226, pp. 1064–1075, 2018, doi: 10.1016/j.apenergy.2018.06.013.

- [16] P. Capaldi, “A high efficiency 10 kWe microcogenerator based on an Atkinson cycle internal combustion engine,” *Appl. Therm. Eng.*, vol. 71, pp. 913–920, 2014, doi: 10.1016/j.applthermaleng.2014.02.035.
- [17] R. Mikalsen, Y. D. Wang, and A. P. Roskilly, “A comparison of Miller and Otto cycle natural gas engines for small scale CHP applications,” *Appl. Energy*, vol. 86, pp. 922–927, 2009, doi: 10.1016/j.apenergy.2008.09.021.
- [18] “Honda Global | April 3 , 2007 ‘Honda and Climate Energy Begin Retail Sales of freewatt™ Micro-CHP Home Heating and Power System.’” <https://global.honda/newsroom/worldnews/2007/c070403Home-Heating-Power-System.html> (accessed May 18, 2020).
- [19] “2018 Yanmar CHP CP5WN.” <https://www.tractorbob.com/inventory/v1/2018/Yanmar/Energy-Systems/Combined-Heat-Power/CHP/CP5WN--Oklahoma-City-Oklahoma---9723831> (accessed Mar. 05, 2020).
- [20] “How Much Electricity Does an American Home Use? - FAQ - U.S. Energy Information Administration (EIA).” <https://www.eia.gov/tools/faqs/faq.php?id=97&t=3> (accessed Mar. 04, 2020).
- [21] “2015 RECS: Overview.” <https://www.eia.gov/consumption/residential/reports/2015/overview/index.php?src=<> (accessed Mar. 04, 2020).
- [22] C. M. Atkinson, S. Petreanu, N. N. Clark, R. J. Atkinson, T. I. McDaniel, S. Nandkumar, and P. Famouri, “Numerical simulation of a two-stroke linear engine-alternator combination,” 1999, doi: 10.4271/1999-01-0921.
- [23] R. Mikalsen and A. P. Roskilly, “Performance simulation of a spark ignited free-piston engine generator,” *Appl. Therm. Eng.*, vol. 28, no. 14–15, pp. 1726–1733, 2008, doi: 10.1016/j.applthermaleng.2007.11.015.
- [24] H. Kosaka, T. Akita, K. Moriya, S. Goto, Y. Hotta, T. Umeno, and K. Nakakita, “Development of free piston engine linear generator system part 1 - Investigation of fundamental characteristics,” 2014, doi: 10.4271/2014-01-1203.
- [25] S. Schneider, F. Rinderknecht, and H. E. Friedrich, “Design of future concepts and variants of the Free Piston Linear Generator,” 2014, doi: 10.1109/EVER.2014.6844029.
- [26] P. A. J. Achten, “A review of free piston engine concepts,” 1994, doi: 10.4271/941776.
- [27] H. T. Aichlmayr, D. B. Kittelson, and M. R. Zachariah, “Design considerations , modeling , and analysis of micro-homogeneous charge compression ignition combustion free-piston engines,” 2002.
- [28] C. Tóth-Nagy and N. N. Clark, “The linear engine in 2004,” 2005, doi: 10.4271/2005-01-2140.
- [29] R. Mikalsen and A. P. Roskilly, “A review of free-piston engine history and applications,” *Applied Thermal Engineering*, pp. 2339–2352, 2007, doi: 10.1016/j.applthermaleng.2007.03.015.

- [30] M. R. Hanipah, R. Mikalsen, and A. P. Roskilly, "Recent commercial free-piston engine developments for automotive applications," *Appl. Therm. Eng.*, vol. 75, pp. 493–503, Jan. 2015, doi: 10.1016/j.applthermaleng.2014.09.039.
- [31] D. Johnson, M. Darzi, C. Ulishney, M. Bade, and N. Zamani, "Methods to improve combustion stability, efficiency, and power density of a small, port-injected, spark-ignited, two-stroke natural gas engine," in *Proceedings of the ASME 2017 Internal Combustion Engine Division Fall Technical Conference, ICEF 2017*, 2017, vol. 2, doi: 10.1115/ICEF20173557.
- [32] M. Darzi, D. Johnson, C. Ulishney, M. Bade, and N. Zamani, "baseline evaluation of Ignition Timing and Compression Ratio Configurations on Efficiency and Combustion Stability of a Small-Bore, Two-Stroke, Natural Gas Engine," 2017. doi: <https://doi.org/10.1115/IMECE2017-70078>.
- [33] M. Darzi, D. Johnson, C. Ulishney, R. M. B. Bade, N. Zamani Meymian, G. Thompson, N. Clark, and P. Famouri, "Quantification of energy pathways and gas exchange of a small port injection SI two-stroke natural gas engine operating on different exhaust configurations," *SAE Tech. Pap.*, pp. 1–8, 2018, doi: <https://doi.org/10.4271/2018-01-1278>.
- [34] M. Darzi, D. Johnson, R. M. B. Bade, C. Ulishney, N. Zamani Meymian, N. Clark, G. Thompson, and P. Famouri, "Continuously varying exhaust outlet diameter to improve efficiency and emissions of a small SI natural gas two-stroke engine by internal EGR," *SAE Tech. Pap.*, pp. 1–10, 2018, doi: <https://doi.org/10.4271/2018-01-0985>.
- [35] N. B. Hung and O. Lim, "A review of free-piston linear engines," *Appl. Energy*, vol. 178, pp. 78–97, 2016, doi: 10.1016/j.apenergy.2016.06.038.
- [36] R. Mikalsen and A. P. Roskilly, "The design and simulation of a two-stroke free-piston compression ignition engine for electrical power generation," *Appl. Therm. Eng.*, vol. 28, 2008, doi: 10.1016/j.applthermaleng.2007.04.009.
- [37] "Oscillation Characteristic of Single Free Piston Engine Generator | Scientific.Net." <https://www.scientific.net/AMR.383-390.1873> (accessed Mar. 11, 2020).
- [38] Q. Li, J. Xiao, and Z. Huang, "Simulation of a two-stroke free-piston engine for electrical power generation," *Energy and Fuels*, vol. 22, no. 5, pp. 3443–3449, Sep. 2008, doi: 10.1021/ef800217k.
- [39] M. C. Robinson and N. Clark, "Fundamental analysis of spring-varied, free piston, Otto engine device," *SAE Int. J. Engines*, vol. 7, no. 1, pp. 195–220, 2014, doi: 10.4271/2014-01-1099.
- [40] R. Mikalsen and A. P. Roskilly, "The control of a free-piston engine generator. Part 1: Fundamental analyses," *Appl. Energy*, vol. 87, no. 4, pp. 1273–1280, 2010, doi: 10.1016/j.apenergy.2009.06.036.
- [41] R. Mikalsen and A. P. Roskilly, "The control of a free-piston engine generator. Part 2: Engine dynamics and piston motion control," *Appl. Energy*, vol. 87, no. 4, pp. 1281–1287, Apr. 2010, doi: 10.1016/j.apenergy.2009.06.035.
- [42] N. N. Clark, S. Nandkumar, and P. Famouri, "Fundamental analysis of a linear two-cylinder internal combustion engine," Oct. 1998, doi: 10.4271/982692.
- [43] L. Li, Y. Luan, Z. Wang, J. Deng, and Z. Wu, "Simulations of key design parameters and performance optimization for a free-piston engine," Apr. 2010, doi: <https://doi.org/10.4271/2010->

01-1105.

- [44] H. Nguyen Ba, O. Lim, and N. Iida, "Simulation study of SI-HCCI transition in a two-stroke free piston engine fuelled with propane," *SAE Tech. Pap.*, vol. 01, no. 1104, p. 14, 2014, doi: 10.4271/2014-01-1104.
- [45] S. Rathore, S. Mishra, M. K. Paswan, and Sanjay, "A review on design and development of free piston linear generators in hybrid vehicles," 2019, doi: 10.1088/1757-899X/691/1/012053.
- [46] H. O. Farmer, "Free-piston compressor-engines," *Proc. Inst. Mech. Eng.*, vol. 156, no. 1, pp. 253–271, Jun. 1947, doi: 10.1243/pime\_proc\_1947\_156\_043\_02.
- [47] K. Neumann, "Acres of diesels at the Leipzig fair," *Mech. Eng.*, vol. 57, no. 3, pp. 246–247, 1935.
- [48] P. W. Swain, "Acres of DIESELS at the Leipzig Fair," *Power*, vol. 80, pp. 214–216, 1936.
- [49] A. L. London, "Free-piston and turbine compound engine—status of the development," *SAE Transactions*, vol. 62. SAE International, pp. 426–436, 1954, doi: 10.2307/44547338.
- [50] A. T. Braun and P. H. Schweitzer, "The braun linear engine," Feb. 1973, doi: 10.4271/730185.
- [51] L.-J. Li and N. H. Beachley, "Design feasibility of a free piston internal combustion engine/hydraulic pump," *SAE Transactions*, vol. 97. SAE International, pp. 1199–1213, 1988, doi: 10.2307/44547448.
- [52] R. P. Heinz, "Theory of operation of a free piston engine-pump," *SAE Tech. Pap.* 859316, 1985.
- [53] S. Tikkanen, M. Lammila, M. Herranen, and M. Vilenius, "First cycles of the dual hydraulic free piston engine," Sep. 2000, doi: 10.4271/2000-01-2546.
- [54] G. Eichelberg, "Free piston generators," *Schweizerische Bauzeitung*, no. Nov-Dec, pp. 673–679, 661–667, 1948.
- [55] P. Van Blarigan, N. Paradiso, and S. Goldsborough, "Homogeneous charge compression ignition with a free piston: A new approach to ideal otto cycle performance," 1998, doi: 10.4271/982484.
- [56] S. S. Goldsborough and P. Van Blarigan, "A numerical study of a free piston IC engine operating on homogeneous charge compression ignition combustion," *SAE Trans.*, vol. 108, pp. 959–972, 1999, doi: 10.4271/1999-01-0619.
- [57] W. R. Cawthorne, "Optimization of a brushless permanent magnet linear alternator for use with a linear internal combustion engine," West Virginia University Libraries, 1999.
- [58] T. J. Callahan and S. K. Ingram, "Free-piston engine linear generator for hybrid vehicles modeling study," San Antonio, TX, 1995.
- [59] P. Van Blarigan, "Advanced internal combustion electrical generator," *Proc. 2002 U.S. DOE Hydrog. Progr. Rev. NREL/CP-570-30535*, 2002.
- [60] S. S. Goldsborough and P. Van Blarigan, "Optimizing the scavenging system for a two-stroke cycle, free piston engine for high efficiency and low emissions: A computational approach," 2003, doi: 10.4271/2003-01-0001.



- [61] “Free-Piston Engines: A Possible Route to Hybrid-Electric Vehicles | Combustion Research Facility.” <https://crf.sandia.gov/free-piston-engines-a-possible-route-to-hybrid-electric-vehicles/> (accessed Mar. 04, 2020).
- [62] T. A. Johnson, M. T. Leick, and R. W. Moses, “Experimental evaluation of a prototype free piston engine - linear alternator (FPLA) system,” Apr. 2016, doi: 10.4271/2016-01-0677.
- [63] E. Shoukry, S. Taylor, N. Clark, and P. Famouri, “Numerical simulation for parametric study of a two-stroke direct injection linear engine,” 2002, doi: 10.4271/2002-01-1739.
- [64] C. Tóth-Nagy, P. Farmouri, and N. N. Clark, “Compression ignition linear engine design variable effects,” in *American Society of Mechanical Engineers, Internal Combustion Engine Division (Publication) ICE*, Feb. 2011, pp. 1029–1036, doi: 10.1115/ICEF2011-60157.
- [65] R. Mikalsen and A. P. Roskilly, “A computational study of free-piston diesel engine combustion,” *Appl. Energy*, vol. 86, no. 7–8, pp. 1136–1143, 2009, doi: 10.1016/j.apenergy.2008.08.004.
- [66] D. Houdyschell, “A diesel two-stroke linear engine,” West Virginia University, 2000.
- [67] Z. Zhao, F. Zhang, C. Zhao, and Y. Chen, “Modeling and simulation of a hydraulic free piston diesel engine,” 2008, doi: 10.4271/2008-01-1528.
- [68] F. Guo, C. L. Zhao, Y. Huang, and W. Wu, “Experimental study on hydraulic free-piston diesel engine,” in *Proceedings of International Conference on Computer Distributed Control and Intelligent Environmental Monitoring, CDCIEM 2011*, 2011, pp. 786–792, doi: 10.1109/CDCIEM.2011.99.
- [69] J. Mao, Z. Zuo, and H. Feng, “Dimensionless parametric analysis of spark ignited free-piston linear alternator,” in *Thermodynamics - Interaction Studies - Solids, Liquids and Gases*, InTech, 2011.
- [70] “Load Following Controller for Single Free-Piston Generator | Scientific.Net.” <https://www.scientific.net/AMM.157-158.617> (accessed Mar. 04, 2020).
- [71] B. Jia, Z. Zuo, H. Feng, G. Tian, and A. P. Roskilly, “Development approach of a spark-ignited free-piston engine generator,” Oct. 2014, doi: 10.4271/2014-01-2894.
- [72] B. Jia, Z. Zuo, G. Tian, H. Feng, and A. P. Roskilly, “Development and validation of a free-piston engine generator numerical model,” *Energy Convers. Manag.*, vol. 91, pp. 333–341, Feb. 2015, doi: 10.1016/j.enconman.2014.11.054.
- [73] H. Feng, Y. Song, Z. Zuo, J. Shang, Y. Wang, and A. P. Roskilly, “Stable operation and electricity generating characteristics of a single-cylinder free piston engine linear generator: Simulation and experiments,” *Energies*, vol. 8, no. 2, pp. 765–785, 2015, doi: 10.3390/en8020765.
- [74] Y.-X. Li, Z.-X. Zuo, H.-H. Feng, and B.-R. Jia, “Parameters matching requirements for diesel free piston linear alternator start-up,” *Adv. Mech. Eng.*, vol. 7, no. 3, 2015, doi: 10.1177/1687814015574408.
- [75] F. Kock and C. Ferrari, “Flatness-based high frequency control of a hydraulic actuator,” *J. Dyn. Syst. Meas. Control. Trans. ASME*, vol. 134, no. 2, Mar. 2012, doi: 10.1115/1.4005047.

- [76] J. Haag, C. Ferrari, J. H. Starcke, M. Stöhr, and U. Riedel, “Numerical and experimental investigation of in-cylinder flow in a loop-scavenged two-stroke free piston engine,” in *SAE Technical Paper*, 2012, vol. 4, doi: 10.4271/2012-32-0114.
- [77] F. Rinderknecht, “A highly efficient energy converter for a hybrid vehicle concept - Focused on the linear generator of the next generation,” 2013, doi: 10.1109/EVER.2013.6521533.
- [78] F. Rinderknecht, “Iron losses of a linear generator for a hybrid vehicle concept,” in *International Conference on Power Engineering, Energy and Electrical Drives*, 2013, pp. 252–257, doi: 10.1109/PowerEng.2013.6635615.
- [79] D. Carter and E. Wechner, “The free piston power pack: Sustainable power for hybrid electric vehicles,” 2003, doi: 10.4271/2003-01-3277.
- [80] J. Fredriksson and I. Denbratt, “Simulation of a two-stroke free piston engine,” 2004, doi: 10.4271/2004-01-1871.
- [81] S. Goto, K. Moriya, H. Kosaka, T. Akita, Y. Hotta, T. Umeno, and K. Nakakita, “Development of free piston engine linear generator system part 2 - Investigation of control system for generator,” in *SAE Technical Paper*, 2014, vol. 1, doi: 10.4271/2014-01-1193.
- [82] Y. Oh, O. Lim, G. Kim, and N. Iida, “A study for generating power on operating parameters of powerpack utilizing linear engine,” in *SAE Technical Paper*, 2012, vol. 4, doi: 10.4271/2012-32-0061.
- [83] J. Lee, O. Lim, and G. Kim, “An experimental study on the effects of spring stiffness on the combustion and dynamic characteristics of a linear engine,” *J. Mech. Sci. Technol.*, vol. 28, no. 5, pp. 1945–1950, May 2014, doi: 10.1007/s12206-014-0342-9.
- [84] “OLEA Project | Statler College of Engineering and Mineral Resources | West Virginia University.” <https://www.statler.wvu.edu/research/interdisciplinary/energy/olea-project> (accessed Mar. 27, 2020).
- [85] M. C. Robinson, N. N. Clark, and P. Famouri, “Resonance of a spring opposed free piston engine device,” *SAE International Journal of Engines*, vol. 9, SAE International, pp. 576–587, 2016, doi: 10.2307/26284840.
- [86] M. Bade, “Measured and modeled performance of a spring dominant free piston engine generator,” West Virginia University, 2019.
- [87] M. Darzi, “A framework for energy optimization of small , two-stroke , natural gas engines for combined heat and power applications,” West Virginia University, 2019.
- [88] J. Subramanian, “Design , modeling and optimization of reciprocating tubular permanent magnet linear generators for free piston engine applications,” West Virginia University, 2020.
- [89] G. Heiskell, “Development of resonating tubular oscillating linear alternator and engine ; system design and modeling abstract development of resonating tubular oscillating linear alternator and engine ; system design and modeling,” West Virginia University, 2018.
- [90] M. Bade, N. N. Clark, M. C. Robinson, and P. Famouri, “Parametric investigation of combustion

- and heat transfer characteristics of oscillating linear engine alternator,” *J. Combust.*, vol. 2018, 2018, doi: 10.1155/2018/2907572.
- [91] M. Bade, N. N. Clark, P. Famouri, and P. Guggilapu, “Performance comparison of a single cylinder and a dual cylinder free piston engine,” *J. Eng. Gas Turbines Power*, vol. 141, no. 8, pp. 1–9, 2019, doi: 10.1115/1.4043446.
  - [92] M. Bade, N. N. Clark, P. Famouri, and P. D. Guggilapu, “Translator dynamics and performance comparison on one and two cylinder free piston engines,” 2018, doi: 10.1115/IMECE2018-88689.
  - [93] J. Subramanian, G. Heiskell, F. Mahmudzadeh, and P. Famouri, “Study of radial and axial magnets for linear alternator - Free piston engine system,” *2017 North Am. Power Symp.*, 2017, doi: 10.1109/NAPS.2017.8107293.
  - [94] J. Subramanian, F. Mahmudzadeh, M. Bade, and P. Famouri, “Simulation and experimental validation of equivalent circuit parameters and core loss in a tubular permanent magnet linear generator for free piston engine applications,” *2019 IEEE Int. Electr. Mach. Drives Conf.*, pp. 57–62, 2019, doi: 10.1109/IEMDC.2019.8785345.
  - [95] J. Subramanian and P. Famouri, “Analysis of neutral position, magnet - spacer of tubular permanent magnet linear generator for fpe applications,” in *2019 IEEE 28th International Symposium on Industrial Electronics (ISIE)*, Jun. 2019, pp. 232–237, doi: 10.1109/ISIE.2019.8781327.
  - [96] N. Zamani Meymian, N. N. Clark, T. Musho, M. Darzi, D. Johnson, and P. Famouri, “An optimization method for flexural bearing design for high-stroke high-frequency applications,” *Cryogenics (Guildf.)*, vol. 95, pp. 82–94, 2018, doi: 10.1016/j.cryogenics.2018.09.008.
  - [97] N. Zamani Meymian, N. Clark, J. Subramanian, G. Heiskell, D. Johnson, F. Mahmudzadeh, M. Darzi, T. Musho, and P. Famouri, “Quantification of windage and vibrational losses in flexure springs of a one Kw two-stroke free piston linear engine alternator,” *SAE Tech. Pap. 2019-01-0816*, 2019, doi: 10.4271/2019-01-0816.
  - [98] N. Zamani Meymian, M. Darzi, and D. Johnson, “Pre-design investigation of resonant frequency effects on gas exchange efficiencies of a one-kw natural-gas linear engine alternator,” 2020, doi: 10.4271/2020-01-0488.Abstract.
  - [99] S. Chevailler, “Comparative study and selection criteria of linear motors,” *École Polytechnique Fédérale de Lausanne*, 2006.
  - [100] I. Boldea and S. A. Nasar, “Permanent-magnet linear alternators Part I: Fundamental equations,” *IEEE Trans. Aerosp. Electron. Syst.*, vol. AES-23, no. 1, pp. 73–78, 1987, doi: 10.1109/TAES.1987.313337.
  - [101] I. Boldea and S. A. Nasar, “Permanent-magnet linear alternators Part II: Design guidelines,” *IEEE Trans. Aerosp. Electron. Syst.*, vol. AES-23, no. 1, pp. 79–82, 1987, doi: 10.1109/TAES.1987.313338.
  - [102] S. A. Nasar and C. Chen, “Optimal design of a tubular permanent magnet linear alternator,” *Electr. Mach. Power Syst.*, vol. 14, no. 3–4, pp. 249–259, 1988, doi: 10.1080/07313568808909287.
  - [103] S. A. Nasar and C. Chen, “Magnetic circuit analysis of a tubular permanent magnet linear

- alternator,” *Electr. Mach. Power Syst.*, vol. 13, no. 6, pp. 361–371, 1987, doi: 10.1080/07313568708909257.
- [104] R. M. Pai, I. Boldea, and S. A. Nasar, “Complete equivalent circuit of a linear induction motor with sheet secondary,” *IEEE Trans. Magn.*, vol. 24, no. 1, pp. 639–654, Jan. 1987, doi: 10.1109/20.43997.
  - [105] G. E. Dawson, A. R. Eastham, J. F. Gieras, R. Ong, and K. Ananthasivam, “Design of linear induction drives by field analysis and finite-element techniques,” *IEEE Trans. Ind. Appl.*, vol. IA-22, no. 5, pp. 865–873, 1986, doi: 10.1109/TIA.1986.4504805.
  - [106] J. Zou, M. Zhao, Q. Wang, J. Zou, and G. Wu, “Development and analysis of tubular transverse flux machine with permanent-magnet excitation,” *IEEE Trans. Ind. Electron.*, vol. 59, no. 5, pp. 2198–2207, 2012, doi: 10.1109/TIE.2011.2157297.
  - [107] A. Souissi, M. W. Zouaghi, I. Abdennadher, and A. Masmoudi, “MEC-based modeling and sizing of a tubular linear PM synchronous machine,” *IEEE Trans. Ind. Appl.*, vol. 51, no. 3, pp. 2181–2194, May 2015, doi: 10.1109/TIA.2014.2382765.
  - [108] Q. Lu and Y. Ye, “Design and analysis of tubular linear PM generator,” in *IEEE Transactions on Magnetics*, Oct. 2009, vol. 45, no. 10, pp. 4716–4719, doi: 10.1109/TMAG.2009.2022184.
  - [109] T. T. Dang, P. François, L. Prévond, and H. Ben Ahmed, “Theoretical and experimental results of tubular linear induction generator for stirling cogenerator system,” 2010, doi: 10.1109/ICELMACH.2010.5607832.
  - [110] T. T. Dang, M. Ruellan, H. Ben Ahmed, L. Prevond, and B. Multon, “Sizing optimization of tubular linear induction generator for a new stirling micro-cogenerator system,” in *2014 International Symposium on Power Electronics, Electrical Drives, Automation and Motion, SPEEDAM 2014*, 2014, pp. 1362–1367, doi: 10.1109/SPEEDAM.2014.6871993.
  - [111] T. T. Dang, M. Ruellan, L. Prévond, H. Ben Ahmed, and B. Multon, “Sizing optimization of tubular linear induction generator and its possible application in high acceleration free-piston stirling microcogeneration,” *IEEE Trans. Ind. Appl.*, vol. 51, no. 5, pp. 3716–3733, Sep. 2015, doi: 10.1109/TIA.2015.2427284.
  - [112] C. F. Wang and J. X. Shen, “A method to segregate detent force components in permanent-magnet flux-switching linear machines,” *IEEE Trans. Magn.*, vol. 48, no. 5, pp. 1948–1955, May 2012, doi: 10.1109/TMAG.2011.2177852.
  - [113] M. Shujun, C. Jianyun, S. Xudong, and W. Shanming, “A variable pole pitch linear induction motor for electromagnetic aircraft launch system,” *IEEE Trans. Plasma Sci.*, vol. 43, no. 5, pp. 1346–1351, May 2015, doi: 10.1109/TPS.2015.2417996.
  - [114] G. P. Blair, *Design and Simulation of Two-Stroke Engines*. Society of Automotive Engineers, Inc., 1996.
  - [115] J. B. Heywood, *Internal Combustion Engine Fundamentals*. McGraw-Hill College, 1988.
  - [116] A. Boretti and J. Scalzo, “A novel valve-less supercharged small two stroke engine of top brake efficiency above 36% and power density above 100 KW/liter,” Nov. 2013, doi: 10.4271/2013-01-

- [117] Q. Xiong, Y. Moriyoshi, K. Morikawa, Y. Takahashi, T. Kuboyama, and T. Yamada, "Improvement in thermal efficiency of lean burn pre-chamber natural gas engine by optimization of combustion system," Mar. 2017, doi: 10.4271/2017-01-0782.
- [118] V. Pradeep, S. Bakshi, and A. Ramesh, "Direct injection of gaseous LPG in a two-stroke SI engine for improved performance," *Appl. Therm. Eng.*, vol. 89, pp. 738–747, Jul. 2015, doi: 10.1016/j.applthermaleng.2015.06.049.
- [119] J. B. Heywood and E. Sher, *The two-stroke cycle engine : its development, operation, and design*. CRC Press, 1999.
- [120] A. Trattner, S. Schmidt, R. Kirchberger, H. Eichlseder, A. Kölmel, M. Raffenberg, and T. Gegg, "Future engine technology in hand-held power tools," *SAE Int. J. Engines*, vol. 5, no. 4, pp. 1912–1929, 2012, doi: 10.2307/26277591.
- [121] R. Chandra, V. K. Vijay, P. M. V. Subbarao, and T. K. Khura, "Performance evaluation of a constant speed IC engine on CNG, methane enriched biogas and biogas," *Appl. Energy*, vol. 88, no. 11, pp. 3969–3977, Nov. 2011, doi: 10.1016/j.apenergy.2011.04.032.
- [122] A. Yousefi and M. Birouk, "Investigation of natural gas energy fraction and injection timing on the performance and emissions of a dual-fuel engine with pre-combustion chamber under low engine load," *Appl. Energy*, vol. 189, pp. 492–505 Contents, 2017, doi: 10.1016/j.apenergy.2016.12.046.
- [123] E. Shim, H. Park, and C. Bae, "Intake air strategy for low HC and CO emissions in dual-fuel (CNG-diesel) premixed charge compression ignition engine," *Appl. Energy*, vol. 225, pp. 1068–1077, 2018, doi: 10.1016/j.apenergy.2018.05.060.
- [124] E. Navarro, T. J. Leo, and R. Corral, "CO<sub>2</sub> emissions from a spark ignition engine operating on natural gas-hydrogen blends (HCNG)," *Appl. Energy*, vol. 101, pp. 112–120 Contents, 2013, doi: 10.1016/j.apenergy.2012.02.046.
- [125] J. Zheng and J. A. Caton, "Second law analysis of a low temperature combustion diesel engine: Effect of injection timing and exhaust gas recirculation," *Energy*, vol. 38, p. 78e84 Contents, 2012, doi: 10.1016/j.energy.2011.12.034.
- [126] B. Yang, C. Xi, X. Wei, K. Zeng, and M. C. Lai, "Parametric investigation of natural gas port injection and diesel pilot injection on the combustion and emissions of a turbocharged common rail dual-fuel engine at low load," *Appl. Energy*, vol. 143, pp. 130–137 Contents, 2015, doi: 10.1016/j.apenergy.2015.01.037.
- [127] Y. Motoyama and T. Gotoh, "The effect of higher compression ratio in two-stroke engines," 1993.
- [128] J. J. Zheng, J. H. Wang, B. Wang, and Z. H. Huang, "Effect of the compression ratio on the performance and combustion of a natural-gas direct-injection engine," *Proc. Inst. Mech. Eng. Part D J. Automob. Eng.*, vol. 223, no. 1, pp. 85–98, 2009, doi: 10.1243/09544070JAUTO976.
- [129] N. Kapilan, R. P. Reddy, and T. P. Prakash, "Effect of injection timing and compression ratio on the performance and emissions of 2-Stroke SI engine with in-cylinder injection of methanol," Oct. 2005, doi: 10.4271/2005-01-3711.

- [130] A. S. Krishna, J. M. Mallikarjuna, and D. Kumar, "Effect of engine parameters on in-cylinder flows in a two-stroke gasoline direct injection engine," *Appl. Energy*, vol. 176, pp. 282–294 Contents, 2016, doi: 10.1016/j.apenergy.2016.05.067.
- [131] S. Qiu, A. Peterson, and J. Augenblick, "Design equations and scaling laws for linear compressors with flexure springs," 2003, doi: 10.2514/6.2003-6040.
- [132] K. Air and F. Base, "Cryogenics," 1992.
- [133] P. Kittel, "Design Equations and Scaling Laws for Linear Compressors with Flexure Springs," 1992.
- [134] A. S. Gaunekar, T. Göddenhenrich, and C. Heiden, "Finite element analysis and testing of flexure bearing elements," *Cryogenics (Guildf.)*, vol. 36, no. 5, pp. 359–364, 1996, doi: 10.1016/0011-2275(96)81106-4.
- [135] C. C. Lee and R. B. Pan, "Flexure bearing analysis procedures and design charts," *Cryocoolers 9*, vol. 9, pp. 413–420, 1997, doi: 10.1007/978-1-4615-5869-9\_48.
- [136] R. M. Rawlings and S. M. Miskimins, "Flexure springs applied to low-cost linear drive cryocoolers," in *Infrared Technology and Applications XXVI*, 2000, vol. Proc. SPIE, doi: 10.1117/12.409882.
- [137] N. Chen, X. Chen, Y. N. Wu, C. G. Yang, and L. Xu, "Spiral profile design and parameter analysis of flexure spring," *Cryogenics (Guildf.)*, vol. 46, no. 6, pp. 409–419, 2006, doi: 10.1016/j.cryogenics.2005.12.009.
- [138] C. J. Simcock, "Investigation of materials for long life , high reliability flexure bearing springs for stirling cryocooler applications," in *International Cryocooler Conference*, 2007, pp. 335–343.
- [139] Z. S. Al-Otaibi and A. G. Jack, "Spiral flexure springs in single phase linear-resonant motors," in *42nd International Universities Power Engineering Conference*, 2007, pp. 184–187, doi: 10.1109/UPEC.2007.4468943.
- [140] M. V Kavade and C. B. Patil, "Optimization of flexure bearing using FEA for linear compressor," *Int. J. Eng. Sci.*, vol. 1, no. 12, pp. 37–45, 2012.
- [141] W. J. Zhou, L. Y. Wang, Z. H. Gan, R. Z. Wang, L. M. Qiu, and J. M. Pfothner, "The performance comparison of oxford and triangle flexure bearings," in *AIP Conference Proceedings*, 2012, vol. 1434, no. 1, pp. 1616–1623, doi: <https://doi.org/10.1063/1.4707036>.
- [142] R. Prasad K.S., M. Achanur, and D. C., "Shape factor optimization and parametric analysis of spiral arm flexure bearing through finite element analysis studies," *Int. J. Eng. Res. Technol.*, vol. 3, no. 4, pp. 585–588, 2014.
- [143] S. Amoedo, E. Thebaud, M. Gschwendtner, and D. White, "Novel parameter-based flexure bearing design method," *Cryogenics (Guildf.)*, vol. 76, pp. 1–9, 2016, doi: 10.1016/j.cryogenics.2016.03.002.
- [144] L. Peng, T. Wang, Z. Jiao, L. Yan, and C. Chen, "A novel universal analytical model of flexure spring for linear oscillating motor," in *Proceedings of the 14th IFToMM World Congress*, 2015, pp. 421–426, doi: 10.6567/iftomm.14th.wc.ps13.007.

- [145] M. Khot and B. Gawali, "Finite element analysis and optimization of flexure bearing for linear motor compressor," *Phys. Procedia*, vol. 67, pp. 379–385, 2015, doi: 10.1016/j.phpro.2015.06.044.
- [146] "Compressor valve steel — Sandvik Materials Technology." <https://www.materials.sandvik/en/products/strip-steel/strip-products/compressor-valve-steel/> (accessed May 12, 2020).
- [147] J. M. Beswick, *Bearing steel technology*. ASTM International, 2010.
- [148] "Maraging (Vascomax), Maraging 250, Maraging 300, Maraging 350." <http://www.dynamicmetals.net/> (accessed May 12, 2020).
- [149] "Carpenter - Toughness Index for Alloy Comparisons." <https://www.carpentertechnology.com/en/alloy-techzone/technical-information/alloy-selection/toughness-index-for-alloy-comparisons> (accessed May 12, 2020).
- [150] "Titanium Alloy | Titanium 6246 | Ti 6246 | UNS R56260 - Titanium Engineers." <http://www.titaniumengineers.com/ti-6246-6-2-4-6.html> (accessed May 12, 2020).
- [151] R. J. Freund, W. J. Wilson, and D. L. Mohr, *Statistical Methods*, Third. Elsevier Inc., 2010.
- [152] J. I. Ueda and Y. Sadamoto, "A measurement of the effective mass of coil springs," *J. Phys. Soc. Japan*, vol. 66, no. 2, pp. 367–368, 1997, doi: 10.1143/JPSJ.66.367.
- [153] "ANSYS® Academic Research Mechanical." 2018.
- [154] "Solidworks. Education ed." Solidworks Corp.
- [155] M. Kayri, "Predictive abilities of Bayesian regularization and Levenberg–Marquardt algorithms in artificial neural networks: a comparative empirical study on social data," *Math. Comput. Appl.*, vol. 21, no. 2, p. 20, May 2016, doi: 10.3390/mca21020020.
- [156] "Autograph AGS-X Series : SHIMADZU (Shimadzu Corporation)." <https://www.shimadzu.com/an/products/materials-testing-inspection/uni-ttm/autograph-ags-x-series/index.html> (accessed Oct. 22, 2020).
- [157] W. Luecke, D. McColskey, C. McCowan, S. Banovic, R. Fields, T. Foecke, T. Siewert, and F. W. Gayle, "Mechanical properties of structural steels," 2005.
- [158] ASTM E8, *ASTM E8/E8M standard test methods for tension testing of metallic materials 1*, no. C. 2010.
- [159] "Waterjet University - Precision and Quality." <https://wardjet.com/waterjet/university/precision-quality> (accessed Jun. 08, 2020).
- [160] ASM Handbook Committee, *ASME Handbook Volume 12: Fractography*. ASME International, 1987.
- [161] Henrik Sönnnerlind, "Damping in Structural Dynamics: Theory and Sources | COMSOL Blog." <https://www.comsol.com/blogs/damping-in-structural-dynamics-theory-and-sources/> (accessed Oct. 22, 2020).

- [162] J. Camara, *Power Reference Manual*, 2010th ed. Professional Publication Inc.
- [163] B. D. Ghadiri, S. Fallah, and A. Niazmand, "Investigation of harmonic instability of laminar fluid flow past 2D rectangular cross sections with 0.5–4 aspect ratios," *Proc. Inst. Mech. Eng. Part C J. Mech. Eng. Sci.*, vol. 228, no. 5, pp. 828–839, Apr. 2014, doi: 10.1177/0954406213491906.
- [164] T. Engels, D. Kolomenskiy, K. Schneider, and J. Sesterhenn, "Numerical simulation of vortex-induced drag of elastic swimmer models," *Theor. Appl. Mech. Lett.*, vol. 7, no. 5, pp. 280–285, 2017, doi: 10.1016/j.taml.2017.10.001.
- [165] F. White, *Fluid Mechanics*, 7th ed. McGraw Hill, 2011.
- [166] C. Huynh, L. Zheng, and D. Acharya, "Losses in high speed permanent magnet machines used in microturbine applications," *J. Eng. Gas Turbines Power*, vol. 131, no. 2, Mar. 2009, doi: 10.1115/1.2982151.
- [167] J. Billingsley, *Essentials of Dynamics and Vibrations*. Springer International Publishing, 2017.
- [168] D. A. Anslyn, E.V. & Dougherty, *Modern Physical Organic Chemistry*. 2006.
- [169] E. E. Ungar and E. M. Kerwin, "Loss factors of viscoelastic systems in terms of energy concepts," *J. Acoust. Soc. Am.*, vol. 34, no. 7, pp. 954–957, 1962, doi: 10.1121/1.1918227.
- [170] S. J. Elliott, M. G. Tehrani, and R. S. Langley, "Nonlinear damping and quasi-linear modelling," *Philos. Trans. R. Soc. A Math. Phys. Eng. Sci.*, vol. 373, no. 2051, Sep. 2015, doi: 10.1098/rsta.2014.0402.



## **9 Appendix**

### **9.1 FEA: Preprocessing, Solution, and Postprocessing**

A main part of the study on the flexure and LEA machine design, optimization, and analysis was completed using CAD/FEA software. In this section, information on the CAD and FEA modeling is provided.

#### **9.1.1 CAD**

The flexure parts were initially generated in SolidWorks, and for some modifications, the ANSYS SpaceClaim and ANSYS DesignModeler were also used. For this research, SolidWorks releases 17 and 18 were used. Version 17 has the capability to be directly imported and used in the ANSYS Workbench and for this reason, it has more advantages over the version 18. For FEA, ANSYS release 18.2 was used.

For a single flexure, the main CAD feature is the spiral cut, which is defined by the equation of involute of a circle. One edge of a spiral cut was generated using the "Equation Driven Curve" and the other edge was an offset of the first one. Then the two edges were connected at the two sides using arbitrary splines. In defining the spiral equation, independent variables were input as a "Global Parameter." The parameters include flexure's inner and outer diameters, shape factor, and sweep angle. It should be noted that, for the parametric study, the name of parameters that needed to be updated in every iteration in the FEA, should start with a specific Key-name, which by default in ANSYS is defined as DS or DNS. The Key-names can be any user-defined names, but when using dimensions in SolidWorks, the name of a specific dimension should be changed and start with the specific Key\_name in the ANSYS, otherwise, ANSYS will not recognize that dimension as a parameter. The Key\_name in ANSYS can be removed so that every dimension in the SolidWorks will be recognized as a possible parameter in ANSYS, which in large models with many dimensions will occupy more places in the information panes of the ANSYS modeling.

### **9.1.2 FEA**

To complete this research, ANSYS Workbench package was used for the finite element modeling to obtain stress-strain, design optimization, modal analysis, harmonic response, and transient behavior for individual parts as well as the whole LEA machine. As noted before, for the CAD, models were primarily generated in SolidWorks and imported in the ANSYS. For minor modifications, the geometry edit packages in ANSYS were used including DesignModeler and SpaceClaim. The material properties were defined in ANSYS. For fixing an entity to the ground or other parts in assemblies, different approaches were used in ANSYS. For ground constraints, mostly "Fix Support" and "Displacement" BCs were used. However, for attaching parts, "Joints" were preferred over "Contacts." If the friction analysis was not required, to model zero-relative-displacement between two (or more) attached parts, using joints results in decreased computational time and improved convergence. The equivalent option, if contacts were needed, was "Bonded" contact. However, for the friction analysis of a spring package, non-linear frictional contacts were used.

For generating the mesh, ANSYS mechanical internal mesh generation functions were used. To analyze flexure springs in all modeling environments it was assured that there are at least two elements across the thickness of the flexure which is between 2 and 3 mm. For the top and bottom surfaces, the minimum mesh size was between 1 and 3 mm with higher resolution at the outer end curves where stress concentrations existed. Also, the Hexahedron mesh type was selected to reduce the total number of elements. This sizing configuration resulted in between 10k and 30k elements for a flexure spring with 124 mm diameter and 2.5 mm thickness.

For the assembly analysis, the mesh resolution was fine for flexures and coarse for the rest of the bodies. The minimum mesh size selection for other parts in the assembly was between 10 and 20 mm. The element number for the whole assembly varied between 800k to up to 3M elements depending on the model.

### **9.1.3 Optimization**

To find the near optimum flexure design, the design exploration package in ANSYS was used. In the design optimization process in ANSYS, there are three main steps, 1-design of experiments, 2-surface/profile responses, and 3-optimization.

In the first step, the parameters for the analysis that are going to be varied are selected and the lower and upper bounds are defined. In the flexure optimization process, four parameters were selected for the parametric study: outer diameter, sweep angle, thickness, and the number of arms. The range for each parameter is shown in Table 7. The step value for each of these parameters was 3.2 mm,  $\pi/4$  rad, 0.08 mm, and 1, respectively, for the four parameters. Approximately 1500 design points were generated and directly solved in both static mechanical and modal analysis, to calculate the flexure's stiffness, maximum stress, and the natural frequency. Having the results of design points, in step 2, response surfaces are generated using artificial intelligent methods. For the flexure design, a neural network (NN) with three layers was selected. It was selected to increase the total number of design points to 6000 to increase the resolution for the final selection. Compared to other methods, NN worked faster with an acceptable R-squared value higher than 0.95. In this step, the sensitivity charts are also generated. In the last step, design criteria were defined to select the possible candidates amongst all available design points. The trade-off feature in the optimization step was the most valuable information as it demonstrated all of the design points in charts with the selected axis. For this study, very high maximum stress values were removed and the rest of the data were depicted in a chart with the frequency and maximum stress axis.

#### **9.1.4 CFD**

To find the energy loss of the oscillating flexure springs due to resistive drag force, a fluid-structure analysis was performed. To generate the fluid mesh, a round cylinder enclosing a flexure spring(s) were generated in DesignModeler. A "System Coupling" toolbox was used in ANSYS Workbench to connect a transient structural, and a fluid simulation (Fluent) component to transfer the displacement and force between these environments. The shared surfaces of the fluid and solid bodies were defined as "fluid solid interaction" BCs. In the solid environment, a displacement BC was used to move the center of the flexure with different amplitudes and frequency. In the fluid environment, the displacement of the shared surfaces was received as an input, and forces on these shared surfaces calculated using the fluid (air) density, pressure and velocity. A dynamic mesh algorithm was used in Fluent. The elements break-up ratio was set to an appropriate value to assure that the displacement of a shared surface in one iteration was not greater than the length scale of the adjacent fluid elements. With the minimum element size of about 2 mm, located in the flexure

spiral cuts, the setting was to have a length scale of close to 2 mm, and the time step was set that the displacement of one iteration did not exceed 2 mm near the center of the flexure where the maximum displacement occurred. The FSI simulation was solved and continued for one complete cycle. In the CFD solver, a pressure passed coupled algorithm was used and the drag force and drag force coefficients on the shared surfaces were quantified and extracted as the results for the study of geometrical dimensions of flexure on the drag force losses.

For the turbulence model, a two-equation  $k$ - $\varepsilon$  model were implemented. The solution was reached with the residual values of  $1e-6$  for the continuity equation, and  $1e-4$  for the rest of parameters such as turbulence and velocities.

## **9.2 Stress-strain Test Rig**

A test rig was designed for the measurement of flexure's force/displacement relations and also the stress-strain on its arms. The force/displacement was used to calculate the instantaneous axial stiffness of the flexure for the validation of the FEA results and also for the statistical analysis. A Shimadzu 10K tensile test machine was used for applying an axial force to the center of a flexure spring through a shaft which was fixed to the center via a bolted connection. Both the inner and outer perimeters of the spring were fixed to be similar to the main BC in the FEA which was a fixed type.

For the force/displacement tests, the Instron machine program was set to apply a displacement of 10 mm downward at a pace of 5mm/min. The incorporated load cell measured and recorded the instantaneous reaction force from the spring to the machine. The data recording rate was 100 Hz.

The same test procedure was implemented for the stress-strain tests. The Instrone machine programming was unchanged, but to measure the stress magnitude on arms to be compared with the FEA results, three strain gauges were installed on one arm of a titanium flexure. Six bi-linear strain gauges with the nominal resistance of  $120\ \Omega$ , and maximum  $V_{rms}$  of 5.5 volts were installed on three locations: on each side of the flexure, two were installed near both ends of a spiral on one arm and one was installed at the middle on the same arm. Using two strain gauge on two sides of a location on spring (full-bridge installation), result in higher accuracy of strain measurement. Before gluing the strain gauges, the metal surface was cleaned to wipe dust, oil, and grease and

sanded with a sandpaper grit 120. The surface was not polished to ensure the cohesion of the glue and the strain gauge. The strain gauges were connected to an indicator/recorder system. The recorder received the voltage signals from the gauges, converted them into strain values, and recorded them on a USB drive. The record rate of the system was 8 Hz.

### **9.3 Analytical Solution Curve Fitting Performance**

The graphs below show the fitting performances and details of the fitted curve equations of each step, for finding the non-dimensionalized coefficients that were used in the analytical solution. The order of steps was finding the corrective coefficients for the 1- radius of flexure ( $C_r$ ), 2- flexure's thickness ( $C_{th}$ ), and 3- flexure's arm width ( $C_w$ ). The curve fitting toolbox in Matlab<sup>TM</sup> version 2019 was used for the calculations.

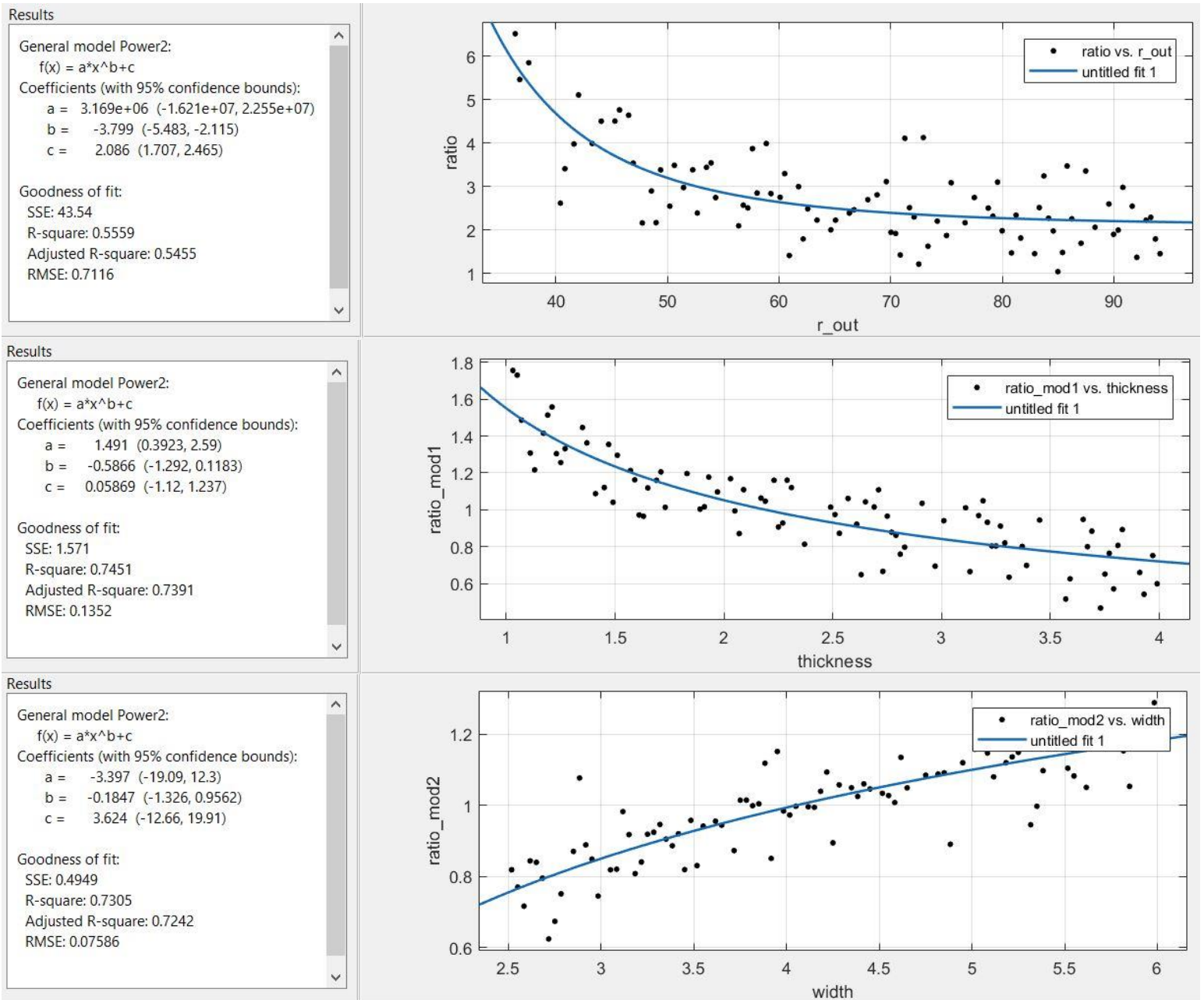


**Figure 115.** Curve fitting details for non-dimensionalized coefficients, top:  $C_r$ , middle:  $C_{th}$ , and bottom:  $C_w$ .

## 9.4 Parametric Study Charts for Titanium Material

Similar results of the optimization process provided in section 3.6, for titanium material are shown.

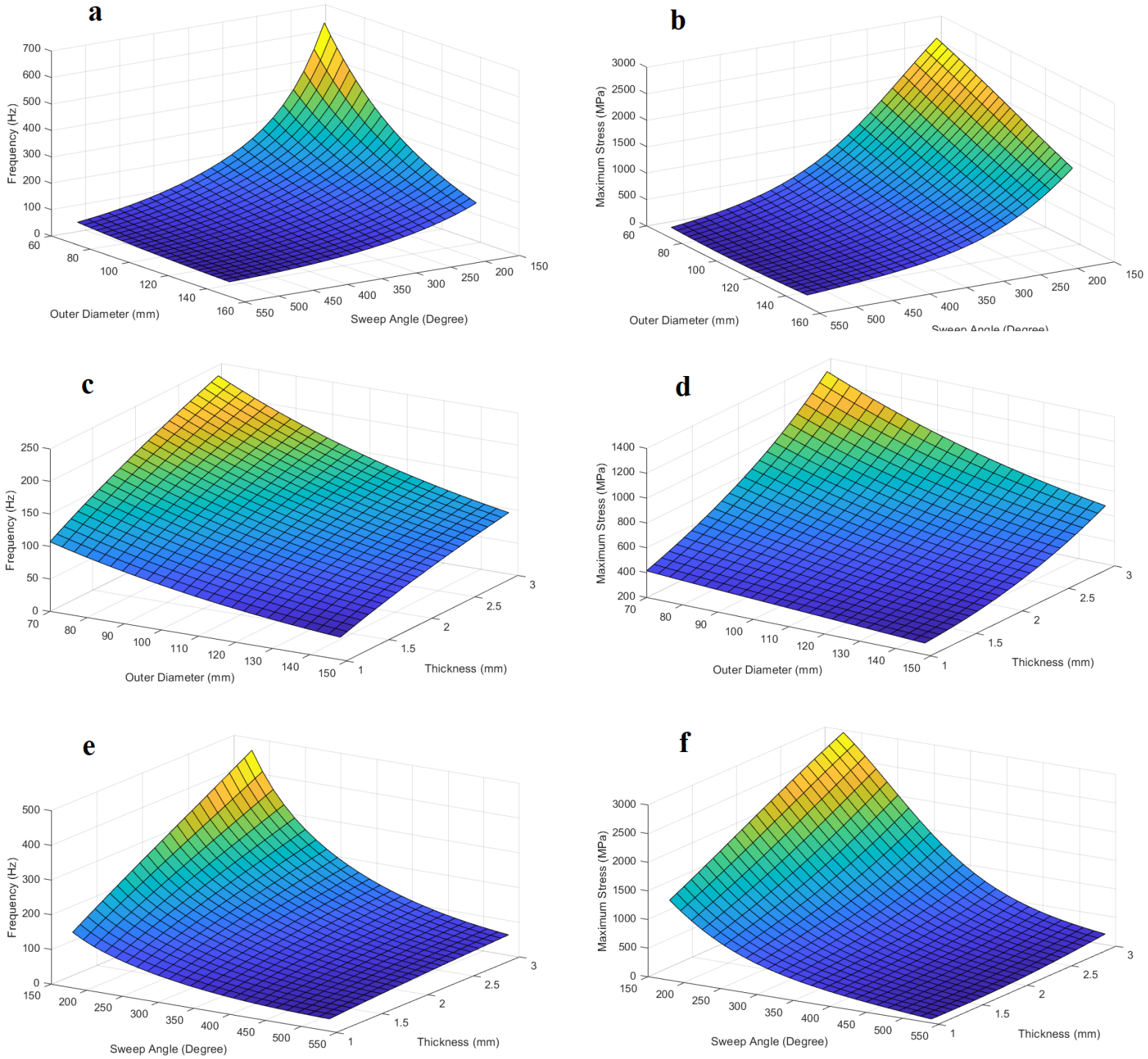


**Figure 116. Titanium material - response surface of interactions of outer diameter and sweep angle on frequency (a) and maximum equivalent stress (b), interactions of outer diameter and thickness on frequency (c) and maximum equivalent stress (d) and interactions of sweep angle and thickness on frequency (e) and maximum equivalent stress (f).**

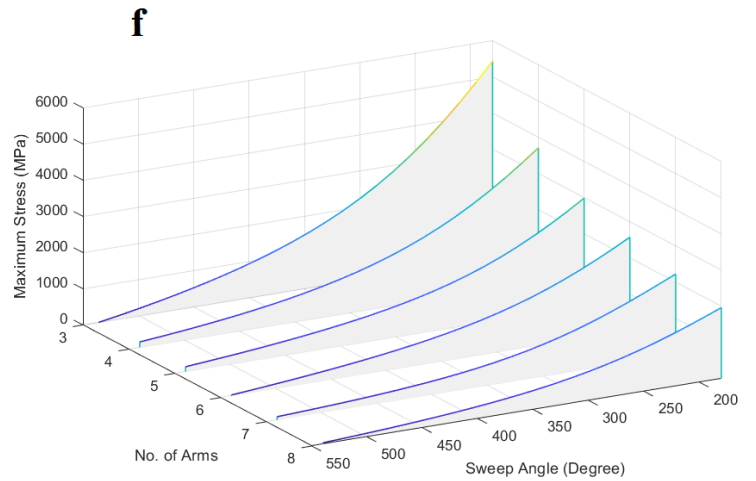
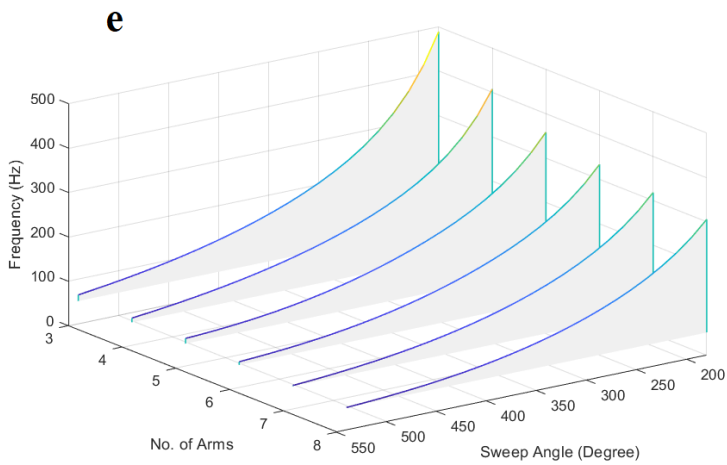
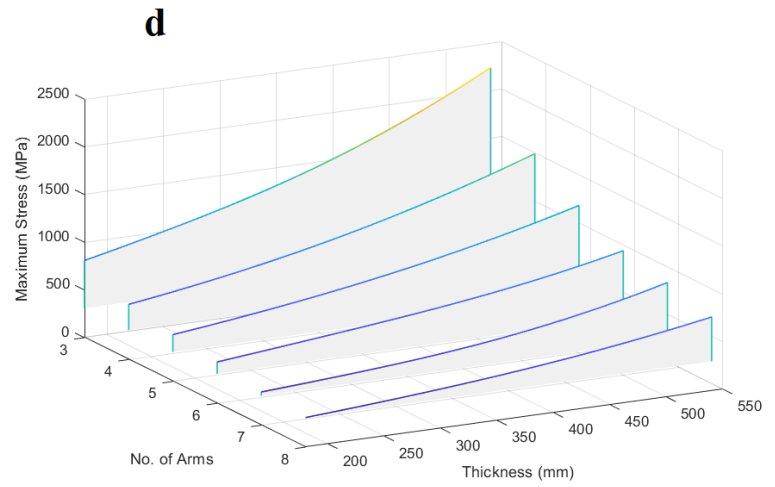
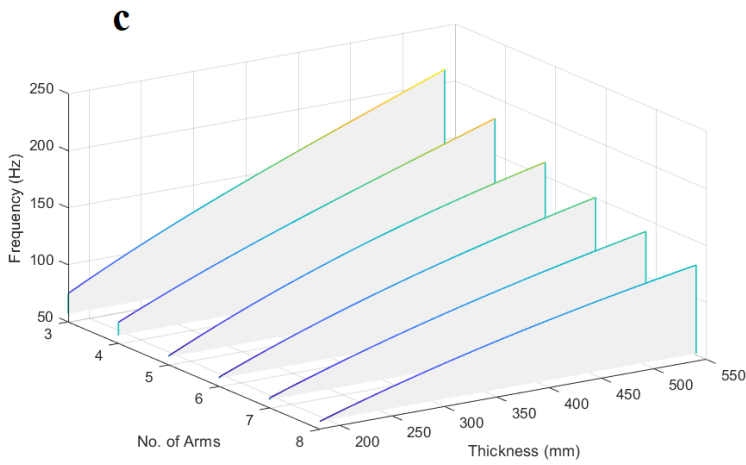
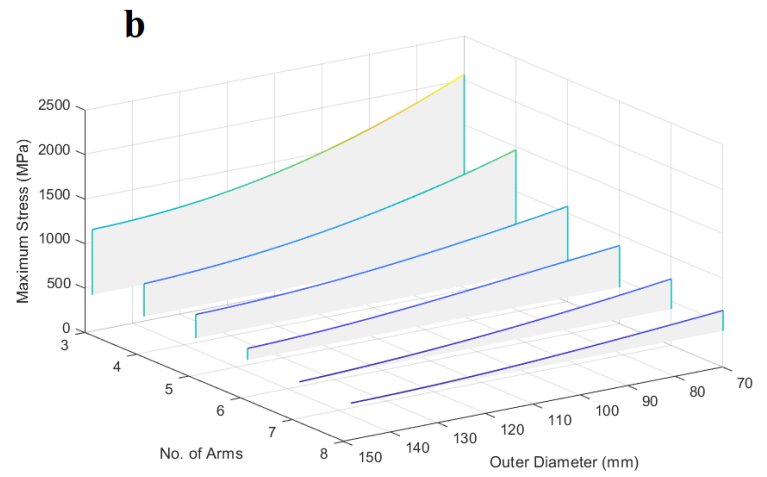
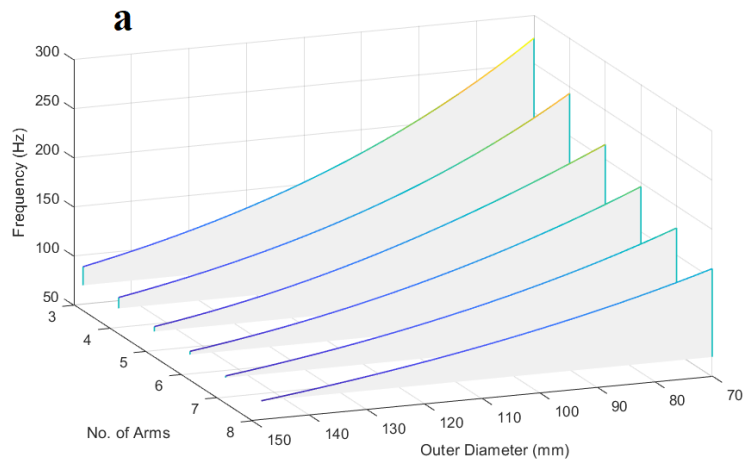


**Figure 117. Titanium material - response profiles of interactions of number of arms and outer diameter on frequency (a) and maximum equivalent stress (b), interactions of number of arms and thickness on frequency (c) and maximum equivalent stress (d) and interactions of number of arms and sweep angle on frequency (e) and maximum equivalent stress (f).**



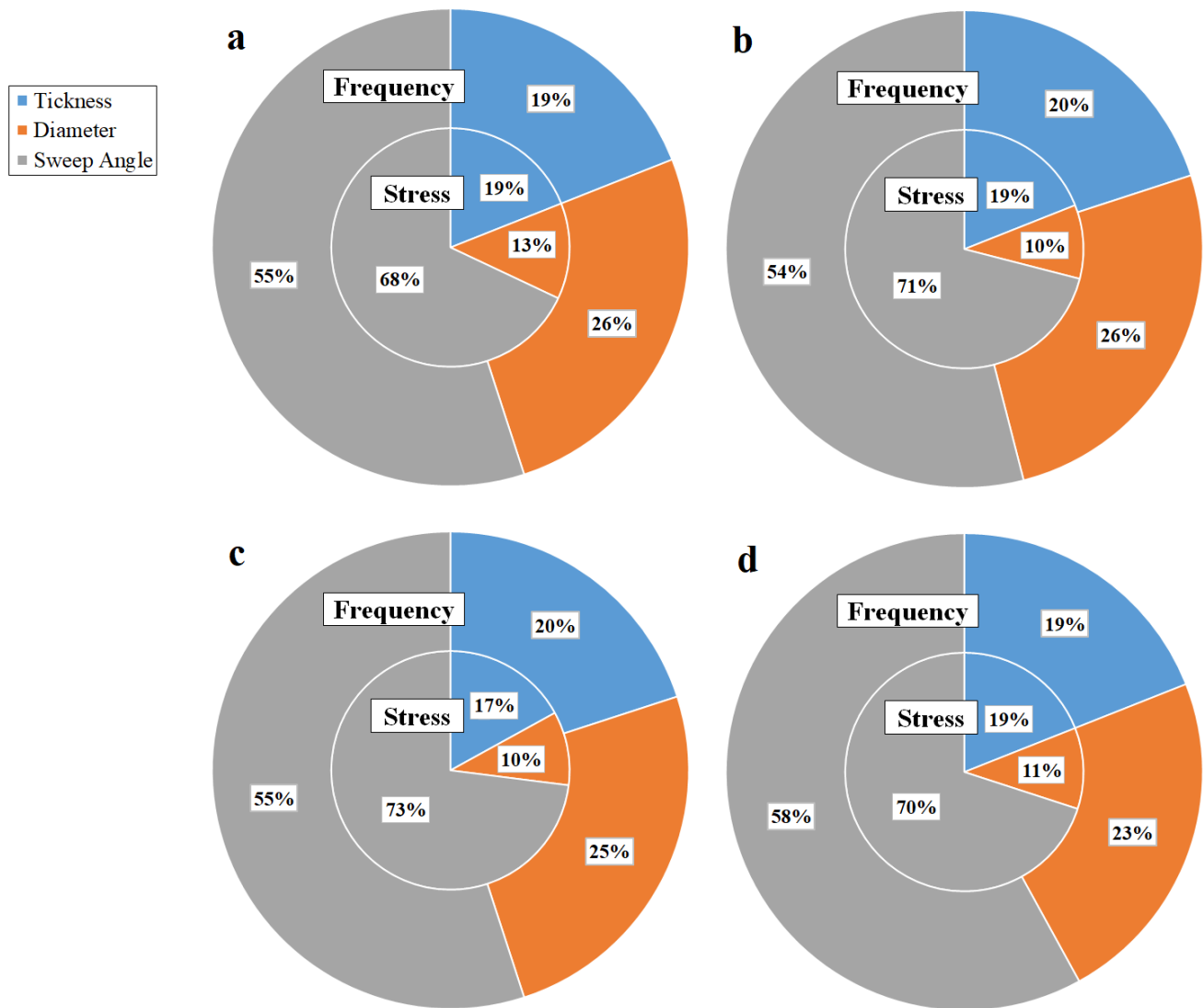


**Figure 118. Titanium material - sensitivity charts for design parameters of a flexure with, a) 4 arms, b) 5 arms, c) 6 arms, d) 7 arms. The inner circles are associated with stress and the outer circles are associated with frequency. Sweep angle is demonstrated to have the most influence on both stress and frequency.**

## 9.5 Neural Network Performance Charts

In this section, the performance of the used neural network is analyzed. All steps were performed in Matlab™ version 2019. Using two hidden layers and 10 neurons at each layer, showed very good fitting results in terms of R-squared numbers of each step. Figure 119 shows the R-squared values and Figure 120 shows the distribution of the error magnitudes.

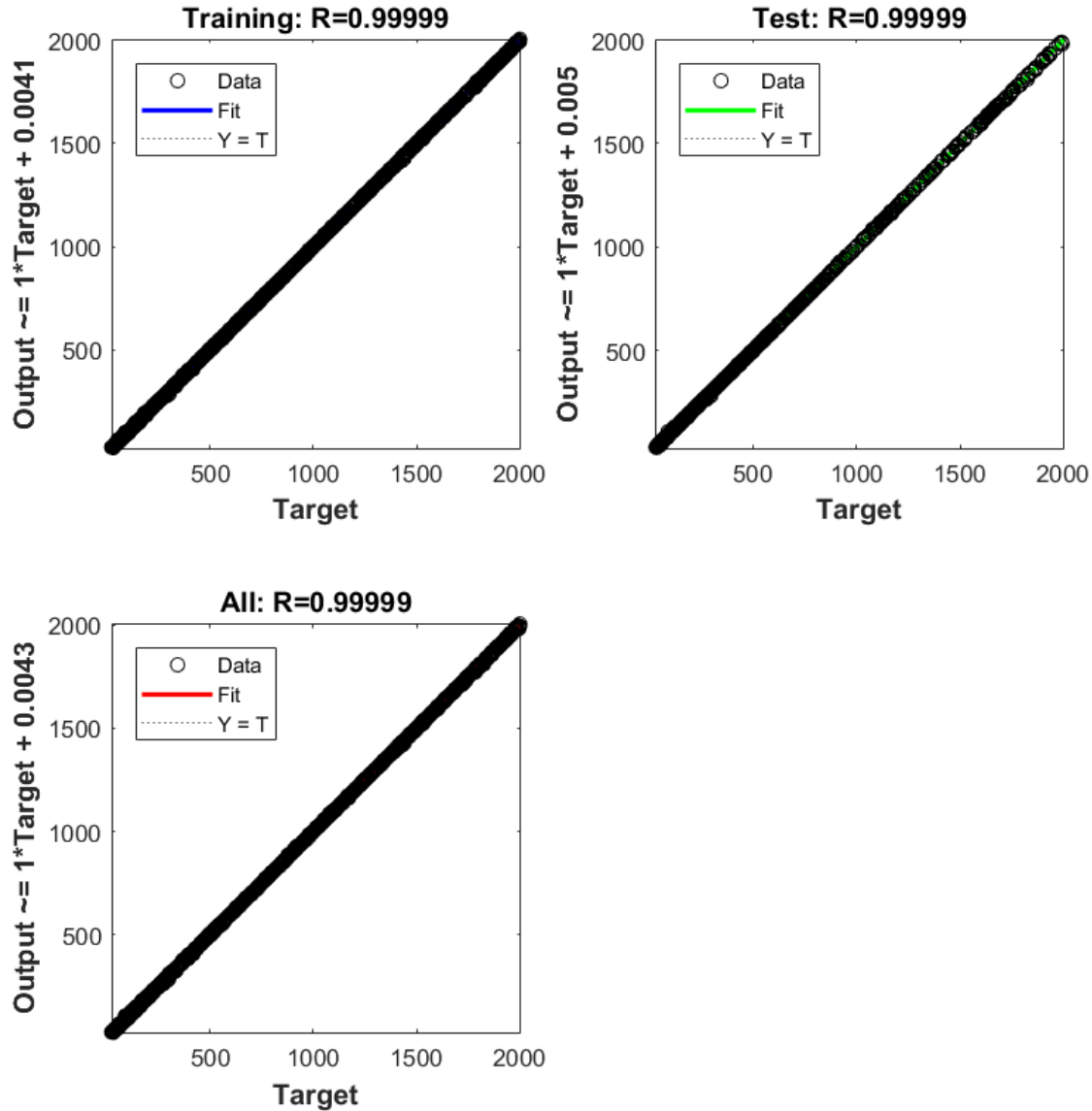


Figure 119. Performance and error results of Bayesian Regularization NN method.

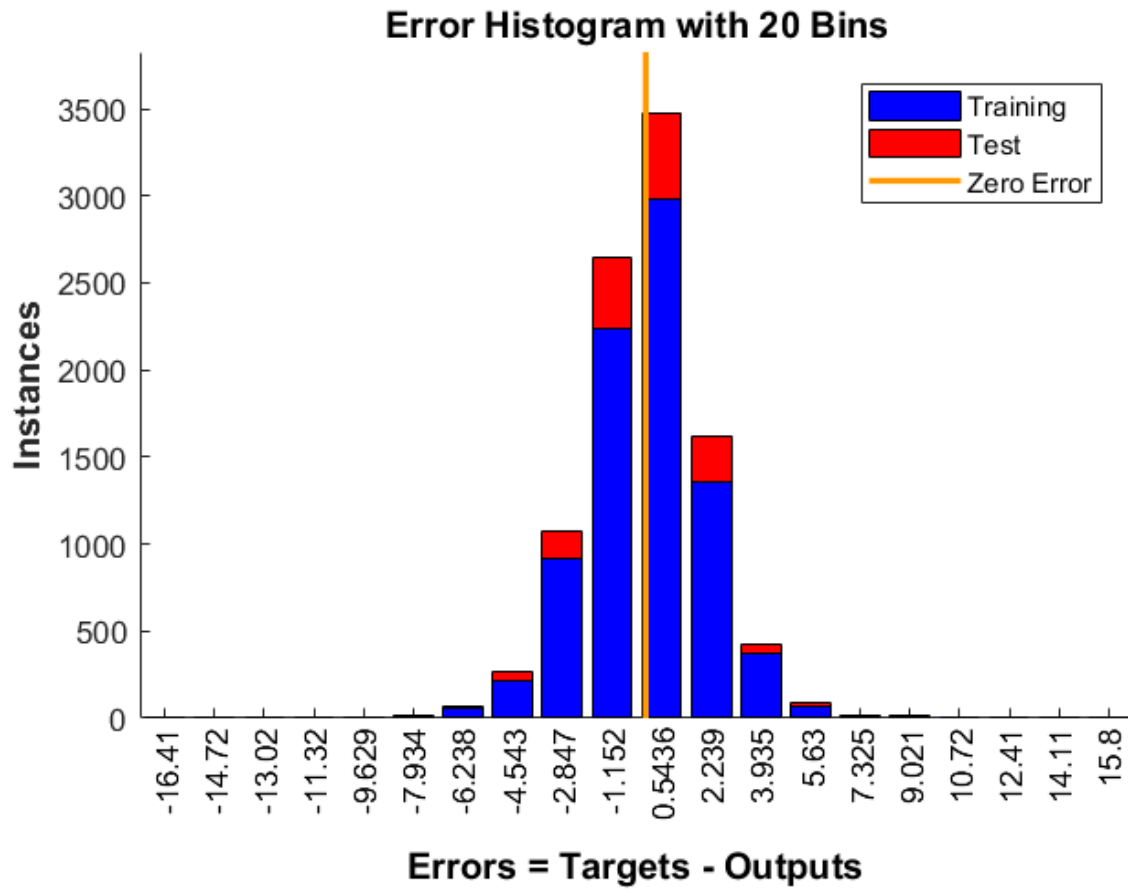


Figure 120. Performance and error results of Bayesian Regularization NN method.

## 9.6 Matlab Function

```
function [Y] = neural_function(x)
%NEURAL_FUNCTION neural network simulation function.
%
%
% Matlab function for primary designing of a flexure spring
% Nima Zamani Meymian, July 2020, WVU
%
% [Y] = neural_function(X,~,~) takes these arguments:
%
% X = Qx4 matrix, input #1
% X format is a [1,4] vector including input parametrs as: ...
% X=[sweep angle (rad),outer diameter (mm), no. arms,thickness (mm)]
%
% and returns:
% Y = Qx2 matrix, output #1
% where Q is the number of samples.
% Y output format is Y=[stress(MPa),frequency(Hz)]
%
%#ok<*RPMT0>
%
%%% example
% x=[6.5,125,5,1.75]
% y=neural_function(x)
%
% x =
%
% 6.5000 125.0000 5.0000 1.7500
%
%
% y =
%
% 604.5177 82.4223
%
% Important Note: The output stress value is for a flexure spring with 10
mm axial
% deflection. For designs with different values, the stress should be scaled
% in a linear manner.
% ===== NEURAL NETWORK CONSTANTS =====
% Input 1
x1_step1.xoffset = [3.142441557;70.03333333;3;1];
x1_step1.gain =
[0.318158993650848;0.0250104210077111;0.4;1.00040511204931];
x1_step1.ymin = -1;
% Layer 1
```

```

b1 = [-0.11531158914072260624;-1.094322751823448403;1.0746174155999457245;
0.79929767682617591795;0.57931896222051670886;0.56640029401678326781;
0.6091617650732965572;0.4972249653023842475;-0.93172927060162036295;
1.3340443198809526226];
IW1_1 = [-0.47780570508886371917 -0.66008203829903544513
0.084360236672797073165
-0.71456803733941265389;-0.52312340726792505574 -0.027171136802864155613
-0.41803092650366302507 -0.51389519804095828981;-0.17288373914992413716
-0.072495576662141889002 1.237659349218474647 0.080100363631448567858;
-0.093300307683494607125 -0.0072307661562114869044 -3.1519592638817561792
0.063928107636819261894;-0.030518340468360515005 0.0096531669651450293518
-1.8644789575344611343 0.096492068925692911496;0.71634531004692814093
0.39272039603492536752 0.5082206389333683294 -0.1223795256379943408;
0.67951622264806199603 0.21703063095385566328 -0.089025900101913441054
-0.18211558636448102466;-0.32000911194486258982 0.21230251177130737839
0.22462339882911347422 0.39758500896282611414;-0.39989380014525105489
-0.0498321243028857358 -0.73837523440761754223 0.10217510409112699754;
-0.1682735698340350472 0.0041568413359087987013 1.5877473462441913377
0.089608078700836368835];
% Layer 2
b2 = [0.32608513000282912664;0.84983065196692475496;-
0.43259501840264530381;
0.78758448410598702605;-0.37442091281539741088;1.3396276473766031145;
7.4283997317109484726;-3.6622919495103762877;0.7518512101911123402;
0.70876722027798177983];
LW2_1 = [-0.22767797057385238957 -0.17483717005391946619
1.8017074350158728269
-0.20047635239394800966 0.21860136265613316908 0.9393155327853612846
-0.93556536746422447326 0.18850708203740282332 0.2480563522583272007
-1.7130521452504863245;-0.20538785021098135419 0.3410101843354879092
-1.6358073951757239328 -0.38587810451203724549 0.62258043867057621945
0.47452312065444035571 0.073365188527253474837 -0.27199845525776977784
0.26245978045804857492 1.3839740729713922995;-0.24284568350021357164
0.87152919806141671 -5.5253434899296021143 -1.0094656862066424541
2.8437052648611151895 0.46267660235031332627 1.7433702681321765482
1.1241379863006550899 -8.3823698389502325767 1.4840186664727426091;
-0.11087832102535781498 -4.9739991391085848927e-05 -2.5490364505959175467
0.77671578106082594939 0.07283199048987779034 -0.062139997830678070367
-0.13735428388511503051 -0.76599522933557107063 -1.2911938876048842939
1.2763369295339257459;0.29331612088879882583 0.096791636794963428758
-0.9687006295505647957 0.42855536965312851505 -0.67863244555400814573
-0.59232260585134521857 0.48807472267066842608 0.023487487256433133009
-0.39988365957144111906 0.81534893882820502764;-0.51562726796459834588
0.24247864069298677436 -0.59073610983754498704 1.9188085252862523422
-0.62746858529947946437 1.1110482844202775876 -1.9513971568077521646
-1.1794103956020736135 -3.3068045868903142015 -1.6066355508521015238;

```

```

0.10667319570742479773 0.016015296786474890467 -0.48118355516494243362
2.6109968714162619108 -8.9491324127937339483 -0.10707143823834236462
-0.24537624448195788363 -0.58833483932215713264 0.1063522775648539781
1.3691741622676976142;-0.00090814313485277113006 0.065244903625501907141
1.988627314002614499 -0.13160116498509907834 -0.23996603354574194689
0.18996578731311075661 -0.24967131172867734756 0.45837456357954337038
0.15545628442722858598 1.4213587900673905207;-0.061983188182280921086
0.010858108433234522905 -0.44175434733951590704 -0.21812188678404839659
0.60458242991057187243 -0.21255346176696601757 -0.088015277879373313152
-1.0138663439524937537 -0.029650868693715311253 1.7155922032756472095;
0.0043389412161577356128 -0.015388850664971214302 -3.254355253278073512
0.81442890943438039919 -1.2049100478988872265 -0.1317698216655276422
1.252745668493591813 -0.2376856211926211826 -0.46042172868879183145
2.6810674771502971403];
% Layer 3
b3 = [-0.094781543903031256759;3.2595932741552386958];
LW3_2 = [1.427634202585845058 0.12364949534717446789 -
0.035046583183189324029
-3.7848054102333805737 2.3593198596245268384 1.2768177802318179115
5.3079020693830889499 -5.8222944706502302026 -5.7986722131289534232
-3.6093861794669992449;-1.1865372016229374097 -2.2594369491842445363
-2.8964877805034472402 -0.3914614396663199658 -2.062094728043092573
0.05304109536938150099 -0.060344262260697403844 -0.8726184638535837701
0.019934245473647155961 -0.61032611046753237893];
% Output 1
y1_step1.ymin = -1;
y1_step1.gain = [0.00102707282758764;0.00508422554604659];
y1_step1.xoffset = [51.04849452;25.4602886];
% ===== SIMULATION =====
X = X';
% Format Input Arguments
isCellX = iscell(X);
if ~isCellX
X = {X};
end
% Dimensions
TS = size(X,2); % timesteps
if ~isempty(X)
Q = size(X{1},2); % samples/series
else
Q = 0;
end
% Allocate Outputs
Y = cell(1,TS);
% Time loop
for ts=1:TS

```

```

% Input 1
Xp1 = mapminmax_apply(X{1,ts},x1_step1);
% Layer 1
a1 = tansig_apply(repmat(b1,1,Q) + IW1_1*Xp1);
% Layer 2
a2 = tansig_apply(repmat(b2,1,Q) + LW2_1*a1);
% Layer 3
a3 = repmat(b3,1,Q) + LW3_2*a2;
% Output 1
Y{1,ts} = mapminmax_reverse(a3,y1_step1);
end
% Final Delay States
Xf = cell(1,0);
Af = cell(3,0);
% Format Output Arguments
if ~isCellX
Y = cell2mat(Y);
Y = Y';
end
end
% ===== MODULE FUNCTIONS =====
% Map Minimum and Maximum Input Processing Function
function y = mapminmax_apply(x,settings)
y = bsxfun(@minus,x,settings.xoffset);
y = bsxfun(@times,y,settings.gain);
y = bsxfun(@plus,y,settings.ymin);
end
% Sigmoid Symmetric Transfer Function
function a = tansig_apply(n,~)
a = 2 ./ (1 + exp(-2*n)) - 1;
end
% Map Minimum and Maximum Output Reverse-Processing Function
function x = mapminmax_reverse(y,settings)
x = bsxfun(@minus,y,settings.ymin);
x = bsxfun(@rdivide,x,settings.gain);
x = bsxfun(@plus,x,settings.xoffset);
end

```